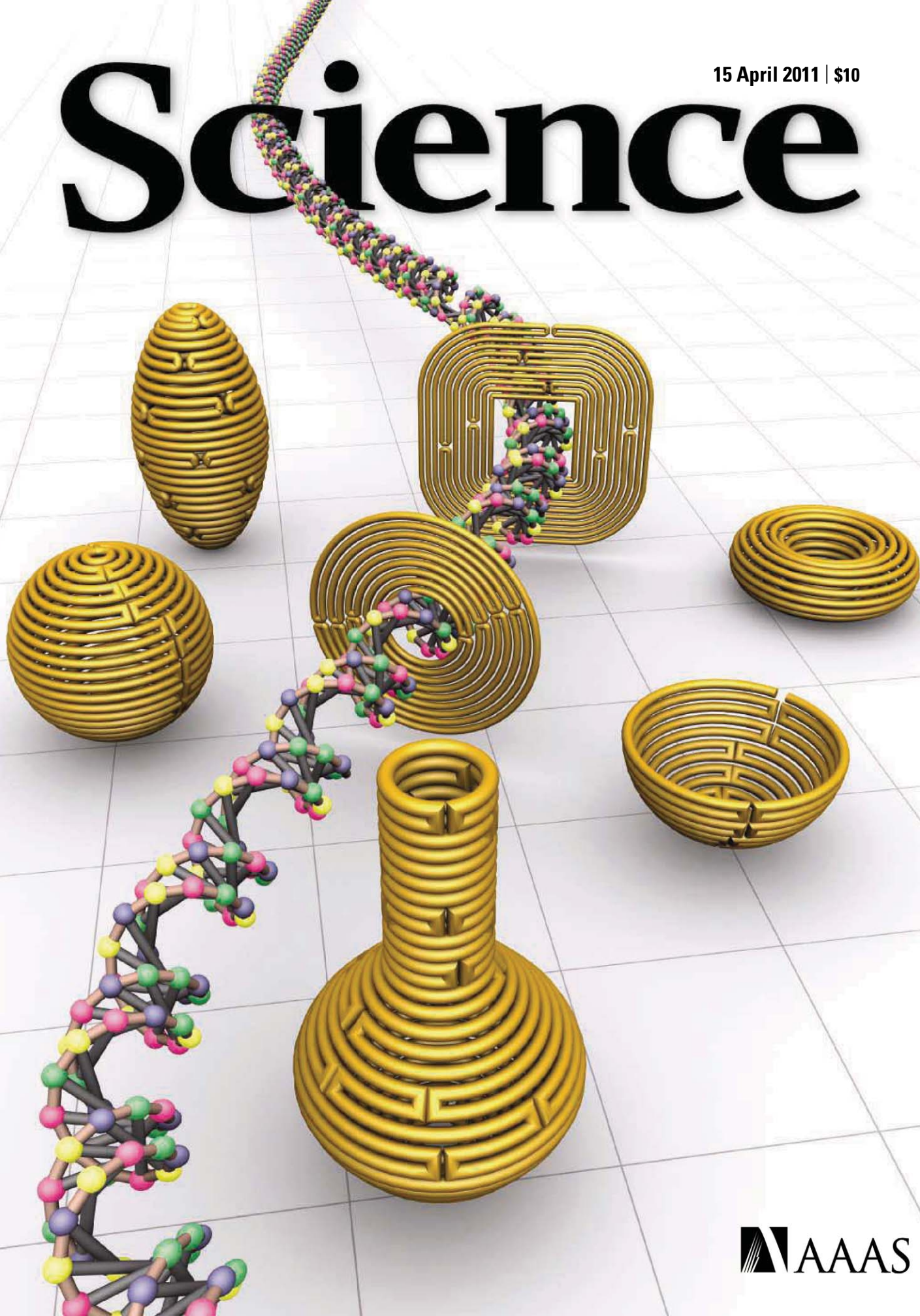


15 April 2011 | \$10

Science



SPECIAL OFFER
\$99 ANTIBODY
SPECIAL

Find out more @
www.epitomics.com/products/promo



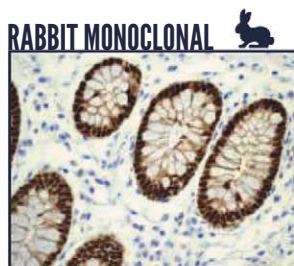
THE RABBIT **MONOCLONAL** ADVANTAGE

- High specificity and affinity
- More diverse epitope recognition
- Improved response to mouse antigens
- Validated in multiple applications and species

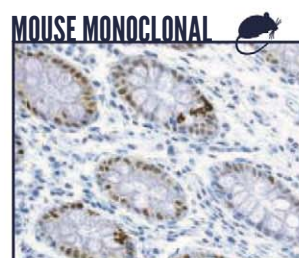
What is the Rabbit Monoclonal Advantage (?)

Rabbit Monoclonal Antibodies (RabMAbs®) provide the combined benefits of superior antigen recognition of the rabbit immune system with the specificity and consistency of a monoclonal antibody, bringing you the highest quality antibody possible.

Find more @ www.epitomics.com/advantage



CDX2 RabMAb



CDX2 MouseMAb

Paraffin-embedded human colon tissue stained with Epitomics' CDX2 RabMAb (Cat.# 2475-1) and Vendor A's CDX2 Mouse Monoclonal under optimal conditions



cell sciences®

cytokine center

Browse our web site of recombinant proteins, including cytokines, growth factors, chemokines and neurotrophins. Daily shipping and competitive pricing are offered. Bulk quantities of many proteins available. Cell Sciences also carries corresponding antibodies and ELISA kits.



LIST OF PROTEINS

4-1BBL	Caspase-3	sFlt-1 (D3)	IL-2	MEC	sRANK
4-1BB Receptor	Caspase-6	sFlt-1 (D4)	IL-3	Mek-1	sRANKL
6 Ckine	CD4	sFlt-1 (D5)	IL-4	MIA	RANTES
ACAD8	CD14	sFlt-1 (D7)	sIL-4 Receptor	Midkine	RELM- α
ACAT2	CD22	Flt3-Ligand	IL-5	MIG / CXCL9	RELM- β
gAcrp30/Adipolean	CD40 Ligand / TRAP	sFlt-4	IL-6	MIP-1 α / CCL3	Resistin
Activin A	CD95 / sFas Ligand	sFlt-4/ Fc Chimera	sIL-6 Receptor	MIP-1 β / CCL4	RPTP β
ACY1	CD105 / Endoglin	Follistatin	IL-7	MIP-3 / CCL23	RPTP γ
ADAT1	CHIPS	FSH	IL-8 (72 a.a.)	MIP-3 α / CCL20	RPTP μ
Adiponectin	CNTF	Fractalkine/ CX3C	IL-8 (77 a.a.)	MIP-3 β / CCL19	SCF
ADRP	Collagen	G-CSF	IL-9	MIP-4 (PARC) / CCL18	SCGF- α
AITRL	CREB	α -Galactosidase A	IL-10	MIP-5 / CCL15	SCGF- β
Akt1	CTACK/CCL27	Galectin-1	IL-11	MMP-3	SDF-1 α
Alpha-Feto Protein (AFP)	CTGF	Galectin-3	IL-12	MMP-7	SDF-1 β
Alpha-Galactosidase A	CTGFL/WISP-2	Gastrointestinal CA	IL-13	MMP-13	Secretin
Angiopoietin-1 (Ang-1)	CTLA-4/Fc	GCP-2	IL-13 analog	Myostatin	SF20
Angiopoietin-2 (Ang-2)	CXCL16	GDF-3	IL-15	Nanog	SHP-2
Angiostatin K1-3	Cytokeratin 8	GDF-9	IL-16 (121 a.a.)	NAP-2	STAT1
Annexin-V	DEP-1	GDF-11	IL-16 (130 a.a.)	Neurturin	c-Src
apo-SAA	Desmopressin	GDNF	IL-17	NFAT-1	TACI
Apolipoprotein A-1	Disulfide Oxidoreductase	GLP-1	IL-17B	beta-NGF	TARC
Apolipoprotein E2	E-selectin	Glucagon	IL-17D	NOGGIN	TC-PTP
Apolipoprotein E3	ECGF	Goserelin	IL-17E	NOV	TECK
Apolipoprotein E4	EGF	GM-CSF	IL-17F	NP-1	TFF2
APRIL	Elafin/SKALP	GPBB	IL-19	NT-1/BCSF-3	TGF- α
Artemin	EMAP-II	GRO α	IL-20	NT-3	TGF- β 1
ATF2	ENA-78	GRO β	IL-22	NT-4	TGF- β 2
Aurora A	Endostatin	GRO γ	IL-31	Ocreotide	TGF- β 3
Aurora B	Enteropeptidase	GRO/MGSA	Insulin	Oncostatin M	Thymosin α 1
BAFF	Eotaxin	Growth Hormone	IP-10	Osteoprotegerin (OPG)	sTIE-1/Fc Chimera
BAFF Receptor	Eotaxin-2	Growth Hormone BP	JE	OTOR	sTIE-2/Fc Chimera
BCA-1 / BLC / CXCL13	Eotaxin-3 (TSC)	GST-p21/WAF-1	JNK2a1	Oxytocin	TL-1A
BCMA	EPHB2	HB-EGF	JNK2a2	p38- α	TNF- α
BD-1	EPHB4	HCC-1	KC / CXCL1	Parathyroid Hormone	TNF- β
BD-2	Eptifibatide	HGF	KGF	PDGF-AA	sTNFR1
BD-3	Erk-2	Histidyl-tRNA synthetase	L-asparaginase	PDGF-AB	sTNFR2
BDNF	Erythropoietin (EPO)	Histrelin	LAG-1	PDGF-BB	TPO
Bivalirudin	Exodus-2	HRG1- β 1	LALF Peptide	Persephin	TRAIL/Apo2L
BMP-2	Fas Ligand	I-309	LAR-PTP	PF-4	sTRAIL R-1 (DR4)
BMP-4	Fas Receptor	I-TAC	LC-1	PIGF-1	sTRAIL R-2 (DR5)
BMP-7	FGF-1 (acidic)	IFN- α	LBP	PIGF-2	TSH
BMP-13	FGF-2 (basic)	IFN- α A	LD-78 β	PKA α -subunit	TSLP
sBMPR-1A	FGF-4	IFN- α 2a	LDH	PKC- α	TWEAK
Brain Natriuretic Protein	FGF-5	IFN- α 2b	LEC/NCC-4	PKC- γ	TWEAK Receptor
BRAK	FGF-6	IFN- β	Leptin	Pleiotrophin	Urokinase
Breast Tumor Antigen	FGF-7/ KGF	IFN- γ	LIGHT	PLGF-1	VEGF121
C5a	FGF-8	IFN-Omega	LIX	Polymyxin B (PMB)	VEGF145
C5L2 Peptide	FGF-9	IGF-I	LKM	PRAS40	VEGF165
C-10	FGF-10	IGF-II	LL-37	PRL-1	VEGF-C
C-Reactive Protein	FGF-16	proIGF-II	Lymphotactin	PRL-2	VEGF-C I525
C-Src	FGF-17	IGFBP-1	sLYVE-1	PRL-3	EG-VEGF
Calbindin D-9K	FGF-18	IGFBP-2	M-CSF	Prokineticin-2	VEGF-E
Calbindin D-28K	FGF-19	IGFBP-3	MCP-1 (MCAF)	Prolactin	HB-VEGF-E
Calbindin D-29K	FGF-20	IGFBP-4	MCP-2	Protirelin	sVEGFR-1
Calmodulin	sFGFR-1 (IIIc) / Fc Chimera	IGFBP-4	MCP-3	PTHrP	sVEGFR-2
Calcitonin Acetate	sFGFR-2 (IIIc) / Fc Chimera	IGFBP-5	MCP-4	PTP1B	sVEGFR-3
Carbonic Anhydrase III	sFGFR-3 / Fc Chimera	IGFBP-6	MCP-5	PTP-IA2	WISP-1
Carcino-embryonic Antigen	sFGFR-4 / Fc Chimera	IGFBP-7	MDC (67 a.a.)	PTP-MEG2	WISP-2
Cardiotrophin-1	sFlt-1 (native)	IL-1 α	MDC (69 a.a.)	PTP-PEST	WISP-3
		IL-1 β	MDH		WNT-1

CELL SCIENCES INC • 480 NEPONSET STREET, BUILDING 12A, CANTON, MA 02021 • INFO@CELLSCIENCES.COM

TOLL FREE: (888) 769-1246 • TEL: (781) 828-0610 • FAX: (781) 828-0542 • WEB: WWW.CELLSCIENCES.COM

www.cellsciences.com

GE Healthcare
Life Sciences

Inspired to Accelerate scale-up

Inspired by your need for fast and predictable scale-up, we introduce ÄKTA™ avant 150, the latest development in our ÄKTA avant series.

Optimize your process with ÄKTA avant 25 and then scale-up seamlessly to ÄKTA avant 150 by automatically converting your methods using UNICORN™ 6.1 software.

ÄKTA avant is designed to fully exploit the advantages of our modern BioProcess™ media like MabSelect™ and Capto™.

Dedicated column formats ensure seamless scalability from process development to manufacturing – from prepacked HiScreen™ columns to HiScale™ to AxiChrom™ with Intelligent Packing.

Want to know more? Register today to receive a copy of the ÄKTA avant 150 Data File.
www.gelifesciences.com/pr-avant

GE, imagination at work, and GE monogram are trademarks of General Electric Company.
ÄKTA, AxiChrom, BioProcess, Capto, HiScale, HiScreen, MabSelect, and UNICORN are trademarks of GE Healthcare companies.
© 2010 General Electric Company – All rights reserved.
First published Sept. 2010
GE Healthcare Bio-Sciences AB, Björkåttan 30, 751 84 Uppsala, Sweden
GE09-10



imagination at work

EDITORIAL

- 283 The Young Academy Movement
Bruce Alberts

NEWS OF THE WEEK

- 288 A roundup of the week's top stories

NEWS & ANALYSIS

- 291 Research Holds Up Well in Final 2011 Agreement
>> Science Podcast
- 292 Fukushima Radiation Creates Unique Test of Marine Life's Hardiness
- 293 Outlook Brightens for Plastic Solar Cells
- 294 Chinese Neurosurgeons Quietly Push for Easing of Brain Operation Ban
- 295 Tennessee House Bill Opens Door to Challenges to Evolution, Climate Change
- 296 A Sign of New Particles or General Restlessness?
- 297 Frightening Risk of Marfan Syndrome, and Potential Treatment, Elucidated
>> Reports pp. 358 and 361

NEWS FOCUS

- 298 Uncertain Future for Tropical Ecology
- 300 Do Jumping Genes Spawn Diversity?
- 302 Lunar and Planetary Science Conference
Asteroid Model Shows Early Life Suffered a Billion-Year Battering
Prime Science Achieved at Asteroid
A Badly Battered Vesta Awaits Dawn's Arrival
Snapshots From the Meeting

LETTERS

- 305 Putting the Ocean Under Review
P. A. Bernal
Low-Dose Radiation Knowledge: Priceless
M. H. Barcellos-Hoff et al.
The Risks and Benefits of Re-Consent
J. S. Forsberg et al.
Response
S. B. Trinidad et al.
- 306 CORRECTIONS AND CLARIFICATIONS

BOOKS ET AL.

- 307 A History of Communications
M. T. Poe, reviewed by C. Kelty
- 308 Genetic Justice
S. Krinsky and T. Simoncelli, reviewed by M. A. Goldman

POLICY FORUM

- 309 Genomics, Biobanks, and the Trade-Secret Model
R. Mitchell et al.

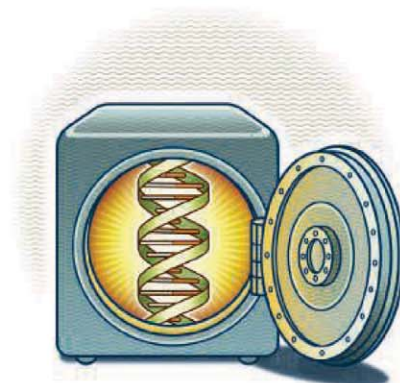
PERSPECTIVES

- 311 Photosynthesis, Reorganized
M. J. West-Eberhard et al.
- 312 Cytonemes Show Their Colors
M. Affolter and K. Basler
>> Report p. 354
- 313 Make It Quantum and Continuous
P. Grangier
>> Report p. 330
- 315 Another Spin on Graphene
A. H. Castro Neto
>> Report p. 328
- 316 A Frontal Challenge for Climate Models
R. Ferrari
>> Research Article p. 318

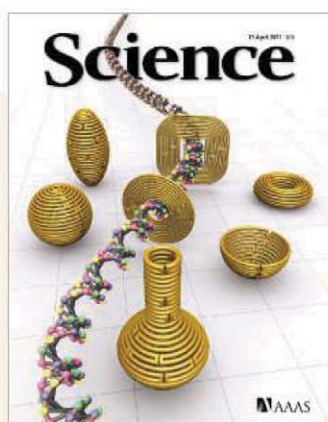
CONTENTS continued >>



page 298



page 309



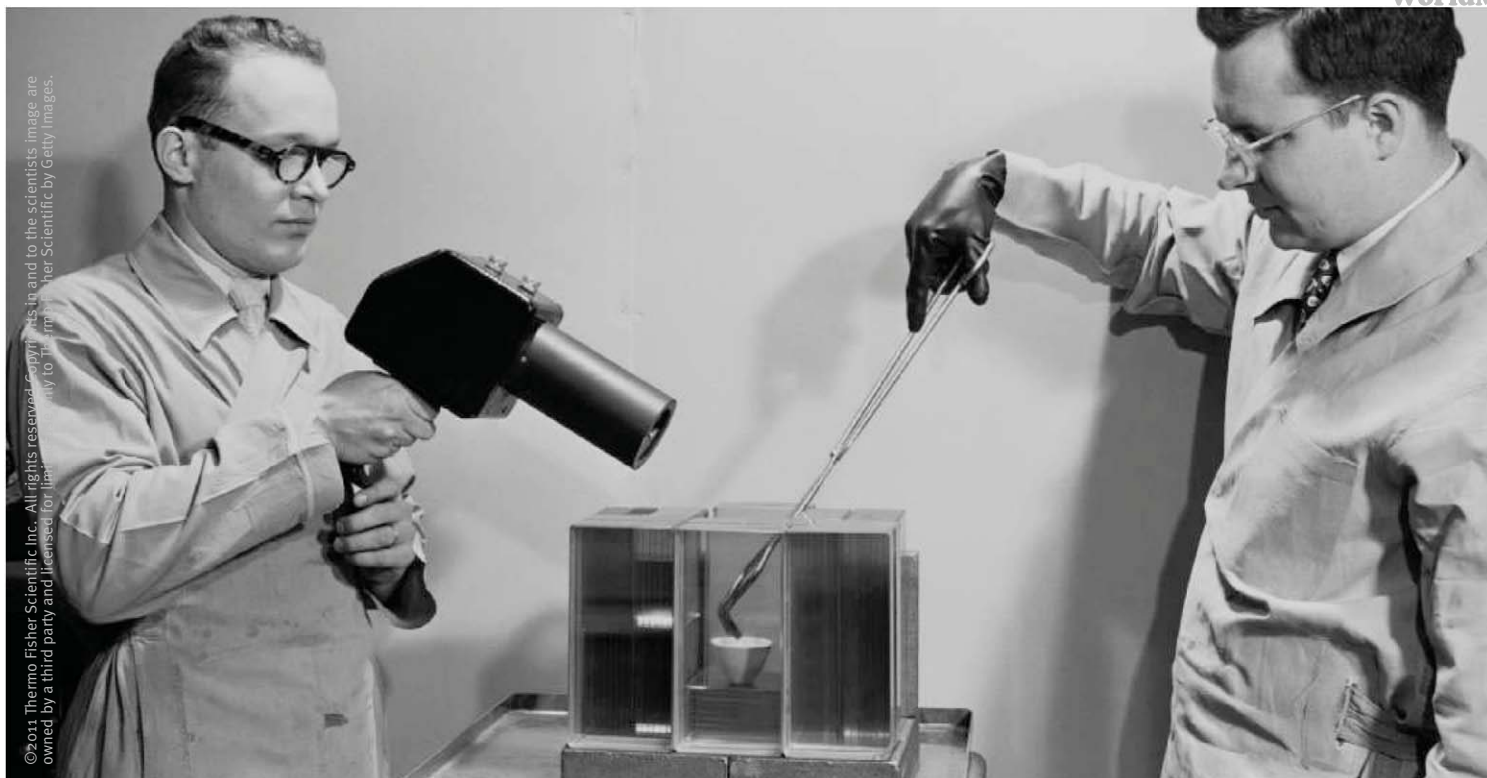
COVER

Schematic representations of DNA nanostructures with complex curvatures including two-dimensional arrangements of concentric rings and three-dimensional shapes, including a nanoflask 70 nanometers tall and 40 nanometers wide (DNA molecule is not shown to scale). On page 342, Han *et al.* describe the creation of these structures using a DNA origami folding technique in which double-helical DNA is bent to follow the rounded contours of the target object.

Image: Dongran Han and Hao Yan, The Biodesign Institute and Department of Chemistry and Biochemistry, Arizona State University

DEPARTMENTS

- 281 This Week in *Science*
- 284 Editors' Choice
- 286 *Science* Staff
- 369 New Products
- 370 *Science* Careers



Limited by an outdated PCR system?

You can run 15 minute PCR protocols and use 50% less consumables and energy by getting away from the old standard. Choose Thermo Scientific Piko Thermal Cyclers, Phusion reagents, and ultra thin wall (UTW) plastic consumables for the most rapid and accurate PCR results. These technologically advanced components can be used individually to improve your current workflow, or as a complete solution for advanced PCR.

- Ultra fast PCR cycling protocols optimized to <15 minutes
- 96-well PCR runs using 50% less plastics, reagents and energy
- PCR kits that allow amplification directly from plant, blood, and tissue samples

Start your PCR experiment today

www.thermoscientific.com/advancedpcr



Everything for PCR

Thermo Scientific PCR portfolio has everything you need for successful PCR including industry leading reagents, high-quality instruments and trusted plastic consumables.

Thermo
SCIENTIFIC

Part of Thermo Fisher Scientific

Moving science forward

Qs & AAAS



www.sciencedigital.org/subscribe

For just US\$99, you can join AAAS TODAY and start receiving *Science* Digital Edition immediately!

Qs & AAAS



www.sciencedigital.org/subscribe

For just US\$99, you can join AAAS TODAY and start receiving *Science* Digital Edition immediately!

RESEARCH ARTICLES

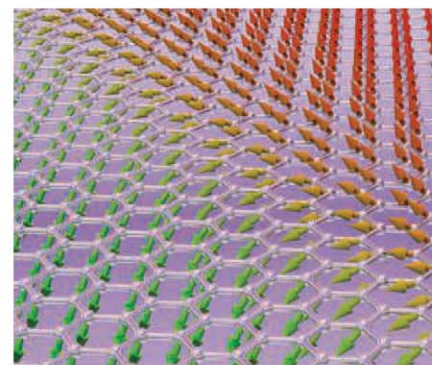
- 318 Enhanced Turbulence and Energy Dissipation at Ocean Fronts**
E. D'Asaro et al.
 Energy in surface ocean currents can dissipate into deep water via enhanced turbulence at the boundaries between water masses.
 >> *Perspective p. 316*
- 322 Structure of an Agonist-Bound Human A_{2A} Adenosine Receptor**
F. Xu et al.
 Changes associated with conformationally selective agonist binding shed light on G protein—coupled receptor activation.

REPORTS

- 328 Giant Nonlocality Near the Dirac Point in Graphene**
D. A. Abanin et al.
 Unusual transport in graphene may be a consequence of the propagation of long-range charge-neutral currents.
 >> *Perspective p. 315*
- 330 Teleportation of Nonclassical Wave Packets of Light**
N. Lee et al.
 Teleportation is demonstrated with bunches of photons.
 >> *Perspective p. 313*
- 333 Enhanced Enantioselectivity in Excitation of Chiral Molecules by Superchiral Light**
Y. Tang and A. E. Cohen
 Light waves tuned to rotate more sharply than circularly polarized light can better discriminate between chiral molecules.
- 336 Deterministic Preparation of a Tunable Few-Fermion System**
F. Serwane et al.
 Optical traps are used to prepare up to 10 cold lithium atoms to be used for simulating few-body fermionic systems.
- 339 A Bicycle Can Be Self-Stable Without Gyroscopic or Caster Effects**
J. D. G. Kooijman et al.
 A new bicycle design points to the importance of mass distribution for stability.
 >> *Science Podcast*
- 342 DNA Origami with Complex Curvatures in Three-Dimensional Space**
D. Han et al.
 Rationally introduced crossover positions bend networks of double-helical DNA strands into complex shapes.

- 346 Phonemic Diversity Supports a Serial Founder Effect Model of Language Expansion from Africa**
Q. D. Atkinson
 Analysis of word sounds suggests that language originated once, in central and southern Africa.
- 349 Interplay Between Changing Climate and Species' Ecology Drives Macroevolutionary Dynamics**
T. H. G. Ezard et al.
 Fossil records show that speciation and extinction are influenced by interaction with other species and with the environment.
- 352 pH-Dependent Gating in a FocA Formate Channel**
W. Lü et al.
 Transport of formate through a pentameric channel is gated by pH-dependent conformational changes.
- 354 Specificity of *Drosophila* Cytonemes for Distinct Signaling Pathways**
S. Roy et al.
 Signaling protein receptors are segregated into different cell protrusions in *Drosophila* cells.
 >> *Perspective p. 312*
- 358 Noncanonical TGF β Signaling Contributes to Aortic Aneurysm Progression in Marfan Syndrome Mice**
T. M. Holm et al.
- 361 Angiotensin II Type 2 Receptor Signaling Attenuates Aortic Aneurysm in Mice Through ERK Antagonism**
J. P. Habashi et al.
 Transforming growth factor- β promotes aortic aneurysm formation through activation of its "noncanonical" signaling pathway.
 >> *News story p. 297*
- 365 Sequential Synaptic Excitation and Inhibition Shape Readiness Discharge for Voluntary Behavior**
K. Kagaya and M. Takahata
 In crayfish, specific neurons produce electrical activity in synchrony with different phases of the walking pattern.

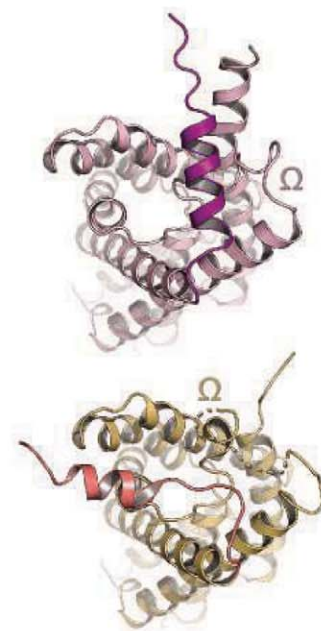
CONTENTS continued >>



pages 315 & 328



page 339



page 352



1000 Free Custom Antibodies

Can't find the antibody you're looking for?

Let Abgent make it for you, FREE! After 10 years of manufacturing 15,000 antibodies, Abgent is giving away an unprecedented offer.

Why? Because finding the right antibody is difficult. If an antibody to a protein of interest isn't available to the scientific community, we'll start a custom project and add it to our pipeline. Together, we'll provide the research solutions the scientific community deserves. Submit your protein today!

Please visit <http://www.abgent.com> for complete promotion rules and to submit your protein of interest.

10239 Flanders Court, San Diego, CA 92121
Tel: (888) 735-7227 or (858) 622-0099



ABGENT

Abgent & BioBay - Partners in advancing research



bioBAY
innovation comes home

BioBay provides total business solutions. As one of the largest biotech hubs hosting over 200 companies, we've built our dedicated, enthusiastic, and highly professional team to serve all needs for research tools innovation.

SCIENCEONLINE

SCIENCEEXPRESS

www.sciencexpres.org

Nocturnality in Dinosaurs Inferred from Scleral Ring and Orbit Morphology

L. Schmitz and R. Motani

Comparison of eye structures between fossils and modern species suggests that Mesozoic archosaurs were active day and night.

10.1126/science.1200043

Industrial Melanism in British Peppered Moths Has a Singular and Recent Mutational Origin

A. E. van't Hof et al.

The locus responsible for the dark form of the peppered moth is identified.

10.1126/science.1203043

Chlorinated Indium Tin Oxide Electrodes with High Work Function for Organic Device Compatibility

M. G. Helander et al.

Closer matching of the energy levels of transparent electrodes and active materials in organic light-emitting diodes improves efficiency.

10.1126/science.1202992

Probing Asthenospheric Density, Temperature, and Elastic Moduli Below the Western United States

T. Ito and M. Simons

Monitoring the response to ocean tidal loads reveals detailed variations in Earth's internal structure.

10.1126/science.1202584

Ethical Framework for Biofuels

A. Buyx and J. Tait

10.1126/science.1206064

>> [Science Podcast](#)

SCIENCENOW

www.sciencenow.org

Highlights From Our Daily News Coverage

Melting Antarctic Ice Causing Penguins to Starve

As global warming kills off ice-loving krill, penguins may be losing food supply.

<http://scim.ag/ice-penguins>

How Distractions Cause 'Senior Moments'

A new study shows why the brains of older adults sometimes struggle to switch between tasks.

<http://scim.ag/senior-moments>

Double the Genes, Double the Flora

Ancient genome duplications fueled seed plant diversity.

<http://scim.ag/genes-flora>

SCIENCE SIGNALING

www.sciencesignaling.org

The Signal Transduction Knowledge Environment

12 April issue: <http://scim.ag/ss041211>

RESEARCH ARTICLE: Estrogen Regulates Tumor Growth Through a Nonclassical Pathway that Includes the Transcription Factors ER β and KLF5
Y. Nakajima et al.

PERSPECTIVE: Estrogen Receptor β —Switching to a New Partner and Escaping from Estrogen
Y.-K. Leung and S.-M. Ho

ER β promotes apoptosis in prostate cancer cells through an estrogen-independent mechanism.

RESEARCH ARTICLE: PI3K β Plays a Critical Role in Neutrophil Activation by Immune Complexes
S. Kulkarni et al.

The β isoform of phosphoinositide 3-kinase may be an effective therapeutic target in inflammatory diseases.

GLOSSARY

Find out what c-Yes, Lyn, and R-Smad mean in the world of cell signaling.

SCIENCE CAREERS

www.sciencereers.org/career_magazine

Free Career Resources for Scientists

Tooling Up: Two Choke Points

D. Jensen

When moving away from the bench and into industry, it is important to realize that there is not just one gaping chasm to cross, but two.

<http://scim.ag/chokepoints>

A Very Visual Scientist

S. Webb

Nickolay Hristov is building a career at the intersection of science and visual art.

http://scim.ag/hristov_visual

Content Collection: Careers in Clinical and Translational Research

Science Careers Staff

Articles on clinical and translational science careers, produced with generous support from the Burroughs Wellcome Fund.

http://scim.ag/translational_collection

SCIENCE TRANSLATIONAL MEDICINE

www.sciencetranslationalmedicine.org

Integrating Medicine and Science

13 April issue: <http://scim.ag/stm041311>

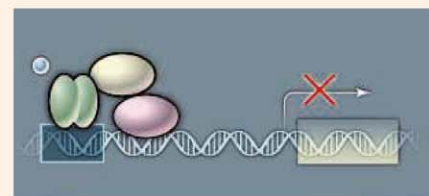
COMMENTARY: One Foundation's Strategy to Accelerate Drug Discovery Through Genomics
L. M. Perkins et al.

The founder of the Multiple Myeloma Research Foundation discusses ways to accelerate drug discovery for a rare disease.

PERSPECTIVE: Community Health Care—Therapeutic Opportunities in the Human Microbiome

J. L. Sonnenburg and M. A. Fischbach

The human microbiome harbors tremendous untapped therapeutic potential.



SCIENCE SIGNALING

Estrogen receptors in a prostate tumor.

RESEARCH ARTICLE: IL-25 Causes Apoptosis of IL-25R-Expressing Breast Cancer Cells Without Toxicity to Nonmalignant Cells
S. Furuta et al.
Mammary epithelial cells secrete an anticancer cytokine, suggesting a new therapeutic approach for breast cancer.

RESEARCH ARTICLE: Targeting Nrf2 Signaling Improves Bacterial Clearance by Alveolar Macrophages in Patients with COPD and in a Mouse Model
C. J. Harvey et al.

Lung macrophages take up bacteria better after stimulation of the Nrf2 antioxidant signaling pathway.

SCIENCE PODCAST

www.sciencemag.org/multimedia/podcast
Free Weekly Show

On the 15 April *Science* Podcast: budgeting for science, an ethical framework for biofuels, re-exploring bicycle stability, and more.

SCIENCE INSIDER

news.sciencemag.org/scienceinsider
Science Policy News and Analysis

SCIENCE (ISSN 0036-8075) is published weekly on Friday, except the last week in December, by the American Association for the Advancement of Science, 1200 New York Avenue, NW, Washington, DC 20005. Periodicals Mail postage (publication No. 484460) paid at Washington, DC, and additional mailing offices. Copyright © 2011 by the American Association for the Advancement of Science. The title SCIENCE is a registered trademark of the AAAS. Domestic individual membership and subscription (51 issues): \$149 (\$74 allocated to subscription). Domestic institutional subscription (51 issues): \$990; Foreign postage extra: Mexico, Caribbean (surface mail) \$55; other countries (air assist delivery) \$85. First class, airmail, student, and emeritus rates on request. Canadian rates with GST available upon request, GST #1254 88122. Publications Mail Agreement Number 1069624. Printed in the U.S.A.

Change of address: Allow 4 weeks, giving old and new addresses and 8-digit account number. **Postmaster:** Send change of address to AAAS, P.O. Box 96178, Washington, DC 20090-6178. **Single-copy sales:** \$10.00 current issue, \$15.00 back issue prepaid includes surface postage; bulk rates on request. **Authorization to photocopy** material for internal or personal use under circumstances not falling within the fair use provisions of the Copyright Act is granted by AAAS to libraries and other users registered with the Copyright Clearance Center (CCC) Transactional Reporting Service, provided that \$25.00 per article is paid directly to CCC, 222 Rosewood Drive, Danvers, MA 01923. The identification code for *Science* is 0036-8075. *Science* is indexed in the *Reader's Guide to Periodical Literature* and in several specialized indexes.



ADVANCING SCIENCE. SERVING SOCIETY



ENLIGHTENED BY SCIENCE

The 2011•12 NEB Catalog & Technical Reference

New England Biolabs introduces its latest award-winning Catalog and Technical Reference, featuring over 100 new products, up-to-date charts, protocols and troubleshooting tips. Our thought-provoking collection of mini-reviews explore the mysteries of the deep ocean.

Featured New Products

OneTaq™ DNA Polymerase – ideal for a wide range of templates, OneTaq offers robust amplification with minimal optimization

EpiMark™ Validated Reagents for Epigenetics – this suite of products is designed to simplify DNA and histone modification studies

NEBNext® Reagents for Sample Preparation – available for DNA or RNA, these reagents facilitate sample prep for next generation sequencing

High Fidelity (HF) Restriction Enzymes – engineered for reduced star activity, HF enzymes offer maximum convenience

Visit www.neb.com/newcatalog to request a copy.





Mixing It Up

The action of winds on the surface of the ocean and processes that change the density of ocean water masses, such as cooling, freezing, and evaporation, create currents and transfer energy to the ocean. The ocean does not continue to circulate faster and faster, however,

because this energy is dissipated through the creation of turbulence. **D'Asaro *et al.*** (p. 318, published online 10 March; see the Perspective by **Ferrari**) present observations from an ocean front within a strong ocean current (the Kuroshio) that show that energy can be transferred from the large to the small scale of turbulence at fronts and dissipated at a significant rate. These findings will help in the generation of accurate simulations of ocean circulation and its effects on climate.

Adenosine Receptor Activation

G protein-coupled receptors (GPCRs) are transmembrane proteins that act as key gatekeepers between external signals and cellular responses. GPCRs that are activated by diffusible ligands are dynamic, but in structural studies GPCRs have generally been cocrystallized with antagonists to stabilize them in their inactive state. **Xu *et al.*** (p. 322, published online 10 March) now report a high-resolution crystal structure of human A_{2A} adenosine receptor bound to a potent agonist, which provides insight into the structural basis of activation.

Tightly Wound Waves

In circularly polarized light, the field vectors rotate while the wave propagates through space. The resultant helical pattern is chiral, and, consequently, the field interacts differently with a single chiral molecule than with its mirror image isomer (enantiomer). For most small molecules, however, the light polarization varies on a spatial scale much larger than the atomic dimensions, and so differential absorption by enantiomers is relatively weak. **Tang and Cohen** (p. 333) have now engineered a more sharply rotating polarization pattern, termed super-chiral light, that shows a greater than 10-fold enhancement in discriminating enantiomers relative to ordinary circular polarization.

The Flavor of Graphene

Graphene, a single-atom-thick layer of graphite, exhibits many phenomena characteristic of two-dimensional systems, such as the quantum Hall

effect. But in addition to charge degrees of freedom, graphene also has the so-called spin and valley (jointly called flavor) degrees of freedom. **Abanin *et al.*** (p. 328; see the Perspective by **Castro Neto**) measured the nonlocal response of graphene samples close to the Dirac or neutrality point, where the charge carrier density tends to zero. A significant voltage drop on one end of the device was observed in response to current flowing through the other end in the presence of a perpendicular magnetic field, consistent with the appearance of long-range flavor currents.

A Few-Atom Trap

Atoms consist of a relatively small number of protons, neutrons, and electrons, which all belong to a class of particles known as fermions. Much is known about these few-fermion systems from the study of naturally occurring elements; however, in order to be able to tune their properties, man-made systems are more desirable. **Serwane *et al.*** (p. 336) created a system of up to 10 fermionic cold atoms in a precisely defined quantum state of an optical dipole trap. Magnetic fields allowed the tuning of the interactions between the fermions and observation of an interaction shift for a system of two fermions.

Bicycle Stability Revisited

It takes practice to learn how to ride a bicycle, but experiments have shown that a riderless bicycle will self-correct its steering against falling. Although bicycles are familiar machines, the mechanics that describes their motion is quite complex, and approximations are needed

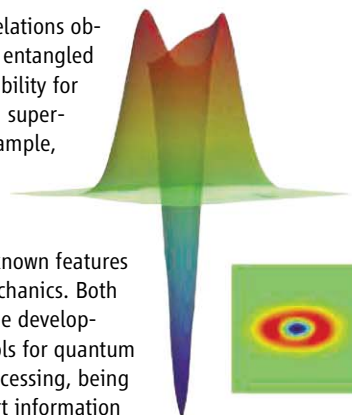
to understand what effects underlie stability. **Kooijman *et al.*** (p. 339) reexamined bicycle steering by performing linear stability calculations and by building a bicycle that canceled gyroscopic effects with counterspinning wheels and that set the steering wheel with its pivot point behind its contact to the ground. Such a bicycle could still move stably. Other factors, such as the mass distribution along the bicycle, also played key roles in steering and stability.

Capturing Bottles in DNA

Several methods can exploit DNA base pairing to create complex shapes. **Han *et al.*** (p. 342; see the cover) describe a method that can create arbitrary closed shapes by first decomposing the shape into circular contour lines and then designing DNA double helices that can bend and follow these contours. Suitable crossover positions link DNA along adjacent contours. Complex shapes, including a 70-nanometer-high nanoflask, were constructed. This design approach is based on simple geometric considerations, and the structures formed in high yield despite their inherent strain.

Teleporting Cats

The strong correlations observed between entangled states and the ability for states to be in a superposition (for example, Schrödinger's cat being dead and



alive) are well-known features of quantum mechanics. Both play a role in the development of protocols for quantum information processing, being able to transport information securely and instantaneously. **Lee *et al.*** (p. 330; see the Perspective by **Grangier**) combine squeezing, photon subtraction, entanglement, and homodyne detection to form a teleporter of nonclassical wave packets of light. The control and manipulation of these "cat" states should prove useful in generating more complex and robust protocols for quantum information science.

The Origin of Language

Human populations are thought to have gone through a series of genetic bottlenecks as they expanded out of Africa, with small segments

Continued on page 282

“A dream told me to do it.”



Carl R. Alving, M.D.
Chief of the Department of Adjuvant & Antigen Research, Division of Retrovirology at the Walter Reed Army Institute of Research
AAAS member

*Dr. Carl Alving
on his inspiration
for inventing
the vaccine patch.*

MemberCentral is the new website that looks at science through the eyes of AAAS members. It celebrates their achievements—like Dr. Alving’s vaccine patch—and their shared belief in the transformative power of science. Use **MemberCentral** to connect with other members, learn about work being done in other fields, and get fresh perspectives on issues ranging from speciation to STEM education.

Visit **MemberCentral** today and get to know the AAAS member community in a whole new way.



MemberCentral.aaas.org

Blogs | Videos | Webinars
Discounts | Downloads | Community

This Week in *Science*

Continued from page 281

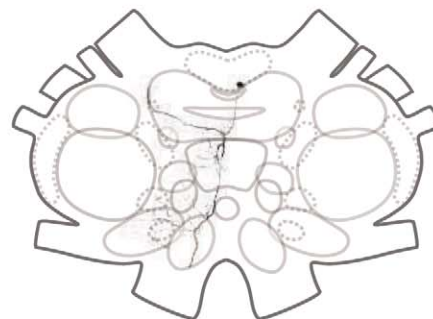
of established populations moving on to found new populations with diminished genetic variation. **Atkinson** (p. 346) analyzed what happened to languages through these population bottlenecks by studying the number of phonemes—perceptually distinct units of sound that differentiate words—in languages across the world. The largest phoneme inventories are found in Africa and the smallest in South America and Oceania. Extrapolating back from the geographic variation in phoneme diversity suggests that language originated in central and southern Africa.

Queens vs. Jesters

Are species-species interactions or the interactions of a species with its environment more important drivers of speciation and extinction? **Ezard et al.** (p. 349) investigated macroevolutionary dynamics of planktonic foraminifera by examining their fossil records, characterizing their ecologies, and dissecting the interplay between species’ ecology and their physical environment. Species with distinct ecologies had significantly different speciation and extinction rates, and the dominance of particular ecologies fluctuated with the changing environment. Extinction appears to be more strongly shaped by environmental change than by diversity-dependence, whereas the reverse may be true for speciation.

Ready, Discharge, Go

In crayfish brains, one can record an increased neuronal spike discharge rate a few seconds before the onset of walking and a subsequent decrease once walking is initiated. However, what the synaptic mechanisms of this so-called readiness discharge are and what types of neurons are involved in the production of this spike activity are unclear. **Kagaya and Takahata** (p. 365) identified a class of cells in the crayfish brain that discharged in advance of electromyographic activity in the walking legs at the beginning of a bout of voluntary walking, but not when walking was triggered by an external stimulus. Other classes of neurons were also identified, including some that were active throughout a bout of walking and some that fired primarily at the end of walking.



Assessing Filopodia Form and Function

During development, *Drosophila* cells form filopodia that protrude in the direction of other cells that produce morphogens that influence their development. **Roy et al.** (p. 354; see the Perspective by **Affolter and Basler**) examined images of cells of developing *Drosophila* embryos and suggest that particular growth factor receptors are sorted into distinct filopodia and cytoplasmic vesicles. Under certain conditions, cells overexpressing fluorescently labeled growth-factor receptors had filopodia that were oriented in a specific direction and appeared to segregate particular receptor types into distinct filopodia. Further investigation of the nature of the receptor-sorting mechanism and its possible function in signaling may elucidate signaling mechanisms controlling development.

Seeking the Right Pathway

Activation of transforming growth factor- β (TGF- β) signaling promotes the development of aortic aneurysms in the connective tissue disorder Marfan syndrome (MFS). Losartan, a drug that inhibits TGF- β signaling, is in clinical trials for this disorder. Like many cytokines, TGF- β activates multiple intracellular signaling pathways. In the context of aortic disease, TGF- β has been assumed to act through the “canonical” Smad pathway. **Holm et al.** (p. 358) and **Habashi et al.** (p. 361) now show that the “noncanonical” TGF- β pathway, which involves the signaling proteins ERK1/2, is the prominent driver of aortic disease in MFS mice and that it is this pathway through which losartan exerts its beneficial effects. Analysis of ERK1/2 activation status in MFS patients may help optimize losartan dosage, and drugs specifically targeting the noncanonical pathway may merit exploration as possible therapies for aortic aneurysms.

CREDIT: KAGAYA AND TAKAHATA



Bruce Alberts is Editor-in-Chief of *Science*.

The Young Academy Movement

I HAVE OFTEN ARGUED ON THIS PAGE THAT SCIENTISTS NEED TO DO MORE THAN SIMPLY ADVANCE their individual research projects. Maintaining excellence in the global scientific enterprise will require constant adjustments to policies and programs. In addition, much more outreach by scientists will be needed to make science better understood by the general public and by governments. Promising progress toward both of these goals comes from a movement that is forging new organizations of young scientists—the “young academies”—around the world. A few weeks ago, a new international organization, the Global Young Academy, held its initial meeting in Berlin to discuss spreading the idea to many more nations (www.globalyoungacademy.org). This effort deserves full support from all of society.

In 2000, a new type of organization, Die Junge Akademie (the Young Academy), was created as a joint venture by two German academies. This Young Academy was described as “an organization intended to harness the resources of both academies in ways that would fertilize research fields with new ideas and bolster career pathways, as well as invigorate older academies by involving the young scientific community in critical policy-related work.”* In 2005, a similar Young Academy was established in the Netherlands. The success of these two experiments has recently inspired six other nations to create their own Young Academies: Egypt, Nigeria, Pakistan, Sudan, Thailand, and Uganda; all nations where the tolerance and rationality inherent to science will be invaluable.

I see this empowerment of young scientists as the next step in a process that began in 1993 in New Delhi, when the national academies of sciences from more than 60 nations came together to develop a coherent scientific position on world population issues in preparation for the major 1994 United Nations International Conference on Population and Development in Cairo. This first-ever meeting of the world’s science academies soon created the InterAcademy Panel (IAP), now a vibrant global network of more than 100 member academies (www.interacademies.net). The IAP functions as a mutual support organization for the existing science academies around the world.

But the empowerment of national science academies with distinguished, well-established members can leave a gap between these influential organizations and the young, dynamic scientists who represent the future in each nation. This is precisely the gap that has been filled by the Young Academies: each a group of fewer than 200 scientists, typically selected by their national science academies to serve in 4-year leadership roles. Through its connection to a prestigious national science academy, each Young Academy is empowered to exert national leadership in advancing science through projects that the young scientists themselves determine. These young scientists can often be more effective than their older peers in interactions with society and with politicians. They also bring new energy to these interactions, with a better gender balance due to the advances that women scientists have made in recent decades.

By bringing together outstanding scientists from many different disciplines, Young Academies catalyze the formation of multidisciplinary scientific collaborations that generate innovative new discoveries. Participation in a Young Academy also strengthens a nation’s scientific enterprise by training its next generation of leaders. The work exposes them to important policy issues while building networks of trusted personal relationships that can bridge disciplines for a lifetime. And by providing a shortcut for outstanding young scientists to exert national leadership, Young Academies can be highly effective in recruiting a nation’s most talented students to scientific careers—a critical issue for the future of every nation.

By fusing the promotion of the larger goals of science with an integration of young scientists into public service, the Young Academy movement is well positioned to drive the creation of the tolerant, rational societies that the world so badly needs.

— Bruce Alberts



10.1126/science.1206690

*V. ter Meulen, G. Stock, *Science* **330**, 1455 (2010).

EDITED BY KRISTEN MUELLER AND JAKE YESTON



ECOLOGY

Hibernators Take It Slow

Hibernation is thought to have evolved as a strategy for avoiding extreme environmental conditions in seasonal climates. Hibernators, however, are also found in the tropics and will sometimes continue to hibernate after mild conditions, and plentiful food, return. Other forces, therefore, may act to make hibernation, which is present in nearly half of all mammalian orders, a common strategy. Hibernation lowers metabolism and conserves energy, but as animals enter hidden dens and burrows to hibernate, it also removes them from the external environment, perhaps affecting survival. Turbill *et al.* reviewed the published literature on 19 species of mammalian hibernators and found that, indeed, annual survival and total life span in hibernating mammals are greater than they are in nonhibernators of the same size. Hibernators also have a "slower pace of life," including a delay in maturity, lower annual reproductive output, and longer generation time. This analysis suggests that small hibernating mammals may trade high annual reproduction for a longer reproductive life, a successful life history strategy that is seen more often in large, long-lived mammals. — SNV

Proc. R. Soc. London Ser. B **278**, 10.1098/rspb.2011.0190 (2011).

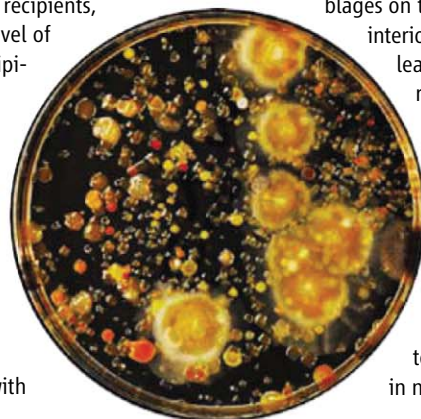
BIOMEDICINE

Signs of Rejection

Recipients of heart transplants are treated with powerful immunosuppressants to prevent organ rejection, but complications still occur. Early signs of rejection are often monitored by an invasive procedure that requires heart tissue biopsy. A noninvasive diagnostic test was recently approved in the United States, in which blood cells from heart transplant recipients are monitored for the expression of genes associated with immune-mediated rejection.

Snyder *et al.* have designed a potentially complementary noninvasive test based on the concept that during organ rejection, dying cells in the organ release donor DNA that might be

detectable in the recipient's bloodstream by high-throughput sequencing methods. In a small proof-of-principle study of archived blood samples from heart transplant recipients, the authors showed that the level of cell-free donor DNA in the recipient's blood increased substantially when there was an acute cellular rejection episode and then declined again once the patient received more aggressive treatment. Although an encouraging start, the predictive value of this test will become clear only from much larger studies in which its performance is compared with



that of biopsies and with conventional clinical measures of heart function, such as echocardiograms. — PAK

Proc Natl. Acad. Sci. U.S.A. **108**, 10.1073/pnas.1013924108 (2011).

MOLECULAR BIOLOGY

A Complicated Start

In the eukaryotic cell nucleus, DNA is compacted through its association with histone proteins. These are assembled into octamers to form nucleosomes; "linker" DNA connects nucleosomes and is associated with histone H1. DNA-histone interactions must be modified, however, for transcription to occur. Although much is known about transcription-induced changes to core histones, how linker histones are affected is less understood. Vicent *et al.* examined histone H1 dynamics at hormone receptor target genes and showed that four enzyme complexes act immediately after hormone induction. First, the ASCOM complex induces an activating H3K4me3 signal, which is increased by displacement of the demethylating complex KDM5B. This is followed by the rapid recruitment of the ATP-dependent NURF remodeling complex, CDK2 promoter binding and phosphorylation, and displacement of histone H1. Finally, the core histone proteins are displaced to allow access to hormone receptor target genes. Thus, substantial enzymatic complexity is required for the "eviction" of linker H1 to set up a remodeled chromatin template for regulated gene expression. — BAP

Genes Dev. **25**, 10.1101/gad.621811 (2011).

EVOLUTION

Location, Location, Location

Experimental studies of bacteria-phage interactions can model both disease evolution and coevolutionary theory. Koskella *et al.* used DNA sequencing to compare the bacterial assemblages on the surface and in the

interior of horse chestnut tree leaves, and then used a series of cross-inoculation experiments to assess both the strength and spatial scale of phage adaptation to local bacterial populations. From this, they found that the spatial scale at which phages adapt to parasitic bacteria in natural communities

CREDITS (TOP TO BOTTOM): GEORGE MCCARTHY/CORBIS; BRITT KOSKELLA AND ZACHARY BURTON

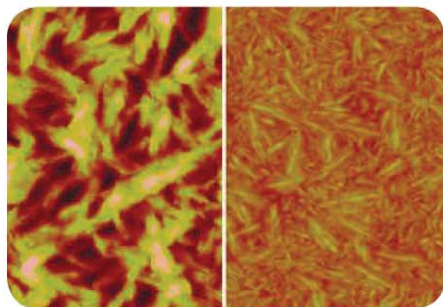
depends on the host environment in which the phage-bacterial interaction occurs. The tree, rather than the individual leaves on a tree, best explained phage local adaptation for both the exterior and interior leaf surface. The degree of adaptation varied by location, however, with phage from the leaf interior showing higher adaptation as compared to those from the leaf exterior. These differences could not be explained by the differences in host bacterial compositions between the two sites. Thus, even across micrometers, the local environment affects the degree and spatial structure of adaptation and probably plays a role in coevolution. — LMZ

Am. Nat. **177**, 440 (2011).

MATERIALS SCIENCE

Silicon Goes Organic

Though organic- (i.e., predominantly carbon-) based solar cells are less efficient than their inorganic counterparts, they have the advantage of being processed from solutions and thus can be fashioned at large scale on curved or flexible substrates. Graham *et al.* explored the use of polydimethylsiloxane (PDMS) as a solvent additive for improving organic solar cell performance



without the need for subsequent thermal or solvent annealing steps. Low concentrations of PDMS were added in the fabrication of cells, with thiophene and isoindigo-containing oligomers as the electron donor and PC₆₁BM as the acceptor. There was significant variation in the efficiencies of the cells obtained in each of the three labs where the experiments were performed, but in all cases the addition of PDMS improved the cell performance and decreased the variability between cells fabricated within a single lab. The PDMS strongly altered the film morphology, with a decrease in roughness and feature size (as shown left to right above), and reduced the need for postfabrication thermal annealing. Because plastic syringes are commonly used for fabricating organic solar cells, the variability in reported efficiencies may be partly due to syringe-derived PDMS contamination. — MSJ

ACS Appl. Mater. Interfaces **3**, 10.1021/am2000328 (2011).

PLANETARY SCIENCE

Hammering Rims into Place

Chondrites, the most primitive of meteorites, are fragments of parts of asteroids that never melted or suffered substantial alteration and thus sample the materials from which the solar system formed. They contain millimeter-sized grains called chondrules, which are surrounded by rims of finer grains. How these rims formed has been a matter of debate. Did they sample dust accreted onto the chondrules while these were still freely floating in the early protoplanetary nebula, or did they suffer alteration after the chondrules were incorporated into the meteorite's parent asteroid? To solve this question, Bland *et al.* used 3D electron backscatter diffraction to look at the preferred orientation of grains around the chondrules in a chondritic meteorite. Away from the chondrules, grains share a single preferred orientation that suggests they were compressed while in the asteroid. In the rims, in contrast, the grains have different orientations, which are spherically symmetric, centered on the chondrules. The analysis suggests that the rims were emplaced outside the parent asteroid and oriented themselves in response to gentle collisions in the protoplanetary nebula. — MJC

Nat. Geosci. **4**, 244 (2011).

CHEMISTRY

Isotopes Spinning Apart?

The fractionation of a mixture of stable isotopes is typically governed by mass differences. A few processes, however, exhibit a mass-independent effect, such as the impact of molecular symmetry on oxygen isotope fractionation during the formation of ozone in the atmosphere. The effects of an external gradient on isotopic fractionation are not as well understood, but recent experiments have demonstrated that under certain conditions, O₂ gas shows signs of mass-independent fractionation along a thermal gradient. Building on these efforts, Sun and Bao systematically examined possible factors controlling this phenomenon in O₂ and SF₆ gases to determine a physical mechanism. In both cases, the experimental data are consistent with the temperature gradient manipulating the different isotopes in accord with their associated differences in nuclear spin (as distinct from mass). Because the mechanism operates for two gases with very different molecular and nuclear configurations, it could be common among low-density gases with spin differences, such as those abundant in molecular clouds or solar nebulae (e.g., CO and H₂O). — NW

Rapid Commun. Mass Spectrom. **25**, 765 (2011).



AAAS is here –

increasing diversity in the scientific work force.

AAAS is working to ensure that every student with an aptitude for science, technology, engineering, and mathematics gets an opportunity to pursue a chosen profession, no matter what the challenges. For over 30 years AAAS's ENTRY POINT! program has placed talented, differently abled students in paid internships with leading scientific employers. As a AAAS member your dues support these efforts.

If you're not yet a AAAS member, join us. Together we can make a difference.

To learn more, visit aaas.org/plusyou/entrypoint



1200 New York Avenue, NW
Washington, DC 20005

Editorial: 202-326-6550, FAX 202-289-7562

News: 202-326-6581, FAX 202-371-9227

Bateman House, 82-88 Hills Road
Cambridge, UK CB2 1LQ

+44 (0) 1223 326500, FAX +44 (0) 1223 326501

SUBSCRIPTION SERVICES For change of address, missing issues, new orders and renewals, and payment questions: 866-434-AAAS (2227) or 202-326-6417, FAX 202-842-1065. Mailing addresses: AAAS, P.O. Box 96178, Washington, DC 20090-6178 or AAAS Member Services, 1200 New York Avenue, NW, Washington, DC 20005

INSTITUTIONAL SITE LICENSES please call 202-326-6755 for any questions or information

REPRINTS: Author Inquiries 800-635-7181

Commercial Inquiries 803-359-4578

PERMISSIONS 202-326-7074, FAX 202-682-0816

MEMBER BENEFITS AAAS/Barnes&Noble.com bookstore www.aaas.org/bn; AAAS Online Store www.apisource.com/aaas/ code MKB6; AAAS Travels: Betchart Expeditions 800-252-4910; Apple Store www.apple.com/epstore/aaas; Bank of America MasterCard 1-800-833-6262 priority code FAA3YU; Cold Spring Harbor Laboratory Press Publications www.cshlpress.com/affiliates/aaas.htm; GEICO Auto Insurance www.geico.com/landingpage/go51.htm?logo=17624; Hertz 800-654-2200 CDP#343457; Office Depot https://bsd.officedepot.com/portalLogin.do; Seabury & Smith Life Insurance 800-424-9883; Subaru VIP Program 202-326-6417; VIP Moving Services www.vipmayflower.com/domestic/index.html; Other Benefits: AAAS Member Services 202-326-6417 or www.aaasmember.org.

science_editors@aaas.org (for general editorial queries)
science_letters@aaas.org (for queries about letters)
science_reviews@aaas.org (for returning manuscript reviews)
science_bookrevs@aaas.org (for book review queries)

Published by the American Association for the Advancement of Science (AAAS), *Science* serves its readers as a forum for the presentation and discussion of important issues related to the advancement of science, including the presentation of minority or conflicting points of view, rather than by publishing only material on which a consensus has been reached. Accordingly, all articles published in *Science*—including editorials, news and comment, and book reviews—are signed and reflect the individual views of the authors and not official points of view adopted by AAAS or the institutions with which the authors are affiliated.

AAAS was founded in 1848 and incorporated in 1874. Its mission is to advance science, engineering, and innovation throughout the world for the benefit of all people. The goals of the association are to: enhance communication among scientists, engineers, and the public; promote and defend the integrity of science and its use; strengthen support for the science and technology enterprise; provide a voice for science on societal issues; promote the responsible use of science in public policy; strengthen and diversify the science and technology workforce; foster education in science and technology for everyone; increase public engagement with science and technology; and advance international cooperation in science.

INFORMATION FOR AUTHORS

See pages 784 and 785 of the 11 February 2011 issue or access www.sciencemag.org/about/authors

EDITOR-IN-CHIEF **Bruce Alberts**

EXECUTIVE EDITOR

Monica M. Bradford

NEWS EDITOR

Colin Norman

MANAGING EDITOR, RESEARCH JOURNALS **Katrina L. Kelner**

DEPUTY EDITORS **R. Brooks Hanson, Barbara R. Jasny, Andrew M. Sugden**

EDITORIAL SENIOR EDITORS/COMMENTARY Lisa D. Chong, Brad Wible; **SENIOR EDITORS** Gilbert J. Chin, Pamela J. Hines, Paula A. Kiberstis (Boston), Marc S. Lavine (Toronto), Beverly A. Purnell, L. Bryan Ray, Guy Riddihough, H. Jesse Smith, Phillip D. Szuroim (Tennessee), Valda Vinson, Jake S. Yeston, Laura M. Zahn (San Diego); **ASSOCIATE EDITORS** Kristen L. Mueller, Jelena Stajic, Sacha Vignieri, Nicholas S. Wigginton; **BOOK REVIEW EDITOR** Sherman J. Suter; **ASSOCIATE LETTERS EDITOR** Jennifer Sills; **EDITORIAL MANAGER** Cara Tate; **SENIOR COPY EDITORS** Jeffrey E. Cook, Cynthia Howe, Harry Jach, Lauren Kmeck, Barbara P. Ordway, Trista Waggoner; **COPY EDITOR** Chris Filiatreau; **SENIOR EDITORIAL COORDINATORS** Carolyn Kyle, Beverly Shields; **EDITORIAL COORDINATORS** Joi S. Granger, Anita Wynn; **PUBLICATIONS ASSISTANTS** Ramatoulaye Diop, Emily Guise, Jeffrey Hearn, Michael Hicks, Lisa Johnson, Scott Miller, Jerry Richardson, Brian White; **EDITORIAL ASSISTANT** Patricia M. Moore; **EXECUTIVE ASSISTANT** Alison Crawford; **ADMINISTRATIVE SUPPORT** Maryrose Madrid; **EDITORIAL FELLOW** Melissa R. McCartney

EDITORIAL DIRECTOR, WEB AND NEW MEDIA Stewart Wills; **SENIOR WEB EDITOR** Tara S. Marathe; **WEB EDITOR** Robert Frederick; **RESEARCH ASSOCIATE** Corinna Cohn; **WEB DEVELOPMENT MANAGER** Martyn Green; **WEB DEVELOPER** Andrew Whitesell

NEWS DEPUTY NEWS EDITORS Robert Coontz, David Grimm (Online), Eliot Marshall, Jeffrey Mervis, Leslie Roberts; **CONTRIBUTING EDITORS** Elizabeth Culotta, Polly Shulman; **NEWS WRITERS** Yudhijit Bhattacharjee, Adrian Cho, Jennifer Couzin-Frankel, Jocelyn Kaiser, Richard A. Kerr, Eli Kintisch, Greg Miller, Elizabeth Pennisi, Lauren Schenckman, Robert F. Service (Pacific NW), Erik Stokstad; **WEB DEVELOPER** Daniel Berger; **INTERN** Sara Reardon; **CONTRIBUTING CORRESPONDENTS** Jon Cohen (San Diego, CA), Daniel Ferber, Ann Gibbons, Sam Kean, Andrew Lawler, Mitch Leslie, Charles C. Mann, Virginia Morell, Gary Taubes; **COPY EDITORS** Linda B. Felaco, Melvin Gattling, Melissa Raimondo; **ADMINISTRATIVE SUPPORT** Scherraine Mack; **BUREAUS** San Diego, CA: 760-942-3252, FAX 760-942-4979; Pacific Northwest: 503-963-1940

PRODUCTION DIRECTOR Wendy K. Shank; **ASSISTANT MANAGER** Rebecca Doshi; **SENIOR SPECIALISTS** Steve Forrester, Chris Redwood, Anthony Rosen; **PREFLIGHT DIRECTOR** David M. Tompkins; **MANAGER** Marcus Spiegler; **SPECIALISTS** Jason Hillman, Tara Kelly

ART DIRECTOR Yael Fitzpatrick; **ASSOCIATE ART DIRECTOR** Laura Creveling; **SENIOR ILLUSTRATORS** Chris Bickel, Katharine Stillitt; **ILLUSTRATOR** Yana Hammond; **SENIOR ART ASSOCIATES** Holly Bishop, Preston Huey, Nayomi Kevitayagala, Matthew Twombly; **ART ASSOCIATE** Kay Engman; **PHOTO EDITOR** Leslie Blizard

SCIENCE INTERNATIONAL

EUROPE (science@science-int.co.uk) **EDITORIAL:** INTERNATIONAL MANAGING EDITOR Andrew M. Sugden; **SENIOR EDITOR/COMMENTARY** Julia Fahrenkamp-Uppenbrink; **SENIOR EDITORS** Caroline Ash, Stella M. Hurtle, Ian S. Osborne, Peter Stern; **ASSOCIATE EDITOR** Maria Cruz; **LOCUM EDITOR** Helen Piskergill; **EDITORIAL SUPPORT** Samantha Hogg, Alice Whaley; **ADMINISTRATIVE SUPPORT** John Cannell, Janet Clements, Louise Hartwell; **NEWS: EUROPE NEWS EDITOR** John Travis; **DEPUTY NEWS EDITOR** Daniel Clery; **CONTRIBUTING CORRESPONDENTS** Michael Balter (Paris), John Bohannon (Vienna), Martin Enserink (Amsterdam and Paris), Gretchen Vogel (Berlin); **INTERN** Jennifer Carpenter

LATIN AMERICA CONTRIBUTING CORRESPONDENT Antonio Regalado

ASIA Japan Office: Asca Corporation, Tomoko Furusawa, Rustic Bldg. 7F, 77 Tenjin-cho, Shinjuku-ku, Tokyo 162-0808, Japan; +81 3 6802 4616, FAX +81 3 6802 4615, inquiry@sciencemag.jp; **ASIA NEWS EDITOR** Richard Stone (Beijing: rstone@aaas.org); **CONTRIBUTING CORRESPONDENTS** Dennis Normile [Japan: +81 (0) 3 3391 0630, FAX +81 (0) 3 5936 3531; dnormile@gol.com]; Hao Xin [China: cindyhao@gmail.com]; Mara Hvistendahl [China: mara@marahvistendahl.com]; Pallava Bagla [South Asia: +91 (0) 11 2271 2896; pbagla@vsnl.com]

EXECUTIVE PUBLISHER **Alan I. Leshner**

PUBLISHER **Beth Rosner**

FULFILLMENT SYSTEMS AND OPERATIONS (membership@aaas.org); **CUSTOMER SERVICE SUPERVISOR** Pat Butler; **SPECIALISTS** Latoya Casteel, LaVonda Crawford, Vicki Linton, April Marshall; **DATA ENTRY SUPERVISOR** Cynthia Johnson; **SPECIALISTS** Shirlene Hall, Tarrika Hill, William Jones

BUSINESS OPERATIONS AND ADMINISTRATION DIRECTOR Deborah Rivera-Wienhold; **BUSINESS SYSTEMS AND FINANCIAL ANALYSIS DIRECTOR** Randy Yi; **MANAGER, FULFILLMENT SYSTEMS** Frits Buningh; **MANAGER, BUSINESS ANALYSIS** Eric Knott; **MANAGER, BUSINESS OPERATIONS** Jessica Tierney; **FINANCIAL ANALYSTS** Priti Pamnani, Celeste Troxler; **BUSINESS ANALYST** Christine Wehr; **RIGHTS AND PERMISSIONS:** ADMINISTRATOR Emilie David; **ASSOCIATE** Elizabeth Sandler; **MARKETING DIRECTOR** Ian King; **MARKETING MANAGERS** Allison Pritchard, Alison Chandler, Julianne Wielga; **MARKETING ASSOCIATES** Aimee Aponte, Mary Ellen Crowley; **SENIOR MARKETING EXECUTIVE** Jennifer Reeves; **DIRECTOR, SITE LICENSING** Tom Ryan; **DIRECTOR, CORPORATE RELATIONS** Eileen Bernadette Moran; **PUBLISHER RELATIONS, RESOURCES SPECIALIST** Kiki Forsythe; **SENIOR PUBLISHER RELATIONS SPECIALIST** Catherine Holland; **PUBLISHER RELATIONS, EAST COAST** Phillip Smith; **FULFILLMENT SUPERVISOR** Iquo Edim; **MARKETING MANAGER** Christina Schlecht; **MARKETING ASSOCIATE** Laura Tutino; **ELECTRONIC MEDIA: DIRECTOR** Lizabeth Harman; **ASSISTANT MANAGER** Lisa Stanford; **SENIOR PRODUCTION SPECIALIST** Ryan Atkins; **PRODUCTION SPECIALISTS** Antoinette Hodal, Nicole Johnston, Kimberly Oster; **DIRECTOR, WEB AND NEW MEDIA** Will Collins; **PROJECT MANAGER** Trista Snyder; **SENIOR PRODUCTION SPECIALIST** Christopher Coleman; **COMPUTER SPECIALISTS** Walter Jones, Kai Zhang

ADVERTISING DIRECTOR, WORLDWIDE AD SALES Bill Moran

COMMERCIAL EDITOR Sean Sanders: 202-326-6430

ASSISTANT COMMERCIAL EDITOR Tianna Hicklin 202-326-6463

PRODUCT (science_advertising@aaas.org); **MIDWEST** Rick Bongiovanni: 330-405-7080, FAX 330-405-7081; **EAST COAST/E. CANADA** Laurie Faraday: 508-747-9395, FAX 617-507-8189; **WEST COAST/W. CANADA** Irena Stickrod: 415-931-9782, FAX 415-520-6940; **UK/EUROPE/ASIA** Roger Gonçalves: TEL/FAX +41 43 243 1358; **JAPAN** ASCA Corporation, Makiko Hara: +81 (0) 3 6802 4616, FAX +81 (0) 3 6802 4615; ads@sciencemag.jp; **CHINA/TAIWAN** Ruolei Wu: +86 1367 1015 294 rwu@aaas.org

WORLDWIDE ASSOCIATE DIRECTOR OF SCIENCE CAREERS Tracy Holmes: +44 (0) 1223 326525, FAX +44 (0) 1223 326532

CLASSIFIED (advertise@sciencereaders.org); **U.S.:** MIDWEST/WEST COAST/SOUTH CENTRAL/CANADA Tina Burks: 202-326-6577; **EAST COAST/INDUSTRY** Elizabeth Early: 202-326-6578; **SALES ADMINISTRATION:** Marci Gallun; **EUROPE/ROW SALES:** Susanne Kharraz, Dan Pennington, Alex Palmer; **SALES ASSISTANT** Lisa Patterson; **JAPAN ASCA Corporation**, Jie Chin +81 (0) 3 6802 4616, FAX +81 (0) 3 6802 4615; careers@sciencemag.jp; **CHINA/TAIWAN** Ruolei Wu: +86 1367 1015 294 rwu@aaas.org; **ADVERTISING SUPPORT MANAGER** Karen Foote: 202-326-6740; **ADVERTISING PRODUCTION OPERATIONS MANAGER** Deborah Tompkins; **SENIOR PRODUCTION SPECIALIST/GRAPHIC DESIGNER** Amy Hardcastle; **PRODUCTION SPECIALIST** Yuse Lajimimuhup; **SENIOR TRAFFIC ASSOCIATE** Christine Hall; **SALES COORDINATOR** Shirley Young

AAAS BOARD OF DIRECTORS RETIRING PRESIDENT, CHAIR Alice Huang; **PRESIDENT** Nina Fedoroff; **PRESIDENT-ELECT** William Press; **TREASURER** David E. Shaw; **CHIEF EXECUTIVE OFFICER** Alan I. Leshner; **BOARD NANCY Knowlton, Stephen Mayo, Raymond Orbach, Julia M. Phillips, Sue V. Rosser, David D. Sabatini, Inder Verma, Thomas A. Woolsey**



ADVANCING SCIENCE, SERVING SOCIETY

SENIOR EDITORIAL BOARD

Cori Bargmann, The Rockefeller Univ.
John I. Brauman, Chair, Stanford Univ.
Richard Losick, Harvard Univ.
Michael S. Turner, University of Chicago

BOARD OF REVIEWING EDITORS

Adriano Aguzzi, Univ. Hospital Zürich
Takuzo Aida, Univ. of Tokyo
Sonia Altizer, Univ. of Georgia
Sebastian Amigorena, Institut Curie
Angelika Amon, MIT
Kathryn Anderson, Memorial Sloan-Kettering Cancer Center
Siv G. E. Andersson, Uppsala Univ.
John A. Bargh, Princeton Univ.
Meinrat O. Andreae, Max Planck Inst., Mainz
Peter A. Borch, Yale Univ.
Ben Barres, Stanford Medical School
Marisa Bartolomei, Univ. of Penn. School of Med.
Jordi Bascompte, Estación Biológica de Doñana, CSIC
Facundo Batista, London Research Inst.
Ray H. Baughman, Univ. of Texas, Dallas
David Baum, Univ. of Wisconsin
Yasmine Belkaid, NIAID, NIH
Philip Bentley, Duke Univ.
Stephen J. Benner, Penn. State Univ.
Gregory C. Beroza, Stanford Univ.
Peer Bork, EMBL
Bernard Bourdon, Ecole Normale Supérieure de Lyon
Ian Boyd, Univ. of St. Andrews
Robert W. Boyd, Univ. of Rochester
Paul M. Brakefield, Univ. of Cambridge
Christian Büchel, Universitätsklinikum Hamburg-Eppendorf
Joseph A. Burns, Cornell Univ.
William P. Butz, Population Reference Bureau
Georgy Buzsáki, Rutgers Univ.
Mats Carlsson, Univ. of Oslo
Mildred Cho, Stanford Univ.
David Clapham, Children's Hospital, Boston
David Clary, Univ. of Oxford
J. M. Claverie, CNRS, Marseille
Jonathan D. Cohen, Princeton Univ.
Alan Cowman, Walter & Eliza Hall Inst.
Robert H. Crabtree, Yale Univ.
Wolfgang Cramer, Potsdam Inst. for Climate Impact Research

F. Fleming Crim, Univ. of Wisconsin
Jeff L. Dangl, Univ. of North Carolina
Tom Daniel, Univ. of Washington
Stanislas Dehaene, Collège de France
Emmanouil T. Dermizakis, Univ. of Geneva Medical School
Robert Desimone, MIT
Claude Despland, New York Univ.
Ap Dijksterhuis, Radboud Univ. of Nijmegen
Dennis Discher, Univ. of Pennsylvania
Scott C. Doney, Woods Hole Oceanographic Inst.
Jennifer A. Doudna, Univ. of California, Berkeley
Julian Downward, Cancer Research UK
Bruce Dunn, Univ. of California, Los Angeles
Christopher Dye, WHO
Michael B. Elowitz, Calif. Inst. of Technology
Tim Elston, Univ. of North Carolina at Chapel Hill
Gerhard Ertl, Fritz-Haber-Institut, Berlin
Barry Evered, Univ. of Cambridge
Paul G. Falkowski, Rutgers Univ.
Ernst Fehr, Univ. of Zurich
Tom Fenchel, Univ. of Copenhagen
Alain Fischer, INSERM
Wulfraim Gerstner, EPFL Lausanne
Karl-Heinz Glassmeier, Inst. for Geophysics & Extraterrestrial Physics
Diane Griffin, Johns Hopkins Bloomberg School of Public Health
Taejip Ha, Univ. of Illinois at Urbana-Champaign
Christian Haass, Ludwig Maximilians Univ.
Steven Hahn, Fred Hutchinson Cancer Research Center
Gregory J. Hannon, Cold Spring Harbor Lab.
Dennis L. Hartmann, Univ. of Washington
Martin Heimann, Max Planck Inst., Jena
Isaac Held, NCAR
James A. Hendler, Rensselaer Polytechnic Inst.
Janet G. Hering, Swiss Fed. Inst. of Aquatic Science & Technology
Ray Hill, Univ. of Washington
Michael E. Himmel, National Renewable Energy Lab.
Kei Hirose, Tokyo Inst. of Technology
David Hodell, Univ. of Cambridge
Ove Hoegh-Guldberg, Univ. of Queensland
David Holden, Imperial College
Lara Hooper, UT Southwestern Medical Ctr at Dallas
Jeffrey A. Hubbell, EPFL Lausanne
Steven Jacobsen, Univ. of California, Los Angeles
Kai Johnsson, EPFL Lausanne

Peter Jonas, Universität Freiburg
William Kaelin, Dana-Farber Cancer Inst.
Barbara B. Kahn, Harvard Medical School
Daniel Kahn, University of California
Bernhard Keimer, Max Planck Inst., Stuttgart
Robert Kingston, Harvard Medical School
Alberto R. Kornblitt, Univ. of Buenos Aires
Leonid Kruglyak, Princeton Univ.
Mitchell A. Lazar, Univ. of Pennsylvania
David Lazer, Harvard Univ.
Virginia Lee, Univ. of Pennsylvania
Ottoline Leyser, Cambridge Univ.
Ole Lindvall, Univ. Hospital, Lund
Marcia C. Linn, Univ. of California, Berkeley
John Lis, Cornell Univ.
Richard Losick, Harvard Univ.
Jonathan Losos, Harvard Univ.
Ke Lu, Chinese Acad. of Sciences
Laura Mackey, CRUK Beatson Inst. for Cancer Research
Andrew P. MacKenzie, Univ. of St Andrews
Anne Magurran, Univ. of St Andrews
Oscar Marin, CSIC & Univ. Miguel Hernández
Charles Marshall, Harvard Medical School
Martin M. Matzuk, Baylor College of Medicine
Graham Medley, Univ. of Warwick
Yasushi Miyashita, Univ. of Tokyo
Richard Morris, Univ. of Edinburgh
Edward Moster, Norwegian Univ. of Science and Technology
P. David Pearson, Univ. of California, Berkeley
Naoto Nagaosa, Univ. of Tokyo
James Nelson, Stanford Univ. School of Med.
Timothy W. Nilsen, Case Western Reserve Univ.
Pär Norlund, Karolinska Inst.
Helga Nowotny, European Research Advisory Board
Stuart H. Orkin, Dana-Farber Cancer Inst.
Christine Ortiz, MIT
Elinor Ostrom, Indiana Univ.
Andrew Oswald, Univ. of Warwick
P. David Pearson, Univ. of California, Berkeley
Reginald M. Penner, Univ. of California, Irvine
John H. J. Petrini, Memorial Sloan-Kettering Cancer Center
Simon Philpott, Univ. of Florida
Philippe Poulin, CNRS
Colin Renfrew, Univ. of Cambridge
Trevor Robbins, Univ. of Cambridge
Barbara A. Romanowicz, Univ. of California, Berkeley
Jens Rostrop-Nielsen, Haldor Tøpsoe

Edward M. Rubin, Lawrence Berkeley National Lab
Mike Ryan, Univ. of Texas, Austin
Shimon Sakaguchi, Kyoto Univ.
Miquel Salmeron, Lawrence Berkeley National Lab
Jürgen Sandkühler, Medical Univ. of Vienna
Randy Seeley, Univ. of Cincinnati
Christine Seidman, Harvard Medical School
Vladimir Shalaya, Purdue Univ.
Joseph Silk, Univ. of Oxford
Davor Solter, Inst. of Medical Biology, Singapore
John Speakman, Univ. of Aberdeen
Allan C. Spradling, Carnegie Institution of Washington
Jonathan Sprent, Garvan Inst. of Medical Research
Elisbeth Stern, ETH Zürich
Ira Tabas, Columbia Univ.
Yoshiko Takahashi, Nara Inst. of Science and Technology
John Thomas, Duke Univ.
Herbert Virgin, Washington Univ.
Bert Vogelstein, Johns Hopkins Univ.
Cynthia Volkert, Univ. of Göttingen
Bruce D. Walker, Harvard Medical School
Douglas Wallace, Leibniz Inst. of Marine Sciences
Ian Walmsey, Univ. of Oxford
David A. Wardle, Swedish Univ. of Agric Sciences
Detlef Weigel, Max Planck Inst., Tübingen
Jonathan Weissman, Univ. of California, San Francisco
Sue Wessler, Univ. of California, Riverside
Ian A. Wilson, The Scripps Res. Inst.
Timothy D. Wilson, Univ. of Virginia
Jan Zaenen, Leiden Univ.
Mayana Zatz, University of Sao Paulo
Jonathan Zehr, Ocean Sciences
Hoda Zoghbi, Baylor College of Medicine
Maria Zuber, MIT

BOOK REVIEW BOARD

John Aldrich, Duke Univ.
David Bloom, Harvard Univ.
Angela Creager, Princeton Univ.
Richard Schweder, Univ. of Chicago
Ed Wasserman, DuPont
Lewis Wolpert, Univ. College London

Submission
deadline
August 1

Your name here.



The GE & Science Prize for Young Life Scientists. Because brilliant ideas build better realities.

Imagine standing on the podium at the Grand Hotel in Stockholm, making your acceptance speech for the GE & Science Prize for Young Life Scientists. Imagine having your essay read by your peers around the world. Imagine discussing your work in a seminar with other prize winners and Nobel Laureates. Imagine what you could do with the \$25,000 prize money. Now stop imagining. If you were awarded your Ph.D. in molecular biology in 2010, then submit your 1000-word essay by August 1, and you can make it reality.

Want to build a better reality? Go to www.gescienceprize.org



GE & Science
Prize for Young
Life Scientists



imagination at work



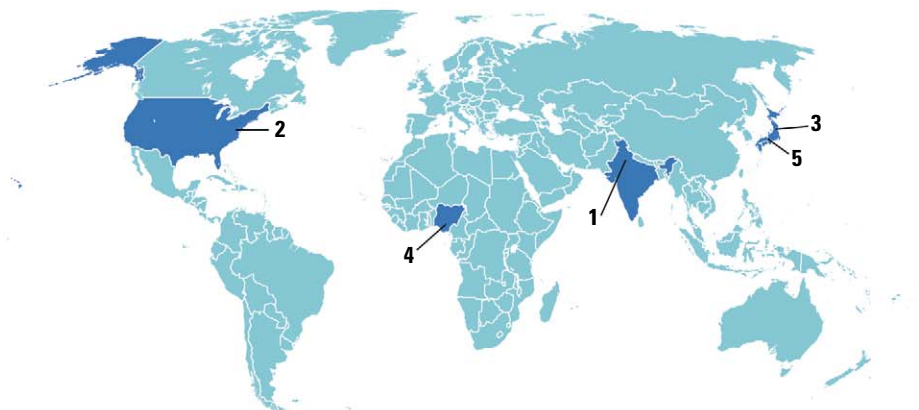
* For the purpose of this prize, molecular biology is defined as "that part of biology which attempts to interpret biological events in terms of the physico-chemical properties of molecules in a cell".

(McGraw-Hill Dictionary of Scientific and Technical Terms, 4th Edition).

GE Healthcare Bio-Sciences AB,
Björkgatan 30, 751 84 Uppsala, Sweden.
© 2011 General Electric Company

— All rights reserved.
28-9402-06AB

AROUND THE WORLD



New Delhi 1

Superbug Gene Found In Tap Water

A gene that causes bacteria to become resistant to antibiotics has been found in drinking water in New Delhi. *NDM-1* is commonly found in *Escherichia coli* but can spread to other bacteria thanks to their ability to swap DNA. The gene confers resistance to antibiotics, including potent, last-resort drugs called carbapenems.



India's warm temperatures, overcrowding, and poor sanitation are likely to blame for the gene's spread into the main water system from bacteria in people's guts, write Timothy Walsh of Cardiff University in the United Kingdom and colleagues in a paper published online last week in *The Lancet Infectious Diseases*. The team, which found the gene in two of 50 tap water samples and 51 of 171 samples taken from puddles and streams in the capital, say the gene could spread farther afield when tourists drink local water supplies and then return home. *NDM-1* has already been found in U.K. hospitals in bacteria infecting people who had medical treatment in India and those admitted with "traveler's tummy." The new finding raises concerns that resistant genes, so far found mainly in gut flora, are becoming widespread in natural environments, where they are highly mobile.

Washington, D.C. 2

U.S. Reaches Spending Deal

A deal between Congress and the White House to cut current government spending by \$38.5 billion will also affect federal research activities. But the final agreement, due to be approved as *Science* went to press, is much gentler on research than earlier versions approved by the Republican-led House of Representatives.

The negotiations that narrowly averted an 8 April government shutdown produced an agreement to lower discretionary spending to \$1.05 trillion for the 2011 fiscal year, which ends on 30 September. The overall federal budget is three times that size, with the majority spent on so-called entitlement programs like Medicare and service on the national debt. So the next debate, over the 2012 budget and extending the \$14 trillion debt ceiling, is expected to be even more contentious. For more, see page 291.

Fukushima, Japan 3

Japan Widens Evacuation Zone

Japanese officials announced this week that they are expanding the evacuation zone around the stricken Fukushima Dai-ichi nuclear reactors after relatively high levels of radiation were found beyond the 20-kilometer evacuation zone and even the 30-kilometer zone within which people have been told to stay indoors. Japan's Nuclear Safety Commission is now recommending relocation over the next month for those living in areas where the accumulated dose over a year will reach 20 millisieverts. That's about seven times the annual dose from natural sources in the United States. The government also raised its rating of the Fukushima incident on the

International Nuclear and Radiological Event Scale from five to the highest level, seven, ranking it on par with the Chernobyl disaster as a "major accident."

The contaminated areas lie northwest of the nuclear power plant, where weather patterns apparently blew a radioactive plume in the early days of the crisis. Radiation levels throughout the region have dropped over the past month as iodine-131, with a half-life of 8 days, decays. But the other main radioisotopes, cesium-134 and cesium-137, have half-lives of 2 years and 30 years, respectively. In areas not targeted for remediation, significant levels of radiation could linger for decades. <http://bit.ly/evac-zone>

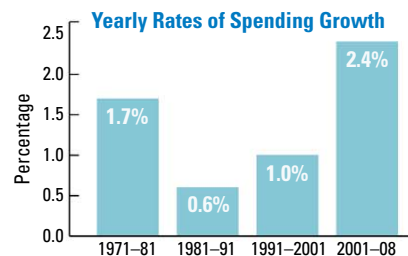
Nigeria 4

African Countries Up Investment In Agricultural R&D

Funding for public agricultural research in sub-Saharan Africa grew more than 20% to \$800 million between 2001 and 2008, according to a report published last week by the International Food Policy Research Institute (IFPRI) in Washington, D.C.

"African countries are starting to recognize the importance of funding agricultural research," says Calestous Juma of Harvard University, who studies agricultural innovation in Africa.

Just six of the 32 nations surveyed dominate these gains, and Nigeria leads the pack, accounting for a third of the overall increase. But as in several other African countries, the



increases—mainly for salaries and building repairs—have not yet made up for the declines of the 1990s. "What these numbers hide is that Nigeria is making up for lost ground," says report co-author Gert-Jan Stads of IFPRI. The funding situation has worsened in 13 countries, often due to large international grants ending.

Philip Pardey, an agricultural economist at the University of Minnesota, Twin Cities, says that rebuilding research capacity can take decades. African nations "have a very long way to go," he says.

CREDITS (TOP TO BOTTOM): BIKAS DAS/AP PHOTO; (SOURCE) IFPRI

Harima Science Park City, Japan 5

World's Second X-ray Laser Declared Done

Scientists now have two x-ray lasers—almost. Physicists at the SPring-8 laboratory in Harima Science Park City in Japan have coaxed x-rays out of the SPring-8 Angstrom Compact Free Electron Laser, or SACLA, lab officials announced. The first x-ray free electron laser, or XFEL, turned on 2 years ago at SLAC National Accelerator Laboratory in Menlo Park, California. However, scientists in Japan have not yet demonstrated “lasing” with the new machine, says SPring-8’s Tsumoru Shintake, technical director for the project. But the Japanese government wanted SACLA completed by the end of its 2010 fiscal year, which ended 31 March, so physicists put on a demonstration that it basically works, Shintake says.

Even if SACLA isn’t quite up and running, the announcement marks a coup for Japanese physicists. The Japanese government approved construction of the 700-meter-long, \$300 million laser, previously known as XFEL/SPring-8, in 2006. In comparison, a bigger XFEL in Europe, funded by Germany, was approved in 2003 but will not be complete until 2014. Experiments at SACLA will begin early next year.

NEWSMAKERS

Three Q’s

Classical archaeologist **Friederike Fless**, 46, left the Free University of Berlin last month to become the first woman to head the German Archaeological Institute (DAI) in its long history.



Founded in 1829, the Berlin-based institute is funded by the German foreign ministry; it employs more than 120 archaeologists and runs excavations in dozens of countries around the world.

Q: What has happened to the DAI’s excavations in North Africa recently?

We were lucky. In Egypt, I think we have no problems—the people living near our excavations defended the sites against looting. We had been working in Tunisia, Morocco, Algeria, and Libya before the changes, and now we want to strengthen that work—although it’s not possible to work in Libya.



Wise Whiskers

Why use eyes when you’ve got whiskers? Like the fingers of a hand, each of a rat’s 60 whiskers moves independently of the others and of the muscles in its cheeks. As the whisker touches an object, the follicle in the skin recognizes both the angle and the amount of pressure being applied. Each follicle then feeds into an individual cluster of neurons in the brain, which integrates the inputs to reveal the shape of the object the rat is exploring.

Now biological and mechanical engineer **Mitra Hartmann** of Northwestern University in Evanston, Illinois, and colleagues have laser scanned rat noses to create a computer model of this delicate phenomenon. The model, published last week in *PLoS Computational Biology*, could lead to a better understanding of how the brain processes the sense of touch. It may also help speed the development of whiskered robots that could perform tasks by using tactile sensations in place of cameras. <http://scim.ag/rat-whiskers>

Q: What are your priorities?

Fundraising is an important thing for me. It’s an international phenomenon that we have financial problems. Universities in America are having the same issues; everyone’s struggling with financial cutbacks. We have to work on raising the profile of the DAI, and this is one of the most important things I have to do in the next few years.

Q: What are your thoughts on being the DAI’s first female president?

It’s not a problem for me. I’ve been living with this situation for 46 years. For German society, I think it’s a normal development. Change started years ago: First we had more female students in the universities, then more female graduate students and professors. At a certain moment, it’s a natural development that the DAI has a female president.

Peripatetic Nobelist Dies at 85

Baruch Blumberg, who went by the nickname Barry, is best known for winning the Nobel Prize in physiology or medicine in 1976 for discovering the hepatitis B virus and inventing a vaccine against it. When he died on 5 April at age 85, apparently of a heart attack, he was thousands of miles from his home base in Philadelphia, at a NASA conference in California.

That was right in character for Blumberg. On top of years spent working with and even leading NASA’s astrobiology program and a long career at Philadelphia’s Fox Chase Cancer Center, Blumberg remained

constantly on the move.

Last summer, *Science* visited him at his home for a story about retiring researchers who have large collections of samples (*Science*, 9 July 2010, p. 135). Blumberg’s was among the most massive: at the time, he guessed that he’d amassed 450,000 blood samples during his career. To acquire them, he ticked off where he’d traveled to: West Africa, the Arctic, Romania, Italy, Taiwan, the Pacific Islands, and more. His geographic reach was so great that his face appeared on stamps in the Maldives and Angola. “I carried a lab around the world,” he said.



FINDINGS

Cosmic Feast May Be Producing Universe’s Biggest Blast

Astronomers have observed possibly the biggest blast ever seen in the cosmos. When NASA’s SWIFT space observatory first spotted it on 28 March, observers thought it was a massive star blowing up as a supernova and expected it to fade within hours or even minutes. But as *Science* went to press, the blast, while considerably fainter than its maximum intensity, was still going strong.

Observations by the Hubble Space Telescope and NASA’s Chandra X-ray Observatory pin the source to the center of a galaxy 3.8 billion light-years away, suggesting that it’s a black hole.

>>

CREDITS (TOP TO BOTTOM): MITRA HARTMANN (2); FOX CHASE CANCER CENTER/PAUL COHEN; I. WAGNER/DAI

BY THE NUMBERS

37.9 Height, in meters, of Japan's 11 March tsunami in one area, according to a team examining signs of the tsunami's reach. That's tall enough to engulf a 10-story building; seismologists say they expect to find even higher water marks.

30.3% Percentage of U.S. universities where the average faculty salary decreased in 2010–2011, according to a survey by the American Association of University Professors. Male full professors on average made \$114,421, about 14% more than their female counterparts.

>>FINDINGS

It could be that a star flitting too close to the black hole has been grabbed by its gravitational pull. As the black hole consumes the star's gas, it releases enormous amounts of energy in jetlike bursts of particles.



Although astronomers have seen black holes gobbling stars, this blast is putting out far more energy than previously seen. If it stays bright for weeks, astronomers say, they will have to look for another explanation, such as

a dormant quasar suddenly turning on.

<http://scim.ag/big-blast>

Caffeine Fiend? Could Be A Gene Thing

Researchers have found two genetic variants that may help explain why some coffee drinkers keep going back for refills.

Twin studies suggest that genes may account for between 43% and 58% of the variability in coffee-drinking habits. To pinpoint the responsible genes, genetic epidemiologist Marilyn Cornelis of the Harvard School of Public Health, along with colleagues at six institutions, scanned the entire genomes of 47,341 adult subjects from five U.S. studies that had collected data on caffeine intake. Two variants emerged. One neighbored a gene called *CYP1A2*, which “is

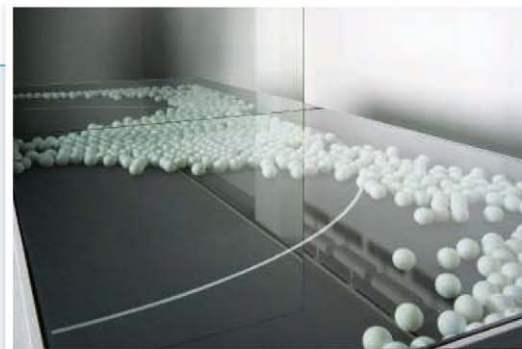
Random Sample

Beyond Entropy

When designing a building or a city, architects usually put things together in an orderly fashion. But in a month-long exhibition beginning 3 May at the Architectural Association School of Architecture in London, Italian architect Stefano Rabolli Pantera has challenged artists, architects, and scientists alike to embrace order's nemesis: entropy.

In the show, titled “Beyond Entropy,” eight interdisciplinary groups explore the second law of thermodynamics in the context of sound, electricity, heat, and gravitational potential energy. The works include a swinging pendulum, connected to a continuously projected image of a building being simultaneously built and destroyed; a 1-meter-high spinning “time machine”; and a pinball-like game (pictured) that invites viewers to flick Ping-Pong balls through a gap in a mirror while ruminating about potential energy. In preparation, each of the teams visited scientific institutions, including the Large Hadron Collider near Geneva, Switzerland, for inspiration.

Pantera says that his motivation for the show is to get people to think about energy not as a problem to try to solve, but “as a new way to think about space.”



up to 95% responsible for caffeine metabolism,” Cornelis says. The other big hit, the team reported last week in *PLoS Genetics*, was a variant near a gene called *AHR*, which



regulates how *CYP1A2* is expressed. Cornelis speculates that the variants could ramp up caffeine metabolism, meaning people who have

the variants require more refills to maintain the same buzz as those who don't. But she says the findings suggest that other genetic variants also come into play.

<http://scim.ag/coffee-gene>

Sex After a Field Trip Yields Scientific First

A U.S. vector biologist appears to have accidentally written virological history simply by having sex with his wife after returning from a field trip to Senegal.

Brian Foy of Colorado State University in Fort Collins and graduate student Kevin Kobylinski got bitten mercilessly while collecting mosquitoes in Senegal for their malaria research. About 5 days after returning home on 24 August 2008, both researchers developed a rash, fatigue, swollen and painful joints, and other unpleasant symptoms. Days later, Foy's wife, Joy Chilson Foy, fell ill as well.

The scientists suspected a mosquito-borne virus, but lab studies failed to turn up

a culprit. On his next Senegal trip, however, Kobylinski told the tale to Andrew Haddow, a medical entomologist at the University of Texas Medical Branch at Galveston whose grandfather had isolated a virus called Zika in Uganda in 1947. Haddow suggested that the obscure mosquito-borne agent might be to blame—and sure enough, lab tests turned up Zika antibodies in samples from all three.

Zika-transmitting mosquitoes don't live in northern Colorado. A paper published online 2 weeks ago in *Emerging Infectious Diseases* points instead to “vaginal sexual intercourse in the days after patient 1 [Foy] returned home”—which would be the first known case of sexual transmission of a mosquito-borne virus. “My wife wasn't happy,” says Foy; she is, however, an author of the paper.



Bitten. Kobylinski (left) and Foy (right) with entomologist Massamba Sylla in Senegal.

CREDITS (TOP TO BOTTOM): VALERIE BENNETT/THE ARCHITECTURAL ASSOCIATION SCHOOL; ISTOCKPHOTO.COM; NASA/SWIFT/STEFAN IMMLER; COURTESY OF BRIAN FOY



U.S. BUDGET

Research Holds Up Well In Final 2011 Agreement

When the dust settles on the spending bill—negotiated just an hour before the federal government would have shut down last week—scientists can breathe more easily.

U.S. research agencies were largely spared from deep cuts in current spending. The legislation, up for a vote as *Science* went to press, would trim \$38.5 billion from 2010 budget levels. But it marks a major retreat from the \$61 billion cut approved in February by the Republican-led House of Representatives that would have hobbled basic research across the federal government and ravaged energy and climate programs (*Science*, 25 February, p. 997; 18 March, p. 1378).

The cuts average 1% for major research agencies such as the National Institutes of Health, the National Science Foundation, the Department of Energy's (DOE's) Office of Science, and the research labs at the National Institute of Standards and Technology (NIST). The agreement also preserves the new Advanced Research Projects Agency—Energy and the Administration's signature education program, called Race to the Top, which funds exemplary elementary and secondary school programs.

The so-called continuing resolution (CR), which prescribes spending levels for the second half of the 2011 fiscal year, won't end the partisan battles over the budget. This week, the House planned to vote on a nonbinding 2012 budget resolution to cut trillions of dollars over the next 10 years. And on 13 April,

President Barack Obama laid out his own vision for fiscal restraint in a speech at George Washington University in Washington, D.C.

The ongoing political battle is reflected in the press releases issued this week by the chairs of the appropriations committees in each body of Congress. The Republican House stresses the magnitude of the cuts, while the Senate, in which Democrats hold a slim majority, emphasizes how many of the Obama Administration's priorities in research and education were preserved.

"When this agreement is signed into law," declares Representative Harold Rogers (R-KY), "this Congress will have taken the unprecedented step of passing the largest nondefense spending cut in the history of our nation." Rogers adds that "the goal of this new Republican majority [is] to keep precious tax dollars where they are needed most—in the hands of businesses and individuals—so that they can create jobs and grow our economy."

Senator Daniel Inouye (D-HI) sounds like he's talking about a different spending bill. "The final legislation rejects the draconian cuts and onerous policy riders proposed in H.R. 1 [the House bill]," he declares. "This bill preserves critical programs, including Head Start [for preschool education], Pell

Budget buddies? House Speaker John Boehner and Senate Majority Leader Harry Reid after a White House meeting last week on the budget.

grants [for college students], and vital scientific and medical research."

Indeed, research is treated relatively well compared with other portions of the federal government. NIH will receive \$30.7 billion, down \$300 million from 2010 levels, while NSF will get \$6.8 billion, a \$65 million trim. The cuts amount to roughly 1% once the bill's 0.2% across-the-board reduction to all non-defense programs is included.

DOE's Office of Science would make a spectacular recovery from the 18% cut the House approved in H.R. 1. The final bill gives it \$4.88 billion, only \$30 million less than in 2010. The CR also preserves the \$600 million biological and environmental research office, one of six programs in the office, which the House wanted to gut. And the \$500 million budget for NIST's core research labs would shrink by just \$7 million, although NIST would not receive new money for its technology innovation program to support industry-led research or for construction grants to universities. The NSF, DOE science, and NIST budgets are all on a 10-year doubling trajectory.

This is the eighth CR of the 2011 fiscal year, which began on 1 October 2010. The previous Congress, controlled by Democrats, was unable to complete work on the 2011 budget, and there have been more CRs since the Republicans took control of the House in January.

The House's first attempt at a 2011 budget would have cut \$35 billion from 2010 levels. But fiscal conservatives, prodded by 87 rookie legislators, rejected that as too timid. A week later House leaders came back with an additional \$26 billion in cuts, along with language on several hot-button policy issues such as abortion, and the measure passed the House on 19 February.

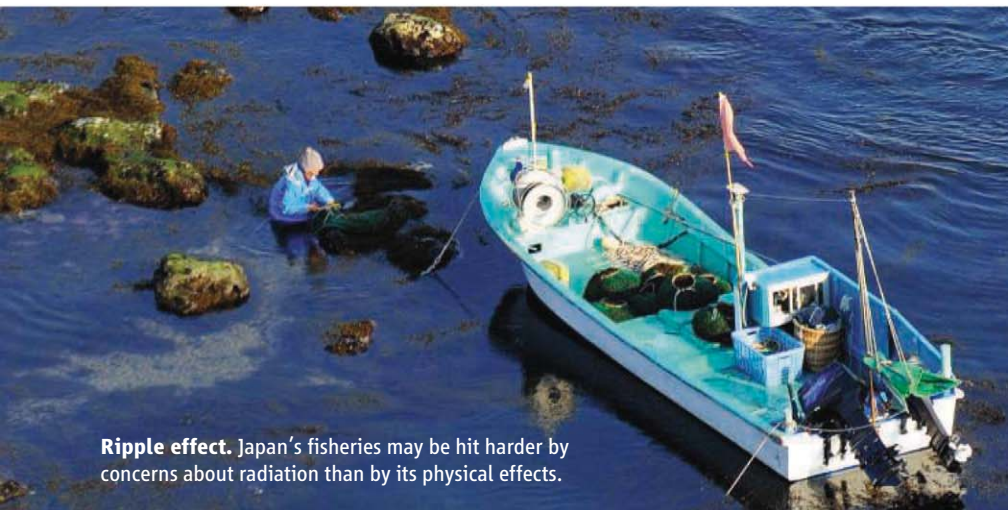
The Senate, under the Democrats, had initially balked at any cuts and backed the president's promise for a 3-year freeze on discretionary domestic spending. Under pressure to show greater fiscal restraint, Inouye later presented a plan that would have trimmed \$10 billion from 2010 levels. On 9 March, however, the Senate rejected both the House-passed version and the Senate plan.

Those votes, followed the next week by the adoption of another CR that expired on 8 April, set the stage for last week's final round of budget negotiations. Now comes the battle over the 2012 budget.

—JEFFREY MERVIS

Online
sciencemag.org
Podcast interview
with author
Jeffrey Mervis.

CREDIT: PABLO MARTINEZ MONSIVALES/AP PHOTO



Ripple effect. Japan's fisheries may be hit harder by concerns about radiation than by its physical effects.

RADIOECOLOGY

Fukushima Radiation Creates Unique Test of Marine Life's Hardiness

When radiation readings from water monitors around the leaking Fukushima Daiichi plant began rising this month, spiking at 7.5 million times Japan's legal limit for radioisotopes in public water, government agencies reacted sharply. For the first time in history, the Japanese government set a limit on radiation in seafood and began screening fish. India and China recently banned imports of food products from certain areas of Japan, and the U.S. Food and Drug Administration began conducting its own radiation screens on seafood imports.

Monitoring food makes sense, according to radiation geochemist William Burnett of Florida State University in Tallahassee, but he warns against overreacting to the perceived risk of ocean contamination. "Stopping eating sushi, that's crazy," he says, based on what is known about isotope accumulation in marine animals and reports on radiation in the sea near Fukushima. Although radioactive elements could spread quickly through the food chain, Burnett and others say it's unlikely that would lead to a significant risk for humans. What it could mean for ocean-dwelling organisms is another matter—one that scientists are eager to investigate.

Many marine species are good at absorbing radioactive isotopes from the water, and experts across the world are beginning to prioritize studies they'd like to do in Japan once the situation stabilizes. "It's another opportunity to study impact on the environment, and many countries will use this opportunity," says marine radioecologist Bruno Fievet of

the French Institute for Radiological Protection and Nuclear Safety (IRSN) in Cherbouurg. "Probably we will see traces of this accident for many years," he says.

Little is known about the impact of radioactivity on many marine organisms, in part because they are remarkably resistant. Fievet says that a deadly dose of radioactivity for crustaceans and mollusks is orders of magnitude larger than a lethal dose for humans, which makes it dangerous and inefficient for researchers to conduct lab experiments. Harming organisms in the lab, Fievet says, requires levels of radioactivity that are "very, very high compared to what is observed in the marine environment at Fukushima."

The creatures' simple physiology and the salty environment also offer them some protection. Just as potassium iodide tablets can saturate the human thyroid and prevent radioactive iodine from binding, the abundant ocean salts reduce the absorption of radioactive ions by sea creatures.

At the same time, Fievet adds, just because there's no immediate hazard is "not a reason not to worry." Water close to the plant contains particulate radioisotopes, including cesium-137 and iodine-131, which organisms can incorporate into their bodies through their skin or food. Cesium-137 is more worrisome because its 30-year half-life means that it will be around for many decades. The resulting internal dose could induce mutations, stunt growth, and cause reproductive defects. Some organisms are exceptional at taking up isotopes and concentrating them in

their bodies. Larger organisms that eat them may receive a high dose of radiation all at once, possibly increasing the risk of harm.

In terms of cleaning up the ocean, however, this bioaccumulation could be a boon. Phytoplankton, the base of most marine food chains, can concentrate plutonium a million-fold as it sticks to the surface of their membranes. Larger organisms that eat phytoplankton can't assimilate plutonium, so they excrete it as concentrated fecal matter that sinks to the bottom of the ocean and away from the vast majority of marine life near the surface. Similarly, brown seaweed, a staple of miso soup and sushi bars, acts as an iodine sponge, concentrating the element 10,000-fold compared with the surrounding water. Some researchers have even proposed planting the ocean full of brown seaweed to soak up radioactive iodine, but Fievet says this idea has been more or less rejected because it would simply transfer the problem from water into seaweed.

Most researchers believe that in the end the ocean will take care of itself through its vast size. Off the coast of Japan, the sea floor drops quickly, providing a large dilution factor. The International Atomic Energy Agency (IAEA) reports that over a span from the coast to 31 kilometers out, radiation drops 1000-fold. After dilution, says marine biologist Nicholas Fisher of Stony Brook University in New York, added radiation quickly becomes indistinguishable from the natural background level. "The bit introduced by man is a drop in the bucket," he says.

Fievet says that IRSN scientists have begun formulating studies they'd like to undertake with collaborators in Japan. U.S. radioecologists from a number of U.S. universities, the U.S. Department of Energy, and IAEA's Marine Environment Laboratories have also expressed interest in beginning long-term studies. "We are faced with a unique situation" in which an accident is having a direct impact on the sea, says Dominique Boust, director of IRSN's radioecology lab.

In the meantime, Fisher says, "While it's nice to know the isotope concentration in water, it's more critical to know what it is in marine organisms." The National Research Institute of Fisheries Science in Japan has begun screening a number of species and has found elevated cesium-137 in a few fish. Even so, research from weapons testing and the Chernobyl accident found that large fish that accumulate cesium-137 excrete it over time. Compared with other toxins that humans put into the marine environment, researchers conclude, the danger to Japan's fish from the radiation spill is very low. **—SARA REARDON**

CREDIT: © EVERETT KENNEDY BROWN/EPA/CORBIS

SOLAR ENERGY

Outlook Brightens for Plastic Solar Cells

The global market for solar cells has been growing at more than 30% a year for much of the past decade. But to match the scale of coal or nuclear power anytime soon, the technology will have to do much better. Silicon cells, the premier solar technology, convert 15% to 20% of the energy in sunlight to electricity, and their price has been dropping steadily. But many industry observers worry that a price floor could be near, because the cells require expensive clean-room technology to manufacture. Thin films of copper, indium, gallium, and selenium are 15% efficient and cheap, but indium is in short supply. Cadmium-telluride thin films, which rely on rare tellurium, are in much the same boat.

"The door is still open for a technology that gives you 15%, is cheap, and uses abundant materials," says Michael McGehee, a materials scientist at Stanford University in Palo Alto, California. It's an opening that makers of plastic solar cells hope to fill.

For years the efficiency of polymer-based cells scraped along at a feeble 3% to 5%. But things have improved markedly over the past 2 years. In early April, Mitsubishi Chemical reportedly set a new efficiency record, producing organic solar cells with a 9.2% conversion efficiency, according to *The Nikkei*, a Japanese business daily. Meanwhile, three other companies—Konarka Technologies in Lowell, Massachusetts; Solarmer Energy Inc. in El Monte, California; and Heliatek in Dresden, Germany—are now reporting cells with efficiencies greater than 8%. Many researchers in the field are confident that the figure could soon top 10% and possibly reach 15%.

"The efficiency of organics is lower than other technologies," says Bernard Kippelen, an optics expert at the Georgia Institute of Technology in Atlanta. "But they are catching up at a fast pace."

Just what lies behind the efficiency gains in the companies' cells is hard to determine, as they have released few details about how they are made. But progress has been coming in areas beyond efficiency as well. For example, researchers led by Wei You, a chemist at the University of North Carolina, Chapel Hill, reported online 4 March in the *Journal of the American Chemical Society* devising two novel polymer-based light absorbers that catch less light than some polymers but are better at converting what they do catch to electricity. In recent years, most makers of

polymer solar cells have focused on designing polymers that absorb all visible light down into the reds, the low-energy end of the spectrum. The hope has been that maximizing the amount of light absorbed would improve the cells' energy conversion. Although that approach has been somewhat successful, the red absorbers are less successful than higher-energy light-absorbing polymers at converting absorbed light to electricity.

You and his colleagues created two new violet-to-yellow light absorbers, which give up on harvesting the reds but do a better job with what they do catch. The result was single-layer polymer cells with a 7.3% effi-

ciency, in part because the solvents used to print the top solar-cell layers can dissolve those underneath. Polymer tandem makers try to prevent that by laying down a barrier layer between the two cells. But just the right barriers can be hard to make, because they must be not only conductive to collect electrical charges in the cells but also optically transparent. At the American Chemical Society (ACS) meeting 2 weeks ago,* Yang Yang, a physicist at UC Los Angeles, reported that his group had modified a common interlayer material known as PEDOT, making it five orders of magnitude more conductive. That should make it a far better barrier layer and improve the performance of tandem cells, work the group is now trying to carry out.

Another concern for organic solar cells has been lifetime. As anyone who has left children's plastic toys in the backyard over the summer knows, sun can degrade many organic materials. That's of particular concern for solar cells that must hold up under relentless sun exposure. In hopes of addressing this concern, McGehee and colleagues at Stanford have constructed an apparatus to speed up lifetime testing of organic solar cells.

At the ACS meeting, McGehee reported that the first light-absorbing polymer his lab tested, known as PCDTBT, lasted 7 years. That may seem short to someone looking to get decades of power out of the devices, but McGehee says efforts to improve the lifetime of these devices are just beginning. "I think that it's encouraging," he says. Many organic-solar-cell researchers are starting to share his sunny outlook.

—ROBERT F. SERVICE

RECENT EFFICIENCY GAINS

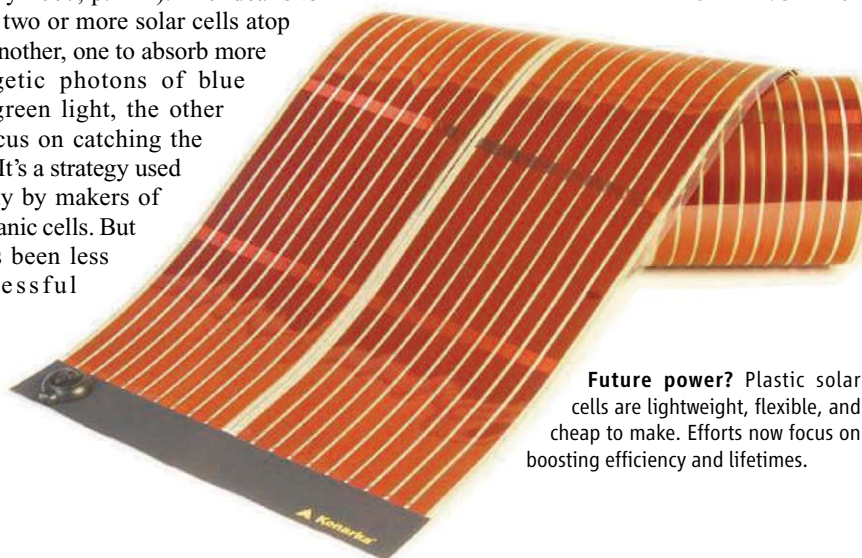
Company	Date	Efficiency
Solarmer Energy Inc.	July 2010	8.13%
Heliatek	October 2010	8.30%
Konarka	November 2010	8.30%
Mitsubishi Chemical	April 2011	9.2%*

*According to media reports.

On the rise. Makers of organic solar cells report steady gains in electrical output.

ciency. "That's impressive work," says Alan Heeger, a physicist at the University of California (UC) Santa Barbara, who won the chemistry Nobel Prize in 2000 for his work on conducting polymers and has pioneered work on polymer solar cells. Heeger notes that the new polymer should be ideally suited to pairing with a second, red-absorbing cell to make higher efficiency "tandem" cells.

Heeger's group reported the first tandem polymer solar cells 4 years ago (*Science*, 13 July 2007, p. 222). The idea is to stack two or more solar cells atop one another, one to absorb more energetic photons of blue and green light, the other to focus on catching the reds. It's a strategy used widely by makers of inorganic cells. But it has been less successful



Future power? Plastic solar cells are lightweight, flexible, and cheap to make. Efforts now focus on boosting efficiency and lifetimes.

*American Chemical Society, 27–31 March, Anaheim, California.



Last resort. When other treatments fail, brain surgery may be the only hope for some schizophrenia patients, Sun Bomin says.

PSYCHOSURGERY

Chinese Neurosurgeons Quietly Push For Easing of Brain Operation Ban

SHANGHAI, CHINA—Xiaolin used to hear voices. She was also prone to violent fits, during which she would hurl chairs and assault her parents. In 2000, when she was 31 years old, Xiaolin was diagnosed with schizophrenia. Over the next 5 years she was treated with drugs and 70 courses of electroconvulsive therapy. Nothing worked.

Then Xiaolin went under the knife. In December 2005, Sun Bomin, a neurosurgeon at Ruijin Hospital here, performed a procedure called stereotactic ablation in which he drilled two holes into her skull and burned tiny sections of her brain. After the surgery, when Xiaolin's father first saw her in the recovery room, he was amazed. "She looked calm and was even reading a magazine," he says. "She never read books before because she would say that 'others' forbid her." Six years later, he says, she's doing great.

Xiaolin's case is one that makes Chinese neurosurgeons lose sleep at night. She regained a normal life—but the procedure is now outlawed. Concerned about reports that many psychiatric patients were not benefiting from psychosurgery, or were even suffering irreparable harm, China's health ministry issued a regulation in 2008 that limits brain surgery to a few conditions for which it is recognized as a last resort. Experimental applications, such as stereotactic ablation for schizophrenia, are forbidden.

Sun chafes at the ban but doesn't blame the ministry. The problem, he says, is the absence of international guidelines. At a World Society for Stereotactic and Functional Neurosurgery (WSSFN) meeting here last month, researchers and neurosurgeons sought to clarify which brain operations for psychiatric conditions

should be allowed and which should be experimental or off-limits. The consensus forged at the meeting—the first such forum since the 1970s—may encourage the health ministry to revise its psychosurgery guidelines, Sun says. But unscrupulous clinics are casting a shadow on the practice in China.

Psychosurgery has come a long way since the dark ages of lobotomy, a now-discredited procedure in which large tracts of neural fibers in the frontal lobe were cut to pacify patients with psychosis. In contrast to that blunt approach, stereotactic ablation targets small foci of brain tissue. In the 1960s and 1970s, the technique grew in popularity as an experimental treatment for depression and for obsessive-compulsive disorder (OCD) cases that fail to respond to drugs or other therapies, says WSSFN President Takaomi Taira, a neurosurgeon at Tokyo Women's Medical University. Then about a decade ago, he says, deep-brain stimulation—in which surgeons implant electrodes in a patient's brain that send electrical impulses to specific brain regions—sparked renewed interest in surgical management of psychiatric disorders. Unlike stereotactic ablation, deep-brain stimulation doesn't leave an irreversible lesion.

Riding that tide of interest, hospitals in China began to practice psychosurgery widely to cope with a legion of psychiatric patients. According to the Chinese Center for Disease Control and Prevention, China had some 100 million psychiatric patients last year, more than any other country. Approximately 16 million suffer from severe disorders.

Besides using stereotactic ablation for OCD and depression, hospitals in China began experimenting with psychosurgery

for schizophrenia—by destroying cells in the anterior limb of the internal capsule, for example—and addictive behavior. That made some experts uneasy; they were not convinced that the wellspring of these disorders in the brain can be pinned down so easily. "There is no internationally recognized theory basis for using brain surgery to treat schizophrenia or drug addiction. The circuit and the target spots are not clear," says Mei Gang, a psychiatric physician at Nanjing Brain Hospital.

Responding to such concerns, the health ministry issued a regulation in 2008 that limits psychosurgery to refractory OCD, depression, and anxiety disorders. The rule notes that the procedure is high-risk and controversial and sets qualifications for neurosurgeons entitled to perform it.

The rule resulted in a sharp drop in operations. For instance, Nanjing Brain Hospital did 31 such operations in 2003, then four in 2008, and three in 2010. In 2007, the highly rated neurosurgery department at Huashan Hospital here conducted 20 psychosurgery operations; it has not performed a single one since the rule came out. "The procedure is valuable, but it should not be widely used now and needs to be tested," says Huashan neurosurgeon Lang Liqin. She notes that some psychosis patients who showed marked progress after surgery experienced significant personality changes—for example, they became mentally sluggish.

The health ministry's crackdown covers only civilian hospitals; scores of military hospitals are not subject to the regulation. Some military hospitals have voluntarily established stricter screening systems. In Nanjing, 454 Hospital of the People's Liberation Army carried out more than 300 psychosurgery procedures a year before 2008; it performs half as many nowadays, says Wang Yifang, head of neurosurgery at the hospital. Although 454 has a solid reputation, some military hospitals are less transparent and their psychosurgery operations are more troubling, according to one Chinese neurosurgeon who requested anonymity. Taira, meanwhile, objects to the practice of some Chinese clinics that advertise psychosurgery for profit or fame. Such abuses, he says, will harm the field's healthy development.

A health ministry committee is now reviewing the qualifications of hospitals that it will license to practice psychosurgery. The review is expected to sanction experimental applications at a handful of topflight hospitals, Sun says. For some patients, he insists, that may be their only hope of a normal life.

—WANG XIAO

Wang Xiao is a writer in Shanghai.

CREDIT: COURTESY OF SUN BOMIN



Political warfare. Tennessee legislator Bill Dunn's bill labeling the teaching of evolution and climate change as "controversial" subjects mirrors efforts in seven U.S. states this year.

EVOLUTION IN THE SCHOOLS

Tennessee House Bill Opens Door to Challenges to Evolution, Climate Change

U.S. science educators are wringing their hands over what they characterize as a significant legislative victory for those who oppose the teaching of evolution.

Last week, the Tennessee House of Representatives overwhelmingly approved an innocuous-sounding measure allowing science teachers in the state to help their students "develop critical thinking skills." The legislation, which specifically mentions the teaching of "biological evolution, the chemical origins of life, global warming, and human cloning," is expected to become law next month after the state Senate embraces an identical version and the governor signs it.

Scientists say HB 368, and the corresponding Senate bill, SB 893, would actually have the opposite effect on critical thinking by introducing nonscientific beliefs into science classes and by undermining the principles of scientific inquiry. "These bills misdescribe evolution as scientifically controversial," say prominent Tennessee scientists, including medicine Nobelist Stanley Cohen of Vanderbilt University in Nashville, in a letter sent to legislators before last week's 70–23 vote. They write that teachers who are encouraged "to emphasize what are misdescribed as the scientific weaknesses of evolution ... are likely to include scientifically unwarranted criticisms."

The bill's sponsor, Republican Bill Dunn of Knoxville, says scientists are deliberately distorting the intent of the legislation.

He acknowledges that it is derived from a model bill crafted by the Discovery Institute, an organization based in Seattle, Washington, that questions evolution and promotes intelligent design. But Dunn says the bill would merely allow teachers to offer students "objective, scientific facts" during classroom discussions without fear of being "bullied" into silence by the scientific mainstream.

Dunn, a veteran legislator who this year helped the state's new governor push through various education reforms, including changes to teacher tenure laws, says most critics haven't bothered to read the bill. In particular, Dunn says, opponents have misinterpreted language about controversial teaching methods as an attack on evolutionary theory. "If you dare even question or call something controversial," Dunn says, "there seems to be this Pavlovian response. Only, instead of drooling at the mouth, they foam at the mouth." The "mean-spirited" criticism of his bill, he adds, has convinced him that "scientists are just as prejudiced and subjective as the average person walking down the street."

Scientists' fears that the bill would allow the teaching of creationism are unfounded, according to Dunn, who points to a clause that declares the legislation "shall not be con-

strued to promote any religious doctrine." But Barbara Forrest, a philosophy professor at Southeastern Louisiana University in Hammond, who closely tracks the debate over teaching evolution, believes those words mean exactly the opposite. "The religious disclaimer is in every one of these bills," she says. "It's a dead giveaway that it IS a creationist bill. If it were truly only about teaching science controversies, they wouldn't need a disclaimer."

Tennessee isn't the only state in which so-called academic freedom statutes have been introduced in recent years (*Science*, 9 May 2008, p. 731). This year's tally alone is nine in seven states, according to the National Center for Science Education, an Oakland, California, group that tracks the debate. Although most died in committee, two bills—in Florida and Texas—are still pending. In 2008, Louisiana adopted a measure that allows science teachers to use supplemental material in exploring "the strengths and weaknesses" of evolutionary theory and other topics (*Science*, 23 January 2009, p. 451). Dunn says he asked Louisiana school officials this spring how many "problems" they have had since the bill was enacted and that their answer was "zero." Forrest says a bill will be introduced next week to repeal the measure.

Bart Gordon, the former chair of the science committee in the U.S. House of Representatives who represented a central Tennessee district for 26 years before retiring in January, agrees with Forrest that the bill is part of a disturbing trend among elected officials at the state and national levels. "It's an unfortunate statement of the times in Tennessee," says Gordon, who was a vocal advocate for better science education during his tenure in Congress. "Why don't people think that climate change is real? You asked me last year why I decided to retire. Well ..."

Dunn says he believes the bill, which he admits he did not write himself and introduced as a favor to a former colleague, will improve science education by stimulating classroom discussion. "You gather a whole bunch of facts and figure out what is happening—that's what science is," he explained during last week's floor debate. But his staunch advocacy of the measure—veteran Tennessee politics reporter Ed Cromer describes Dunn as "a person of faith who's very sincere and passionate about his beliefs"—has also come at a price.

"As I told a friend the other day," Dunn says, "If I ever introduce another bill with the word 'evolution' in it, please shoot me. I never expected things to get this nasty."

—JEFFREY MERVIS

Online
sciencemag.org
S Q&A with the
bill's sponsor.

HIGH-ENERGY PHYSICS

A Sign of New Particles or General Restlessness?

Particle physicists haven't discovered anything truly surprising in 35 years, so a mere hint of something odd works them up in a hurry. So it was last week, when, aided by press reports, news spread that scientists in the United States may have spotted a bit of matter unlike any seen before. But even as they contemplate the implications, physicists are taking the result with a grain of salt. The supposed signal could be an experimental artifact, caution the researchers who found it. And if a new particle *is* there, physicists may have to perform theoretical contortions to explain why they didn't spot it before. "I think the result is rather inconclusive," says Christopher Hill, an experimenter at Ohio State University in Columbus, who was not involved in the work.

a collision or decay kicks out a particle called a quark. A quark cannot exist on its own but must be bound to other quarks or an antiquark. So the energetic quark quickly rips more quarks and antiquarks out of the vacuum of empty space, and they instantaneously form particles called mesons, each containing a quark and an antiquark. From the energies and momenta of the two jets, researchers can infer the mass of the particle that produced them.

CDF researchers see about 250 events in which the jets seem to come from a particle weighing about 155 times as much as proton. Those events show up as an unexpected peak in a data plot (see diagram). The chances that random jets or jet pairs from other sources would produce a fake signal

for new particles. To see the peak, they must subtract out a huge "background" produced by events containing a W and random jets. If that subtraction isn't just right, it could produce a fake signal. "The real question is how well do we understand that [background]," says Joseph Lykken, a theorist at Fermilab.

But those caveats have not stopped theorists from trying to explain the curious bump in terms of new particles. Felix Yu, a theorist at the University of California, Irvine, suggests that the new particle could be one known as a Z' (pronounced Z-prime), which would convey a new force much like a very short-range electromagnetic force. Estia Eichten, a theorist at Fermilab, and colleagues say the particle could be a "technipion," a particle predicted by a type of theory called "technicolor," which posits a new kind of strong nuclear force.

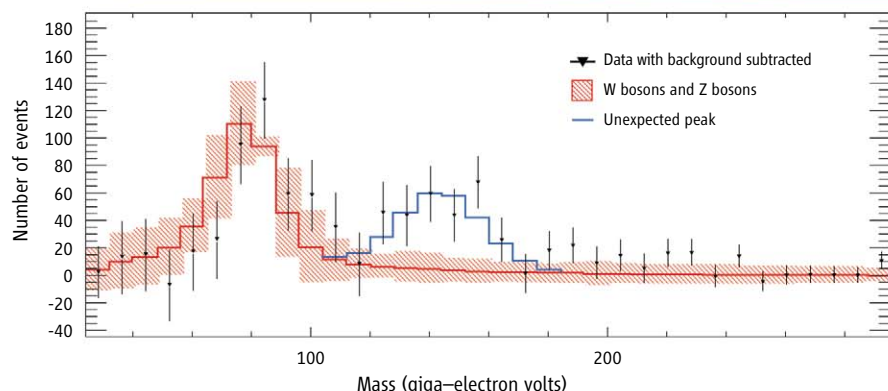
To have escaped notice until now, however, a particle would have to have some weird properties. Generally, a Z' ought to decay into an electron and an antielectron. In fact, experimenters have already searched for and failed to find that decay. So Yu's Z' must not decay that way for some reason. The technipion may face similar problems. CDF researchers are searching for the long-sought Higgs boson, the key to physicists' understanding of mass, by looking for events in which it is produced with a W boson and in which the Higgs decays into two jets specifically triggered by particles called bottom quarks. The hypothetical new particle hasn't shown up in those Higgs searches, so it must not often decay into bottom quarks, as one would expect a technipion to do.

For those reasons, some physicists say such explanations of the bump seem contrived or "unnatural." "Yesterday, these models weren't popular," Hill says. Yu counters that "having a theory that looks pretty but doesn't fit the data isn't natural."

The supposed signal should be confirmed or ruled out in short order. The CDF team has analyzed only half of the data it has already collected. And the Tevatron's other large particle detector, D0, has a data set as big as CDF's. If the particle is there, D0 should see it, too. "We hope that within a few weeks you'll be hearing from us," says Dmitri Denisov, a physicist at Fermilab and co-spokesperson for the D0 team. In the meantime, physicists will enjoy the buzz.

—ADRIAN CHO

PUZZLING PLOT



Mountain or molehill? In this plot of the mass inferred from each pair of jets, the right peak could signal new particles. The left peak is created by familiar W and Z bosons that decay into jets.

The finding comes from the 700-member team working with the CDF particle detector at Fermi National Accelerator Laboratory (Fermilab) in Batavia, Illinois. The team analyzed the billions of collisions of protons and antiprotons produced by Fermilab's atom smasher, the 25-year-old Tevatron, which will shut down this year. Those high-energy collisions can blast into fleeting existence massive subatomic particles not seen in the everyday world. Physicists try to identify those particles by studying the combinations of familiar particles into which they decay.

In this case, experimenters searched for collisions that produced a particle called a W boson, which weighs about 86 times as much as a proton, along with some other particle that disintegrates into two sprays of particles called "jets." A jet arises when

that strong are 1 in 1300, the physicists estimate. "We've been struggling for 6 months to make this peak go away, and we haven't been able to do it," says Robert Roser, a physicist at Fermilab and co-spokesperson for the CDF team. Still, he says, the signal is "not even close" to strong enough to claim a discovery.

Experimenters have several reasons to be cautious. The analysis depends critically on physicists' understanding of jets. CDF does not measure every particle in a jet, so researchers must make a 25% upward correction to a jet's measured energy. If the uncertainty in that fudge factor is bigger than they estimate, "then maybe the excess isn't so significant," says Shahram Rahatlou of Sapienza University of Rome.

CDF physicists must also take care that they haven't mistaken random pairs of jets



Tall order. Marfan syndrome leads to increased height, as seen in the boy third in line, and a risk of a ruptured aorta and other connective tissue problems.

MEDICINE

Frightening Risk of Marfan Syndrome, And Potential Treatment, Elucidated

Five years ago, a pediatric cardiologist set in motion a new treatment for Marfan syndrome that upended the field. Marfan is a genetic condition that weakens connective tissue throughout the body, including in the lungs, the skeleton, and the cardiovascular system. The biggest risk for patients with Marfan syndrome is a ruptured aorta, which can kill them. Surgery to remove the affected piece of the aorta can prevent a rupture, but over time other parts of the artery also start to expand and weaken. Right now most patients take beta-blocker drugs to try to keep aneurysms at bay, but more than half of Marfan patients eventually still need surgery.

Harry Dietz of Johns Hopkins University in Baltimore, Maryland, thought he might have found a better way. A blood pressure drug called losartan that he tested in mice virtually erased the risk of aneurysms (*Science*, 7 April 2006, pp. 36 and 117); in humans, losartan has long been considered quite safe. That result prompted several clinical trials, which are ongoing. Some patients have even sought the drug on their own.

Yet beneath this bench-to-bedside story, “there were important questions and controversies that were left unanswered,” Dietz says. This week, on pages 358 and 361, Dietz and his colleagues parse the molecular cascades that lead to aneurysms in Marfan syndrome, shedding light on why losartan looks so promising. “These are describing a lot of the issues that could underlie” why losartan helped those mice as reported, to much excitement, back in 2006, says Alan Daugherty, a vascular pathologist at the Uni-

versity of Kentucky, Lexington.

At the same time, other work has been exploring just how messy the aneurysm puzzle is and examining whether Dietz’s finds reach beyond Marfan.

In 2006, Dietz discovered that blocking a protein called transforming growth factor- β (TGF- β) with losartan in mice somehow stopped the enlargement and weakening of the aorta. To understand the link between TGF- β and aortic aneurysm, he and his colleagues then looked at several cell-signaling proteins controlled by TGF- β .

In this latest mouse study, Dietz’s group saw that a protein driven by TGF- β , called ERK (for extracellular signal-regulated kinase), was activated. To follow up, the researchers partnered with the U.S. National Institutes of Health’s Chemical Genomics Center, which screens molecules for potential drugs. An ERK-inhibiting drug was in trials for cancer, and Dietz’s lab tested it on its mice. The result: “It completely eliminated aneurysm development,” just like losartan had, Dietz says.

He’d previously believed that an unrelated class of proteins called Smad, which losartan targets very efficiently through TGF- β , was the reason the drug worked so well. But the group discovered that a different treatment that blunts Smad and not ERK didn’t prevent aneurysms nearly as effectively—suggesting that ERK was the real culprit. This new work has narrowed the focus to ERK’s role in aneurysms and shown that losartan is an especially potent ERK blocker in mice.

Despite losartan’s apparent promise, backup options for treatment are always welcome, and this new work suggests alternatives. “We don’t know the potential of losartan to treat all the features of Marfan syndrome,” Dietz says.

Using drugs against proteins further “downstream” than TGF- β —in other words, specific proteins that TGF- β helps control—can hone in on what is actually going wrong in the disease. “We want to drill down; we want to get as close to the critical event as possible,” Dietz says. Think of it as picking out specific dominos in a line instead of the one that knocks all the others over. Activated TGF- β switches on ERK and Smad—but only ERK, Dietz and his colleagues say, leads to aneurysms in this disease.


The domino analogy only goes so far, however. The biology is not “a simple cartoon,” says Bruce Gelb, a pediatric cardiologist at Mount Sinai Medical Center in New York City. In addition to caring for Marfan patients, Gelb studies a genetic disease called Noonan syndrome in which ERK is also hyperactivated. Yet those patients rarely suffer aneurysms.

Another question is whether the signaling pathways Dietz has been studying play a role in aneurysms beyond Marfan syndrome. Last year, a French group reported in *The Journal of Clinical Investigation* that blocking TGF- β , as Dietz has done in mice, made a different kind of aneurysm, in the abdomen of mice, much worse. “We should be careful about extrapolating what happens in one aneurysmal disease to another,” says Ziad Mallat, the cardiologist who led the research and is now at the University of Cambridge in the United Kingdom.

The big question now is whether losartan will outshine current treatments, particularly beta blockers, in preventing aneurysms in Marfan patients. The largest clinical trial just finished enrolling the last of its 608 participants. Results are still a few years off.

Gelb, who, like Dietz, is involved in that trial, is cautious about betting on losartan’s success. The trial hasn’t been halted yet, he says, which it could have been if losartan proved extraordinarily effective. He welcomes the new work because it could offer alternatives—although those may be more experimental, and potentially less safe, than losartan.

—JENNIFER COUZIN-FRANKEL



Science with a view. Ubii research camp is one of two field stations in Papua New Guinea run by Binatang Research Center.

Uncertain Future For Tropical Ecology

Three premier research outfits are scaling back ambitions—and struggling to maintain local staffs as funds grow scarce

MADANG PROVINCE, PAPUA NEW GUINEA—Joseph Kua peers at the computer screen of a survey tripod perched precariously on a jungle hill. The 30-year-old oversees part of a team that will spend much of this year logging species in a 50-hectare plot of pristine rainforest. That may sound like the makings of a doctoral dissertation, but Kua has only a high school diploma. A native of a remote mountain village, Kua spent 2 years helping a Czech graduate student study bark beetles and then several months learning how to conduct biodiversity surveys. He's one of 18 paraecologists—locals trained to do the nuts and bolts of ecology research—employed by the New Guinea Binatang Research Center (BRC), a tropical ecology institute here on Papua New Guinea's north coast.

Western researchers point to the work of Kua and other paraecologists as an example of excellent science on a shoestring. By hiring and training locally, scientists can boost productivity and cut costs, all while supporting conservation. On the backs of paraecologists, BRC and two similar outfits in Costa Rica—the National Biodiversity Institute (INBio) and a group at Area de Conservación Guanacaste (ACG) led by University of Pennsylvania ecologist Daniel Janzen—over the past 2 decades have discovered thousands of species and churned out hundreds of peer-reviewed articles. Although most paraecologists start with little science knowledge, some have gone on to earn advanced degrees and take key positions in national forest management and conservation.

It's "a brilliant approach that builds relevant local capacity at modest cost," says Thomas Lovejoy, a biologist at George Mason University in Fairfax, Virginia, and a former

chief biodiversity adviser to the World Bank. Thanks to paraecologists, BRC, INBio, and ACG "have had a profound impact on tropical ecology over the last 2 decades, most fundamentally through the sheer number of species identified and documented," says Elizabeth Losos, president of the Organization for Tropical Studies, a consortium of 63 universities and institutes headquartered in Durham, North Carolina.

But paraecologists may be a vanishing breed. Money woes now bedevil all three projects and threaten the concept of local, long-term hiring for field research. INBio has shrunk its taxonomic staff from 50 in 2005 to 31 today. At ACG, Janzen and his wife, Penn biologist Winnie Hallwachs, are scrambling to avoid having to lay off 29 parataxonomists they supervise. The U.S. National Science Foundation turned down a grant application Janzen submitted last year—leaving them without NSF money for the first time in 48 years. BRC, meanwhile, is struggling to find stopgap funding after losing the longtime support of the U.K. government's Darwin Initiative. The challenges are "lethal and nerve-racking," Janzen says.

Funding crises at the three premier centers are the result of a perfect storm of problems. Donors have shifted funding away from taxonomy for more than a decade, leaving a huge backlog of unidentified specimens. A panel that reviewed Janzen's NSF grant application rated it as "outstanding" but expressed this concern: "Although previous work has been very successful in identifying species new to science, it is not clear from the proposal how, when or if these novel species will be described." INBio's 2005 decision to downsize was

driven partly by a backlog of unidentified specimens, says INBio Director Rodrigo Gámez. "The world does not have the number of taxonomists required to process [so many new species]," he says.

The global financial crisis intensified the problem. The Darwin Initiative was one of many donors that curtailed grants, accepting no new applications last year and driving up competition for other funds. And as projects have scaled back, some researchers worry that paraecologists are taking jobs from graduate students. One unnamed reviewer noted that Janzen's NSF grant proposal was "unusual in that no students are trained directly by [Janzen] or intellectually engaged in the project." Janzen insists that students would have worked under his supervision at ACG. Moreover, he says, local staffers often become excellent scientists and conservation leaders and deserve opportunities to learn. "Some people in the ivory tower see [paraecologists] as incredibly useful support. Others see them as huge competition," Janzen says.

Today's problems are a far cry from the heady early days. Janzen coined the term "paraecologist" in 1989, when he used a U.S. Agency for International Development grant to train 16 Costa Rican villagers and park service staff in collection and preservation of field specimens. "The concept," he says, "is to take someone out of the farming community and teach them what you expect a good graduate student to be able to do in carrying out an inventory."

Some pioneering paraecologists took jobs at INBio, which Janzen cofounded and where he continues to serve as an unofficial adviser. INBio started with the lofty vision

CREDIT: CRAIG SIMONS



"Tropical ecologists are still sending often overqualified postdocs or graduate students to do the type of fieldwork that could be done better and more efficiently by paraecologists."

—VOJTECH NOVOTNY,
BRC

Leading the way. Paraecologist Joseph Kua (*right, top*) is helping to oversee a survey of tree species. Local staffers are Binatang's lifeblood, says Director Vojtech Novotny.

of inventorying every species in Costa Rica and finding sustainable ways to use the country's immense biodiversity. While its leaders have since scaled back their ambitions—for example, deciding not to sample mollusks and nematodes—they have discovered two species on average each week since 1989. "Within a few years of the initiation of INBio in Costa Rica," Losos says, "the number of insect species known to exist in the country increased more than fivefold."

Paraecologists have enabled large-scale and long-term research at ACG and BRC as well. Janzen's project has cataloged more than 9000 butterfly and moth species in the 120,000-hectare ACG, a feat that could have been accomplished only with paraecologists, he says: Hiring graduate students would have required "a budget 10 times bigger."

In Papua New Guinea, BRC is running two major initiatives. The project Kua helps lead will count every tree with a diameter of 1 centimeter or more in a 50-hectare plot; it will contribute to efforts by the Center for Tropical Forest Science, a project run by the Smithsonian Institution and Harvard University, to understand how forests change over many years. A second project is inventorying herbivorous insects on every plant in a 1-hectare plot of highland rainforest. So far, researchers have documented only a thimbleful of roughly 50,000 plant-insect interactions presumed to exist, such as a caterpillar that feeds on specific fig tree species, says BRC Director Vojtech Novotny, an ecologist who splits his time between BRC and the University of South Bohemia in the Czech Republic. "We definitely need such large studies simply because of the complexity of tropical rainforest," he says.

Costs are also significantly lower than for studies that involve flying in researchers and equipment. At BRC, paraecologists earn roughly \$300 a month plus training fees and receive room, board, and health care. Village assistants earn \$4 a day and benefits—a welcome wage in a region with few job opportunities. "In most businesses and even intellectual activities, Western countries are outsourcing while tropical ecologists are still sending often overqualified postdocs or graduate students to do the type of fieldwork that could be done better and more efficiently by paraecologists," Novotny says.

As a bonus, he says, paraecologists help doctoral students carry out dissertation research more quickly, and they promote conservation. "The forest research sites in Papua New Guinea show locals that conserving forests can bring a sustainable income," says Chris Dahl, a 35-year-old BRC deputy director who started as a paraecologist in 1994. Local knowledge can also pay off. Five years ago, for example, villagers angered over a land dispute threatened to raze a BRC field station. Paraecologists defused the tension by presenting the villagers with a pig—a traditional peace offering.

These days BRC itself could use an offering. Staff now "absolutely have to raise new grants" this year, Novotny says. "If we don't, we'll become dormant here." Janzen faces similar problems. When NSF turned down his grant application last summer, he scrambled to raise \$500,000 from private sources, enough to pay staff salaries through this coming July, and began building what he hopes will become a \$10 million endowment. He also reapplied to NSF with a slimmed-down proposal. Even if he

Vanishing breed. INBio parataxonomist Marcos Moraga (*top*) prowls for insects. At another field site in Costa Rica, Daniel Janzen (*above*) is scrambling to avoid having to lay off parataxonomists.

gets the grant, he says, he must raise at least \$400,000 a year from other sources to maintain his budget.

At INBio, until 2005 a pair of 7-year grants had covered most of the inventory program's \$900,000 annual budget. Today, almost its entire \$471,000 budget is self-funded, largely by ventures that include a biodiversity theme park, a publishing house, a bioprospecting unit, and an environmental consultancy. INBio built those businesses as Costa Rica grew richer in the 1990s and foreign governments cut aid to projects, including INBio.

Here in Papua New Guinea, BRC is hunkering down for a hard year. Whereas visiting scientists can pack up and go home when grant money dries up, Novotny must meet payroll for the station's staff—including its indispensable paraecologists. "We really can't afford to have a gap in funding, even for a single year," he says. New growth is out of the question, he adds. "Now our best-case scenario is to stabilize the place."

—CRAIG SIMONS

Craig Simons is a writer in Beijing.



Puzzling out diversity. Fred Gage (middle), Alysson Muotri (right), and Maria Carol Marchetto (left) suspect that jumping genes might affect the brain's development.

RETROTRANSPOSONS

Do Jumping Genes Spawn Diversity?

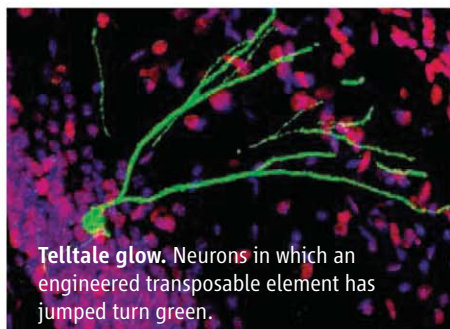
The data are clear. Transposable elements move in developing brain cells. But the question remains: Does the brain tolerate them or take advantage of them?

In theory, the behavior of inbred mice reared and housed under seemingly identical conditions should be as similar as their perfectly matched genes. But, to the frustration of researchers, the rodents don't act like exact copies of each other. "You control for everything you can, and in behavioral tests, the variance is enormous," says Fred Gage, a neuroscientist at the Salk Institute for Biological Studies in San Diego, California. Even within a single litter, he says, "one mouse will be unusually smart, another below average."

Of the possible explanations for such differences, Gage and his colleagues have found evidence for a particularly unexpected one: jumping genes in the brain. Formally known as transposable elements, they are small bits of genetic material that can move around the genome. They have generally been seen as troublemakers; when they jump, they can land in places that cause mutations or otherwise skew the expression of important genes. But Gage and his former postdoc Alysson Muotri, now at the University of California, San Diego, argue that such changes might have a positive side, helping to generate diversity in brain cells. Such diversity might be important in brain development, they think, providing the raw material for building a flexible organ able to react to new environments and situations. And because a transposable element creates a slightly different genome each time it moves, it could explain why genetically "identical" mice aren't identical after all.

It's far from a proven idea, but it has started to gain attention among geneticists who study jumping genes. The team's discoveries have prompted some scientists to expand their ideas about the role of these mobile bits of DNA, which they have frequently dismissed as "junk" that got in the way of sequencing an organism's genome and identifying its genes.

The data from brain cells "overturned a dogma" that transposable elements primarily jump in germ cells and tumor cells, says John Moran, a geneticist at the University of Michigan Medical School in Ann Arbor, who is a co-author of several of Gage and Muotri's papers. "They opened people's eyes to say, 'Wait, might there be other places where these elements can jump?' And where people have started to look, they have started to find them," he says. That includes, surprisingly, very early embryos, which means that tissues other than the brain might also be affected by jumping genes. Still unclear is what effect the movements of transpos-



Telltale glow. Neurons in which an engineered transposable element has jumped turn green.

able elements are having on the brain, let alone elsewhere in an animal's body, Moran and others caution. "What is the functional consequence? At this point, it remains speculative," says Pierre Vanderhaeghen, a developmental biologist at the University of Brussels.

Copy-and-paste parasites

Gage and Muotri's work focuses on a transposable element called L1 that can copy itself and paste the new version elsewhere in the genome. Such copy-and-paste jumping genes are called retrotransposons because their replication machinery is similar to that of retroviruses, such as HIV. They are considered genetic parasites because they use an organism's genome to proliferate. Over time, they have been quite successful: Scientists estimate that the human genome includes more than 500,000 copies of L1. Most have mutations in key stretches of their DNA sequence and can't replicate. But roughly 100 copies are active, able to spawn new L1s that jump to new chromosomal locations.

Most of the time, cells keep these elements under wraps, tagging the L1 DNA with methyl groups, which prevent its genes from being expressed and making the enzymes that perform the copying and pasting. But from time to time, as a cell removes methylation to allow the expression of important genes, the L1s escape their shackles and new copies start jumping again. "They're like the velociraptors in *Jurassic Park*," Moran says. "They keep banging on the fence, looking for a way to get through. Sometimes they succeed."

Because they are parasites that need to commandeer their host's machinery, what better place to jump than into the cells that will give rise to sperm and eggs? Any new working copy of L1 in a gamete will then be passed on to every cell in the resulting offspring. The fact that nearly 45% of the human genome is made up of jumping genes and their remnants demonstrates that heritable jumps have happened quite often in evolution.

Many scientists had assumed that somatic cells—those that don't give rise to sperm or eggs—would keep their transposable elements under stricter control to prevent the potential damage the jumps can cause. For many years, tumor cells were the only adult cells that seemed to have actively jumping elements.

But researchers hadn't really been looking elsewhere for jumping genes. In fact, because there are so many inactive copies of L1 cluttering the genome, many experiments are designed to filter out their DNA. But in 2002, researchers in Gage's lab spotted

CREDITS (TOP TO BOTTOM): JOE BELCOVSON, SALK INSTITUTE FOR BIOLOGICAL STUDIES; CAROL MARCHETTO (SALK) AND ALYSSON MUOTRI (UCSD)

something surprising as they were searching for signals that play a role in the development of brain cells. They were searching for genes that were overexpressed in rat neural progenitor cells, which give rise to neurons and other brain cells, and unexpectedly found L1 RNA expressed at high levels.

When Muotri joined the lab, Gage asked him to follow up on the observation. To find out whether the L1 elements were really jumping in developing brain cells, the scientists used a genetically engineered copy that incorporates the gene for green fluorescent protein (GFP). When this modified L1 is active in a cell, the cell glows green. In 2005, the scientists reported in *Nature* that when they inserted the transgenic L1 into cultured rat neural stem cells, many of the differentiating cells turned green, indicating that the L1 was making new copies of itself. They also found that cells in which L1 jumped were more likely to become neurons and that one of the newly created L1s inserted next to a gene important to neuronal differentiation, increasing its expression (*Science*, 17 June 2005, p. 1729).

Muotri's research background was in cancer, in which L1s were thought to cause trouble in cells, so he was initially taken aback by the suggestion that such elements might be useful. "If they were really being mobilized in neural stem cells, they could cause cancer or do other damage," he says. "But we soon realized that might not be the whole story."

Because their research suggests that L1 activity happens in normal neural stem cells, the researchers wondered whether jumping DNA plays a regular role in brain development. The mammalian brain produces far more neurons than it needs, and during development—even into childhood in humans—it ultimately prunes many of its cells and connections. Gage, Muotri, and their colleagues hypothesize that L1's effects on neuronal genes during development provide a range of neurons with subtly different properties on which a kind of natural selection then acts. "In evolution, there are two players: generation of diversity and then selection," Gage says. The L1 activity "provides enough [neuronal] diversity so that you can optimize your response to the variety of environments you might encounter throughout life."

Jumping all over

Since their initial findings, the researchers have strengthened their case, extending their work from rodent to human cells. In August 2009, Gage, Moran, and their colleagues reported in *Nature* that L1 elements also jump in lab-grown human neural stem cells. Again they found that the new copies

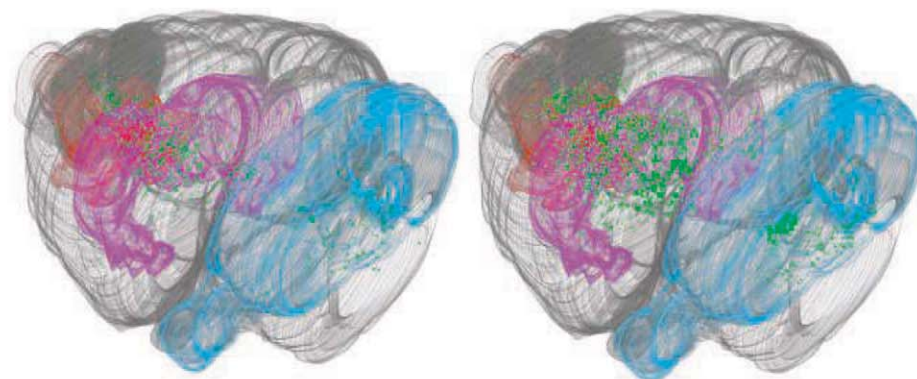
of L1 sometimes landed near genes that are expressed in neurons, suggesting that such jumps could alter important functions of the brain cells. They also documented significantly more copies of L1 in the genomes of brain cells from an adult human than in the liver or heart cells from the same individual. Using an extremely sensitive PCR technique, they estimated that brain cells had about 80 additional copies of L1 compared with other tissues. Furthermore, within the brain, the scientists found even higher numbers of L1s in the hippocampus, an area in which neurons continue to form throughout life. So in theory, L1s could influence both adult neurogenesis and initial brain development.

The same week, in *Nature Neuroscience*, Muotri, Gage, and colleagues reported another link between L1 and the brain. They showed that a molecule called Wnt can trigger the expression of a transcription factor called NeuroD1, which can help induce the develop-

MeCP2 mutation would affect L1's behavior in brain cells. To find out, the researchers inserted the GFP-engineered L1 into the genome of mice carrying an *MeCP2* mutation and found that the rodent brains were full of green cells—indicating that the L1 was jumping much more often than in normal mouse brains.

Researchers outside Gage's lab are impressed but perplexed. "The work itself is such a high order of technical proficiency. It's really a tour de force," says Anthony Furano, who studies L1 at the U.S. National Institute of Diabetes and Digestive and Kidney Diseases in Bethesda, Maryland. "Now the question is, what does it mean? Is this having an important effect on the phenotype of neuronal cells?"

Other researchers are starting to take a closer look at L1 elements in different developmental stages. In 2007, Moran and his colleagues found that L1 is active in human



Leaving their mark. Transposable elements are more active in the brains of mice carrying the mutation that causes Rett's syndrome (*right*) than those of control mice. Each green dot represents a new jump.

ment of neurons in the adult brain. The same Wnt-mediated pathway, they found, also triggers expression of L1. A month later, the researchers reported online in *Hippocampus* that exercise, known to prompt the growth of new neurons, also triggered increased expression of L1 in the brains of mice. "They have clearly established the idea that L1 retrotransposition seems to be triggered by neurogenesis," Vanderhaeghen says.

The story took a new twist last November when the team reported in *Nature* that the gene underlying Rett syndrome is connected to L1. Rett syndrome affects children who carry a mutation in a gene called *MeCP2*, causing developmental problems, including some symptoms that resemble autism. The gene is involved in methylation, and work in other labs had shown that *MeCP2* cooperates with a gene already known to silence L1. Maria Carol Marchetto, a postdoc in Gage's lab (and Muotri's wife), wondered how the

embryonic stem cells, suggesting that they might also be jumping in early embryos. Last year, Haig Kazazian Jr., a geneticist until recently at the University of Pennsylvania and now at Johns Hopkins University in Baltimore, Maryland, and his colleagues reported in *Genes and Development* that L1 elements are indeed active in the earliest embryos of mice, before the embryo implants in the uterus. When an L1 replicates in one of the few cells of an early embryo, that new copy will propagate into a subset of the body's final tissues, making them genetically distinct from the rest of the animal. Given how often this may happen in the early embryo, there may be much more genomic variation within individuals than most researchers had assumed. "We were really surprised," Kazazian says, to find more L1 jumps in early embryos than even in sperm or egg cells. "It made us think that maybe [Gage] is on to something."

—GRETCHEN VOGEL

MEETINGBRIEFS>>

LUNAR AND PLANETARY SCIENCE CONFERENCE | 7–11 MARCH 2011 | THE WOODLANDS, TEXAS

Asteroid Model Shows Early Life Suffered a Billion-Year Battering

Life was hard on early Earth, but geologists and now planetary scientists are reporting evidence of even more biotic stress several billion years ago: a prolonged pummeling by huge asteroids that would have dwarfed the one that killed off the dinosaurs.

Geologists were the first to suspect that the Archean eon—the time from 3.8 billion years ago to 2.5 billion years ago—suffered far more big hits than anyone had thought. In the past decade, routine fieldwork began turning up odd, centimeters-thick rock lay-

ers that turned out to contain impact debris: droplets of molten rock that crystallized and fell to form a layer of distinctive little balls, or spherules. The dinosaur-killer impact 65 million years ago was the only impact of the past half-billion years big enough to create a widespread spherule layer.

During the Archean, however, big, spherule-bed-generating impacts were far more frequent than that, geologists have reported at prior meetings here. Taken together, the known impact beds suggest that there was a

Big splat. A huge impact 2.54 billion years ago deposited this centimeter-thick layer of whitish spherules—crystallized droplets of molten rock.

large impact every 40 million years on average in the Archean, not every 500 million years, as has lately been the case.

At this meeting, planetary dynamicist William Bottke of the Southwest Research Institute in Boulder, Colorado, and colleagues offered an explanation for the severe, lengthy pummeling. A raised impact rate at any time means the smaller bodies of the solar system must have been shaken up gravitationally. For example, to explain the brief burst of impacts 3.9 billion years ago, called the late heavy bombardment, a group of planetary dynamicists has proposed that an inward drift of the giant planets Jupiter and Saturn could have gravitationally shaken up the asteroid belt between Mars and Jupiter and scattered asteroids toward Earth and its moon (*Science*, 17 July 2009, p. 262). But the resulting shower of impacters would have lasted only 100 million years or so, not the billion years geologists have found, so it can't explain the prolonged Archean shower.

Bottke and colleagues now think they have an explanation. Last year at the meeting, they proposed that as Jupiter and Saturn moved inward, they also scattered asteroids out of a now-missing inner band of the asteroid belt. In the researchers' computer simulations, many of those asteroids scattered into

Prime Science Achieved at Asteroid

A crippled Hayabusa spacecraft barely made it back to Earth last June, and it returned only a wisp of a sample from Itokawa, the asteroid it visited in 2005. But at the meeting, Japanese researchers announced that the little spacecraft that could has scored a solid scientific success. Detailed analyses of the sample—the first ever returned from an asteroid—have confirmed the oft-contentious claim that the most common type of meteorite falls to Earth from a class of asteroids long cloaked by a mysterious discoloration.

The first chore for Hayabusa analysts was to get their sample out. The spacecraft's malfunctioning sampling mechanism did collect asteroidal rock particles, just mostly smaller than 10 micrometers. A specially designed extraction tool was a bust. A Teflon spatula

worked much better. In the end, turning the canister upside down and rapping it 20 times with a screwdriver did the trick. All told, there were about 1500 particles from Itokawa smaller than 100 micrometers.

Next, researchers across Japan applied an alphabet soup of microanalytical techniques—XRD, XRF, UMT, FIB, TEM, SEM, EPMA, and SIMS—to 52 particles. Their directly determined chemical, mineralogical, and isotopic compositions, it was hoped, would finally settle a decades-long debate (*Science*, 14 July 2006, p. 158). Judging solely from spectral colors, researchers had found that S-type asteroids—the most common in the inner asteroid belt—appeared to have a composition different from the most common type of meteorite found on Earth, the ordinary chondrites.

Closer remotely observed spectral signatures eventually led most researchers to conclude that exposure to the rigors of space had

“weathered” the surfaces of ordinary chondrite asteroids until they no longer spectroscopically resembled chondritic meteorites. By 2001, astronomer Richard Binzel of the Massachusetts Institute of Technology and his colleagues concluded from telescopic observations that Itokawa was indeed chondritic—a member of the compositionally distinct LL subclass of ordinary chondrite meteorites.

Hayabusa analyses presented at the meeting now clearly show that Itokawa is a space-weathered ordinary chondrite, and an LL ordinary chondrite at that. That brings an “irrefutable closure to the long-standing ‘S asteroid conundrum,’” says asteroid specialist Clark Chapman of the Southwest Research Institute in Boulder, Colorado. “This is a stunning validation of the power of remote-sensing mineralogical analysis of asteroids.” Next up, analyzing more Hayabusa particles to pin down what sort of space weathering muddled the field for so long.

CREDIT: BRUCE SIMONSON/OBERLIN COLLEGE

sharply tilted orbits just inside the asteroid belt. The asteroids still lingering in this outlier group are called the Hungaria asteroids.

This year, Bottke and colleagues report that the Hungaria asteroids could have been the source of all those Archean impacts. That's possible because once scattered into the realm of the Hungarias, a body is particularly slow to leave it and possibly hit Earth. This dynamical "stickiness" could have prolonged the bombardment of the inner solar system through the Archean and even a ways into the Proterozoic of 0.5 billion to 2.5 billion years ago.

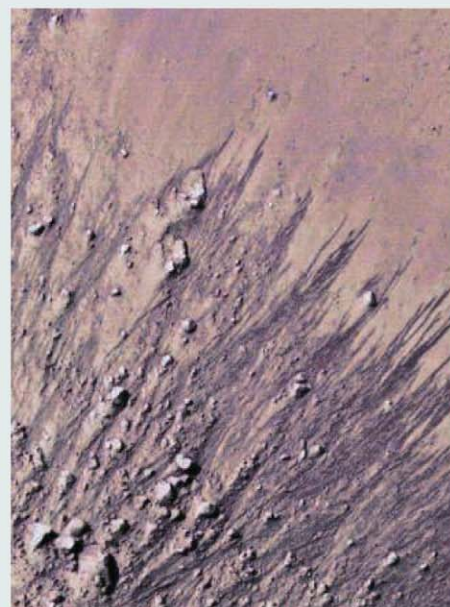
The group's model gave a good match to what scientists see: the number of current Hungaria asteroids, the number of huge impact basins on the moon, the number of dinosaur-killer-size impacts on the early moon, and the number of impact-generated spherule beds on the Archean Earth. "I'm always a little leery of results from one or a few simulations," says Renu Malhotra of the University of Arizona in Tucson, herself a dynamical modeler, "but it seems plausible. I don't see any obvious problems."

The larger Archean impacts would have been disastrous—boiling off the upper ocean, for example—but how the later Archean pounding affected the single-celled life in the oceans then remains to be seen. Bottke sees some eerie coincidences, however; for example, both the end of huge impacts and the first appearance of atmospheric oxygen occurred 2.5 billion years ago. "Do connections exist?" he asks in his meeting abstract.

"The game is afoot!"

Snapshots From the Meeting >>

Briny flows on Mars? No one has proved that the water on Mars gets warm enough to flow, but Alfred McEwen of the University of Arizona in Tucson said at the meeting that he has pictures of "the most viable targets for actual liquid on Mars today." Taken by the camera on board Mars Reconnaissance Orbiter, for which McEwen is the principal investigator, the pictures seem to show multitudes of rivulets that have dampened and darkened the soil and may even have cut shallow, meterwide channels as they streamed from rock outcrops down steep slopes. McEwen and colleagues found that their "transient slope lineae" form where and when the ground would be warm enough for liquid water or brine and fade away after summer warmth. Even if water were involved, it may be too salty for life, McEwen noted, but these lineae certainly bear watching.



Sure looks watery. These dark, sometimes channelled features may be rivulets of water, of water-soaked soil, or of something not wet at all.

Craterin' time on Mars. The slow, steady drizzle of meteorites onto a planet, like sand falling in an hourglass, is the only clock Mars scientists have to keep track of geologic time. So the surprising report that Mars suffers 100 new crater-forming meteorite hits a year garnered some attention. Planetary scientist Ingrid Daubar of the University of Arizona in Tucson and her colleagues used two cameras on board the Mars Reconnaissance Orbiter to identify 201 fresh impact sites formed in recent years. That's surprisingly close to an estimate other researchers had made by extrapolating from counts of much larger, ancient craters to small, modern ones—not a guaranteed sort of calculation. The finding lends tentative support to crater-counting dating of geologically recent events on Mars, from the cycling of ice ages to the cutting of gullies by ever-elusive liquid water.

—R.A.K.

A Badly Battered Vesta Awaits Dawn's Arrival

Planetary scientists are waiting eagerly for July, when the Dawn spacecraft is due to arrive at asteroid Vesta. If greater complexity makes for greater scientific interest, they're in for a bonanza. The asteroid belt's second-most-massive body has had quite a complicated life. It melted early on to form an iron core and rocky mantle and crust, spewed volcanic outpourings, and then suffered a massive impact.

Now, to spice things up even more, a group of impact modelers is arguing that the object that crashed into Vesta and reshaped its geology was eight times as massive as previously thought. "Vesta really gets messed up by this impact," impact specialist H. Jay Melosh of Purdue University in West Lafayette, Indiana, said at the meeting.

When the Hubble Space Telescope gave astronomers their first fuzzy glimpse of Vesta

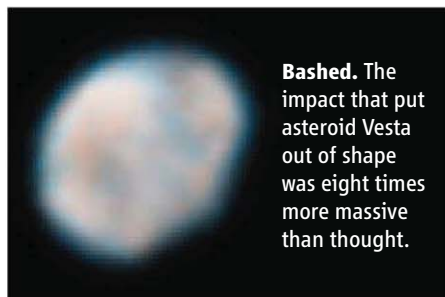
in 1997, they saw an impact crater 460 kilometers in diameter—nearly as wide as the asteroid itself—centered at its south pole. Researchers estimated that another asteroid about 40 kilometers in diameter had plowed into Vesta at 20,000 kilometers per hour.

Impact modelers Boris Ivanov of the Institute for Dynamics of Geospheres in Moscow, Melosh, and Elisabetta Pierazzo of the Plan-

etary Science Institute in Tucson, Arizona, set out to put a firm number on the size of the Vesta impactor. They ran a computer simulation of the collision using impactors of different sizes until the final model Vesta matched the squashed shape seen in Hubble images. The best fit required an 80-kilometer impactor—twice the size previously assumed, with eight times the mass and thus eight times the impact energy.

Geologists should get an eyeful on Dawn's arrival. "I would be astonished if we didn't see some mantle exposed" in the crater, Melosh says. Mantle rock from as deep as a few tens of kilometers down may be visible in the crater's center where rock rises into a peak. Crust, on the other hand, would have been thrown across the rest of Vesta all the way to the antipode, possibly in shapes that might be mistaken for more conventional geologic forms such as crustal folds. Interesting indeed.

—RICHARD A. KERR



Bashed. The impact that put asteroid Vesta out of shape was eight times more massive than thought.

Exclusive savings.

No mess.



Auto • Homeowners • Motorcycle • More

AAAS members could get an additional discount on car insurance. Get your FREE quote today.

GEICO
geico.com

1-800-368-2734

Motorcycle coverage is underwritten by GEICO Indemnity Company. Homeowners coverage is written through non-affiliated insurance companies and is secured through the GEICO Insurance Agency, Inc. Discount amount varies in some states. Discount is not available in all states or in all GEICO companies. One group discount applicable per policy. Coverage is individual. In New York a premium reduction is available. Some discounts, coverages, payment plans and features are not available in all states or companies. Government Employees Insurance Co. • GEICO General Insurance Co. • GEICO Indemnity Co. • GEICO Casualty Co. These companies are subsidiaries of Berkshire Hathaway Inc. GEICO: Washington, DC 20076. GEICO Gecko image © 1999-2011. © 2011 GEICO

Probing Cancer Pathways

How Chemical Biology Can Inform Oncology Research

Webinar

May 3, 2011

12 noon ET, 9 am PT,
4 pm GMT, 5 UK

PARTICIPATING EXPERTS

Leonard Zon, M.D.
HHMI/Children's Hospital
and Harvard Medical School

Hakim Djaballah, Ph.D.
Memorial Sloan-Kettering
Cancer Center

Gregory Verdine, Ph.D.
Harvard University

During normal growth and differentiation, maintaining the appropriate homeostatic balance in a cell is paramount. This fundamental level of control is achieved through the interaction of small molecule chemical modulators with those proteins involved in cellular signaling. Researchers can take advantage of these regulatory interactions to study signaling pathways, for instance by designing chemicals that reverse the hyper-proliferation phenotype seen in many cancers. These small molecules can be used both as tools to interrogate a particular pathway and as precursors for drug development. This webinar will provide an overview of how chemical biology can be used in various model systems to both advance our understanding of basic cell signaling mechanisms as well as aid in the discovery of novel small molecule therapeutics for cancer.

REGISTER NOW!

Sign Up At:
www.sciencemag.org/webinar

Brought to you by the
AAAS/Science Business Office



Webinar sponsored by



Qs & AAAS



www.sciencedigital.org/subscribe

For just US\$99, you can join AAAS TODAY and start receiving *Science* Digital Edition immediately!

Qs & AAAS



www.sciencedigital.org/subscribe

For just US\$99, you can join AAAS TODAY and start receiving *Science* Digital Edition immediately!



LETTERS

edited by Jennifer Sills

Putting the Ocean Under Review

IN 2002, AT THE WORLD SUMMIT ON SUSTAINABLE DEVELOPMENT, heads of state who gathered in Johannesburg decided to put the ocean under permanent review (1). The UN's shorthand name for the project—"Regular Process"—emphasizes the importance of conducting this assessment regularly, with an initial plan of an ocean review every 5 years.

This decision was made because the sector-by-sector management of human activities in the ocean has proven insufficient. Land degradation is an accepted technical term in management, and many actions are taken to mitigate its effects, yet ocean degradation, until now, has been invisible (2).

In December 2010, the UN General Assembly committed to carrying out the first cycle of the assessment from 2010 to 2014. This high-level political engagement is encouraging. Unfortunately, civil society, nongovernmental organizations, and the expert community seem to lack engagement in the process. Not many natural or social scientists know about the "UN Regular Process," and fewer still associate this name with the first Integrated Global Assessment of the Ocean. Science-based policy-making is far from being a universal practice, and the availability of data and information in different regions is highly variable. This first assessment will be far from perfect, despite being global; there will, of course, be functional and geographical gaps. Nevertheless, there is a lot to be learned as the process moves forward.



A science-based assessment cannot be purely politically driven. I urge the marine scientific community to become acquainted and engaged with this ongoing process, reaching out through scientific societies and academies to the national representatives overseeing it in the UN General Assembly. The group of 25 experts designated by the UN to help with the technical scientific tasks estimates that between 1500 to 2000 experts will be needed to properly conduct the assessment and the subsequent peer review (3). The relevance, saliency, and credibility of the assessment ultimately depend on the involvement of many scientists and experts all over the world.

PATRICIO A. BERNAL

Global Marine and Polar Program, IUCN, Gland, 1261, Switzerland. E-mail: patricio.bernal@iucn.org

References

1. United Nations, "Report of the World Summit on Sustainable Development," Johannesburg, South Africa, 26 August to 4 September 2002 (United Nations, New York, 2002), chap. 1, resolution 2, Annex paragraph 36 (b).
2. B. S. Halpern *et al.*, *Science* **319**, 948 (2008).
3. Working Group of the General Assembly, Recommendations adopted by the Ad Hoc Working Group of the Whole (Oceans and Law of the Sea, 2011); www.un.org/Depts/los/global_reporting/global_reporting.htm.

Low-Dose Radiation Knowledge Worth the Cost

THE PAST TWO U.S. SCIENCE FUNDING NEWS articles have highlighted budget cuts proposed for the Department of Energy's Office of Science ("Attack on climate studies would shutter entire DOE biology program" and "A strong defense of science—and a stiff upper lip," News & Analysis, J. Mervis, 18 March,

pp. 1378 and 1379). Notably, the proposal would also substantially reduce funding of the Low-Dose Research Program that is dedicated to understanding the relationship between biological responses and health consequences of low-dose radiation. Ironically, the news since these announcements has been punctuated by radiation leaks from failures at Japan's nuclear power plants, congressional hearings on radiation from airport screening, discussion of radiation risks

from CT scans in children, and reports of high radiation doses mistakenly administered in otherwise benign radiological diagnostics. The public is reasonably concerned that radiation exposures pose a health risk, but remains confused about the degree and nature of this risk.

Given the important questions remaining about radiation exposure, hazards, and protection, it would be false economy to cut the current yearly allocation of \$18 million from the Office of Biological and Environmental Research budget of \$588 million. The program is a crucial component of the federal radiation research portfolio. Whereas high-dose effects are well studied, new systems biology and genetic approaches are just beginning to provide insight into the low-dose range.

Letters to the Editor

Letters (~300 words) discuss material published in *Science* in the past 3 months or matters of general interest. Letters are not acknowledged upon receipt. Whether published in full or in part, Letters are subject to editing for clarity and space. Letters submitted, published, or posted elsewhere, in print or online, will be disqualified. To submit a Letter, go to www.submit2science.org.

As recent events have shown, lack of knowledge is far more expensive than this relatively modest dollar investment. Reducing resources to understand the effects of radiation exposure to humans will inevitably fuel unwarranted public stress and worry. Sustained funding of this successful effort has paid, and will continue to pay, a substantial societal benefit that expands knowledge of low-dose radiation effects and informs public policy.

MARY HELEN BARCELLOS-HOFF,^{1,2*}

DAVID J. BRENNER,³ ANTONE L. BROOKS,⁴

SILVIA FORMENTI,² LYNN HLATKY,⁵ PAUL A. LOCKE,⁶

ROY SHORE,⁷ THOMAS TENFORDE,⁸

ELIZABETH L. TRAVIS,⁹ JACQUELINE WILLIAMS¹⁰

¹Department of Radiation Biology, New York University School of Medicine, New York, NY 10016 USA. ²Department of Radiation Oncology, New York University School of Medicine, New York, NY 10016 USA. ³Center for Radiological Research, Columbia University Medical Center, New York, NY 10032, USA. ⁴Retired Professor of Radiation Biology, Washington State University, Richland, WA 99352, USA. ⁵Center of Cancer Systems Biology, St. Elizabeth's Medical Center, Tufts University School of Medicine, Boston, MA 02135, USA. ⁶Doctor of Public Health Program, Department of Environmental Health Sciences, Johns Hopkins Bloomberg School of Public Health, Baltimore, MD 21205, USA. ⁷Radiation Effects Research Foundation, 5-2 Hijiya Koen, Minami-ku, Hiroshima 732-0815, Japan. ⁸National Council on Radiation Protection and Measurements, Bethesda, MD 20814-3095, USA. ⁹Mattie Allen Fair Professor in Cancer Research, Department of Experimental Radiation Oncology, Division of Radiation Oncology, The University of Texas MD Anderson Cancer Center, Houston, TX 77030, USA. ¹⁰Department of Radiation Oncology, James P. Wilmot Cancer Center, University of Rochester, Rochester, NY 14642, USA.

*To whom correspondence should be addressed. E-mail: mhbarcellos-hoff@nyumc.org

Note

1. The views expressed are those of the signatories and not necessarily of their institutions.

The Risks and Benefits of Re-Consent

IN THE POLICY FORUM "RESEARCH PRACTICE and participant preferences: The growing gulf" (21 January, p. 287), S. B. Trinidad *et al.* claim that the preferences of individuals are not respected when existing research data and samples are used for new purposes with-

out obtaining consent. This allegedly threatens genomic research and prompts a need to "consider how the consent process could foster respectful engagement, rather than merely mitigate risk."

We support respectful engagement, but question whether it should be achieved by obtaining informed consent. Individuals may support repurposing of data without further consent if they understand the obstacles presented by the process: resource consumption (1), risk of bias (2), and disincentives for initializing new projects (3). We argue that respectful engagement should be pursued through public education and debate on issues such as the necessity of research, the risks involved, and the safeguards that society has put in place to protect both individuals and groups of people against harm.

Participants do not only have interests as research subjects, but also as citizens who stand to benefit from constructive research. Given the potential benefits, observational research that imposes only diminutive risks can justifiably be performed without consent.

Trinidad *et al.* are right to claim that research practice should be reframed to align with participant interests, but their view of these interests is too limited. By focusing on the participants' narrowly defined interests as research subjects, the proposed policy increases the gulf between research practice and the participants' desire to have access to optimal healthcare.

JOANNA STJERNSCHANTZ FORSBERG,*

MATS G. HANSSON, STEFAN ERIKSSON

Centre for Research Ethics and Bioethics, Uppsala University, Uppsala, Sweden.

*To whom correspondence should be addressed. E-mail: joanna.forsberg@crb.uu.se

References and Notes

1. S. Noble *et al.*, *J. Health Serv. Res. Pol.* **14**, 77 (2009).
2. K. M. Dunn, K. Jordan, R. J. Lacey, M. Shapley, C. Jinks, *Am. J. Epidemiol.* **159**, 1087 (2004).
3. M. G. Hansson, *Br. Med. J.* **340**, c2335 (2010).
4. The research underlying this Letter was made possible by grants from The Swedish Research Council through BBMRI.se. The funders had no influence on the conceptualization or writing of the Letter.

CORRECTIONS AND CLARIFICATIONS

News & Analysis: "More negative data for link between mouse virus and human disease," by J. Cohen (11 March, p. 1253). The figure caption should have been labeled "Viral puzzle." The caption has been corrected in the HTML version online.

Reports: "Layer-by-layer removal of graphene for device patterning" by A. Dimiev *et al.* (4 March, p. 1168). The final reference was missing. It should have stated: This work was funded by the AFOSR (FA9550-09-1-0581), the AFRL through University Technology Corporation (09-S568-064-01-C1), the Office of Naval Research Graphene MURI Program (00006766), and M-I SWACO, LLC.

Reports: "Complete fourth metatarsal and arches in the foot of *Australopithecus afarensis*" by C. V. Ward *et al.* (11 February, p. 750). In Fig. 4B, the y axis should have been labeled "MT4 base ML/DP," not "MT4 base DP/ML."

Reports: "Small RNA duplexes function as mobile silencing signals between plant cells" by P. Dunoyer *et al.* (14 May 2010, p. 912). The image in Fig. 3B (center panel) was previously published as Fig. 1e in P. Dunoyer *et al.*, *Nat. Genet.* **39**, 848 (2007).

Response

WE AGREE WITH FORSBERG AND COLLEAGUES that re-consent for new uses of research samples is not always necessary (or even possible) and that respectful engagement goes well beyond consent procedures. As we noted in our Policy Forum and previous work (1, 2), one of the most important findings of studies on participants' views is that many have a positive ongoing interest in the research process. Developing better ways to inform participants about research, and to elicit their input and support, will benefit scientists and participants alike.

We disagree with Forsberg *et al.*'s assertion that consent is unnecessary for research deemed by experts to be low risk and beneficial to society. Although we agree that research studies meeting these criteria may sometimes be done ethically without consent, there is a need for meaningful public input as to what constitutes "low risk" and how societal benefit is determined. When research involves large-scale genomic analysis, collection of health records, and submission of data to a federal repository—as was the case in the re-consent example we discussed (1, 2)—many would argue that such research does not qualify as low risk. We also question the implication that all citizens have a vested interest in research as it is currently practiced. Vast and well-documented health disparities exist around the world, with a disproportionate burden borne by communities that are increasingly of interest to genetic researchers. Yet relatively few research studies address the needs and concerns of these communities (3). More generally, health research often neglects important practical questions important to achieving better population health (4).

Innovative ways to engage participants and communities may lead to a productive examination of research agendas. In this context, re-consent—although not always necessary—has the potential to serve as a small but important way to promote participant awareness and engagement.

SUSAN B. TRINIDAD,^{1*} STEPHANIE M. FULLERTON,¹

EVETTE J. LUDMAN,² GAIL P. JARVIK,³

ERIC B. LARSON,² WYLIE BURKE¹

¹Department of Bioethics and Humanities, University of Washington, Seattle 98185, USA. ²Group Health Research Institute, Seattle 98101, USA. ³Department of Medicine, Division of Medical Genetics, University of Washington, Seattle 98195, USA.

*To whom correspondence should be addressed. E-mail: sbtrini@uw.edu

References

1. E. J. Ludman *et al.*, *J. Empir. Res. Hum. Res. Ethics* **5**, 9 (2010).
2. S. B. Trinidad *et al.*, *Genet. Med.* **12**, 486 (2010).
3. S. Rennie, *Hastings Center Rep.* **41**, 40 (2011).
4. S. H. Woolf, *JAMA* **299**, 211 (2008).

MEDIA AND SOCIETY

58 Ways of Looking at a Blackberry

Christopher Kelty

Nowadays, historians don't generally produce theories of everything, which makes Marshall Poe's *A History of Communications* an exception of note. Although the title might lead one to believe that this is a particular history of communications technologies "from speech to the Internet," such an assumption would fail to grasp the ambition, maybe even hubris, of the work. The book is an attempt to explain not just the evolution of communication but also how communication technologies and practices relate to human needs, social institutions, and cultural values in complex networks of biological and cultural evolution that affect every aspect of our humanity. It's likely to excite some readers and repulse others; as far as historians are concerned, it's likely to seem a project at the far edges of plausibility.

Even more surprising, the author is not a historian of communications or a media theorist but an accomplished historian of early modern Russia (at the University of Iowa). Poe's interest in the subject, as he points out, arose from his apprenticeship to Harvard classicist Albert Lord, who with Milman Parry proposed that epic poetry was not only orally transmitted but composed orally as well. The idea constitutes one of the problems of "orality and literacy" that are central to the field of media and communications studies. But Poe's interest likely also comes from the fact that he is a geek. During a turn writing for *Atlantic Monthly*, he published a widely read article, "The Hive," which made the case that Wikipedia is less an encyclopedia than a snapshot of current common sense about everything (1). He has also experimented with new forms of scholarly production, including an archive of videos about famous photographs (2) and a podcast, *New Books in History* (3).

A History of Communications is clearly a labor of love, and Poe brings the historian's craft to bear on it. The work is rich with

sources and references on subjects from neocortex size to literacy in classical antiquity to the origins of print pornography. Indeed, the book can feel a bit like Wikipedia itself, covering everything as needed, from the divine right of kings to hard-core music, from the welfare state to the ARPANET. Nonetheless, the book has a clear structure and an even clearer theory—or at least a clearly structured one.

That theory is very schematic: new media arise because new economic conditions reveal technical insufficiencies, which drive increased demand from organized interests, which lead to new media. And by new media Poe means the big ones—writing, printing, audiovisual media, and the Internet. Poe decomposes each new medium into several attributes, and for each of these (such as accessibility, range, or searchabil-

ity) he proposes a series of network attributes, social practices, and cultural values that follow. So for instance, the accessibility of a medium can be high or low (speech is high; writing before the printing press is low). High accessibility implies a network attribute of being diffused, which in turn implies a social practice of equalization and a cultural practice of egalitarianism; low accessibility implies a concentrated network, hierarchy, and elitism. Each of the eight attributes generates a similar series, yielding a table of 56 attributes and a complexity that would make advanced users of the I Ching blush.

The five principal chapters are structured identically, as an explanation of each new medium in terms of this table of attributes. Each starts with a section "Why we [talk, write, print, watch and listen, or surf]," which looks at the evolution of the medium before and after it comes into existence as well as its relations to human nature (understood as the evolutionary capacities of our bodies and brains). In a following section, "What [talking, manuscripts, print, audiovisual media, Internet] did," each of the attributes and their implications are explored.

Although this structure sounds tedious, Poe's conversational style makes the work more readable than one might expect. The chapters are filled with both grand historical claims (about, for instance, the rise of science and capitalism) and compelling anecdotes drawn from Poe's obviously enormous and wide-ranging reading. All these permutations are explained using clear examples, and the table of attributes lends every explanation a suspicious momentum. At the end, Poe satisfies any remaining skeptics with concrete answers to the questions of whether the evolution of communication has left us better off materially, sensorily, and spiritually: yes, yes, and no.

Poe's grand historical narrative unsurprisingly makes frequent reference to Marx; the author even arrogates to himself the role of a latter-day Marx: "He described the 'forces of production' marching to ever greater heights, and we have described the 'forces of communication' doing the same." And like Marx's work, this book might be less an explanation, or theory of everything, than it is a tool or grid for

A History of Communications

Media and Society from the Evolution of Speech to the Internet

by Marshall T. Poe

Cambridge University Press, Cambridge, 2011. 349 pp. \$85. ISBN 9781107004351. Paper, \$24.99. ISBN 9780521179447.



Printing press descending from heaven. J. V. Schley's frontispiece to Prosper Marchand's *Histoire de l'origine et des premières progrès de l'imprimerie* (The Hague, 1740).

The reviewer is at the Department of Information Studies, Center for Society and Genetics, University of California, Los Angeles, Box 957221, 1323 Rolfe Hall, Los Angeles, CA 90095-7221, USA. E-mail: ckelly@ucla.edu

exploring the history of media. Whether or not the combinatorial approach to a grand history works, *A History of Communications* is nonetheless a good resource for asking deeper questions about media and their effects on us.

References

1. M. T. Poe, *Atl. Mon.* **2006**, 86 (2006); www.theatlantic.com/magazine/archive/2006/09/the-hive/5118.
2. <http://mechanicalicon.com>.
3. <http://newbooksinhistory.com>.

10.1126/science.1204124

SCIENCE AND THE LAW

Genes in Police Files

Michael A. Goldman

Scientists might roll their eyes when they hear concerns about DNA fingerprinting evidence. What's all the fuss? After all, it doesn't seem to matter whether the chances we have the wrong person for a crime are one in a million or one in a billion, a DNA match or mismatch seems clear enough, and the more DNA profiles we have in the data banks the better off we ought to be. The proliferation of CSI forensic drama series on television makes the use of DNA evidence all the more routine. In *Genetic Justice*, however, Sheldon Krinsky and Tania Simoncelli present a clear and convincing case for caution—one surprisingly balanced despite strong influence from the American Civil Liberties Union.

The book offers a lucid and accurate presentation of DNA forensic technology that will be useful to any nonspecialist. It also provides an informative discussion of the American legal canon relevant to the collection of DNA information along with a detailed comparative study across the United Kingdom, Japan, Germany, Australia, and Italy.

There's little doubt that our rapidly growing understanding of the genetic basis of health, physical, and behavioral characteristics will bring DNA profiling to a level far beyond the "identity" information that the current 13 CODIS (Combined DNA Index System) loci provide. There will still be errors, and the prediction of most traits is by nature uncertain. From a DNA sample at the scene of a crime, we may get a height range and skin tone that smack of an eyewitness description and may be as fraught with error.

The company DNA Witness used this as a business model, envisioning that a sample of DNA at a crime scene could be the only bit of evidence needed. We may also obtain a measure of a subject's "genetic tendency" toward violent crime, probabilistic yet seductively real. Even when there isn't a match at a crime scene, the mere fact that someone's DNA profile is in a database and displays "bad genes" could trigger a preemptive arrest—and soon we're in the world of Philip K. Dick's "The Minority Report."

The ideal of a vast database, barcoding everyone so that any crime scene DNA could be matched to an individual, isn't as enticing as it at first seems. The fact that forensic DNA laboratories already have a multi-year backup may become a minor issue as technologies improve. But the inclusion of more innocent people in a database doesn't really increase the chances of finding a guilty match, while it does increase the chances of false positives.

In reading *Genetic Justice*, one begins to wonder whether DNA fingerprinting is of any use at all. Done right, it surely is. An accurate mismatch can rule out a suspect readily, and a perfect match between crime scene DNA and a suspect otherwise identified by traditional crime-detection methods could provide powerful corroboratory evidence. The problem is that it isn't always done right. Maybe the crime scene DNA was a little degraded, so the match wasn't exact but only good enough. Maybe the "suspect" wasn't actually in the database, but a near-match suggested that someone in the database might be a relative of the perpetrator. Although the data can be pretty solid, here we're no longer looking at something as clear as a match or a mismatch, and law enforcement must haul in a few more people for "voluntary" DNA testing—a drag-net. The authors comment, "DNA is starting to look much more like a surveillance tool than a tool for criminal investigation."

The problem with simple conceptual extensions such as identifying relatives is that, according to the authors, the protocols were designed for reduced "stringency" matches resulting from allelic dropouts in a simple exclusion-inclusion test of a suspect rather than in a scan of eight million people in a database. Krinsky and Simoncelli set forth the serious issues around the overrepresentation of minorities in databases and the resulting greater chance of implicating an innocent individual from a minority population. They take a fairly postmodernist view

of the field, seeing a "great divide between those who see ... errors as exceptions to the rule of science as an objective and truth-telling endeavor and those who instead view it as an inherently social enterprise open to human fallibilities."

The authors conclude with ten "axioms" to ensure their vision of justice: (i) One should exercise the same care with forensic

DNA information that we currently use with medical records. (ii) Individuals should expect that their DNA information will be private whether it is obtained for legal or medical use or inadvertently "shed" with a few skin cells. (iii) Police must have a reasonable suspicion before they can require a person to provide DNA for purposes of identification. (iv)

"The taking of DNA constitutes a search" and requires probable cause. (v) Data banks should retain DNA profiles only from persons convicted of crimes. (vi) DNA dragnets, involving samples and profiles of non-suspect individuals, should be subject to "written informed-consent procedures and proper protections against coercion." (vii) Warrants should be required to acquire and analyze DNA samples from family members of people identified through partial matches. (viii) "Surreptitious taking, testing, or storing of DNA from suspects or their relatives ... should be prohibited." (ix) Crime-scene DNA testing should be limited to identity determination and to the prediction "of externally perceptible traits whose DNA markers have been scientifically validated." (x) Samples should be destroyed after DNA profiling to ensure that only the CODIS identification data are obtained.

We must face the likelihood that in the coming years abundant genetic information, for both medical and legal use, will be available, inexpensive, and probably uncontrollable. It will reveal much about our health and our ancestry, and it will identify us if there are traces of our DNA at the scene of a crime—whether or not we had anything to do with that crime. Understanding how to acquire and interpret that data properly while respecting privacy and the presumption of innocence will require an educated public, an informed medical establishment, and a vigilant legal system. Although *Genetic Justice* is a bit plodding and a little heavy on the downside of forensic DNA technology, reading it is a good start.

10.1126/science.1204097

Genetic Justice
DNA Data Banks,
Criminal Investigations,
and Civil Liberties
by Sheldon Krinsky and
Tania Simoncelli
Columbia University Press,
New York, 2011.
424 pp. \$29.95, £19.95.
ISBN 9780231145206.

The reviewer is at the Department of Biology, San Francisco State University, San Francisco, CA 94132-1722, USA. E-mail: goldman@sfsu.edu

GENOMICS

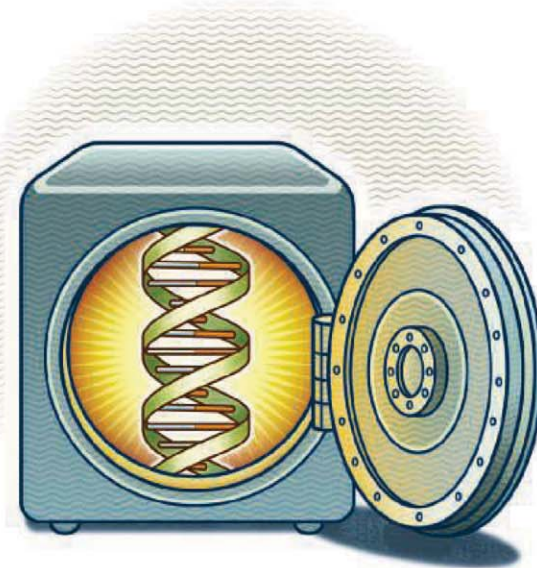
Genomics, Biobanks, and the Trade-Secret Model

Robert Mitchell,^{1*} John M. Conley,² Arlene M. Davis,² R. Jean Cadigan,² Allison W. Dobson,² Ryan Q. Gladden²

Genomic biobanks—repositories of human DNA and/or associated data, collected and maintained for biomedical research—present ethical challenges different from those traditionally associated with medical research. Historically, when researchers obtained and used tissue samples, it was for defined purposes and the nature of the research was disclosed to contributors, who were asked to consent to the specific research project. With genomic biobanks, in contrast, the entity holding the samples may not be involved in the research, and future uses of the samples may be unknown. Although traditional research promised confidentiality and/or anonymity to participants, advances in DNA technology may render these safeguards meaningless (1–3). As a consequence, many ethicists argue that traditional informed consent may be illusory if not impossible (1, 4) and that different approaches to the ethics of genetic sample collections are needed (5, 6).

Ethicists have used two broad strategies to address this challenge. One approach seeks to adjust existing notions of informed consent and government regulation to the new realities of genomic biobanking. For example, proposals advanced by Greely (1, 7) and Caulfield (4) call for donors to give initial “general permission,” “broad consent,” or “authorization” to a range of possible research activities. They couple this initial consent with enhanced regulation and the requirement that donors can learn about prospective research and (if they desire) remove their information or samples.

Other proposals favor novel legal and ethical frameworks. Winickoff and Winickoff’s “charitable trust” model (5), for example, conceives of a biobank as a trust with the



public as the beneficiary. The managers of the biobank become trustees, with all associated legal obligations. They further propose donor-appointed advisory boards and internal ethical review boards, and they would allow individual biobanks to adopt bylaws responsive to their own needs. Another model characterizes the donor-researcher relationship as one of “stewardship,” with the researcher or institution having the duty to manage carefully and responsibly the samples entrusted to their care (6). Although charitable trust and stewardship models might expand public accountability and ensure new modes of governance over collected samples, it is unclear whether they would fundamentally shift the balance of power between researchers and donors.

We propose an approach that emerged from semistructured interviews with healthy volunteers who had been recruited to join a biobank (8). Whether or not they joined, our interviewees generally understood their relation with the biobank in terms that differed from those described in the Web-based and print informed-consent materials available to them. For example, some understood that the small sum of money (\$20) they received for their participation was equivalent to payment for the “sale” of their blood or DNA, and many believed that they would be recontacted if researchers found something “bad”

An alternative to traditional informed-consent approaches to human subjects could provide flexibility and increased participation.

in their DNA. Yet these beliefs did not appear to be simply the result of confusion or misunderstanding. Rather, they seemed to be based on principles similar to those underlying the concept of a trade secret.

The conventional legal definition of a trade secret is any knowledge or information that is not generally available or readily ascertainable, confers an economic advantage on its proprietor over those who do not know it, and is the subject of reasonable efforts to maintain secrecy. Trade-secret protection differs fundamentally from patent protection. Patent law prohibits any unauthorized use of the patented invention, even if innocent; a trade secret is

protected only against access or use in violation of a duty of confidentiality or if it was obtained through improper means. Someone with legitimate and unrestricted access to a product embodying a trade secret may “reverse-engineer” it, i.e., study the product in hopes of learning the trade secret. Nor are trade secrets subject to the technical requirements imposed on patentable subjects. U.S. law permits patents only on new, useful, and nonobvious inventions or discoveries, but any information can be protected as a trade secret.

Trade-secret owners often allow others to exploit their secrets under contracts or licenses that create a relationship between licensor and licensee. The licensor retains ownership of the trade secret but permits specific uses as long as the licensee complies with the conditions specified in the license. A well-known example of a long-running trade secret is the Coca-Cola formula. The company provides the formula to bottlers only under strict confidentiality agreements.

Because an individual who participates in a biobank does not “invent” or even “discover” his or her DNA, it is difficult to consider the specimen contributor as having patent rights. However, it is possible to think of the information encoded by an individual’s DNA as something of unique value for a certain kind of “business” (biomedical

¹Institute for Genome Sciences and Policy and English Department, Duke University, Durham, NC 27708, USA.

²School of Law, Department of Social Medicine, and Center for Genomics and Society, University of North Carolina, Chapel Hill, NC 27599–3380, USA.

*Author for correspondence. E-mail: rmitch@duke.edu

research). Moreover, the situation of participants in biobank research is analogous to that of small-time commercial inventors who possess a trade secret, have no way to exploit it themselves, but understand that it might have value to others and so consider conditions under which they might make it available.

Both commercial trade-secret licenses and informed-consent practice typically address compensation, limits on access and use, measures for maintaining secrecy, and provisions for allocating rights in case of future technological improvements. However, informed-consent practice focuses on limits to access and use and measures for maintaining secrecy, and attempts to minimize consideration of compensation and rights to future technological improvements. By understanding individual contributions to a biobank in terms of trade-secret theory, researchers and bioethicists can address all four conditions with greater flexibility than currently possible.

A principle of current research oversight is that money should not be considered a benefit to the participant, and its role as an inducement is controversial and closely monitored (9). This principle is based on the fear that exchanging money for participation casts doubt, especially in cases of medical or economic vulnerability, on whether consent has been given freely. Although further research needs to be done on vulnerable populations, our model suggests that, in cases of healthy individuals contributing specimens and information to biobanks, we should think of the relations between subjects and research in terms of an exchange [especially since some contributors already understand their participation as a financial transaction (8, 10)].

The trade-secret model does not require that an exchange take the form of money. Specimen contributors could choose among several levels of licenses, from permitting relatively free use of their samples and information to an arrangement that imposed restrictions on the researchers. For example, a license could stipulate that if contributor DNA aids in the development of a commercial product, a portion of the profits would be used to support community public-health measures. Or it could provide for a contributor to receive individual research results (11).

Nor would the trade-secret model necessarily require separate negotiations with each individual (especially important for research that depends on accumulating very large collections of specimens). It would allow, for example, a limited menu of options for contributors, analogous to university technology transfer offices that offer “express licenses”

with a limited number of nonnegotiable, boilerplate agreements to prospective licensees of university technology.

The trade secret model would simplify informed consent. Contributors would be informed of known risks associated with specimen contribution and the possibility of presently unforeseen risks and would be advised to consider all risks when deciding whether to participate and at what level of “compensation” and control.

Even when licensors prefer monetary payment, it does not seem likely that the trade-secret model would increase the size of payments to research participants. Our research suggests that individuals who already understand their participation in terms of the trade-secret model are willing to participate in research for relatively small amounts of money. Undue financial influence, a major concern for those overseeing research, should also not be an issue here. The trade-secret approach simply permits owners of a secret to put a price on the risk they are willing to bear. Our proposal also seems likely to increase the number of people willing to participate in research by allowing some current nonparticipants to resolve concerns not dealt with by traditional informed consent.

Our proposal admittedly moves in a direction opposite to that of recent regulations that attempt to increase the number of samples available for research by exempting some specimens from human subject protection (12). These regulations render invisible the participation of individuals in biobank research. In the long run, forthright negotiation with potential participants, as in our proposal, may be as successful in encouraging participation as current attempts to create a human-subjects exemption.

Our proposal shares with other recent approaches an emphasis on research participant autonomy. Patient-advocacy groups such as PXE International and Genetic Alliance (13) emerged when contributors felt treated solely as “sources” of biological specimens, and these groups responded by taking control of a gene patent (and, in the case of Genetic Alliance, biobanking itself) both to encourage and to impose conditions on research (14). Efforts to promote democratic deliberation about the goals of and ethical restrictions on biobanking (15) also emphasize that individuals participating in research are not simply passive “research subjects.” Finally, community-based participatory research approaches (16) are based on the principle that researchers and communities should work together from the start

to define research problems, establish protocols, and interpret results.

The trade-secret model obviates the property question of sample ownership that was central to cases such as *Moore v. Regents of the University of California* and *Washington University v. Catalona* (17, 18). In those cases (which were neither broadly reasoned nor nationally binding), individuals were judged to have no rights to specimens once the specimens were removed from their bodies. Under the trade-secret approach, the contributor retains legal ownership of the information embodied in the specimen (not the specimen itself) and sets the conditions under which that information can be used. The status quo says “we can’t predict all the risks nor protect you fully against those we can predict—but trust us.” We begin with the same acknowledgment of risk and uncertainty, but ask, “what do you want in exchange for assuming that risk?”

References and Notes

1. H. T. Greely, *Annu. Rev. Genomics Hum. Genet.* **8**, 343 (2007).
2. K. B. Jacobs *et al.*, *Nat. Genet.* **41**, 1253 (2009).
3. J. E. Lunshof, R. Chadwick, D. B. Vorhaus, G. M. Church, *Nat. Rev. Genet.* **9**, 406 (2008).
4. T. Caulfield, R. E. G. Upshur, A. Daar, *BMC Med. Ethics* **4**, 1 (2003).
5. D. E. Winickoff, R. N. Winickoff, *N. Engl. J. Med.* **349**, 1180 (2003).
6. S. M. Fullerton, N. R. Anderson, G. Guzauskas, D. Freeman, K. Fryer-Edwards, *Sci. Transl. Med.* **2**, 15cm3 (2010).
7. H. T. Greely, *Wake Forest Law Rev.* **34**, 737 (1999).
8. R. J. Cadigan, A. M. Davis, in *Governing Biobanks*, J. Kaye and M. Stranger, Eds. (Ashgate Publishing, Farnham, UK, 2009); pp. 117–133.
9. U.S. Food and Drug Administration, Payment to Research Subjects—Information Sheet, Guidance for Institutional Review Boards and Clinical Investigators, www.fda.gov/RegulatoryInformation/Guidances/ucm126429.htm.
10. C. E. M. van Gelderen, T. J. F. Savelkoul, W. Dokkum, J. Meulenbelt, *Eur. J. Clin. Pharmacol.* **45**, 15 (1993).
11. T. Caulfield *et al.*, *PLoS Biol.* **6**, e73 (2008).
12. U.S. Office for Human Research Protections (OHRP), Guidance on Research Involving Coded Private Information or Biological Specimens (OHRP, Bethesda, MD, 2008); www.hhs.gov/ohrp/policy/cdbiol.pdf.
13. S. F. Terry, P. F. Terry, K. A. Rauen, J. Uitto, L. G. Bercovich, *Nat. Rev. Genet.* **8**, 157 (2007).
14. C. Waldby, R. Mitchell, *Tissue Economics* (Duke Univ. Press, Durham, NC, 2006).
15. H. Longstaff, M. M. Burgess, *Public Underst. Sci.* **19**, 212 (2010).
16. M. Minkler, N. Wallerstein, Eds., *Community-Based Participatory Research for Health* (Jossey-Bass, San Francisco, 2003).
17. *Moore v. Regents of the University of California*, 793 P.2d 479 (Cal. 1990).
18. *Washington University v. Catalona*, 490 F.3d 667 (8th Cir. 2007), cert. denied, 552 U.S. 1166 (2008).
19. Supported by grant P50HG004488 from the U.S. National Human Genome Research Institute (NHGRI), NIH. The content is solely our responsibility and does not necessarily represent the official views of the NHGRI or the NIH.

PLANT SCIENCE

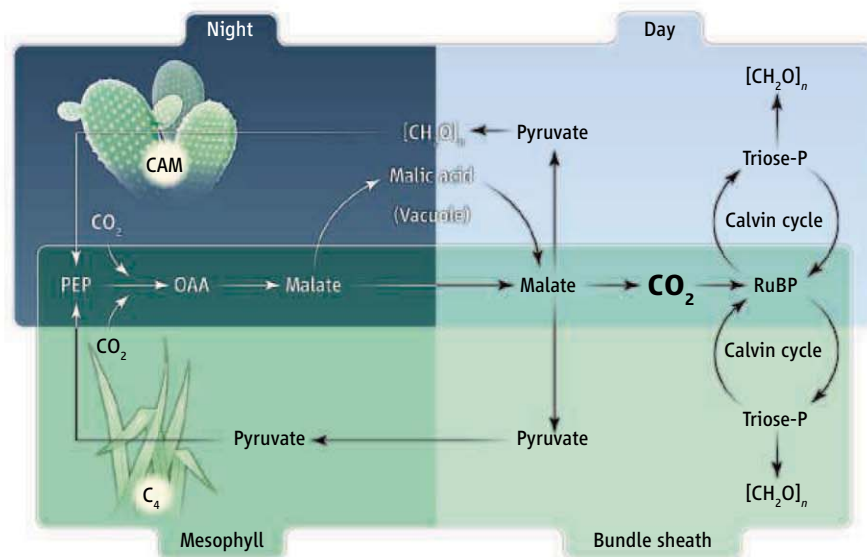
Photosynthesis, Reorganized

Mary Jane West-Eberhard,¹ J. Andrew C. Smith,² Klaus Winter³

Photosynthesis—the conversion of carbon dioxide (CO₂) into organic compounds using energy from sunlight—occurs via three pathways in terrestrial plants. The most common and ancient of these is C₃ photosynthesis, whereas C₄ photosynthesis and crassulacean acid metabolism (CAM) are derived from C₃. Despite great taxonomic diversity across plants that use C₄ and CAM photosynthesis, the core biochemical characteristics of each are similar in many independent plant lineages. How does such convergent biochemistry arise? Shared biochemical properties suggest that C₄ and CAM photosynthesis may have arisen through the reorganization of metabolic processes already present in C₃ plants. Modified expression of these processes would have been subject to selection and genetic accommodation in producing the distinctive derived phenotypes.

CAM plants conserve water by conducting most of their gas exchange in the relatively cool atmosphere at night, allowing, for example, succulent agaves and cacti to grow in strongly water-limited semidesert habitats and supporting many species of epiphytic bromeliads and orchids in microclimatically arid niches in tropical forests (1). C₄ plants benefit from the elimination of photorespiration and grow more rapidly than their C₃ relatives in hot environments in the tropics and subtropics (2). Economically important CAM plants like pineapple, agaves (sisal, tequila), and orchids (vanilla), and C₄ plants like maize, sugarcane, and sorghum, can thus grow under conditions less suitable for C₃ plants such as rice, wheat, and barley. And some may have potential as bioenergy crops (3).

In C₃ photosynthesis, atmospheric CO₂ is captured by ribulose-1,5-bisphosphate carboxylase-oxygenase (RuBisCO), the first enzyme in the Calvin cycle, through which inorganic carbon is fixed into organic form within the chloroplasts of leaf mesophyll tissue. C₄ and CAM photosynthesis involve auxiliary mechanisms outside the chloroplasts that fix atmospheric CO₂ via a phosphoenol-



Similar separations. The CO₂-concentrating mechanisms (for delivery to the Calvin cycle) in CAM (**top**) and C₄ (**bottom**) plants are temporally and spatially separated, respectively. [CH₂O]_n, carbohydrates; OAA, oxaloacetate.

pyruvate carboxylase (PEPC)—malate pathway before delivering it at increased concentration to RuBisCO in the chloroplast. This maximizes the carboxylation activity of RuBisCO while suppressing the wasteful photorespiratory oxygenase activity of this bifunctional enzyme.

The CO₂-concentrating mechanisms of C₄ and CAM plants depend on the same feature—separation of the auxiliary CO₂-fixation process from the Calvin cycle (see the figure). In C₄ photosynthesis, the separation is spatial. Fixation of CO₂ by PEPC occurs in mesophyll cells; the four-carbon products such as malate or aspartate diffuse to the adjacent thick-walled bundle-sheath cells where RuBisCO is localized, and where CO₂ is released by decarboxylation. In CAM plants, the separation is temporal. PEPC is active at night, producing malic acid that is sequestered in large intracellular vacuoles; the following day the plant's gas-exchange pores (stomata) close, malic acid is released from the vacuole, and CO₂ is available at enhanced concentrations for fixation by RuBisCO.

Among the angiosperms (flowering plants), C₄ photosynthesis has evolved more than 45 times in 19 families (4), and CAM in more than 30 families (1), with multiple origins even within plant families such as

Comparative physiology suggests that reorganization and co-option of ancestral traits drove diversification of C₄ and CAM photosynthesis.

the bromeliads (5) and orchids (6). As in many other organisms, the repeated independent origins of C₄ and CAM photosynthesis may have been possible due to evolution by reorganization (7, 8)—the co-option and modification of ancient metabolic pathways. Such modifications can be initiated by mutation or by environmental change, and then accommodated, under selection, by genomic change as the adaptive phenotype evolves (8). Although C₄ and CAM photosynthesis are considered major evolutionary innovations, few, if any, of their essential components are completely new (4, 9, 10). All of the enzymes required in these pathways appear to be homologs of ancestral forms found in C₃ species (9–11). Gene duplication, alternative splicing of mRNA, and changes in cis-regulatory elements or enhancers that control gene expression can maintain essential ancestral functions alongside new ones (7).

Genes from C₃ species may already possess the cis-regulatory elements necessary for recruitment into C₄ photosynthesis (“conserved functional latency”) (12), requiring only modification of a trans-acting factor to produce cell-specific expression. The distinctive temporal patterns of gene expression in CAM plants might be gov-

¹Smithsonian Tropical Research Institute, c/o Escuela de Biología, Universidad de Costa Rica, Costa Rica. ²Department of Plant Sciences, University of Oxford, South Parks Road, Oxford OX1 3RB, UK. ³Smithsonian Tropical Research Institute, Balboa, Ancon, Republic of Panama. E-mail: mjwe@sent.com; andrew.smith@plants.ox.ac.uk; winterk@si.edu

erned by transcription factors implicated in the endogenous circadian rhythm of these plants (13).

However, reorganized expression of ancestral pathways only partly explains the recurrent origins of C_4 and CAM. Particular morphological and biochemical variants may have facilitated the increased compartmentalization of the Calvin cycle that allows auxiliary carbon concentration to work, and may help explain why C_4 and CAM are phylogenetically separated rather than interspersed within the lineages where they recur. Does such reorganization begin with a new mutation, or can environmental stress induce the expression of a new pathway using preexisting genetic variants? The close C_3 relatives of C_4 and CAM plants are key species for answering such questions. In some plants, CAM photosynthesis is envi-

ronmentally inducible and facultative (14), and several examples exist of C_3 – C_4 “intermediates,” typically from marginal arid or saline habitats (4). Therefore, perhaps a primordial version of CAM or C_4 could originate as a response to environmental stress in a subpopulation of C_3 individuals genetically disposed to express it, exploiting the standing or cryptic genetic variation (15) already present in the population. This would help to explain the examples of convergent evolution at the molecular level in multiple independent lineages of C_4 grasses (11). Reflections on the evolutionary origins of C_4 and CAM photosynthesis may also help refine genetic research and expand its possibilities.

References

1. K. Winter, J. A. C. Smith, Eds., *Crassulacean Acid Metabolism: Biochemistry, Ecophysiology and Evolution* (Springer-Verlag, Berlin, 1996).

2. E. J. Edwards *et al.*, *Science* **328**, 587 (2010).
3. C. Somerville, H. Youngs, C. Taylor, S. C. Davis, S. P. Long, *Science* **329**, 790 (2010).
4. R. F. Sage, *New Phytol.* **161**, 341 (2004).
5. D. M. Crayn, K. Winter, J. A. C. Smith, *Proc. Natl. Acad. Sci. U.S.A.* **101**, 3703 (2004).
6. K. Silvera, L. S. Santiago, J. C. Cushman, K. Winter, *Plant Physiol.* **149**, 1838 (2009).
7. J. R. True, S. B. Carroll, *Annu. Rev. Cell Dev. Biol.* **18**, 53 (2002).
8. M. J. West-Eberhard, *Developmental Plasticity and Evolution* (Oxford, New York, 2003).
9. J. M. Hibberd, S. Covshoff, *Annu. Rev. Plant Biol.* **61**, 181 (2010).
10. J. C. Cushman, H. J. Bohnert, *Plant Physiol.* **113**, 667 (1997).
11. P.-A. Christin, D. M. Weinreich, G. Besnard, *Trends Genet.* **26**, 400 (2010).
12. N. J. Brown *et al.*, *Science* **331**, 1436 (2011).
13. S. F. Boxall *et al.*, *Plant Physiol.* **137**, 969 (2005).
14. K. Winter, J. A. M. Holtum, *Plant Physiol.* **143**, 98 (2007).
15. R. D. H. Barrett, D. Schluter, *Trends Ecol. Evol.* **23**, 38 (2008).

10.1126/science.1205336

CELL BIOLOGY

Cytonemes Show Their Colors

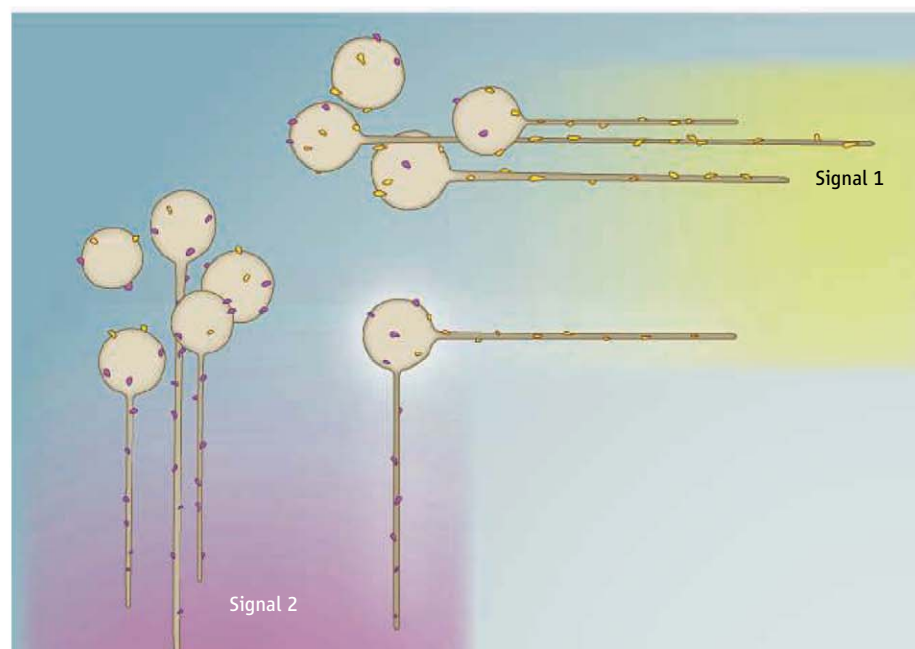
Markus Affolter¹ and Konrad Basler²

Cells in multicellular organisms need to communicate in order to generate organs and tissues of appropriate shape and function. The “information” content of the communication consists of modulating the activity of biochemical signaling pathways. The “hardware” that is used to convey and collect such signals sometimes includes specialized structures, such as the synapses of neurons and molecular complexes that enable cells to adhere to each other or other surfaces. In many instances, cells actively explore their environment by producing extensions such as filopodia, lamellipodia, axons, and dendrites. The exact role of such extensions in non-neuronal cells remains, in most cases, unexplored. On page 354 of this issue, Roy *et al.* (1) help fill in some of the blanks. They report on the properties of filopodial extensions in the wing, eye, and tracheal system of *Drosophila*. They show that these extensions are dedicated to certain signaling pathways by the segregation of the corresponding receptors on their surfaces. The authors call these cell projections, which are based on the protein actin, cytonemes (Latin for “cell thread”). Their

findings point to a scenario in which cells produce a signaling molecule that triggers other cells in the vicinity to form cytonemes, which ultimately become stable and are used for propagating specific intercellular signals.

In developing *Drosophila*, cells create extensions dedicated to specific signaling pathways.

The exclusive, nonoverlapping localization of specific signaling receptors to dedicated cytonemes comes as a surprise, especially because cells often express receptor components for many pathways, potentially



Reaching out. Cells exposed to a gradient of a chemical signal (purple shading, lower left, and yellow shading, upper right) extend thread-like structures called cytonemes with surface receptors (purple and yellow oblongs) toward the signal source. Cytonemes specialize to propagate a specific signal. Researchers speculate that some cells could extend multiple types of cytonemes, each carrying a different signal.

¹Biozentrum der Universität Basel, CH-4056 Basel, Switzerland. ²Institute of Molecular Life Sciences, University of Zürich, CH-8057 Zürich, Switzerland. E-mail: markus.affolter@unibas.ch; konrad.basler@imls.uzh.ch

enabling them to respond readily to an array of incoming signals. Roy *et al.* used receptors of different signaling pathways, tagged with fluorescent proteins, to study their distribution in cytonemes of developing *Drosophila* tissues. They found that in the eye primordium, one receptor, the epidermal growth factor receptor (EGFR), was present only in extensions that pointed posteriorly (to the back). Although cytonemes extending in the dorsoventral (toward the belly) directions were present in these cells, they did not contain fluorescent EGFR. To test whether an individual cell was able to localize different receptors to distinct cytonemes, the authors expressed two different, color-tagged receptors in the air sac primordium, which lies on a structure called the wing imaginal disc: green Tkv, a version of the bone morphogenetic protein (BMP)/Decapentaplegic (Dpp) type I receptor; and red Btl, a cherry-tagged version of the receptor for the fibroblast growth factor (FGF) signal. Then they analyzed the distribution of receptors. They found that cytonemes contained either green or red punctae, suggesting that the receptors Tkv and Btl segregate to separate types of cytonemes.

These findings paint the following picture: Cells sense a given signaling molecule (ligand) on their surface, send out long filopodia, and then sort receptors to these extensions according to the ligand that induced them in the first place. Such extensions might then establish and maintain a connection to the cell, which acts as the signal source, giving them stability and the ability to send signals in a specific direction. In a previous study (2), researchers observed transport of EGFRs from the filopodial tip to the base, so it is conceivable that cytonemes likewise transport receptor-ligand complexes back to the cell body.

Almost nothing is known about cytoneme function, despite their initial discovery more than a decade ago (3) and recent advances on understanding where cytonemes form and what receptors they express. Hsiung *et al.* (4) had proposed that cytonemes in the *Drosophila* wing are used in ferrying Dpp, an important protein morphogen involved in fruit fly development, from source to target cells; the extensions are thus used to determine a cell's distance to the source. However, investigators have proposed several other models for distributing positional information, such as morphogen gradients established by facilitated diffusion, in combination with concentration-dependent responses ("readouts"). In the developing air sac primordium, studies have shown that FGF signaling triggers cell migration (5, 6), possibly by FGF-transport-

ing filopodia that bring activated FGF receptors to the cell bodies. Studies have also suggested that Notch-Delta signaling occurs on filopodial cell contacts between non-neighboring cells of the notum, the dorsal portion of an insect's thoracic segment (7). Clearly, a role in cell-to-cell signaling is emerging. At present, however, no genetic tools exist to specifically remove cytonemes and analyze the ensuing functional consequences.

Roy *et al.*'s description of specific cytoneme types raises a number of intriguing questions. For example, how do cells sort different receptors into different types of cytonemes? How can cytonemes be directed or stabilized specifically along an ascending sig-

nal gradient? Such new questions, however, should not distract the field from resolving the fundamental issue of whether cytonemes have anything to do with morphogen-mediated patterning.

References

1. S. Roy, *Science* **332**, 354 (2011).
2. D. S. Lidke *et al.*, *J. Cell Biol.* **170**, 619 (2005).
3. F. A. Ramirez-Weber, T. B. Kornberg, *Cell* **97**, 599 (1999).
4. F. Hsiung, F.-A. Ramirez-Weber, D. D. Iwaki, T. B. Kornberg, *Nature* **437**, 560 (2005).
5. M. Sato, T. B. Kornberg, *Dev. Cell* **3**, 195 (2002).
6. C. Cabernard, M. Affolter, *Dev. Cell* **9**, 831 (2005).
7. M. Cohen, M. Georgiou, N. L. Stevenson, M. Miodownik, B. Baum, *Dev. Cell* **19**, 78 (2010).

10.1126/science.1205971

PHYSICS

Make It Quantum and Continuous

Philippe Grangier

Robust teleportation of a fragile Schrödinger's-cat state was achieved with nonclassical wave-like states of light.

Quantum light looks like a mysterious thing: Is it wave, or particle, or both, or neither? Since the very beginning of quantum optics, physicists have been looking for graphical ways to represent the quantum state of light in order to understand it better. One can then visualize quite surprising quantum objects, such as the so-called Schrödinger's-cat state: In classical terms, it would be an oscillation having two opposite phases at the same time, like the famous cat being both living and dead. Such exotic quantum states can now be prepared in the lab, and even better, they can be teleported—that is, destroyed in one place and recreated in another one, as shown by Lee *et al.* (1) on page 330 of this issue.

But how to visualize what is going on? One way is by using phase space—in other words, to represent in Cartesian coordinates the sine and cosine components of the quantized electric field, which are similar to the position Q and momentum P of a quantum harmonic oscillator. The quantities Q and P obey the Heisenberg Principle—they cannot be known simultaneously with high accuracy. A best compromise is a so-called Glauber's coherent state, where the variances of Q and P are equal and take a value usually called the "vacuum noise level."

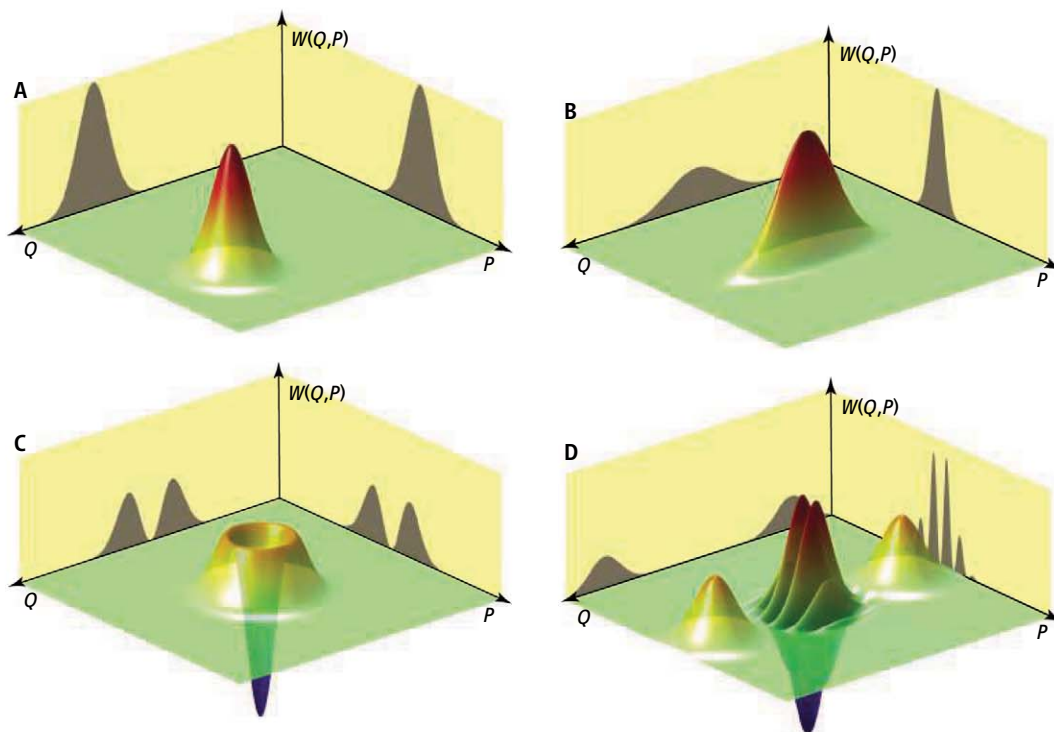
More interestingly, a "squeezed state" can be created by using a nonlinear crystal (an optical parametric down-converter), which turns a single photon into a pair of photons of lower energy. The variance of one variable (for example, P) can be made smaller than vacuum noise, at the expense of the variance of the other variable, Q , getting larger (2). If one now considers two separate beams 1 and 2, the pairs of continuous variables (Q_1, P_1) and (Q_2, P_2) can be entangled—their measurement outcomes are not independent but show very strong quantum correlations. For the beams to be entangled, it is sufficient that the quantities $(Q_1 - Q_2)$ and $(P_1 + P_2)$ simultaneously have a small variance. Such a continuous-variable entangled state can be used to teleport a coherent state (3)—that is, to destroy it and then to recreate it remotely—using the entangled beams as a resource for transmission (4–6).

To visualize these objects, it is convenient to introduce a mathematical tool called the Wigner function $W(Q, P)$, which is very close to being a probability distribution of the electric field in the (Q, P) plane—except that it can take on negative values. For a coherent state, $W(Q, P)$ is a cylindrically symmetric Gaussian function that peaks at coordinates that are just the average values of the sine and cosine components of the electric field. The width of the peak corresponds to the vacuum noise

Institut d'Optique, 91127 Palaiseau, France. E-mail: philippe.grangier@institutoptique.fr

Negative values and positive results.

The Wigner function is a way to describe how “quantum” a light pulse is. Progressing from most classical to most quantum, the Wigner functions are shown for (A) the coherent state, (B) a squeezed state, (C) the single-photon state, and (D) a Schrödinger’s-cat state. The projections or “shadows” of the Wigner function (shown on the sides) are the measured probability distributions of the quantum continuous variables Q or P . The Wigner function is a Gaussian function for (A) and (B), but it takes negative values for the strongly quantum states (C) and (D). These negative features vanish very quickly in the presence of decoherence. In the experiment by Lee *et al.*, a quantum state similar to (C) and (D) was teleported and kept the negative values of the Wigner function. This result demonstrates an extraordinary degree of experimental control over such fragile quantum objects.



(see the figure, panel A). For a squeezed state, the peak is still Gaussian but now has two-fold symmetry. One variance, say along P , is smaller than the vacuum noise, while the other one is larger (see the figure, panel B). For all optics experiments done during the last century, $W(Q, P)$ was some kind of Gaussian and therefore looked like a “real” (positive) probability distribution.

More surprisingly, the number state, where the number of photons in a light pulse is well defined, has a $W(Q, P)$ function that is negative at the origin (see the figure, panel C). Negative values are allowed because true probabilities are obtained by integrating these distributions—the integral over P gives the true probability distribution of Q . The integral of $W(Q, P)$ over any component of the electric field is the probability distribution of its orthogonal component (these appear as “shadows” in the figure panels).

This shadow idea is behind the method used to obtain $W(Q, P)$ experimentally. Many projections are measured so that $W(Q, P)$ can be reconstructed by a process called quantum tomography. All of the states with negative Wigner functions are called “nonclassical,” because their discrete or continuous properties (or both) are now mixed and are purely quantum features. Many states with negative Wigner functions have recently been realized experimentally, including number states with one (7) or two photons (8), photon-added states (9), and entangled states with negative Wigner func-

tions (10). Of particular interest here are superpositions of coherent states with opposite phases, which are called Schrödinger’s kittens (11–13) or Schrödinger’s cats (14, 15), depending on their size (see the figure, panel D).

Such highly quantum states are desirable for efficient quantum information processing tasks, such as entanglement distillation in quantum communication, or as logical gates for quantum computing. These tasks involve many operations and are quite vulnerable to decoherence—the degradation of entanglement by unwanted coupling to the environment. A natural question is how well highly quantum states can be controlled in a basic processing operation.

The quantum teleportation of a Schrödinger’s-cat state by Lee *et al.* successfully combined many operations. They generated a highly entangled state—the resource for teleportation—and independently a Schrödinger’s-kitten state, the one to be teleported. Then, after the appropriate steps including the destruction of the initial kitten, they “recreated” this kitten in another place, still with negative features in its Wigner function. These final negative features can only be observed if the quality of the teleportation is high enough. This quality is measured by a number, called the fidelity, which must be greater than 2/3 for the operation to be successful. This 2/3 value is the so-called no-cloning limit, which also ensures that no other copy of the initial state

can remain at the end (16, 17): The cat state must really be “erased” somewhere in order to be able to “reappear” elsewhere.

Overall, such an achievement is certainly very impressive, and it goes beyond pure experimental virtuosity. It shows that the controlled manipulation of quantum objects has progressed steadily and achieved objectives that seemed impossible just a few years ago, and that tools are now available to tackle more ambitious goals.

References and Notes

1. N. Lee *et al.*, *Science* **332**, 330 (2011).
2. R. E. Slusher, L. W. Hollberg, B. Yurke, J. C. Mertz, J. F. Valley, *Phys. Rev. Lett.* **55**, 2409 (1985).
3. A. Furusawa *et al.*, *Science* **282**, 706 (1998).
4. C. H. Bennett *et al.*, *Phys. Rev. Lett.* **70**, 1895 (1993).
5. D. Bouwmeester *et al.*, *Nature* **390**, 575 (1997).
6. D. Boschi, S. Branca, F. De Martini, L. Hardy, S. Popescu, *Phys. Rev. Lett.* **80**, 1121 (1998).
7. A. I. Lvovsky *et al.*, *Phys. Rev. Lett.* **87**, 050402 (2001).
8. A. Ourjoumtsev, R. Tualle-Broui, P. Grangier, *Phys. Rev. Lett.* **96**, 213601 (2006).
9. V. Parigi, A. Zavatta, M. Kim, M. Bellini, *Science* **317**, 1890 (2007).
10. A. Ourjoumtsev, F. Ferreyrol, R. Tualle-Broui, P. Grangier, *Nat. Phys.* **5**, 189 (2009).
11. A. Ourjoumtsev, R. Tualle-Broui, J. Laurat, P. Grangier, *Science* **312**, 83 (2006).
12. J. S. Neergaard-Nielsen, B. M. Nielsen, C. Hettich, K. Mølmer, E. S. Polzik, *Phys. Rev. Lett.* **97**, 083604 (2006).
13. H. Takahashi *et al.*, *Phys. Rev. Lett.* **101**, 233605 (2008).
14. A. Ourjoumtsev *et al.*, *Nature* **448**, 784 (2007).
15. T. Gerrits *et al.*, *Phys. Rev. A* **82**, 031802(R) (2010).
16. F. Grosshans, P. Grangier, *Phys. Rev. A* **64**, 010301(R) (2001).
17. M. Ban, *Phys. Rev. A* **69**, 054304 (2004).
18. We thank A. Ourjoumtsev for help with the figures.

PHYSICS

Another Spin on Graphene

Antonio H. Castro Neto^{1,2}

Graphene, the one-atom-thick face of carbon (1), startled the condensed matter community from the get-go. It exhibits a large number of new and exotic optical and electronic effects that have not been observed in other materials (2, 3). Most of these effects arise because of two important properties of graphene—the strength of the bonds that keep the carbon atoms together and the peculiar electronic structure of the honeycomb lattice. The electronic excitations in graphene are said to behave like Dirac particles, that is, their energy is proportional to their momentum (4). Furthermore, graphene is opening doors for an entirely new technology based on two-dimensional (2D) crystals. On page 328 of this issue Abanin *et al.* (5) report another completely unexpected effect that involves nonlocality and quantum mechanics at ambient conditions.

Quantum mechanics (QM), the theory of the microscopic universe, associates an amplitude and a phase to an object. Amplitude and phase represent the dual nature of QM; the amplitude is the “particle” aspect and the phase the “wave” aspect. A system is coherent when its phase is well defined (unlike classical mechanics, in QM particles interfere either constructively or destructively if they have a well-defined phase). Quantum effects disappear either when one looks into the macroscopic world or when one goes to high temperatures. This happens because macroscopic objects (like you and me) are all incoherent from the QM point of view. In some rare cases, such as superconductors or superfluids at very low temperatures, it is possible to have a coherent macroscopic state. However, the coherence is destroyed when the temperature is increased because of the uncontrolled motion of all

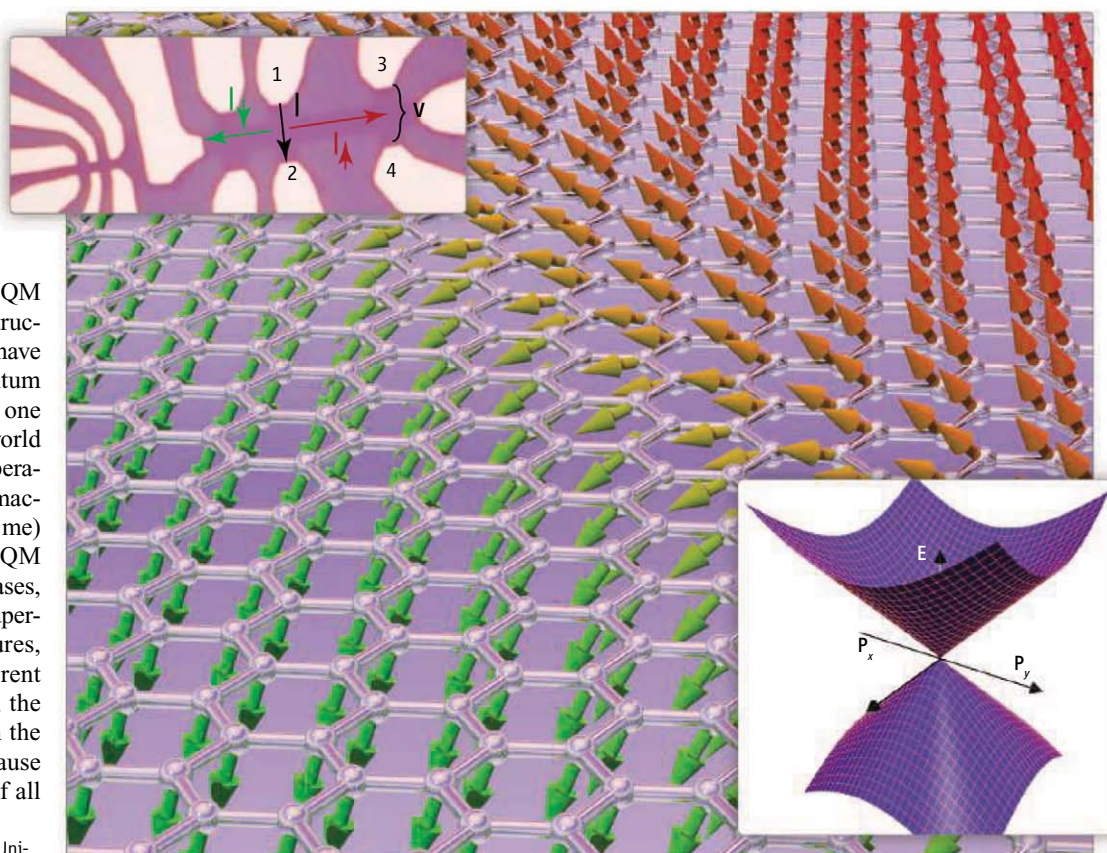
the particles involved. Furthermore, in the great majority of physical systems (micro or macro), the effects are local, that is, an object is only influenced directly by its immediate surroundings. Abanin *et al.* show that graphene exhibits nonlocal quantum effects at room temperature.

In their experiments, an electrical current is passed between two electrodes in close proximity to each other (see the figure, upper inset), and they detect a voltage far away from those electrodes. In an ordinary material under the same conditions (at room temperature and small magnetic fields), this would not happen because the electrons are incoherent and behave classically. After a few collisions with impurities in the system, the electrons would lose their phase information and undergo random walk. To reach nonlocal contacts, this would be a walk too far, and no voltage would be generated. This

Electrical measurements on graphene reveal further exotic electronic properties of this one-atom-thick material.

indicates that graphene is behaving in a quantum mechanical way and creating a nonlocal voltage under unexpected conditions. How is this possible?

There are very few examples of nonlocal transport in electronic systems. A typical example is the quantum Hall effect. In the classical Hall effect, which is observed in any metal, electrons experience a Lorentz force that is perpendicular to applied electrical and magnetic fields, leading to the appearance of a new electric field, or voltage (the Hall voltage), which is perpendicular to the original applied field. When a large magnetic field is applied to a 2D metal, the electronic states become quantized, and the classical Hall effect turns into the quantum Hall effect. The energy gaps associated with these states are large; hence, the bulk of the system is nonconductive. However, there are states at the edge of the sample that carry electric charge.



Probe here, measure there. (Upper inset) A graphene device in which a current is applied between electrodes 1 and 2 and a voltage is measured in distant electrodes 3 and 4, due to the splitting of the spin currents (up and down), as shown in the main figure. (Lower inset) Graphene electronic dispersion and its Dirac point.

CREDIT: TATIANA RAPPOPORT/UNIVERSIDADE FEDERAL DO RIO DE JANEIRO

¹Graphene Research Centre, National University of Singapore, Singapore 117542.

²Department of Physics, Boston University, Boston, MA 02215, USA. E-mail: neto@bu.edu

These edge states always propagate in one direction (and for that, they are called “chiral”) as a result of combination of the Lorentz force and the confining potential in the edge of the sample. Chirality allows currents to propagate large distances coherently. However, this is not the case in the experiments of Abanin *et al.* because the magnetic fields used are not large enough to produce coherent quantized levels. Nonlocal transport can also occur in systems with long-range order due to electron-electron interactions, such as charge density waves and superconductors. In those cases, the state of the many-body system is coherent over macroscopic scales and the electrons behave cooperatively. However, no such long-range order has ever been detected in graphene.

What Abanin *et al.* advocate as the reason for this anomalous behavior is the unusual physics that occurs at the so-called Dirac

point [the point where the cones meet (see the figure, lower inset)] in the presence of a magnetic field. At this particular point, graphene is electrically neutral and its electrical resistance is high. However, small magnetic fields can produce charges with well-defined spin that points either up or down relative to the applied field. As a consequence, the Hall resistance of graphene (the ratio of the Hall voltage to the applied current) close to the Dirac point suffers a large change, and spin-up and spin-down currents are produced in opposite directions (see the figure). Thus, we are faced with a very unusual situation in which the charge of the electron still behaves incoherently (and hence, classically) but its spin behaves coherently (and thus, quantum mechanically). A similar effect occurs in metals and semiconductors with strong coupling between the spin and orbital degrees of freedom of the electrons (6). However, in ideal,

flat graphene (as the ones supported in boron nitride), the spin-orbit coupling is too weak. In the presence of ferromagnetic contacts (7), one would be able to use this effect at room temperature and macroscopic distances for new graphene-based spintronics in 2D, with the electron spin as the quantum degree of freedom. This discovery adds a new chapter to the rich history of graphene.

References and Notes

1. K. Novoselov *et al.*, *Science* **306**, 666 (2004).
2. R. R. Nair *et al.*, *Science* **320**, 1308 (2008).
3. N. Levy *et al.*, *Science* **329**, 544 (2010).
4. A. H. Castro Neto, F. Guinea, N. M. R. Peres, K. S. Novoselov, A. K. Geim, *Rev. Mod. Phys.* **81**, 109 (2009).
5. D. A. Abanin *et al.*, *Science* **332**, 328 (2011).
6. Y. K. Kato, R. C. Myers, A. C. Gossard, D. D. Awschalom, *Science* **306**, 1910 (2004).
7. N. Tombros, C. Jozsa, M. Popinciuc, H. T. Jonkman, B. J. van Wees, *Nature* **448**, 571 (2007).
8. I thank Tatiana Rappoport for discussions.

10.1126/science.1204496

OCEAN SCIENCE

A Frontal Challenge for Climate Models

Raffaele Ferrari

The ocean surface is filled with a convoluted web of “fronts” that separate waters of different temperatures and salinities (see the figure). Just as thin ducts in the lung called alveoli facilitate the rapid exchange of gases when breathing, fronts are the ducts through which heat, carbon, oxygen, and other climatically important gases enter into the deep ocean. A lack of observations, however, has hampered progress in understanding the dynamics of fronts, which can be as narrow as hundreds of meters and as wide as tens of kilometers. Global satellite measurements of ocean-surface velocities and air-sea fluxes, for instance, are only available at resolutions of a few hundred kilometers. Although shipboard researchers can sample vertical ocean profiles down to centimeter scales, only rarely do they collect profiles that are less than 100 km apart. On page 318 of this issue, D’Asaro *et al.* (1) present a breakthrough in observing ocean fronts, providing direct observations of the workings of the Kuroshio front off Japan on scales from

kilometers to millimeters. This detailed and wide-ranging portrait was made possible by the development of towed instruments that continuously sample the waters behind a steaming ship, the deployment of freely drifting instruments that follow ocean currents, and the exercising of a great deal of ingenuity in keeping all these tools along the front for a few weeks in 2007.

The convergence of waters at an ocean front can result in water masses sinking rapidly, at rates of 10 to 100 m/day, compared to typical rates of 1 to 10 m/day in the rest of the ocean. These rapid vertical velocities may be key in determining the exchange rate of heat, carbon dioxide, and other gases between the atmosphere and the deep ocean. Fronts, however, are an important element of the ocean-atmosphere coupled climate system, and in efforts to predict the response of climate to anthropogenic activities, such as the burning of fossil fuels. Currently, however, ocean models used for climate studies are based on grids that are coarser than the typical widths of fronts because of computer speed limitations. Although these models can be tuned to reproduce the collective effect of fronts in the present climate, their

An unusually detailed portrait of an ocean front off Japan could help improve climate predictions.

capability to predict the impact of fronts on future climate is unknown. We are essentially running models of the ocean lungs that do not include alveoli.

Recent work on the stability of fronts seems to indicate that air-sea exchange at fronts is short-lived. The evidence suggests that the exchange is strong when the front first forms, but is suppressed a short time later, when the front becomes unstable. In satellite images, the instability appears as a meander in the front (see the bottom left of the figure); it pushes waters from the light (warm) side of the front over waters on the dense (cold) side (2, 3). The resulting buoyant layer of warmer, lighter water on top of the front is very stable and suppresses any vertical transport, effectively closing the exchange pathway with the atmosphere. This scenario is observed when the atmospheric forces that influence ocean fronts (atmospheric forcing), such as winds, heat loss, or evaporation, are weak. In contrast, D’Asaro *et al.* show that when the atmospheric forces are strong, the exchange pathway remains open. This is because small-scale turbulence develops that mixes heat and gases across the buoyant surface

Department of Earth, Atmospheric, and Planetary Sciences, Massachusetts Institute of Technology, Cambridge, MA 02139, USA. E-mail: rferrari@mit.edu

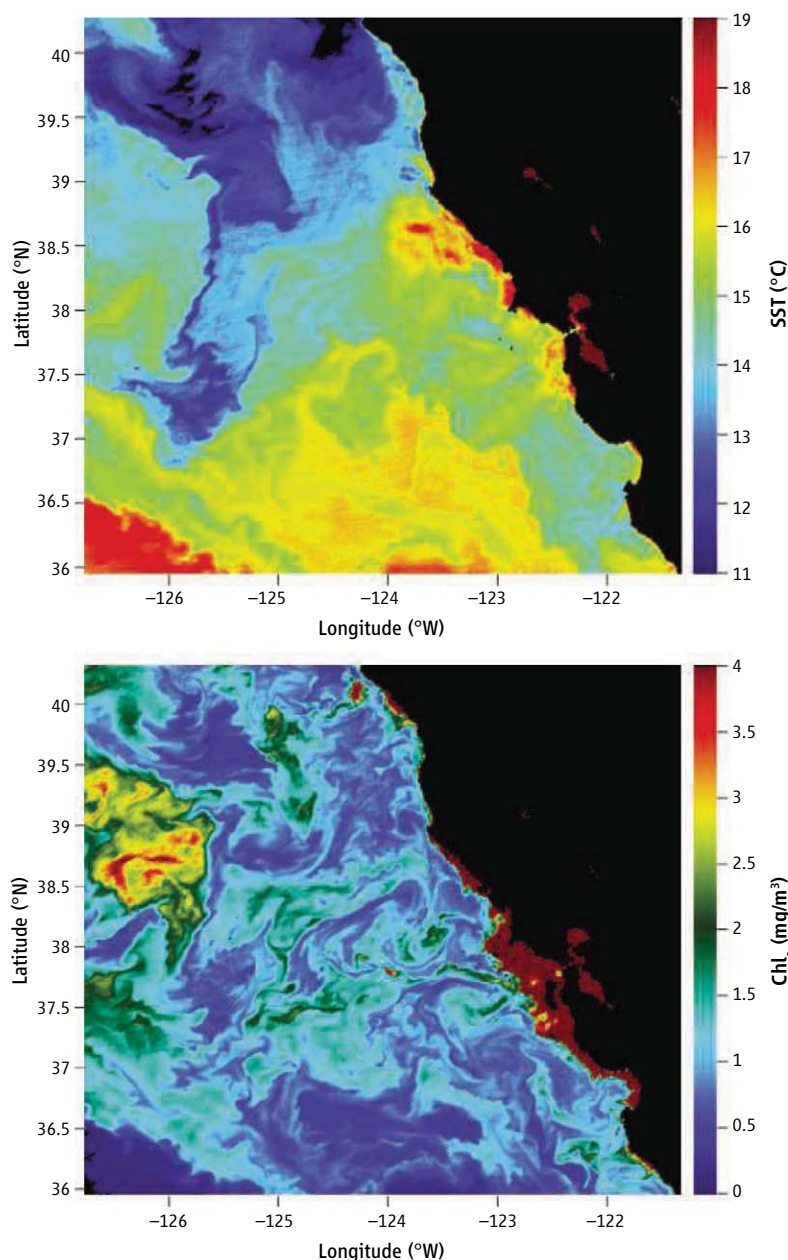
layer. The onset of strong small-scale turbulence at forced fronts has also been observed in numerical simulations (4). So, in a sense, the ocean takes a deep breath every time the winds or surface heat losses are strong.

The generation of small-scale turbulence at oceanic fronts has important implications for global ocean circulation and how the ocean dissipates energy. The ocean is set into motion at global scales by atmospheric winds. The large-scale ocean currents then break into eddies with scales of hundreds of kilometers. If the ocean is to achieve equilibrium, the energy must be converted into heat and radiated back to space (5). Ocean eddies are strongly constrained by Earth's rotation, however, and they transfer little energy to smaller-scale motions. Energy dissipation is confined either to the eddy's top, where fronts develop and become unstable, or to the eddy's bottom boundary, where dissipation is generated by topographic corrugations (6).

D'Asaro *et al.*'s observations may help solve this puzzle of where energy is dissipated. They report that at the Kuroshio front, the energy dissipation resulting from frontal instabilities peak at 10 times the mean work done by the winds to maintain the front. These high dissipation rates are, however, of short duration and occur probably 1% of the time. The implication is that only 10% of the energy input into the ocean over a year is lost through frontal instabilities—more quantitative estimates confirm this result. Extrapolating to the global ocean suggests that most dissipation occurs when eddies rub against topographic features on the sea floor, and that these areas become the graveyard of ocean energy. This extrapolation is uncertain and is offered mostly to challenge readers to improve it.

Biogeochemically, fronts shape the

physical and chemical environment for ocean ecology and carbon uptake on scales of kilometers. Phytoplankton are at the base of the ocean ecosystem and can grow only in the euphotic layer, the upper 10 to 100 m of the ocean that receive sufficient light for photosynthesis. However, phytoplankton also need nutrients (nitrogen, phosphorus, inorganic carbon), which are abundant only a few hundred meters below the surface. Fronts, with their strong vertical velocities (7), can lift nutrients into the euphotic layer and enhance the productivity of the ocean. They can also increase light exposure by modulating the rate at which phytoplankton is mixed below the euphotic layer. Satellite images of phytoplankton abundance, inferred from ocean color, show that



To the front. Sea-surface temperatures (SST) (**top**) and chlorophyll concentrations (**bottom**) highlight ocean fronts off the California coast as measured by the MODIS instrument operating on the NASA Aqua spacecraft on 6 October 2002.

fronts are regions of enhanced growth (see the figure).

Given the importance of frontal physics for ocean dynamics and biogeochemistry, how are we going to make substantial progress in understanding and quantifying the effect of fronts on the global climate system? Two upcoming observational programs provide hope. The first campaign is funded by the U.S. Office of Naval Research. Over the next 2 years, it will deploy an impressive array of instruments along the Gulf Stream front off the east coast of the United States and will make detailed physical measurements on scales ranging from hundreds of kilometers down to millimeters. The second campaign, the Surface Water Ocean Topography mission planned by NASA, is more ambitious and involves measuring sea-surface height from space, using techniques that will provide a 1-cm accuracy over a distance of 10 km. Klein *et al.* (8) suggest that, at this resolution, sea-surface height can be used to reconstruct global maps of the vertical velocities associated with

major fronts and to provide the first global assessment of frontal physics in the ocean.

References and Notes

1. E. D'Asaro, C. Lee, L. Rainville, R. Harcourt, L. Thomas, *Science* **332**, 318 (2011); 10.1126/science.1201515.
2. B. Fox-Kemper, R. Ferrari, R. Hallberg, *J. Phys. Oceanogr.* **38**, 1145 (2008).
3. X. Capet, J. McWilliams, M. Molemaker, A. Shchepetkin, *J. Phys. Oceanogr.* **38**, 44 (2008).
4. J. R. Taylor, R. Ferrari, *J. Phys. Oceanogr.* **40**, 1222 (2010).
5. C. Wunsch, R. Ferrari, *Annu. Rev. Fluid Mech.* **36**, 281 (2004).
6. A. Sen, R. B. Scott, B. K. Arbic, *Geophys. Res. Lett.* **35**, L09606 (2008).
7. P. Klein, G. Lapeyre, *Annu. Rev. Mar. Sci.* **1**, 351 (2009).
8. P. Klein *et al.*, *Geophys. Res. Lett.* **36**, L12603 (2009).
9. I acknowledge the Office of Naval Research for support (award N000140910458) and J. Taylor for useful comments and help with the figures.

10.1126/science.1203632

Enhanced Turbulence and Energy Dissipation at Ocean Fronts

Eric D'Asaro,^{1*} Craig Lee,¹ Luc Rainville,¹ Ramsey Harcourt,³ Leif Thomas²

The ocean surface boundary layer mediates air-sea exchange. In the classical paradigm and in current climate models, its turbulence is driven by atmospheric forcing. Observations at a 1-kilometer-wide front within the Kuroshio Current indicate that the rate of energy dissipation within the boundary layer is enhanced by one to two orders of magnitude, suggesting that the front, rather than the atmospheric forcing, supplied the energy for the turbulence. The data quantitatively support the hypothesis that winds aligned with the frontal velocity catalyzed a release of energy from the front to the turbulence. The resulting boundary layer is stratified in contrast to the classically well-mixed layer. These effects will be strongest at the intense fronts found in the Kuroshio Current, the Gulf Stream, and the Antarctic Circumpolar Current, all of which are key players in the climate system.

Although the basic characteristics of ocean circulation have been well known for many decades, a detailed understanding of its energetics has emerged only recently (*1*).

The energy sources are well understood: Wind stress acting on surface currents (or “wind-work”), particularly in the Southern Ocean, is the dominant energy source, with little net input from

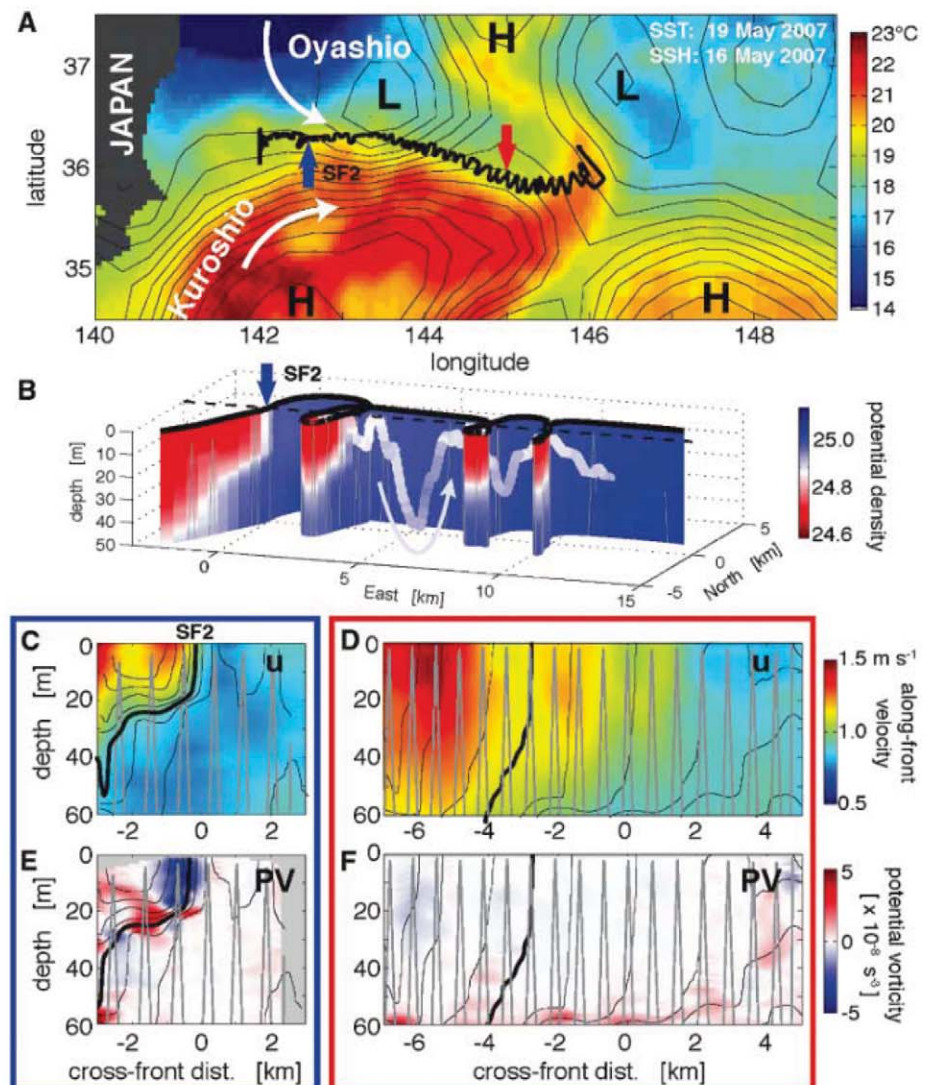
heating/cooling or precipitation/evaporation. The energy sinks, however, are less well understood. Energy dissipation requires a cascade of energy through nine orders of magnitude, from the size of the ocean to the centimeter scales of viscous dissipation. A cascade of processes supports this flux. Instabilities of the large-scale circulation lead to the generation of a rich field of eddies with typical scales of 100 km at mid-latitudes. The dynamics of these eddies are highly constrained by Earth's rotation such that their currents are nearly geostrophic (that is, the flow is governed by a balance between Coriolis and horizontal pressure forces). A turbulent, geostrophic eddy field tends to flux energy to larger rather

¹Applied Physics Laboratory and School of Oceanography, University of Washington, Seattle, WA 98105–6698, USA.

²Department of Environmental Earth System Science, Stanford University, Palo Alto, CA 94305–4216, USA. ³Applied Physics Laboratory, University of Washington, Seattle, WA 98105–6698, USA.

*To whom correspondence should be addressed. E-mail: dasaro@apl.washington.edu

Fig. 1. (A) Sea surface temperature (SST) map (37°) of experimental area with sea surface height (SSH) (δ) shown as contours (0.1-m interval). The thick black line denotes the ship track. Blue and red arrows mark sections shown below in blue and red boxes (C to F), respectively. L and H mark low- and high-pressure centers, respectively. **(B)** Triaxus and float data around SF2 [blue box (C and E)], with Triaxus density shown as a colored curtain hanging beneath the ship track and float trajectory shown as a ribbon colored by density beneath the surface track (dashed line). Sections show along-front velocity [(C) and (D)] and total PV [(E) and (F)] for SF2 (left, blue box) and for a later section (right, red box). Black contours plot potential density in each section, with the thick line marking $\sigma_\theta = 25.0$ kg m⁻³ and thinner lines plotted at 0.05 intervals. Gray lines denote the Triaxus profile track.



than smaller scales, thus providing no obvious path to dissipation. Recent simulations (2–4) with very-high-resolution models suggest a new path from the eddy field toward dissipation through the formation of submesoscale fronts, regions of strong lateral gradient in the upper ocean, with horizontal scales of 1 to 10 km. Instabilities of these fronts could then cascade energy from the frontal scale to dissipation.

The simulations also suggest that the surface “mixed-layer” of the ocean is greatly modified in the presence of fronts. For one, the boundary layer is stratified, not mixed, and deepens by the action of turbulent motions that derive part of their energy from the frontal circulation as opposed to atmospheric forcing (4, 5). This is a shift from the classical paradigm of a surface boundary layer driven by the atmosphere, with implications for climate dynamics. The surface boundary layer is the mediator for air-sea interaction and therefore influences processes that play an integral role in the climate system such as the oceanic sequestration of carbon and the subduction, or transfer, of heat, salt, and dissolved gasses from the ocean’s surface to its interior. Oceanic sequestration of carbon and subduction occur to a

large degree in the proximity of the ocean’s main currents: the Gulf Stream, the Antarctic Circumpolar Current, and the Kuroshio Current (6, 7). These currents are regions of strong lateral density gradients; therefore, their surface boundary layers could be substantially affected by frontal dynamics. Here, we present experimental evidence from a front in the Kuroshio showing that this is indeed the case.

Evolution of the front. Measurements were taken from 18 to 21 May 2007 (days 137 to 140) near the start of the Kuroshio extension off the coast of Japan. Here, the cold subpolar gyre waters of the Oyashio Current meet the warm subtropical gyre waters of the Kuroshio Current to form the Kuroshio front (Fig. 1A). The region is rich in eddies, as illustrated by the sea surface height contours in Fig. 1A (8). Measurements focused on an exceptionally sharp front [the “sharpest front” (SF), blue arrow in Fig. 1] formed by a strongly confluent flow between two eddies acting on the contrast between the warm Kuroshio water and the cold Oyashio water. Measurements were made by deploying a subsurface, neutrally buoyant Lagrangian (water-following) float (9) in the frontal region, acoustically tracking it from

the ship, and surveying a ~5-km region around the float using the Triaxus profiling vehicle towed behind the *R/V Melville* (10). An example of the sampling strategy is shown in Fig. 1B. The float provided a reference frame moving with the frontal water, so that changes in frontal structure can be interpreted as attributable to its temporal evolution. The vertical motion of the float within the boundary layer also provided estimates of the turbulence intensity and dissipation rate. Measurements included temperature, salinity, and pressure on both platforms and velocity profiles obtained by combining ship and Triaxus data (fig. S3) (10).

Confluent flow (evident in Fig. 1A) concentrates the large-scale north-south temperature and salinity gradients into a smaller region, thus forming the SF. During day 137, estimates from the large-scale velocity field derived from satellite altimetry show a north-south convergence of north velocity $\partial v / \partial y < 0$ (v , northward velocity; y , northward distance) and an east-west divergence of east velocity $\partial u / \partial x > 0$ (u , eastward velocity; x , eastward distance), both of magnitude $\sim 0.5 \times 10^{-5} \text{ s}^{-1}$. Estimates from direct velocity measurements (fig. S3) (10) along the front and $\pm 3 \text{ km}$ to either side confirm the north-south convergence and the acceleration of the along-front velocity ($\partial u / \partial x \approx -\partial v / \partial y \sim 1.2 \pm 0.7 \times 10^{-5} \text{ s}^{-1}$). The observed front thinned laterally by about a factor of 2 during this period (Fig. 2A), a rate close to that predicted from these velocity gradients, thus forming and maintaining the SF through day 137. Both confluence components dropped to zero by day 138.5 and then become divergent with a magnitude of $0.5 \pm 0.5 \times 10^{-5} \text{ s}^{-1}$. Thus, the SF is a transient region of strong density gradient generated by strong local confluence and embedded within the larger-scale Kuroshio front.

A section across the SF (Fig. 1C) shows it to be less than 1 km wide in surface density and ~20 m deep (11). A surface-velocity maximum, the frontal jet, is found on the warm side of the front (Fig. 1C). The shear below this jet extends across the frontal region and has a substantial geostrophic component, but with a shear magnitude that is roughly half that expected geostrophically from the horizontal density gradient. A similar section taken 2 days and 220 km downstream (Fig. 1D) shows a much wider (4 km) and deeper (60 m) frontal zone. The large horizontal density gradients across the front have eroded, although the net contrast remains about the same, and the volume of water with intermediate properties has increased (Fig. 1, C and D). Thus, the decay of the SF appears to be due to a combination of local diffusion and mixing.

Turbulence and mixing at the front. Measurements collected by the Lagrangian float at the SF quantify the rate of turbulent mixing. The float interspersed periods of Lagrangian drift with profiles and surfacing for communication. During the 16 drifts, the float was water-following in three dimensions, with its vertical velocity measuring the vertical velocity of the water. During

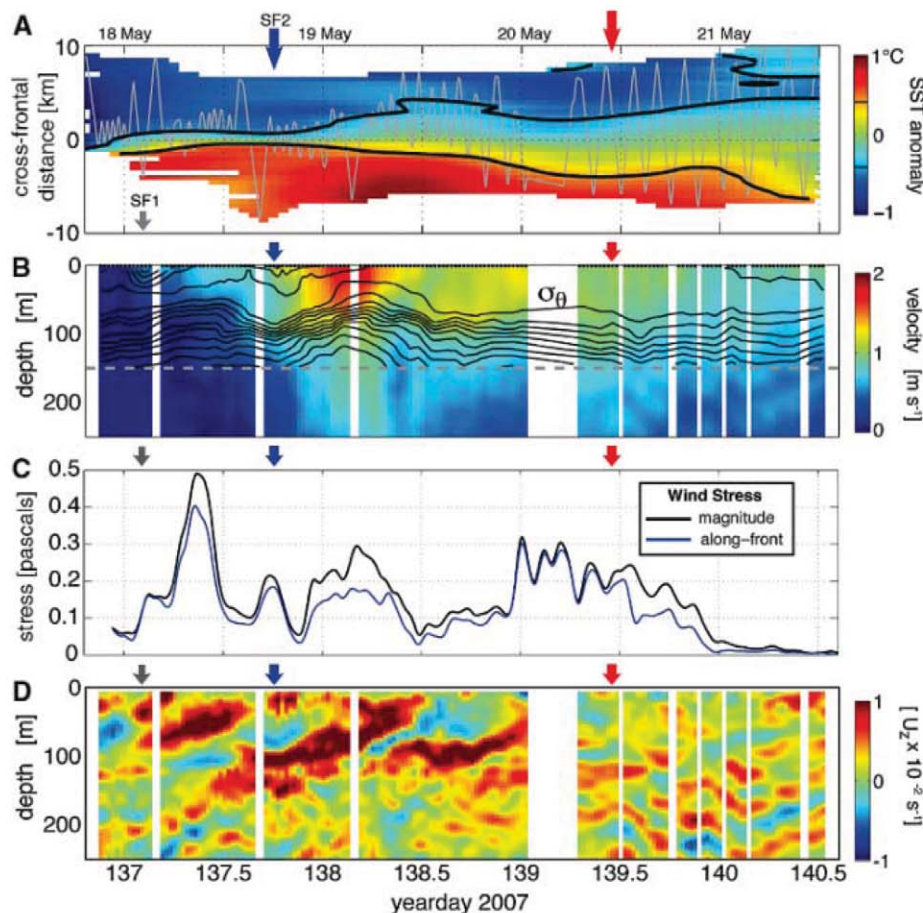


Fig. 2. (A) SST anomaly (relative to SST along the front) from ship surveys plotted relative to float position. Vertical axis is cross-frontal distance. (B) Depth-time section of along-front velocity following the float with potential density contoured at 0.2-kg m^{-3} intervals where available in the upper 150 m. (C) Wind stress (22, 23) magnitude and along-front component in pascals. (D) Vertical shear (U_2) of zonal velocity as a function of depth and time along the front.

profiles and surfacings, the float purposefully moved relative to the water and was thus not Lagrangian. The float sampled the SF during two of the drifts, which will hereafter be called SF1 and SF2. During these drifts, especially SF2, the float was exactly at the front, as indicated by: (i) its track (Fig. 1B), which follows the frontal interface mapped by the Triaxus; (ii) its density (Fig. 3B), which is intermediate between that of the warm and cold sides of the front; and (iii) its location at the maximum in horizontal density gradient (Figs. 1B and 3A). During these drifts, the float repeatedly cycles across the upper-ocean boundary layer (Fig. 3E), tracing the trajectories of boundary-layer water parcels and thus measuring their vertical velocity. Numerous other measurements in both convection (12, 13) and wind-forced boundary layers (14–17) confirm that the vertical motion of these floats is due to upper-ocean turbulence.

Fig. 3. (A) Horizontal buoyancy gradient, proportional to minus the density gradient (represented by color), computed from *R/V Melville's* hull-mounted temperature sensor plotted as a function of time and potential density. The black line denotes the float trajectory, whereas the white line plots the position of maximum buoyancy gradient. (B) Density profiles at SF2 from float (blue) and Triaxus (gray) used in Fig. 1B. Two Triaxus profiles are highlighted (black). (C) Vertical velocity variance from floats (14–17) for wind-forced upper-ocean boundary layers as a function of wind speed. Confidence intervals (95%) were computed as in (14). SF2 lies well above all other data. U_{10} , the wind speed at 10-m height. (D) Time series of boundary-layer-integrated dissipation estimated from the float-acceleration spectrum (black solid circle), float VKE averaged over each float drift (open circles), 1-hour-averaged float VKE (gray line with dashed line interpolating between drifts), EBF computed at float averaged over drifts (red circles), and EBF computed at maximum density gradient (red line, 1.5-hours running average). (E) Float depth during Lagrangian drifts (yellow filled areas) and boundary-layer depth (black bars) estimated as twice the mean float depth.

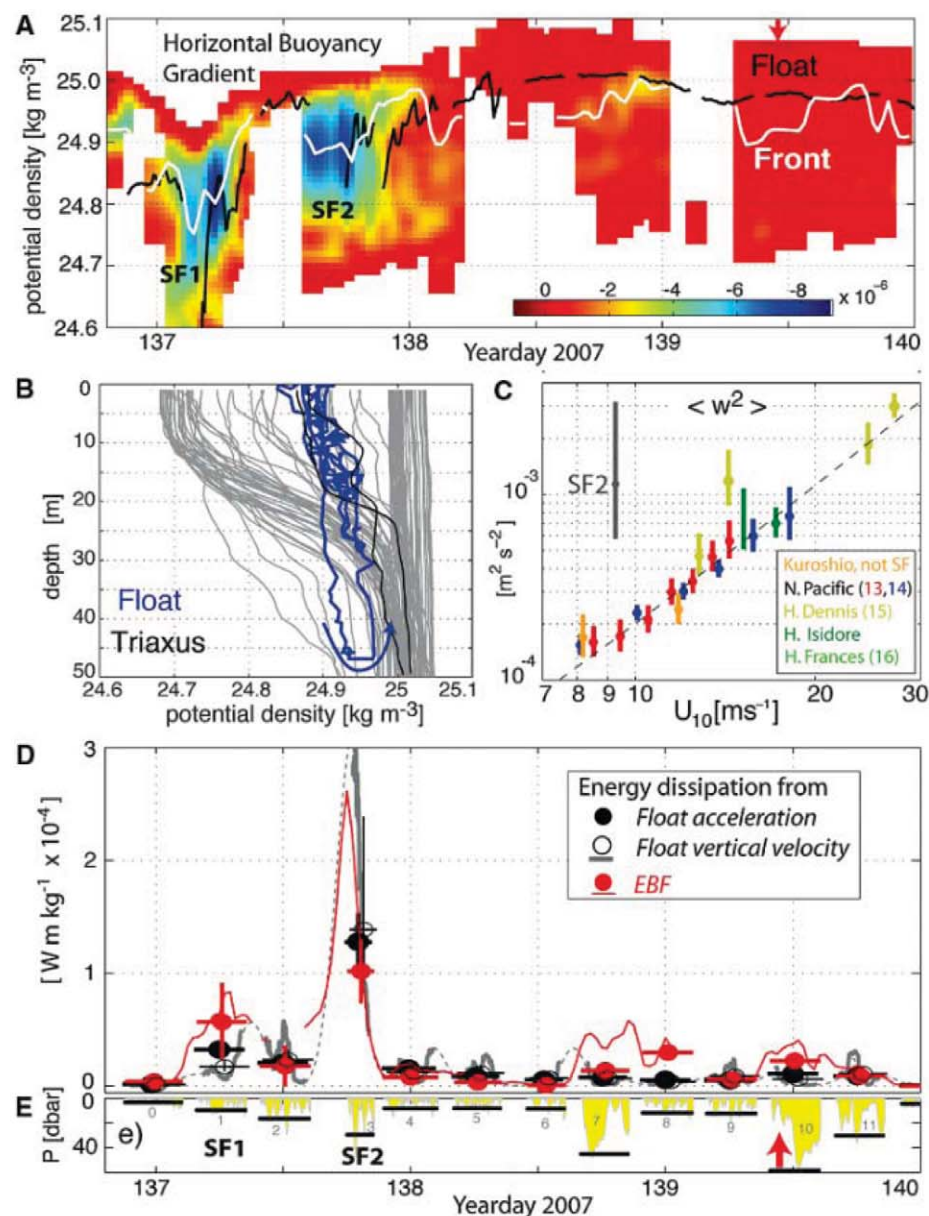
What is the energy source for this turbulence? Numerous float observations of the average vertical kinetic energy (VKE) in the upper-ocean boundary layer show a remarkably good correlation between VKE and the 10-m wind speed (Fig. 3C). This correlation indicates that wind is usually the major source of energy for upper-ocean turbulence (18). However, the VKE during SF2 (gray in Fig. 3C) lies far (a factor 6) above these values, suggesting that wind cannot explain the anomalously high turbulence levels at SF2.

In Fig. 3D, the anomalously high turbulence at SF2 is shown in terms of energy dissipation rate; that is, the flux of energy through the turbulence. The average dissipation in the boundary layer is estimated from the frequency spectra of float vertical acceleration (Fig. 3D, black circles, and fig. S4) (10, 19) and plotted as depth-integrated dissipation by multiplying by the boundary-layer depth (Fig. 3E) (20). Dissipation

rate and energy are closely linked so that a second estimate with higher time resolution can be formed from the VKE (Fig. 3D, solid and dashed gray traces and open circles) (21). The average dissipation at SF2 rises by a factor of ~10 to 20 above the nonfrontal values with the VKE estimate suggesting that even higher values occurred just before the measurements began.

Cooling of the ocean by the atmosphere drives boundary-layer turbulence with an average dissipation rate given by the surface buoyancy flux (12). At SF2, very weak cooling occurs (22, 23), with a buoyancy flux of less than 0.3% of the measured dissipation. Atmospheric cooling cannot explain the anomalously high turbulence levels at SF2.

In summary, SF2 is unremarkable in wind stress (Fig. 2C) or in velocity (Fig. 2B), but is highly anomalous in turbulence level (Fig. 3, C and D) and in lateral gradient (Fig. 2A).



Potential vorticity and frontal instability.

We hypothesize that a flux of energy from the front itself accounts for the enhanced turbulence levels at SF2. The boundary layer at SF2 is stably stratified (Fig. 3B) yet highly sheared in the vertical direction due to the presence of a strong jet along the front (Fig. 2, B and C). This latter condition makes the flow potentially susceptible to symmetric instability (SI) (4), which extracts kinetic energy from the geostrophic frontal jet. The Ertel potential vorticity (PV) (24) is the key quantity for diagnosing this instability; a flow is unstable to SI when the PV is negative (25). PV can become negative due to the combination of a sufficiently strong vertical shear and lateral density gradient and a sufficiently weak vertical density gradient. These conditions can occur within the boundary layer of a strong front, with the front providing the shear and lateral gradient and the boundary layer having a reduced stratification. Simulations (4, 5) indicate that under these conditions SI will grow, become unstable to secondary, smaller-scale instabilities (26), and feed a turbulent cascade to dissipation, resulting in a fully turbulent boundary layer drawing its energy from the front.

We used velocity and density data taken by the ship to evaluate the PV on each of the nearly 100 crossings of the front (fig. S5) (10, 24). We found negative PV near the surface (Fig. 1E) for 0.2 days at SF2 and nowhere else (Fig. 1F). The front at SF2 is therefore unstable to SI, suggesting that the turbulence at SF2 is drawing energy from the frontal shear.

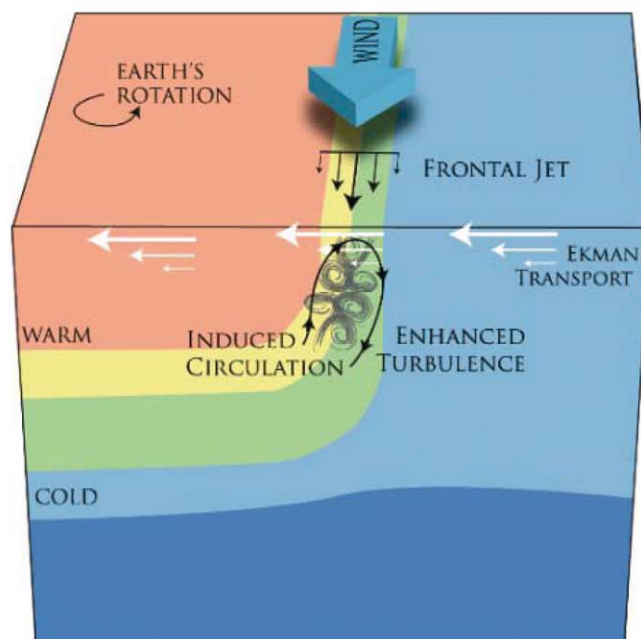
The simulations indicate that SI at a front occurs when the wind blows perpendicular to the frontal gradient (27, 28), which is typically in the direction of the frontal velocity (Fig. 4). Such a

“down-front” wind drives a net transport of water perpendicular to the frontal jet to carry heavy water across the front, from the cold side to the warm side. This Ekman transport advects heavy water over light water, reducing the stratification, and thus reducing the PV and promoting SI. The Ekman buoyancy flux (EBF) (27), computed from the product of the down-front wind stress (Fig. 2C) and the cross-frontal density gradient (Fig. 3A), is a measure of this effect. Simulations (4) suggest that turbulence in a fully developed boundary layer of depth H and driven by down-front winds extracts kinetic energy from the frontal jet at a depth-integrated rate given by $H(EBF)/2$ and dissipates it within the boundary layer. This quantity (29) peaks at SF2 (Fig. 3D, red) with a value comparable to the measured dissipation rate, thus providing quantitative evidence supporting the hypothesis that the boundary layer at SF2 was driven primarily by SI induced by a down-front wind.

The structure of the boundary layer also supports this hypothesis. SI acts to reduce the anomalously negative PV by inducing a circulation that increases the stratification, thereby counteracting the effect of the EBF (Fig. 4). Simulated boundary layers within symmetrically unstable fronts are simultaneously stratified and turbulent (5), in contrast to those outside of fronts, which are generally well mixed. Indeed, the observed density profiles within the front (Fig. 3B) lack mixed layers and are instead stratified at all depths. The Lagrangian float trajectories repeatedly cross this stratification, indicating that the boundary layer at SF2 is both turbulent and stratified (30).

Although SF1 exhibits elevated EBF and dissipation, the thin ($H \approx 10$ m) boundary layer precludes estimating PV and the towed surveys barely cross the front, making EBF errors large.

Fig. 4. Structure of the symmetrically unstable front. A wind blowing down the frontal boundary between warm and cold water induces an Ekman transport perpendicular to the wind and to the front. This carries heavy water from the cold side of the front over light water from the warm side, which, in the presence of the frontal jet and lateral density gradient, acts to reduce the stratification near the surface and makes the front unstable to symmetric instability. The instability draws energy from the frontal jet, leading to enhanced turbulence, and induces a circulation acting to bring warm water to the surface and cold water to depth, thus counteracting the effect of the Ekman transport and keeping the near-surface stably stratified, with warm water over cold water.



An accurate evaluation of the hypothesis is not possible at SF1.

Near-inertial frequency waves. Sections of velocity and shear (Fig. 2, B and D) show that the above frontal processes are associated with deeper structures suggestive of internal waves. In particular, the depth-time section of shear (Fig. 2D) shows alternating diagonal stripes of positive and negative shear with upward phase propagation and a period close to the local inertial period (i.e., half a pendulum day: 0.84 days at this latitude). The north-south component of shear (not shown in Fig. 2) is in quadrature with the east-west component such that the velocity vector rotates clockwise with approximately constant magnitude as a function of both increasing depth and increasing time. This pattern is widely found in the ocean and interpreted as the signature of downward propagating near-inertial frequency internal waves (31). Given the observed stratification and estimating the vertical wavelength and period of the waves to be 200 m and 0.78 days, respectively (based on a least-squares fit on the shear field of the upper 150 m and first 2 days), theory predicts that the waves' downward energy flux is ~ 6 mW/m², which is similar to an estimate for the energy input to near-inertial waves from the winds of 9 mW/m² (32), but only about 6% of the excess turbulent dissipation at the SF2. These calculations suggest that the waves are probably driven by the winds and minimally contribute to the energetics of the turbulence within the boundary layer at the front.

Surprisingly, however, the strong near-surface shear of the sharpest front appears to be part of the deeper near-inertial pattern. The boundary-layer depth (Fig. 3E) also appears to have variability on roughly the same time scale; that is, the increased depth at days 138.7 and 139.6. Thus, it is possible that these inertial motions could play a role in the rapid confluence and diffluence that generate and dissipate the SF, as well as in producing its negative PV. We further speculate that the SI at the front could feed energy into the inertial waves and thus radiate energy into the ocean interior. Because the lateral scale of the near-inertial motions is probably much larger than that of the SF, their overall role in the SF energetics could be substantially larger than that implied by the small local flux density.

Implications. Traditionally, the upper-ocean boundary layer is thought to be driven by the atmosphere through fluxes of heat, moisture, and momentum (33, 34). The observations presented here break from this paradigm by suggesting that lateral density gradients and their geostrophic currents can also play a role in boundary-layer dynamics by supplying energy to turbulence at the expense of the circulation and permitting stratification and turbulence to coexist. Therefore, the greatly enhanced boundary-layer turbulence and dissipation described here in a very sharp Kuroshio front is likely an extreme example of a process that occurs much more widely in the ocean, potentially playing an important role in its dynamics

and energetics. Furthermore, these results are consistent with recent theory on submesoscale processes and thus encourage incorporation of this theory into boundary-layer models. Such physics is not accounted for in present-day climate models. Fronts associated with the Kuroshio, Gulf Stream, and Antarctic Circumpolar Current are key players in the ocean-atmosphere climate system. Inaccurate representation of the boundary layer and flow energetics in frontal regions could thus substantially affect the predictive skill of climate models.

References and Notes

- R. Ferrari, C. Wunsch, *Annu. Rev. Fluid Mech.* **41**, 253 (2009).
- X. Capet, J. C. McWilliams, M. J. Molemaker, A. F. Schepetkin, *J. Phys. Oceanogr.* **38**, 2256 (2008).
- J. Molemaker, J. C. McWilliams, X. Capet, *J. Fluid Mech.* **654**, 35 (2010).
- L. N. Thomas, J. R. Taylor, *Geophys. Res. Lett.* **37**, L18606 (2010).
- J. R. Taylor, R. Ferrari, *J. Phys. Oceanogr.* **40**, 1222 (2010).
- C. L. Sabine et al., *Science* **305**, 367 (2004).
- D. Marshall, *J. Mar. Res.* **55**, 201 (1997).
- The altimeter products were produced by Ssalto/Duacs (Segment Sol Multimissions d'Altimétrie, d'Orbitographie et de Localisation Précise/Data Unification and Altimeter Combination System) and distributed by Aviso (Archiving, Validation and Interpretation of Satellite Oceanographic Data), with support from the Centre National d'Etudes Spatiales (www.aviso.oceanobs.com/).
- E. A. D'Asaro, *J. Atmos. Ocean. Technol.* **20**, 896 (2002).
- See supporting online material for details of instrumentation and calculations.
- Temperature measured continuously on the ship's hull shows a SF that is ~500 m wide, substantially smaller than the sampling scale of the Triaxus towed profiler. Triaxus data show a tight linear relation between potential temperature and potential density in the upper 10 m so that potential density can be accurately predicted from potential temperature (fig. S6A) (10).
- E. L. Steffen, E. A. D'Asaro, *J. Phys. Oceanogr.* **32**, 475 (2002).
- R. R. Harcourt, E. L. Steffen, R. W. Garwood, E. A. D'Asaro, *J. Phys. Oceanogr.* **32**, 493 (2002).
- E. A. D'Asaro, *J. Phys. Oceanogr.* **31**, 3530 (2001).
- R. Tseng, E. A. D'Asaro, *J. Phys. Oceanogr.* **34**, 1984 (2004).
- E. A. D'Asaro, *J. Phys. Oceanogr.* **33**, 561 (2003).
- E. A. D'Asaro, C. McNeil, *J. Mar. Syst.* **66**, 92 (2007).
- For deep mixed layers, not shown in Fig. 3C, surface buoyancy flux can control the turbulence (12).
- R.-C. Lien, E. D'Asaro, G. Dairiki, *J. Fluid Mech.* **362**, 177 (1998).
- Boundary layer depth is computed as twice the mean depth of the float. This will be exactly true for a float whose depth is uniformly distributed across the boundary layer.
- The kinetic energy in the boundary layer will be $\sim 1.5H\langle w^2 \rangle$, where H is the boundary-layer depth, w is vertical velocity, and isotropic turbulence is assumed. This energy will dissipate in an eddy overturning time at approximately $H/\langle w^2 \rangle^{1/2}$, thus predicting a depth-integrated dissipation rate of $1.5\langle w^2 \rangle^{1.5}$. Figure 3D shows a plot of $3\langle w^2 \rangle^{1.5}$. The constant 3 was chosen to best fit the dissipation estimates from acceleration. The difference could easily be due to the expected anisotropy of the boundary-layer turbulence and exact overturning time. The constant could vary with the boundary-layer dynamics; this analysis does not account for this possibility.
- We computed surface fluxes of momentum, heat, and buoyancy from the IMET, Improved Meteorology measurements on the *R/V Melville* using the TOGA/COARE algorithms as implemented in the MATLAB air-sea toolbox (23). This results in estimates of the wind stress $\tau = \rho u_*^2$ (where ρ is air density, and u_* is the friction velocity) and the buoyancy flux J_b .
- C. W. Fairall, E. F. Bradley, D. P. Rogers, J. B. Edson, G. S. Young, *J. Geophys. Res.* **101**, 3747 (1996).
- The Ertel PV is defined as $Q = \omega_a \cdot \nabla b$, the dot product of the absolute vorticity $\omega_a = f\hat{k} + \zeta$ and the gradient of buoyancy $b = -gp/\rho_0$. The coordinates are (x, y, z) for the along-front (east), cross-front (north), and up directions with associated velocity components (u, v, w) . The Coriolis parameter is f , gravity's acceleration is g , potential density is ρ , ρ_0 is a reference density, and ζ is the relative vorticity $\nabla \times \vec{u}$. Computationally, the vertical vorticity is estimated as $\zeta_z = -\partial u/\partial y$ and the cross-front component of vorticity as $\zeta_y = \partial u/\partial z$. The PV can be split into two parts: $Q = Q_V + Q_H$, where $Q_V = (f - \partial u/\partial y)\partial b/\partial z$ and $Q_H = (\partial u/\partial z)\partial b/\partial y$. A geostrophic flow is symmetrically unstable when its PV is negative and $Q_V > 0$.
- T. W. N. Haine, J. Marshall, *J. Phys. Oceanogr.* **28**, 634 (1998).
- J. R. Taylor, R. Ferrari, *J. Fluid Mech.* **622**, 103 (2009).
- More accurately, down-front winds are defined as winds that induce a positive wind-driven buoyancy flux: $EBF = \rho_0^{-1} \vec{\tau}_w \cdot \partial \vec{u}_0/\partial z$, where $\vec{\tau}_w$ is the wind stress and $\partial \vec{u}_0/\partial z = f^{-1} \hat{k} \times \nabla b$ is the geostrophic shear. Thus, down-front winds have a component along the geostrophic shear.
- L. N. Thomas, *J. Phys. Oceanogr.* **35**, 2457 (2005).
- EBF and its statistical error are computed using a density gradient derived from temperature measured on the ship's hull (figs. S6 and S7) (10). Error estimates are dominated by the variance of the temperature observations on either side of the front, the uncertainty in the float position, and the uncertainty of the wind direction.
- Three different measures of stratification—(i) the vertical density gradient measured from the Triaxus profiles (gray in Fig. 3B), (ii) the vertical density gradient from the float trajectories (blue in Fig. 3B), and (iii) the mean difference between CTDs on the top and bottom of the float (not shown in Fig. 3)—all indicate that the stratification is stable. Comparison of the two highlighted Triaxus profiles (black in Fig. 3B) with the float profile shows that although the deeper parts of the float profile differ from the mean Triaxus profile, some Triaxus profiles have a similar structure to that seen by the float.
- K. D. Leaman, T. B. Sanford, *J. Geophys. Res.* **80**, 1975 (1975).
- A simple slab model (35) with no damping and a 25-m-deep layer gains inertial energy at a rate of $\sim 9 \text{ mW/m}^2$ between days 135.5 and 137.5, mostly due to wind bursts near days 136.3 and 137.3. This is sufficient to drive the observed near-inertial energy flux, although the complexities of near-inertial wave generation and propagation in a frontal region such as this (36) make a more exact analysis difficult to conduct.
- Velocity differences across the bottom of the mixed layer also play an important role, but these are mostly driven by local winds (34).
- J. F. Price, R. A. Weller, R. Pinkel, *J. Geophys. Res.* **91**, 8411 (1986).
- E. A. D'Asaro, *J. Phys. Oceanogr.* **15**, 1043 (1985).
- E. Kunze, *J. Phys. Oceanogr.* **15**, 544 (1985).
- New Generation Sea Surface Temperature Development Group, Tohoku University, Sendai, Japan; www.ocean.caos.tohoku.ac.jp/.

Acknowledgments: This work was supported by the Office of Naval Research as part of the Assessing the Effects of Submesoscale Ocean Parameterizations program (grants N00014-05-1-0329/30/31, N00014-08-1-0445/10446/10447, and N00014-09-1-0202). This work would not have been possible without the efforts of staff at the Integrated Observations Group, the Ocean Engineering Department at the University of Washington Applied Physics Laboratory, and the crew and officers of the *R/V Melville*.

Supporting Online Material

www.sciencemag.org/cgi/content/full/science.1201515/DC1
SOM Text
Figs. S1 to S7
References

10 December 2010; accepted 1 March 2011
Published online 10 March 2011;
10.1126/science.1201515

Structure of an Agonist-Bound Human A_{2A} Adenosine Receptor

Fei Xu,¹ Huixian Wu,¹ Vsevolod Katritch,² Gye Won Han,¹ Kenneth A. Jacobson,³ Zhan-Guo Gao,³ Vadim Cherezov,¹ Raymond C. Stevens^{1*}

Activation of G protein-coupled receptors upon agonist binding is a critical step in the signaling cascade for this family of cell surface proteins. We report the crystal structure of the A_{2A} adenosine receptor (A_{2A}AR) bound to an agonist UK-432097 at 2.7 angstrom resolution. Relative to inactive, antagonist-bound A_{2A}AR, the agonist-bound structure displays an outward tilt and rotation of the cytoplasmic half of helix VI, a movement of helix V, and an axial shift of helix III, resembling the changes associated with the active-state opsin structure. Additionally, a seesaw movement of helix VII and a shift of extracellular loop 3 are likely specific to A_{2A}AR and its ligand. The results define the molecule UK-432097 as a "conformationally selective agonist" capable of receptor stabilization in a specific active-state configuration.

G protein-coupled receptors (GPCRs) are critical cellular signal transduction gatekeepers for eukaryotic organisms. Some

GPCRs are activated by ligands that act as agonists; others are inactivated by inverse agonists and antagonists. Efforts to elucidate the crystal

structures of GPCRs bound to diffusible ligands have recently yielded structures for five class A (rhodopsin-like) GPCRs: the β_2 (1–7) and β_1 (8, 9) adrenergic receptors (β_2 AR and β_1 AR), the A_{2A} adenosine receptor (A_{2A}AR) (10), the CXCR4 chemokine receptor (11), and the D3 dopamine receptor (12). All of these structures display a common seven-transmembrane (7TM) topology for GPCRs, as well as substantial variations in functionally divergent regions—especially on the extracellular side of the receptor, which is responsible for the recognition of a vast variety of

¹Department of Molecular Biology, Scripps Research Institute, 10550 North Torrey Pines Road, La Jolla, CA 92037, USA.

²Skaggs School of Pharmacy and Pharmaceutical Sciences and San Diego Supercomputer Center, University of California, San Diego, La Jolla, CA 92093, USA. ³Laboratory of Bioorganic Chemistry, National Institute of Diabetes and Digestive and Kidney Diseases, Bethesda, MD 20892, USA.

*To whom correspondence should be addressed. E-mail: stevens@scripps.edu

ligands. To overcome the challenge of crystallizing highly dynamic receptors, each of these recent studies used GPCRs that were engineered by fusions or mutations to increase their stability and were cocrystallized with stabilizing ligands.

The mechanism of GPCR activation by native ligands (or synthetic agonists), however, is a fundamental question that remains largely unsolved. An initial model for GPCR activation was provided by the crystal structures of retinal-free opsin (13, 14), but the absence of any agonist precludes direct generalization of this result to other GPCRs activated by diffusible ligands. To shed light on the mechanism of ligand-induced GPCR activation, we have determined a 2.7 Å crystal structure of the human A_{2A} AR in complex with the A_{2A} AR agonist 2-(3-[1-(pyridin-2-yl)piperidin-4-yl]ureido)ethyl-6-*N*-(2,2-diphenylethyl)-5'-*N*-ethylcarboxamido-adenosine-2-carboxamide (UK-432097). This highly potent and selective agonist, which was developed as a drug candidate for chronic obstructive pulmonary disease (COPD) treatment (15), represents a substituted derivative of the native ligand adenosine and a series of other prototypical adenosine receptor agonists such as NECA, CGS21680, ATL-146e, and CI-936 (16–18). The availability of both agonist- and antagonist-bound A_{2A} AR structures

now provides the opportunity to resolve the basic question of how ligand binding at the extracellular side of the receptor triggers conformational changes at the intracellular side, where G protein and other effectors bind and initiate the cascade of downstream signaling pathways.

Agonist UK-432097 and its binding cavity. The compound UK-432097 was characterized as a full A_{2A} AR agonist (19–21) (figs. S1 and S2), and its structure in complex with engineered human A_{2A} AR (A_{2A} AR-T4L-ΔC) was determined similarly to that of A_{2A} AR-T4L-ΔC bound to the antagonist ZM241385 at 2.7 Å resolution (10, 22) (table S1). UK-432097 (778 daltons) is more than twice as large as ZM241385 and occupies most of the A_{2A} AR ligand-binding cavity (Fig. 1A and fig. S3). The ligand-binding cavity reveals an extensive ligand-receptor interaction network, including 11 hydrogen bonds, one aromatic stacking interaction, and a number of non-polar (van der Waals) interactions (Fig. 1B and table S2). These interactions explain the high binding affinity and subtype selectivity of this compound and its strong stabilizing effect on A_{2A} AR (table S3).

The bicyclic adenine core of UK-432097 is a common scaffold and is present in nearly all major types of adenosine receptor agonists (e.g.,

NECA, CGS21680, and other nucleosides) and many antagonists (23). This moiety aligns to the triazotriazine core of ZM241385 when the two complex structures are superimposed together (Fig. 1A), as predicted in modeling studies (24, 25). The molecular interactions that anchor ZM241385 in this region are also conserved in the UK-432097 binding cavity, including aromatic stacking with Phe168 in extracellular loop 2 (ECL2), nonpolar interaction with Ile274^{7,39}, and two hydrogen bonds with Asn253^{6,55} (26, 27) (Fig. 1C). Disrupting effects on both agonist and antagonist binding are observed upon mutation of these residues: Phe168 (moderate decrease), Ile274^{7,39} (major decrease), or Asn253^{6,55} (complete loss) (25, 28).

The ribose ring is a key feature of almost all known adenosine receptor agonists that differentiates them from corresponding antagonists. In the A_{2A} AR-UK-432097 complex, the ribose moiety of the ligand inserts deeply into a predominantly hydrophilic region of the binding cavity (Fig. 1), with the 2' and 3' -OH groups both making hydrogen bonds with His278^{7,43} (2.8 Å and 3.1 Å, table S2). The 3' -OH is further anchored by a hydrogen-bonding interaction with Ser277^{7,42} (3.0 Å) (Fig. 1D). Mutation of these two residues to alanine abolishes high-affinity binding of A_{2A} AR agonists (28). His250^{6,52} forms a

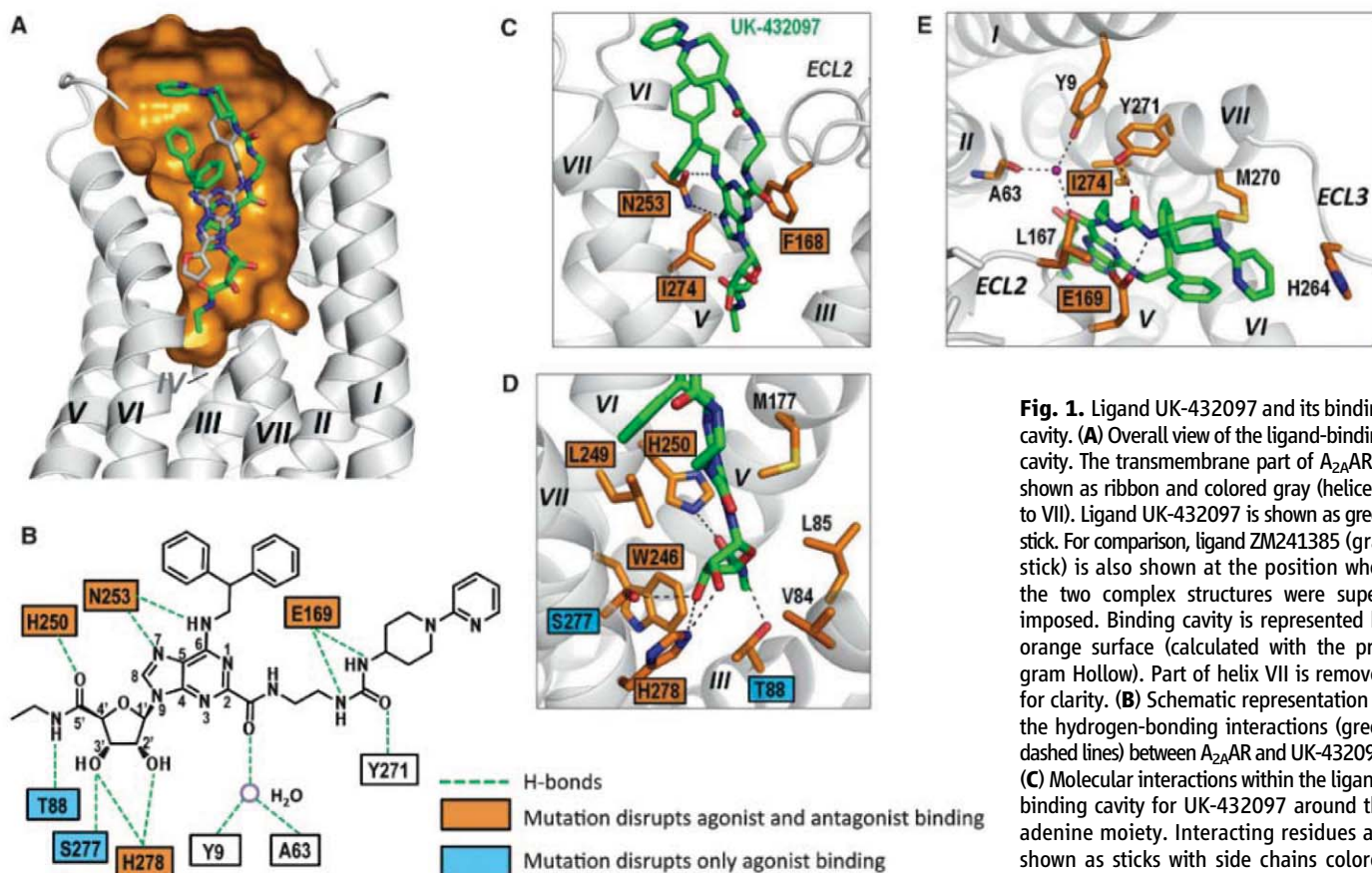


Fig. 1. Ligand UK-432097 and its binding cavity. (A) Overall view of the ligand-binding cavity. The transmembrane part of A_{2A} AR is shown as ribbon and colored gray (helices I to VII). Ligand UK-432097 is shown as green stick. For comparison, ligand ZM241385 (gray stick) is also shown at the position when the two complex structures were superimposed. Binding cavity is represented by orange surface (calculated with the program Hollow). Part of helix VII is removed for clarity. (B) Schematic representation of the hydrogen-bonding interactions (green dashed lines) between A_{2A} AR and UK-432097. (C) Molecular interactions within the ligand-binding cavity for UK-432097 around the adenine moiety. Interacting residues are shown as sticks with side chains colored orange. Hydrogen bonds between A_{2A} AR and ligand are shown as black dotted lines. (D) Molecular interactions around the ribose moiety. (E) Molecular interactions around the ligand substitution sites. A water molecule is shown as a purple sphere. In (B) to (E), residue mutations reported to disrupt agonist and antagonist binding are indicated with orange squares; residue mutations disrupting only agonist binding are indicated with cyan squares. The images were created with PyMOL.

hydrogen-bonding interaction with the carbonyl O4 (3.1 Å) that was not predicted in agonist docking to inactive states of the adenosine receptors. Mutation to alanine or phenylalanine disrupts agonist binding, indicating this residue is important for agonist recognition (29). The ribose 5'-*N*-ethyluronamide substitution in UK-432097, as well as in NECA and many other adenosine receptor agonist chemotypes, is known to provide additional potency. The N2 of this moiety makes a hydrogen bond with Thr88^{3,36} (3.0 Å), in accord with reduction in binding observed for the T88A mutant of A_{2A}AR (30). Besides these polar interactions, the ribose part of the ligand has close contacts with Val84^{3,32}, Leu85^{3,33}, Trp246^{6,48}, Met177^{5,38}, and Leu249^{6,51}. Previous mutagenesis data on V84A or L249A suggested that these nonpolar interactions are essential for agonist binding (25, 29).

The bulky 2-(3-[1-(pyridin-2-yl)piperidin-4-yl]ureido)ethylcarboxamido substitution in UK-432097 is located at the adenine C2 position; similar extended chains are found in many of the selective A_{2A}AR agonists under development (15). The carboxamide moiety forms an indirect water-mediated hydrogen bond with Tyr9^{1,35} and the carbonyl group of Ala63^{2,61}, which contributes to a closer contact of the ligand with helices I and II (Fig. 1E). The urea group is coordinated on both sides by Glu169 (ECL2) forming two hydrogen bonds at N8 and N9 positions (2.8 Å and 2.7 Å) and Tyr271^{7,36} forming one hydrogen bond at O6 (2.7 Å). Finally, the pyridinyl-piperidine moiety leans to the two phenyl rings and bulges toward helix VII and ECL3. This combined moiety might impose an allosteric effect on structural and conformational changes of the receptor and contribute to subtype binding selectivity (18, 31–33).

Antagonist-bound to agonist-bound transformations in A_{2A}AR. A comparison of the A_{2A}AR complexes with antagonist ZM241385 and agonist UK-432097 shows that although the core adenine interactions are conserved between the two structures, binding of the agonist UK-432097 triggers a series of conformational changes within the binding cavity of A_{2A}AR (Fig. 2). Importantly, some of these modest local changes promote large-scale rearrangements in the 7TM helical bundle (Fig. 3). The specific molecular interactions with the ribose moiety of UK-432097 are likely a common feature for all A_{2A}AR agonists, with motions of the ribose-coordinating residues related to the receptor activation. In helix VI, for example, His250^{6,52} moves ~1.8 Å inward to a position that would otherwise clash with the furan ring of ZM241385 and forms a hydrogen bond with the carbonyl group (Fig. 1D and Fig. 2A). The conserved Trp246^{6,48} indole moves ~1.9 Å to avoid a steric clash with the ribose ring of the agonist, a movement that facilitates rotation and tilt of the intracellular side of helix VI below Pro248^{6,50}. Although helix V residues Met177^{5,38}, Asn181^{5,42}, and Val186^{5,47} make only limited nonpolar contacts with the agonist, the movement of His250^{6,52} allows an inward shift of Val186^{5,47},

promoting an inward tilt of the whole intracellular side of helix V (Fig. 2A).

In helix VII, Ser277^{7,42} and His278^{7,43} move about 2 Å closer to helix III and together with the side chain of Thr88^{3,36} form a hydrogen-bonding network coordinating the ribose moiety (Fig. 1D and Fig. 2A). Two residues on the extracellular end of helix VII, Leu267^{7,32} and Met270^{7,35}, form additional nonpolar interactions with the two phenyl rings and piperidine rings of UK-432097, resulting in an outward movement of these two residues along with the extracellular part of helix VII by about 2 Å (Fig. 2B). The motion of the helix VII apex correlates with an even more pronounced (3 to 4 Å) outward movement of the adjacent ECL3 backbone, where the His264 imidazole swings by 100° from beneath the pyridine ring to the top of the ligand-binding cavity (Fig. 2B). Also, Glu169 (ECL2) has a different rotamer conformation than in the A_{2A}AR-ZM241385 structure, where its carboxylic group forms a hydrogen bond with the exocyclic amine of ZM241385. Because of a substitution in the exocyclic amino group of UK-432097, the Glu169 carboxyl group moves about 4 Å to form hydrogen bonds with the urea substituent instead, coordinating both the urea group and the two phenyl rings in position. The latter two changes in ECL3 and ECL2 largely depend on substituted moieties in the agonist and are likely to be specific for UK-432097 or agonists with similar bulky substitutions.

In helix III, coordination of the ribose ring through hydrogen bonding interaction with Thr88^{3,36} side chain, as well as nonpolar contacts with Val84^{3,32} and Leu85^{3,33}, requires a ~2 Å shift of these residues, resulting in an upward shift of the entire helix III along the helical axis (Fig. 2A and Fig. 3A).

Comparison of this A_{2A}AR-agonist complex structure to its antagonist-bound form shows that helices I to IV form a stable helical bundle “core”

with minimal structural changes, while helices V to VII undergo substantial conformational changes (34). The movements are illustrated in Fig. 3, A to D, by graphical superimposition of the two protein conformations (using C α atoms of TM helices), as well as by plotting full residue RMSDs (root mean square deviations; shown on *y* axis) and deviations of C α atoms (shown by color) for individual residues in Fig. 3E. This “RMSD fingerprint” representation conveniently differentiates side-chain rotameric switches (green-blue outliers, marked by residue labels) and global motions of helices (clusters of yellow-red dots).

One of the most prominent changes associated with the agonist-bound structure involves coordinated movements of the intracellular parts of helices VI and V. While the extracellular part of helix VI is fixed in place by the key interactions of Asn253^{6,55} with the exocyclic amino group of UK-432097, the agonist-induced shift of the conserved Trp246^{6,48} promotes an outward tilt of the intracellular part of helix VI by about 3 to 4 Å and clockwise rotation by about 30° (Fig. 3). The shift of helix VI is accompanied by coordinated rotameric switches in Phe201^{5,62} and Tyr197^{5,58} side chains. Whereas in A_{2A}AR-ZM241385 the conserved Tyr197^{5,58} is placed in the middle of the helical bundle between helices III and VI, in the UK-432097-bound form this residue moves outward allowing helix V shift toward helix VI. As a result of this combined tilt, the intracellular ends of helices V and VI move closer together in the A_{2A}AR-UK-432097 structure (~6 Å) as compared to the A_{2A}AR-ZM241385 structure (~8 Å) (Fig. 3D).

Another response to the binding of the agonist UK-432097 is a seesaw-like movement of helix VII around the ribose ring. While interactions of the ribose ring hydroxyls with Ser277^{7,42} and His278^{7,43} pull these residues of helix VII inward, strong clashes of the two phenyl rings with

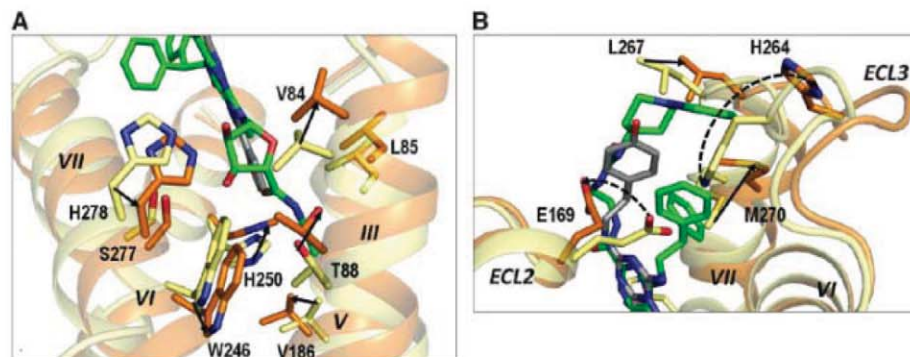


Fig. 2. Ligand-binding cavity comparison between A_{2A}AR-UK-432097 and A_{2A}AR-ZM241385 complexes. Two receptors were superimposed using C α atoms of the TM helices. UK-432097-bound A_{2A}AR is colored orange (ribbon) with ligand in green (stick); ZM241385-bound A_{2A}AR (PDB ID 3EML) is colored yellow (ribbon) with ligand in gray (stick). **(A)** Comparison of the binding pocket around the ligand ribose moiety. Deviating residues (with either backbone or side-chain movement) are shown as sticks. The direction of movement is indicated by black arrows. For clarity, only helices III, VI, VII, and part of helix V are shown. **(B)** Binding pocket comparison around the substitution part of the ligand. Prominent rotameric switches of Glu169 and His264 on ECL2 and ECL3, respectively, are indicated by dotted black arrows. The images were created with PyMOL.

Leu267^{7,32}, Met270^{7,35}, Tyr271^{7,36}, and ECL3 residues push the extracellular part of helix VII outward, creating a lever that promotes a tilt of helix VII. The conserved NPxxY motif composed of Asn284^{7,49}, Pro285^{7,50}, Phe286^{7,51}, Ile287^{7,52}, and Tyr288^{7,53} at the cytoplasmic end of helix VII shifts as much as 4 to 5 Å inward, resulting in reorganizations of these side chains, especially Tyr288^{7,53} (Fig. 3; see also Fig. 4, A and C).

Insight into a GPCR activation mechanism.

The conformational changes observed between the A_{2A}AR-agonist and A_{2A}AR-antagonist complexes can be further understood in the context of comparison with the structural transitions in the light-activated rhodopsin-opsin system (13, 14). Unliganded opsin at low pH adopts a conformation similar to light-activated rhodopsin at physiological pH (35). Concomitant structural

transitions between the inactive rhodopsin and active-like opsin include side-chain switches in the conserved D[E]RY and NPxxY motifs and rearrangements of helices V to VII. Structural superimposition, along with “RMSD fingerprints” of individual residues, between the two pairs of models (inactive and active A_{2A}AR structures; rhodopsin and opsin structures) reveals considerable similarity attributed to a general GPCR activation mechanism (Fig. 4).

The RMSD fingerprint plots shown in Fig. 4D for both inactive-active pairs (A_{2A}AR antagonist–A_{2A}AR agonist; rhodopsin–opsin) of TM domains illustrate similarities between the conformational transitions in these two different receptor systems. For example, a similar pattern is observed of very low deviations in helices I, II, and IV, and of elevated backbone deviations in helices III, V, and VI

[correlation coefficient (R^2) between two sets of RMSDs: $R^2 = 0.64$ for helices I to VI, $R^2 = 0.84$ for helix VI alone]. In contrast, the plot suggests a lack of similarity in helix VII ($R^2 = 0.25$ for helix VII alone).

The predominant feature common between opsin and A_{2A}AR is the overall movement of helices V and VI, with their extracellular parts being the least mobile and intracellular parts deviating markedly. The conserved Trp^{6,48} is an important residue triggering the motion of helix VI during activation in A_{2A}AR; however, contrary to the previous “toggle switch” model, this residue does not undergo a rotamer transition, but rather moves along with the backbone in both opsin and A_{2A}AR. The overall backbone shifts in both opsin and A_{2A}AR are accompanied by rotameric switches of Tyr^{5,58}; however, the observed changes in this residue upon activation are very different: Whereas in opsin this side chain swings from outside toward the axis of the TM bundle, the movement in A_{2A}AR is the opposite (36). Also, rotameric changes in nonconserved rhodopsin side chains Phe^{5,55} and Phe^{5,43} were not observed in the same positions of Leu^{5,55} and Phe^{5,43} in A_{2A}AR.

Another characteristic molecular switch in the rhodopsin-opsin activation model is a salt bridge (“ionic lock”) between Arg^{3,50} of the conserved D[E]RY motif in helix III and Glu^{6,30} in helix VI. The ionic lock breaks in opsin upon activation, resulting in rotameric changes in Glu^{6,30} and movement of helix VI away from helix III (Fig. 4A). Although the ionic lock is already broken in the A_{2A}AR-antagonist structure (10), the concerted movements of helices III and VI observed in the A_{2A}AR–UK-432097 complex also pull Arg102^{3,50} and Glu228^{6,30} farther apart, precluding any potential interactions between these residues. A noteworthy difference in this region is that while in our A_{2A}AR-agonist complex structure the middle segment of the cytoplasmic half of helix VI bulges outward by ~3 to 4 Å, the movement of the intracellular tip of helix VI is not as pronounced as in opsin (~3 Å versus 6 to 7 Å, Fig. 4A). However, such partial “attenuation” of the outward tilt of helix VI in this structure may be attributed to the fused T4 lysozyme (T4L), which is likely to limit mobility of the cytoplasmic ends of helices V and VI.

A third featured transition that may be related to activation is a movement of helix III, sliding along its axis toward the extracellular side by ~2 Å, in the context of the overall well-preserved bundle “core” of helices I to IV (37). This movement can be found in both the rhodopsin-opsin and A_{2A}AR systems; in the case of the A_{2A}AR–UK-432097 complex, it allows formation of new contacts with the ribose ring of the agonist.

Conformational changes in helix VII also reveal both common and distinct features for A_{2A}AR and rhodopsin-opsin (Fig. 4). One common feature is a large-scale (>5 Å) movement and rotameric switch of the Tyr^{7,53} side chain in the highly conserved NPxxY motif at the intra-

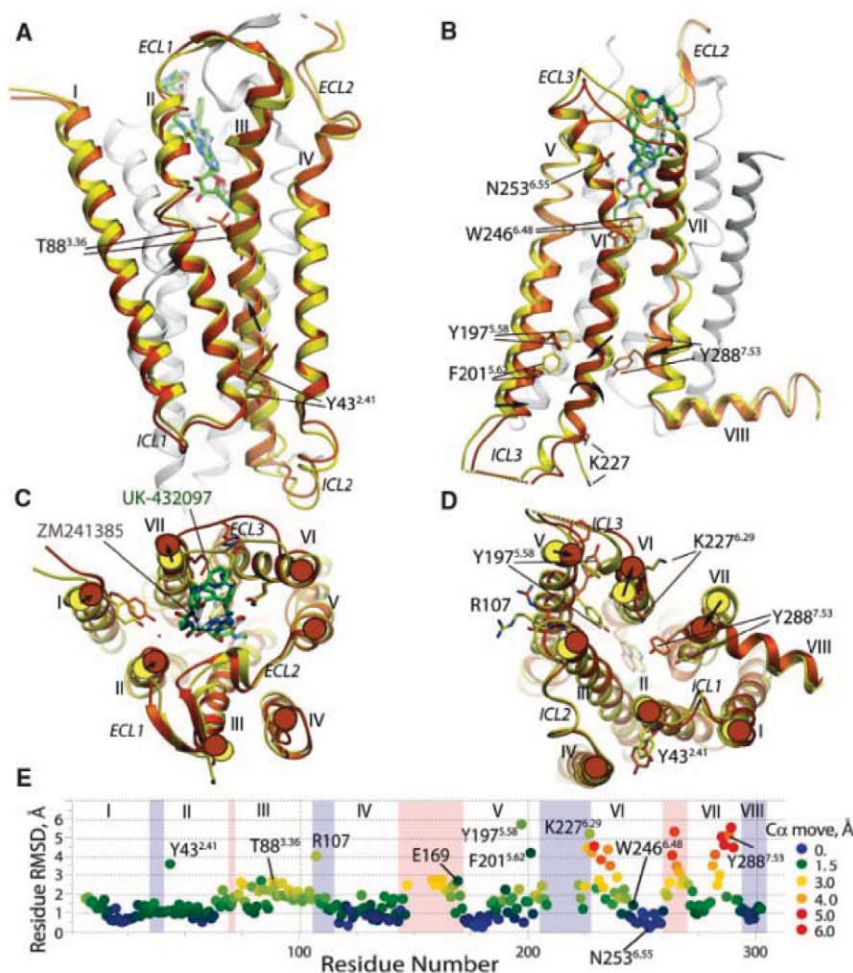
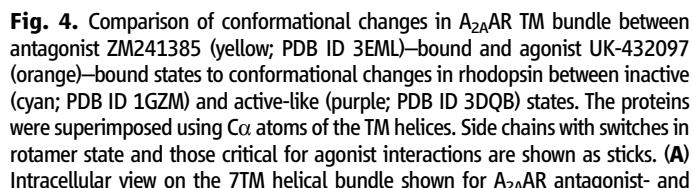


Fig. 3. Analysis of conformational variations between the A_{2A}AR–UK-432097 complex (orange) and the A_{2A}AR–ZM241385 complex (yellow; PDB ID 3EML). Two protein conformations were superimposed using Cα atoms of the TM helices. Heavy-atom RMSDs were calculated for each residue of the receptor. (A) Side view of helices I to IV. (B) Side view of helices V to VIII. (C) Extracellular (top) view. (D) Intracellular (bottom) view. Most pronounced global changes in the TM helices are shown by black arrows. Side chains that change rotamer conformation are shown as sticks. (E) Plot showing individual residue deviations between superimposed A_{2A}AR conformations, where each residue dot is also colored by deviation of its Cα atom (blue-green dots with high RMSD thus represent residues with rotameric switches). Regions of intracellular loops and helix VIII in the plot are shaded blue; the extracellular loops are shaded pink. The images were created with ICM software (Molsoft LLC). Movie S1 is an animated version of this figure.



agonist-bound states (left) and for inactive rhodopsin and active-like opsin (right). **(B)** Comparison of movements in helices V and VI of A_{2A}AR (yellow/orange) and rhodopsin (cyan/purple). **(C)** Same for movements in helix VII. **(D)** Plot compares individual residue deviations in the 7TM bundle for A_{2A}AR and rhodopsin GPCRs; each residue dot is also colored by deviation of its C α atom. Intracellular loops and helix VIII regions are shaded blue; extracellular loops are shaded pink. The images were created with ICM software (Molsoft LLC).

cellular tip of helix VII. In the A_{2A}AR-agonist structure, however, the Tyr288^{7,53} movement is coordinated by a rigid body tilt of helix VII, so that the C α atoms in this region move more than 5 Å. Conversely, in opsin the backbone of helix VII does not move overall, whereas movement of

Tyr^{7.53} is achieved via local bulging of the backbone in this region. This conformational change in Tyr^{7.53} has been implicated in the activation mechanism of rhodopsin and other GPCRs, and is likely to be important for the transition from the inactive to the active state in A_{7A}AR (14, 38–40).

Note that although the changes described above in A_{2A}AR helices III, V, VI, and VII have a major component of “rigid body” movement, a more detailed analysis shows certain conformational plasticity of the helices. In other words, rather than behaving as “rigid sticks,” the movements of TM helices are more consistent with elastic spring behavior (see also fig. S4).

Agonist-bound structures of β_1 ARs and β_2 ARs were recently reported (2, 5, 9). The β_1 AR structures (9) and the structure of β_2 AR bound to an irreversible agonist (5) highlighted important conformational changes in the orthosteric binding site, but they did not exhibit agonist-induced conformational changes at the intracellular side of these receptors. The active-like state conformation in β_2 AR with intracellular conformational changes was achieved by additional stabilization of an agonist-bound receptor with a G protein-mimicking nanobody (2). The nanobody-stabilized, agonist-bound β_2 AR structure revealed large-scale movements of helices III, V, VI, and VII along with rotameric switches of conserved residues at the cytoplasmic G protein-binding interface, similar to those observed in the activated opsin and in the current agonist-bound A_{2A} AR structure. Some variations in the magnitude of these movements may be partially explained by

intrinsic differences between these three receptors, as well as by specific effects of the receptor binding partners. For example, a larger magnitude of helix VII movement in A_{2A}AR may result from conformational changes specific for the bulky UK-432097 ligand, whereas the magnitude of helix VI movement in β₂AR may be exaggerated by the nanobody binding. Despite the similar conformational transformations occurring at the intracellular side of the nanobody-stabilized, agonist-bound β₂AR and the agonist-bound A_{2A}AR, these changes appeared to be induced by rather disparate triggers associated with agonist binding in different receptors. Whereas ligand-induced activation in β₂AR is largely driven by an inward movement of helix V (2, 41), binding of A_{2A}AR agonist does not directly affect helix V; instead, the most pronounced ligand-induced changes involve helices III, VI, and VII.

The observed resemblance in the overall structural rearrangements of A_{2A}AR, opsin, and β₂AR suggests common features of activation mechanism in GPCRs (Fig. 5). Although agonist binding at the extracellular domain triggers only subtle conformational changes within the binding pocket, some of these changes propagate toward the cytoplasmic domains, promoting large-scale 7TM rearrangement required for G protein binding and signaling. Movements on helices V to VII are supported by a relatively stable core bundle composed of helices I to IV. Comparison of activation transitions in A_{2A}AR, opsin, and β₂AR reveals very different types of molecular triggers in the binding pocket, which promote or stabilize an active state. Further understanding of these specific agonist-induced changes in GPCRs may help to establish a structural basis for the functional selectivity of ligands and benefit the design of better agonist-based pharmaceuticals.

Previous work had suggested that it would be difficult to obtain an agonist-bound structure in an active state without additional stabilization by a G protein or a mimetic. Studies of a number of different GPCR types had suggested that the agonists increased the dynamics of the receptor, leading to poor-quality crystal x-ray diffraction. Our study now shows that it is possible to obtain agonist-bound structures at high resolution with a careful choice of conformationally selective ligands, such as the agonist UK-432097 that forms an extensive network of ligand-receptor interactions. It appears that agonist binding does not always induce a greater degree of dynamics on the receptor structure. Given that some ligands, such as UK-432097, predominantly stabilize only one receptor conformation (conformationally selective ligands), whereas others shift the dynamic equilibrium of multiple receptor conformations (42), the variety of agonist types may be broader than previously believed.

References and Notes

- V. Cherezov *et al.*, *Science* **318**, 1258 (2007).
- S. G. Rasmussen *et al.*, *Nature* **469**, 175 (2011).
- S. G. Rasmussen *et al.*, *Nature* **450**, 383 (2007).
- D. M. Rosenbaum *et al.*, *Science* **318**, 1266 (2007).
- D. M. Rosenbaum *et al.*, *Nature* **469**, 236 (2011).
- D. Wacker *et al.*, *J. Am. Chem. Soc.* **132**, 11443 (2010).
- M. A. Hanson *et al.*, *Structure* **16**, 897 (2008).
- T. Warne *et al.*, *Nature* **454**, 486 (2008).
- T. Warne *et al.*, *Nature* **469**, 241 (2011).
- V. P. Jaakola *et al.*, *Science* **322**, 1211 (2008).
- B. Wu *et al.*, *Science* **330**, 1066 (2010).
- E. Y. Chien *et al.*, *Science* **330**, 1091 (2010).
- J. H. Park, P. Scheerer, K. P. Hofmann, H. W. Choe, O. P. Ernst, *Nature* **454**, 183 (2008).
- P. Scheerer *et al.*, *Nature* **455**, 497 (2008).
- S. J. Mantell *et al.*, *Bioorg. Med. Chem. Lett.* **19**, 4471 (2009).
- B. B. Fredholm, A. P. Ijzerman, K. A. Jacobson, J. Linden, C. E. Müller, *Pharmacol. Rev.* **63**, 1 (2011).
- J. M. Rieger, M. L. Brown, G. W. Sullivan, J. Linden, T. L. Macdonald, *J. Med. Chem.* **44**, 531 (2001).
- S. Tchilibon *et al.*, *Bioorg. Med. Chem.* **12**, 2021 (2004).
- The ligand-binding properties of UK-432097 and related nucleosides were examined in membranes from A_{2A}AR-T4L-ΔC-expressing Sf9 cells (fig. S1). The inhibition constant (K_i) of UK-432097 at the A_{2A}AR-T4L-ΔC receptor was 4.75 nM. The agonist property of UK-432097 was characterized with CHO cells expressing human wild-type A_{2A}AR. The efficacy and potency of UK-432097 relative to other three known agonists (NECA, CGS21680, and CI-936) were followed using a cyclic adenosine monophosphate accumulation assay in intact CHO cells. The respective half-maximal effective concentration (EC₅₀) values of UK-432097, NECA, CGS21680, and CI-936 are 0.66 ± 0.19 nM, 5.99 ± 1.86 nM, 3.25 ± 1.22 nM, and 14.5 ± 5.81 nM (fig. S2).
- Z. G. Gao, A. P. Ijzerman, *Biochem. Pharmacol.* **60**, 669 (2000).
- See supporting material on Science Online.
- To overcome the inherent structural flexibility of GPCRs, we used the same engineered A_{2A}AR construct, termed A_{2A}AR-T4L-ΔC, as was used in the A_{2A}AR-ZM241385 complex structure. Briefly, this construct contains an insertion of T4 lysozyme (T4L) at the intracellular loop 3 (ICL3) and removal of C-terminal 96 residues of A_{2A}AR. Stabilization of the A_{2A}AR-T4L-ΔC construct in an active state was achieved by screening a broad range of A_{2A}AR agonists using a thermal stability assay (table S3). Among the tested ligands, UK-432097 exhibited the highest thermal stability (melting temperature ~65°C). The stabilized A_{2A}AR-T4L-ΔC in complex with UK-432097 was crystallized in a cholesterol-doped monoolein lipidic cubic phase (LCP). Crystallographic data were collected on the GM/CA-CAT beamline at the Argonne Photon Source using a 10-μm minibeam. A complete data set at 2.7 Å resolution was assembled using data collected from 20 crystals. The final model includes residues Ile3 to Leu308 of the human A_{2A}AR, residues 2 to 161 of T4L replacing the ICL3 of A_{2A}AR (Lys209 to Ala221), two partial lipid [OLC, (2R)-2,3-dihydroxypropyl (9Z)-octadec-9-enoate] chains, six water molecules, and the agonist UK-432097 bound in the ligand-binding cavity. Part of the extracellular loop 2 (ECL2; Pro149 to Gln157) was not modeled because of a weak electron density.
- G. Cristalli, C. E. Müller, R. Volpini, *Handb. Exp. Pharmacol.* **193**, 59 (2009).
- A. A. Ivanov, D. Barak, K. A. Jacobson, *J. Med. Chem.* **52**, 3284 (2009).
- V. P. Jaakola *et al.*, *J. Biol. Chem.* **285**, 13032 (2010).
- In Ballesteros-Weinstein numbering, a single most conserved residue among the class A GPCRs is designated x.50, where x is the transmembrane helix number. All other residues on that helix are numbered relative to this conserved position. Numbers decrease toward the N terminus and increase toward the C terminus. This numbering system is used as superscript only for labeling residues on transmembrane helices (but not for those on loop regions). For clarity, residues for A_{2A}AR use both standard and Ballesteros-Weinstein numberings, whereas residues for other GPCRs use only Ballesteros-Weinstein numbering throughout this text.
- J. A. Ballesteros, H. Weinstein, *Methods Neurosci.* **25**, 366 (1995).
- J. Kim, J. Wess, A. M. van Rhee, T. Schöneberg, K. A. Jacobson, *J. Biol. Chem.* **270**, 13987 (1995).
- Q. Jiang, B. X. Lee, M. Glashofer, A. M. van Rhee, K. A. Jacobson, *J. Med. Chem.* **40**, 2588 (1997).
- Q. Jiang *et al.*, *Mol. Pharmacol.* **50**, 512 (1996).
- P. J. Conn, A. Christopoulos, C. W. Lindsley, *Nat. Rev. Drug Discov.* **8**, 41 (2009).
- Z. G. Gao *et al.*, *Mol. Pharmacol.* **63**, 1021 (2003).
- V. Katritch, I. Kufareva, R. Abagyan, *Neuropharmacology* **60**, 108 (2011).
- Note that global superimposition of TM helical bundle in this case almost exactly overlaps common features of A_{2A}AR-ZM241385 and A_{2A}AR-UK-432097 complexes, so that the Asn253^{6.55} α-carbonyls of A_{2A}AR are within 0.2 Å and exocyclic amines of ZM241385 and UK-432097 are within 0.6 Å distance.
- R. Vogel, F. Siebert, *J. Biol. Chem.* **276**, 38487 (2001).
- K. P. Hofmann *et al.*, *Trends Biochem. Sci.* **34**, 540 (2009).
- K. Sansuk *et al.*, *Mol. Pharmacol.* **79**, 262 (2011).
- S. Ahuja, S. O. Smith, *Trends Pharmacol. Sci.* **30**, 494 (2009).
- S. Vanni, M. Neri, I. Tavernelli, U. Rothlisberger, *J. Mol. Biol.* **397**, 1339 (2010).
- J. Wess, S. J. Han, S. K. Kim, K. A. Jacobson, J. H. Li, *Trends Pharmacol. Sci.* **29**, 616 (2008).
- V. Katritch *et al.*, *J. Mol. Recognit.* **22**, 307 (2009).
- X. J. Yao *et al.*, *Proc. Natl. Acad. Sci. U.S.A.* **106**, 9501 (2009).
- This work was supported by the Intramural Research Program of the National Institute of Diabetes and Digestive and Kidney Diseases (K.A.J. and Z.-G.G.), PSI-Biology grant U54 GM094618 for structure production, and NIH Roadmap Initiative grant P50 GM073197 for technology development. R.C.S. thanks N. Dekker at AstraZeneca for suggesting the UK-432097 compound for biochemical and structural studies. We thank J. Velasquez for help on molecular biology; C. Cornille-Ty, T. Trinh, and K. Allin for help on baculovirus expression; E. Chien and W. Liu for advice on protein purification and LCP crystallization; I. Wilson, M. Hanson, and A. Ijzerman for careful review and scientific feedback on the manuscript; K. Kadyshkevskaya for assistance with figure preparation; A. Walker for assistance with manuscript preparation; L. Heitman for A_{2A}AR compounds used in thermal stability studies; Y. Zheng and M. Caffrey for use of an in meso robot (built with support from NIH grant GM075915, NSF grant IIS0308078, and Science Foundation Ireland grant 02-IN1-B266); and J. Smith, R. Fischetti, and N. Sanishvili for assistance in development and use of the minibeam and beamtime at GM/CA-CAT beamline 23-ID at the Advanced Photon Source, which is supported by National Cancer Institute grant Y1-CO-1020 and National Institute of General Medical Sciences grant Y1-GM-1104. R.C.S. is a founder and member of the board of directors of Receptos, a GPCR structure-based drug discovery company. Atomic coordinates and structure factors have been deposited in the Protein Data Bank with identification code 3QAK.

Supporting Online Material

www.sciencemag.org/cgi/content/full/science.1202793/DC1
Materials and Methods
Tables S1 to S3
Figs. S1 to S4
References
Movie S1

12 January 2011; accepted 1 March 2011
Published online 10 March 2011;
10.1126/science.1202793

Giant Nonlocality Near the Dirac Point in Graphene

D. A. Abanin,^{1,2} S. V. Morozov,^{1,6} L. A. Ponomarenko,¹ R. V. Gorbachev,¹ A. S. Mayorov,¹ M. I. Katsnelson,³ K. Watanabe,⁴ T. Taniguchi,⁴ K. S. Novoselov,¹ L. S. Levitov,^{5*} A. K. Geim^{1*}

Transport measurements have been a powerful tool for discovering electronic phenomena in graphene. We report nonlocal measurements performed in the Hall bar geometry with voltage probes far away from the classical path of charge flow. We observed a large nonlocal response near the Dirac point in fields as low as 0.1 tesla, which persisted up to room temperature. The nonlocality is consistent with the long-range flavor currents induced by the lifting of spin/valley degeneracy. The effect is expected to contribute strongly to all magnetotransport phenomena near the neutrality point.

Graphene continues to attract intense interest, especially as an electronic system in which charge carriers are Dirac-like particles with linear dispersion and zero rest mass. Transport measurements in graphene have unveiled a number of unusual phenomena, including two new types of the quantum Hall effect (QHE), minimum metallic conductivity, bipolar superconductivity, and Klein scattering (*1–4*). In a number of experiments, unusual behavior was found at low temperatures (*T*) and high magnetic fields (*B*) near the so-called Dirac or neutrality point (NP), where charge carrier density *n* tends to zero (*5–9*). However, the NP is also hardest to access experimentally because of charge inhomogeneity (electron-hole puddles) and limited carrier mobilities (μ). Furthermore, the fundamental neutral degrees of freedom in graphene, such as spin and valley, evade detection by the standard electrical measurement techniques, even in the best-quality samples (here the valley degree of freedom refers to the inequivalence of the pair of conical valence/conduction bands in the Brillouin zone, which touch at Dirac points).

In this work, we performed nonlocal measurements, previously used to probe the dynamics of population imbalance for edge modes in quantum Hall systems (*10, 11*) as well as spin diffusion (*12*) and magnetization dynamics (*13*). The advantage of nonlocal measurements is that they allow one to filter out the ohmic contribution resulting from charge flow and, in doing so, detect more subtle effects that otherwise can remain unnoticed (*10–14*). The measurements

were carried out by using more than 20 devices of two different types. Type I devices were made in the conventional way, with graphene placed on top of an oxidized Si wafer (*1–7*), hereafter referred to as GSiO. Type II devices contained thin crystals of hexagonal boron nitride placed between graphene and SiO₂ (*15*) (referred to as GBN). All the devices were made in the Hall bar geometry by following the microfabrication procedures described previously (*1, 6, 15–17*). The GSiO devices had mobility μ of $\sim 10,000$ cm²/Vs, whereas GBN devices showed much higher μ , between 50,000 and 150,000 cm²/Vs for carrier concentrations $n \sim 10^{11}$ cm⁻² (*17*). Typical charge inhomogeneity n_0 estimated from the rounding of the conductivity minimum was $\sim 10^{10}$ and 10^{11} cm⁻² for GBN and GSiO devices, respectively. All of our samples exhibited a qualitatively similar nonlocal response; however, its absolute value was 10 to 100 times larger in GBN samples. Unless stated explicitly, the results described below refer equally to both device types.

Figure 1A shows a representative GSiO device, used to describe different measurement geometries. In the standard Hall bar geometry, so that current I_{14} flows between contacts 1 and 4 and voltage V_{23} is measured between contacts 2 and 3, the longitudinal resistivity ρ_{xx} [calculated as $(w/L) \times R_{23,14}$, where L and w are the length and width of the Hall bar, and $R_{23,14} = V_{23}/I_{14}$] shows the standard QHE behavior for monolayer graphene, with wide regions of zero ρ_{xx} accompanied by well-defined plateaus in Hall resistivity ρ_{xy} (Fig. 1B and fig. S1).

In the following, we focus on the nonlocal resistance, R_{NL} . The measured signal (e.g., $R_{35,26}$ in Fig. 1C) cannot be understood in terms of the classical picture of charge flow. Indeed, a fraction of applied current I_{26} , which flows sideways and reaches the remote region between contacts 3 and 5, is exponentially small in the separation L . Using the van der Pauw formalism (*18*), it is straightforward to show that the expected Ohm's law contribution to R_{NL} behaves as $\approx \rho_{xx} \exp(-\pi L/w)$ for both zero and nonzero B (*17*). For our devices, L ranged from 3 to 15 μm and w between 1 and 2 μm . For a typical $L/w = 5$, this translates into minute $R_{NL} < 10^{-3}$ ohm. In agreement with this estimate, $R_{NL}(B = 0)$ was indistinguishable from zero at our maximum resolution (Fig. 1C).

The situation changes radically in finite B : R_{NL} remains zero at zeros of ρ_{xx} , but between the QHE zeros it can reach values of ~ 1 kilohm, even in the conventional GSiO devices, and exhibits the same overall oscillating pattern as ρ_{xx} (Fig. 1C). Although the pattern always remained the same, the amplitude of the nonlocal response varied significantly for different devices. In particular, R_{NL} depended on an exact contact configuration (that is, $R_{35,26} \neq R_{34,26}$), yet with the Onsager relation $R_{35,26}(B) \neq R_{26,35}(B) = R_{35,26}(-B)$ satisfied (fig. S3). R_{NL} was found to become smaller with increasing L and in the presence of

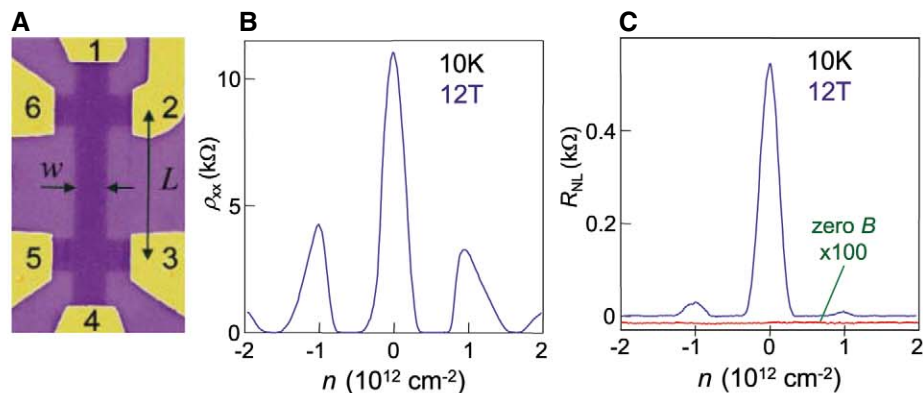


Fig. 1. Local and nonlocal geometries. (A) Electron micrograph (false color) of a GSiO device. The width $w = 1 \mu\text{m}$ and length L of the Hall bar are indicated. (B) Longitudinal resistivity ρ_{xx} as a function of carrier density n in a perpendicular $B = 12$ T. (C) In the nonlocal geometry, no signal can be detected in zero B (the red curve is downshifted for clarity and magnified). The magnetic field gives rise to large R_{NL} shown for standard-quality devices (GSiO type). To ensure that there was no contribution from inductive coupling and thermopower, we used both dc and low-frequency ac measurements with typical driving currents I of $1 \mu\text{A}$. R_{NL} was confirmed to be independent of I by varying it over two orders of magnitude.

¹Manchester Centre for Mesoscience and Nanotechnology, University of Manchester, Manchester M13 9PL, UK. ²Princeton Center for Theoretical Science and Department of Physics, Princeton University, Princeton, NJ 08544, USA. ³Theory of Condensed Matter, Institute for Molecules and Materials, Radboud University Nijmegen, Heyendaalseweg 135, 6525 AJ Nijmegen, Netherlands. ⁴National Institute for Materials Science, 1-1 Namiki, Tsukuba, 305-0044 Japan. ⁵Department of Physics, Massachusetts Institute of Technology, Cambridge, MA 02139, USA. ⁶Institute for Microelectronics Technology, 142432 Chernogolovka, Russia.

*To whom correspondence should be addressed. E-mail: levitov@mit.edu (L.S.L.); geim@man.ac.uk (A.K.G.)

extra leads between current and voltage contacts (fig. S3). The strong sample and contact dependence did not allow us to quantify the spatial scale involved in the nonlocality, but it can be estimated as exceeding L (that is, $\sim 10\text{ }\mu\text{m}$) in $B > 5\text{ T}$ and $T < 100\text{ K}$. To emphasize the importance of nonlocal transport near the NP, in (17) we describe the standard Hall measurements in two configurations, $R_{35,42}$ and $R_{35,46}$, where the same voltage probes were used and the only difference was the swap of one of the current leads. In a classical conductor, this should cause no effect whatsoever, but in graphene, nonlocal transport leads to profound differences between the two supposedly equivalent measurements (fig. S1).

To elucidate the origin of the unexpected nonlocality at the NP, we studied its T and B dependence. The peaks in R_{NL} at filling factors $\nu = 4$ and 8 completely disappear above 70 K , simultaneously with the disappearance of the zeros in ρ_{xx} . Therefore, the nonlocality at $\nu = 4$ and 8 can be attributed to the standard QHE edge-state transport (10, 11). In contrast, the nonlocal signal at the NP ($\nu = 0$) is found to be much more robust (Fig. 2), extending well beyond the QHE regime, into the regime where even Shubnikov–de Haas

oscillations are completely absent. At 300 K , the nonlocality remains quite profound, with $R_{\text{NL}} \sim 1$ kilohm at several tesla and a remnant signal observable in $B \ll 1\text{ T}$. This behavior implies that the nonlocality at the NP occurs via a mechanism that is different from the QHE edge-state transport (10, 11, 17).

Figure 2C reveals two temperature regimes. At high T , R_{NL} decreases slowly with increasing T , whereas below $\sim 30\text{ K}$, one can see a rapid increase in R_{NL} . The latter correlates with an increase in ρ_{xx} for GBN devices and can be attributed to the onset of an energy gap that opens at $\nu = 0$ at low T (5, 7, 9, 15). By using the Corbino geometry, we found that the gap did not exceed 20 K at 12 T for GSiO (17). Similar values were reported by other groups (7, 19). For certain gapped states, the nonlocality can arise because of countercirculating edge states (6). To test this possibility, we carried out nonlocal measurements on devices patterned to have a channel widening that increased devices' edge length more than 10-fold, while L between the current and voltage contacts remained the same (17). No significant difference in R_{NL} was observed in such devices as compared to those with no widening.

This and other observations described in (17) provide evidence against edge transport and suggest a bulk transport mechanism even in the low- T gapped state. This conclusion is also consistent with the insulating behavior found in previous magnetotransport studies at the NP (5, 7, 9, 15). The observed sharp increase in R_{NL} at low T (Fig. 2C) may indicate that the dominant nonlocality mechanism changes as the system goes into the gapped state.

Below we discuss the high- T regime, where the gap opening at the NP is irrelevant, because no nonlocal signal could be detected even at $\nu = 4$ and 8 , despite cyclotron gaps being large ($\sim 500\text{ K}$). The nonlocality observed at high T and low B calls for a quasiclassical explanation that does not involve Landau quantization. At the same time, one has to find a mechanism that naturally extends into the low- T regime, where the observed nonlocality becomes increasingly more profound. One possible explanation is the flavor Hall effect (FHE), a bulk mechanism in which nonlocality is mediated by neutral excitations, such as spin and valley flavors, and which works in both quasiclassical and QHE regimes, providing a natural explanation for our experimental findings (17).

The basic physics of the FHE is illustrated in Fig. 3, which for simplicity refers to the case of spin. The Zeeman splitting shifts the Dirac cones for opposite spin projections relative to each other. At the NP, the spin splitting produces a finite concentration of electrons with spin-up (\uparrow) and holes with spin-down (\downarrow) (Fig. 3A). When electric current is applied, the Lorentz force creates opposite spin-up and spin-down currents, leading to a spatial spin imbalance at zero net Hall voltage at the NP (Fig. 3B). The phenomenology is similar to the spin Hall effect (SHE) resulting from spin-orbit interaction (20–22), yet our SHE effect relies on the Zeeman splitting induced by B and occurs in the absence of spin-orbit interaction. In graphene, the SHE can generate long-range spin currents, due to slow spin relaxation (2, 23), and produce a nonlocal voltage at a remote location via a reverse SHE, as illustrated in Fig. 3B.

Figure 3C plots the modeled SHE behavior for R_{NL} in GSiO, which captures the main features of the experimental data, most importantly the peak at the NP in $R_{\text{NL}}(n)$. The model also predicts maximum value $R_{\text{NL}} \sim h/4e^2$, which corresponds to a cutoff due to Landau level broadening (17). Such values are indeed observed in GBN devices (Fig. 2C). The T and B dependences predicted from the simple model are in qualitative agreement with the experiment. The agreement can be further improved by taking into account valley splitting that can give rise to neutral valley currents and additional nonlocality. In particular, the onset of the valley splitting due to interaction effects (19) may be responsible for the observed increase in R_{NL} below 30 K . Although our measurements did not probe flavor currents directly, the indirect evidence is overwhelming. The nonlocal phenomena are very rare and, given that we have ruled out

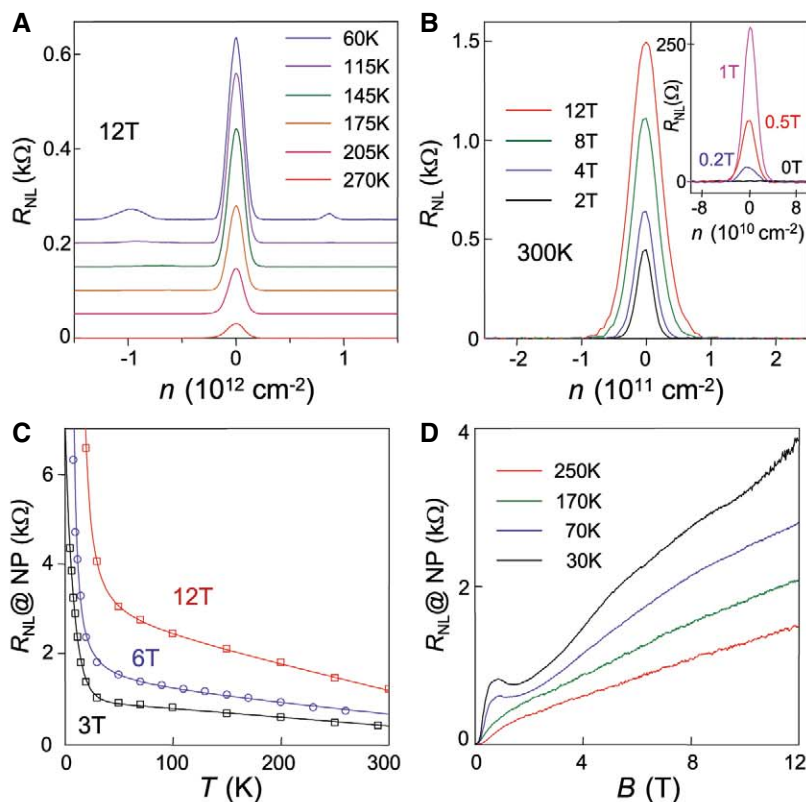


Fig. 2. Nonlocal transport in graphene. (A) R_{NL} for the GSiO device in Fig. 1 at different T . In high B , the nonlocality at $\nu = 4$ persists up to liquid nitrogen T . The nonlocal signal at the NP is even more robust with increasing T . (B) Room- T R_{NL} for a GBN device with $\mu \approx 140,000\text{ cm}^2/\text{Vs}$, and with nonlocal voltage contacts separated from the current path by $L = 5\text{ }\mu\text{m}$. The inset magnifies R_{NL} in small B . Even at 0.1 T , R_{NL} remains substantial ($\sim 10\text{ }\Omega$). GSiO devices exhibit a qualitatively similar behavior but with room- T values of $R_{\text{NL}} \sim 100$ times smaller (17). (C and D) R_{NL} at the NP as a function of T for several values of B and as a function of B for several values of T , respectively. The data are for the same GBN device as in (B). The solid curves in (C) are guides to the eye.

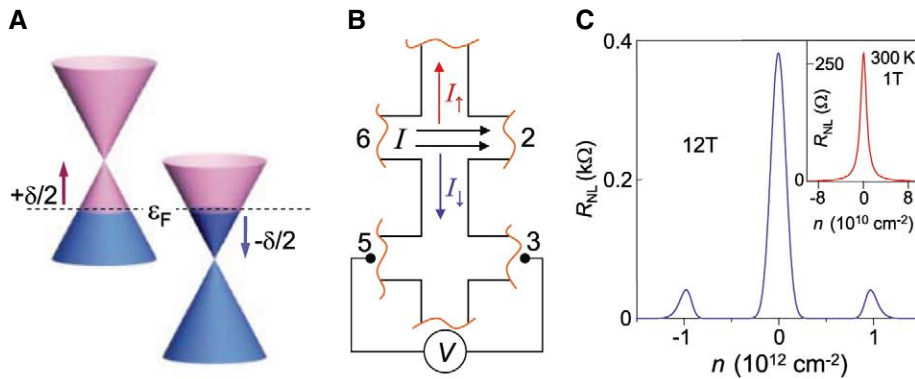


Fig. 3. SHE in graphene and nonlocal transport mediated by spin diffusion. **(A)** Zeeman splitting at charge neutrality produces two pockets filled with electrons and holes having opposite spin. **(B)** In the presence of the Lorentz force, I gives rise to transverse spin currents I_\uparrow and I_\downarrow . Because the force has opposite signs for electrons and holes, the net charge current is zero, whereas the net spin current is nonzero. The resulting imbalance in the up/down spin distribution can reach remote regions and generate a voltage drop V . **(C)** R_{NL} predicted in our model for the QHE regime (main panel) and the quasiclassical regime (inset). The best-fit parameters $n_0 = 4 \times 10^9$ cm $^{-2}$ and Landau level broadening $\Gamma = 200$ K are typical for GBN and GSiO devices, respectively. R_{NL} grows with decreasing n_0 and Γ (17), which is consistent with much larger R_{NL} measured in our GBN devices.

edge-state transport mechanisms, we believe that the spin/valley Hall effect is the only remaining explanation for our findings.

The profound nonlocality described here is an essential attribute of electron transport in graphene. The nonlocality is consistent with neutral currents generated by the SHE at high T and, possibly, by the valley Hall effect at liquid-helium T . Nonlocal transport, being directly sensitive to neutral degrees of freedom, provides valuable in-

formation that is inaccessible by conventional electrical measurements.

References and Notes

1. A. K. Geim, K. S. Novoselov, *Nat. Mater.* **6**, 183 (2007).
2. A. H. Castro Neto, F. Guinea, N. M. R. Peres, K. S. Novoselov, A. K. Geim, *Rev. Mod. Phys.* **81**, 109 (2009).
3. H. B. Heersche, P. Jarillo-Herrero, J. B. Oostinga, L. M. Vandersypen, A. F. Morpurgo, *Nature* **446**, 56 (2007).

4. A. F. Young, P. Kim, *Nat. Phys.* **5**, 222 (2009).
5. J. G. Checkelsky, L. Li, N. P. Ong, *Phys. Rev. B* **79**, 115434 (2009).
6. D. A. Abanin *et al.*, *Phys. Rev. Lett.* **98**, 196806 (2007).
7. Z. Jiang, Y. Zhang, H. L. Stormer, P. Kim, *Phys. Rev. Lett.* **99**, 106802 (2007).
8. B. E. Feldman, J. Martin, A. Yacoby, *Nat. Phys.* **5**, 889 (2009).
9. X. Du, I. Skachko, F. Duerr, A. Luican, E. Y. Andrei, *Nature* **462**, 192 (2009).
10. P. L. McEuen *et al.*, *Phys. Rev. Lett.* **64**, 2062 (1990).
11. R. J. Haug, *Sem. Sci. Tech.* **8**, 131 (1993).
12. Y. Tserkovnyak, S. Brataas, G. E. W. Bauer, B. I. Halperin, *Rev. Mod. Phys.* **77**, 1375 (2005).
13. F. J. Jedema, M. S. Nijboer, A. T. Filip, B. J. van Wees, *Phys. Rev. B* **67**, 085319 (2003).
14. S. Washburn, R. A. Webb, *Rep. Prog. Phys.* **55**, 1311 (1992).
15. C. R. Dean *et al.*, *Nat. Nanotechnol.* **5**, 722 (2010).
16. R. V. Gorbachev *et al.*, *Small* **7**, 465 (2011).
17. See supporting material on Science Online.
18. L. J. van der Pauw, *Philips Tech. Rev.* **20**, 220 (1958).
19. Y. J. Song *et al.*, *Nature* **467**, 185 (2010).
20. J. Sinova *et al.*, *Phys. Rev. Lett.* **92**, 126603 (2004).
21. Y. K. Kato, R. C. Myers, A. C. Gossard, D. D. Awschalom, *Science* **306**, 1910 (2004).
22. J. Wunderlich, B. Kaestner, J. Sinova, T. Jungwirth, *Phys. Rev. Lett.* **94**, 047204 (2005).
23. N. Tombros, C. Jozsa, M. Popinciuc, H. T. Jonkman, B. J. van Wees, *Nature* **448**, 571 (2007).
24. Supported by the Engineering and Physical Research Council (UK), the Royal Society, U.S. Office of Naval Research, U.S. Air Force Office of Scientific Research, and the Körber Foundation. We thank D. Elias, P. Blake, E. Hill, F. Schedin, S. Anissimova, and I. Grigorieva for their help.

Supporting Online Material

www.sciencemag.org/cgi/content/full/332/6027/328/DC1

SOM Text

Figs. S1 to S8

References

26 October 2010; accepted 28 February 2011
10.1126/science.1199595

Teleportation of Nonclassical Wave Packets of Light

Noriyuki Lee,¹ Hugo Benichi,¹ Yuishi Takeno,¹ Shuntaro Takeda,¹ James Webb,² Elanor Huntington,² Akira Furusawa^{1*}

We report on the experimental quantum teleportation of strongly nonclassical wave packets of light. To perform this full quantum operation while preserving and retrieving the fragile nonclassicality of the input state, we have developed a broadband, zero-dispersion teleportation apparatus that works in conjunction with time-resolved state preparation equipment. Our approach brings within experimental reach a whole new set of hybrid protocols involving discrete- and continuous-variable techniques in quantum information processing for optical sciences.

In the early development of quantum information processing (QIP), a communication protocol called quantum teleportation was discovered (1) that involves the transportation of an unknown arbitrary quantum state $|\psi\rangle$ by means of entanglement and classical information. Ex-

perimental realizations of quantum teleportation (2, 3) and more advanced related operations (4) in the continuous-variable regime have been achieved by linear optics methods, although only for Gaussian states so far. However, at least third-order nonlinear operations are necessary for building a universal quantum computer (5)—something that Gaussian operations and Gaussian states alone cannot achieve. Photon subtraction techniques based on discrete-variable technology can provide useful nonlinearities and are used to generate Schrödinger's-cat states and other optical non-Gaussian states (6). Schrödinger's-cat states are of particular interest in this context, as they

have been shown to be a useful resource for fault-tolerant QIP (7). It is therefore necessary to extend the continuous-variable technology to the technology used in the world of non-Gaussian states.

We have combined these two sets of technologies, and here we demonstrate such Gaussian operations on nonclassical non-Gaussian states by achieving experimental quantum teleportation of Schrödinger's-cat states of light. Using the photon subtraction protocol, we generate quantum states closely approximating Schrödinger's-cat states in a manner similar to (8–11). To accommodate the required time-resolving photon detection techniques and handle the wave-packet nature of these optical Schrödinger's-cat states, we have developed a hybrid teleporter built with continuous-wave light yet able to directly operate in the time domain. For this purpose we constructed a time-gated source of Einstein-Podolsky-Rosen (EPR) correlations as well as a classical channel with zero phase dispersion (12). We were able to bring all the experimental parameters up to the quantum regime, and we performed successful quantum teleportation in the sense that both our input and output states are strongly nonclassical.

A superposition of the quasi-classical coherent state $|\alpha\rangle$ is one of the consensus definitions of a Schrödinger's-cat state $|\text{cat}\rangle$, typically written

¹Department of Applied Physics, School of Engineering, University of Tokyo, 7-3-1 Hongo, Bunkyo-ku, Tokyo 113-8656, Japan. ²Centre for Quantum Computation and Communication Technology, School of Engineering and Information Technology, University College, University of New South Wales, Canberra, ACT 2600, Australia.

*To whom correspondence should be addressed. E-mail: akiraf@ap.t.u-tokyo.ac.jp

$|\text{cat}\rangle \propto |\alpha\rangle \pm |-\alpha\rangle$. Such optical Schrödinger's-cat states are known to be approximated by multiple photon subtractions from a squeezed vacuum state (6). In these protocols, a squeezed vacuum state $\hat{S}(s)|0\rangle$ is weakly tapped via a subtraction channel, where $|0\rangle$ is the vacuum state and $\hat{S}(s)$ is the squeezing operator with squeezing parameter s . When a photon detection event occurs in the subtraction channel, $\hat{S}(s)|0\rangle$ is projected by the quantum action of the photon detector onto a non-Gaussian state, which can be tuned to approximate a Schrödinger's-cat state (8–10). The approximation is not perfect and can be quantified by means of the fidelity figure $F_{\text{cat}} = |\langle \text{cat} | \hat{S}(s) | 0 \rangle|^2$ (13).

To represent the superposition nature of these states, we use the Wigner formalism where for any quantum state $|\phi\rangle$ one associates a quasiprobability distribution $W(x, p)$, where x and p are the phase-space position and momentum parameters. $W(x, p)$ is called the Wigner function and holds information exactly equivalent to $|\phi\rangle$ (14). Although the position \hat{x} and momentum \hat{p} quadrature operators and the vector state $|\phi\rangle$ are abstract objects, $W(x, p)$ is always a definite real-valued function that can be numerically reconstructed if one performs a complete phase-resolved sequence of homodyne measurement $\hat{x}\cos\theta + \hat{p}\sin\theta$, a process called quantum tomography (15, 16). $W(x, p)$ is not a true probability distribution, however, as there exist quantum states whose Wigner functions are not positive. $|\phi\rangle$ is defined to be a strongly nonclassical state when its Wigner function $W(x, p)$ fails to be a positive distribution. Negativity in $W(x, p)$ turns out to be an especially useful description of the nonclassicality of a Schrödinger's-cat state $|\text{cat}\rangle$; $|\alpha\rangle$ and $|-\alpha\rangle$ induce two “classical” Gaussians in phase space, the superposition of which creates an oscillating interference pattern inducing negativity in $W(x, p)$. In contrast, a statistical mixture of $|\alpha\rangle$ and $|-\alpha\rangle$ would never show such negativity.

In a quantum teleportation process, the input W_{in} and output W_{out} Wigner functions are related by the convolution (denoted \circ)

$$W_{\text{out}} = W_{\text{in}} \circ G_{\text{exp}(-r)} \quad (1)$$

where r is the EPR correlation parameter, G_{σ} is a normalized Gaussian of standard deviation σ , and \hbar (Planck's constant divided by 2π) has been set to 1 (17). When finite quantum entanglement r is used, W_{out} will be a thermalized copy of W_{in} . Only with infinite r will G_{σ} become a delta function so that $W_{\text{in}} = W_{\text{out}}$. The quality of quantum teleportation is usually evaluated according to the teleportation fidelity $F_{\text{tele}} = \langle \phi^{\text{in}} | \hat{\rho}^{\text{out}} | \phi^{\text{in}} \rangle$, which can be written as $F_{\text{tele}} = 1/[1 + \exp(-2r)]$ for Gaussian states (18). More important for our case, negative features of W_{in} (if any) can only be teleported and retrieved in W_{out} when $F_{\text{tele}} \geq 2/3$ (19), a threshold

also known as the no-cloning limit (20). However, the practical lower bound on F_{tele} will be higher because of decoherence and experimental imperfection of W_{in} (21). We have thus defined the success criterion of Schrödinger's-cat-state teleportation as the successful transfer of its nonclassical features, or alternatively, successful teleportation of the Wigner function W_{in} negativity.

Our experimental quantum teleporter and Schrödinger's-cat-state source (Fig. 1) upgrade the experiments described in (3) and (10), respectively. We use three optical parametric oscillators to generate the necessary squeezed vacua. One is used for the Schrödinger's-cat-state preparation; the other two are combined together on a half beam splitter whose two exit ports are the resulting pair of EPR-correlated beams. The teleportation is conducted in three steps. Alice first

receives both the input state and her EPR beam and performs two joint quadrature measurements, obtaining results x_0 and p_0 . Bob then receives Alice's measurements $\beta = (x_0 + ip_0)/\sqrt{2}$ through the classical channels and applies the displacement operator $\hat{D}(\beta)$ on his EPR beam. A final stage consists of a third homodyne detector for tomography at the teleporter output. We emphasize that Alice and Bob do not assume any prior knowledge of the input state and adhere to unity-gain teleportation, so that the teleporter does not have any restriction regarding the specific family of quantum states it can faithfully teleport.

To benchmark our teleporter, we first evaluate the fidelity F_{tele} of teleportation of the vacuum state $|0\rangle$, the coherent state of amplitude zero. At quantum optical frequencies where the mean

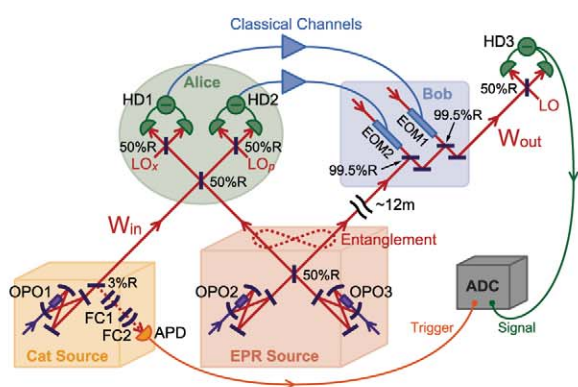


Fig. 1. Experimental setup. OPO, optical parametric oscillator; APD, avalanche photodiode; HD, homodyne detector; LO, local oscillator; EOM, electro-optical modulator; ADC, analog-to-digital converter; FC, filtering cavity. See (12) for details.

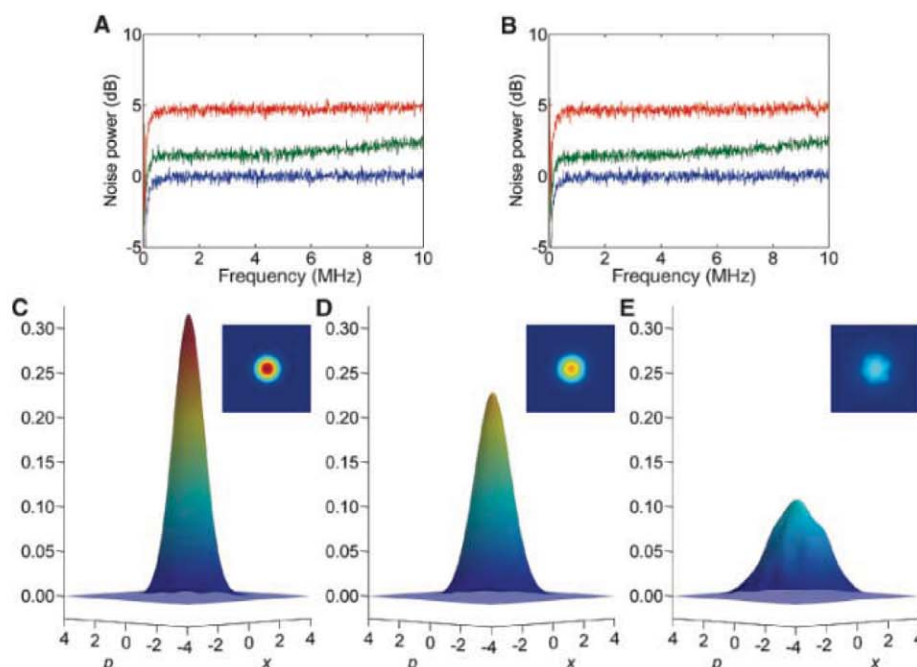


Fig. 2. Broadband teleportation of the vacuum state $|0\rangle$. (A and B) Experimentally measured power spectra of the photocurrents calculated by Fourier transform are shown for the position (A) and momentum (B) quadratures. Blue, shot-noise input; green, quantum teleportation output; red, teleportation output without entanglement. (C to E) Reconstructed Wigner functions of the input state $|0\rangle$ (C), quantum teleported vacuum (D), and classically teleported vacuum (E).

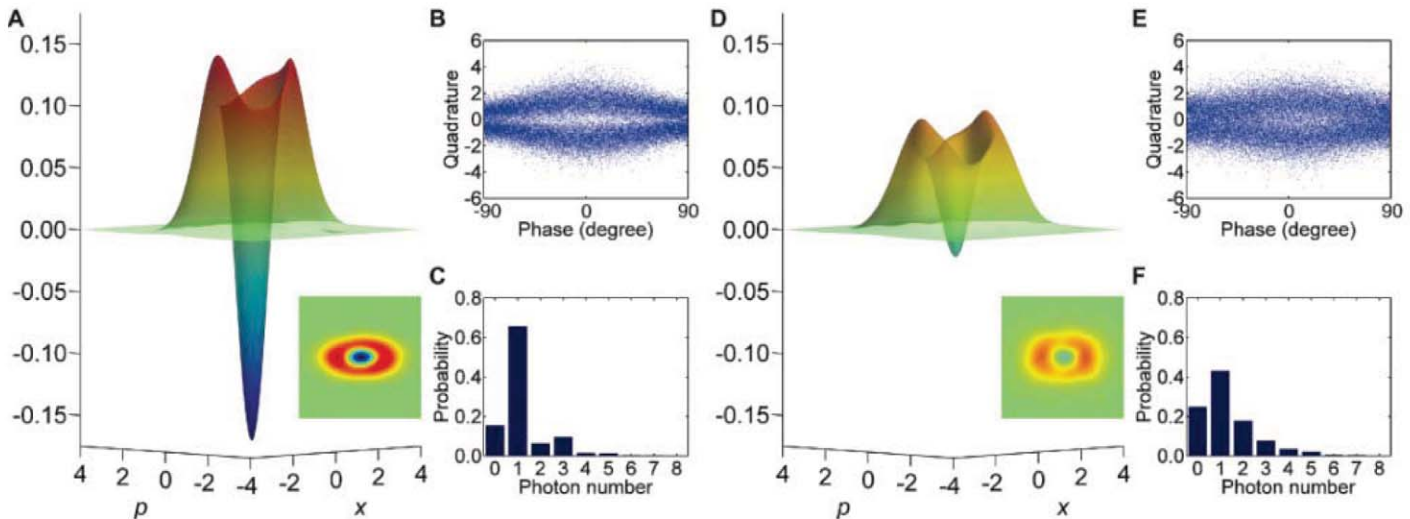


Fig. 3. Teleportation of Schrödinger's-cat states. (A to C) Experimentally measured input state's Wigner function W_{in} (A), marginal distribution (B), and photon number distribution (C). (D to F) Experimentally measured output state's Wigner function W_{out} (D), marginal distribution (E), and photon number distribution (F).

thermal photon number is virtually 0, this is simply done by blocking the input port of the teleporter. The teleported vacuum photocurrent is expected to have uniform Gaussian statistics with a variance $\sigma^2 = \frac{1}{2} + [\exp(-2r)]$ ($\hbar = 1$) from which we can deduce teleportation fidelity (Fig. 2). The blue traces are the shot-noise level, the noise spectrum of the input vacuum $|0\rangle$. The red traces are the classical limit of teleportation obtained by turning off the entanglement between Alice and Bob ($r = 0$). We measure 4.8 dB of added noise above the shot noise, in agreement with the expected teleportation fidelity of 0.5. When Alice and Bob share entanglement, the added noise drops to that shown by the green traces: 1.4 dB above the shot noise around 1 MHz, corresponding to a fidelity of 0.83. This is in agreement with the experimental figure of -6.9 dB that we observe in direct measurement of the EPR correlations shared between Alice and Bob.

In contrast to quantum teleportation experiments conducted to date for narrow sidebands of light (2, 3), our setup operates over a wide frequency bandwidth, as required by the nature of our input state. Because its generation relies on the detection of a single photon and the induced projection, a Schrödinger's-cat state made via photon subtraction is a short wave packet of light. A phenomenological way to picture these wave packets is to consider them as the closed boxes containing the macroscopic superposition states as in Schrödinger's original idea. This requires Alice and Bob to teleport every frequency component of these "box-like" wave packets for faithful teleportation to occur. In this way, Alice and Bob do not need to actually teleport the Schrödinger's-cat states directly, but merely the potential boxes containing them. Consequently, Alice and Bob do not need to know when a detection event occurs; rather, they are only concerned with continuous and faithful "box" wave-packet teleportation, whichever state lies in the

box. In fact, Alice and Bob actually teleport most of the time a squeezed vacuum state $\hat{S}(s)|0\rangle$.

In essence, our teleporter is a time-resolved apparatus that deconstructs the input wave packets into a stream of infinitely small time bins and reconstructs them at the output, within the extent of what we refer to as the teleportation bandwidth. This bandwidth is clearly visible in both of the green experimental traces where the added noise slowly increases with frequency (Fig. 2). This is a direct consequence of the finite bandwidth of squeezing used for entanglement. However, across the frequencies relevant to our input state, teleportation fidelity is always greater than the no-cloning limit of $2/3$, a necessary regime for negativity teleportation. A very careful implementation of the classical channel has been required (12) to achieve experimental realization of this fidelity.

To verify the success of Schrödinger's-cat-state teleportation, we perform experimental quantum tomography of the input and output states independently (Fig. 3). Both input and output marginal distributions exhibit the characteristic eye shape of photon-subtracted squeezed states, with a clear lack of detection events around the origin for any phase. Although necessary, this feature alone is not sufficient to confirm the presence of negativity in W_{in} or W_{out} . The reconstructed input Wigner function W_{in} shows the two positive Gaussians of $|\alpha\rangle$ and $|\alpha\rangle$ together with a central negative dip [$W_{\text{in}}(0, 0) = -0.171 \pm 0.003$] caused by the interferences of the $|\alpha\rangle$ and $|\alpha\rangle$ superposition. The output Wigner function W_{out} retains the characteristic non-Gaussian shape as well as the negative dip [$W_{\text{out}}(0, 0) = -0.022 \pm 0.003$] to a lesser degree. The degradation of the central negative dip and the full evolution of W_{in} toward W_{out} can be fully understood using Eq. 1 with a model of W_{in} , as was done in (21). Given the measured input state negativity of $W_{\text{in}}(0, 0) = -0.171$ and -6.9 dB of squeezing, the results of (21) predict an output negativity value of -0.02 , in good

agreement with measured output negativity. Although this figure does not take into account the input-state squeezing, a more detailed model shows that a squeezing parameter $s = 0.28$ affects output negativity in the third decimal place only (12). The experimental input and output states have an average photon number $\langle \hat{n} \rangle$ equal to 1.22 ± 0.01 and 1.33 ± 0.01 , respectively (12). The increase in the output-state size is due to teleportation-induced thermalization. We calculate that the fidelity F_{cat} is as high as 0.750 ± 0.005 for the input Wigner function W_{in} with the nearest Schrödinger's-cat state having an amplitude $|\alpha_{\text{in}}|^2 = 0.98$ (12). However, after the teleportation W_{out} fidelity is reduced to 0.46 ± 0.01 , with the nearest Schrödinger's-cat state having an amplitude $|\alpha_{\text{out}}|^2 = 0.66$. If W_{out} fidelity is calculated with $|\alpha_{\text{in}}|^2 = 0.98$, then $F_{\text{cat}} = 0.45 \pm 0.01$.

We have demonstrated an experimental quantum teleporter able to teleport full wave packets of light up to a bandwidth of 10 MHz while at the same time preserving the quantum characteristic of strongly nonclassical superposition states, manifested in the negativity of the Wigner function. Although F_{cat} and $W(0, 0)$ drop in the teleportation process, there is no theoretical limitation other than available squeezing, and stronger EPR correlations would achieve better fidelity and negativity transmission. The various more complex states generated as an application of photon subtraction so far (22, 23) can be, in principle, readily sent through our broadband quantum teleporter. This opens the door to universal QIP and further hybridization schemes between discrete- and continuous-variable techniques (24).

References and Notes

1. C. H. Bennett et al., *Phys. Rev. Lett.* **70**, 1895 (1993).
2. A. Furusawa et al., *Science* **282**, 706 (1998).
3. M. Yukawa, H. Benichi, A. Furusawa, *Phys. Rev. A* **77**, 022314 (2008).
4. J. Yoshikawa et al., *Phys. Rev. A* **76**, 060301 (2007).

5. S. Lloyd, S. L. Braunstein, *Phys. Rev. Lett.* **82**, 1784 (1999).
6. M. Dakna, T. Anhut, T. Opatrný, L. Knöll, D.-G. Welsch, *Phys. Rev. A* **55**, 3184 (1997).
7. A. P. Lund, T. C. Ralph, H. L. Haselgrove, *Phys. Rev. Lett.* **100**, 030503 (2008).
8. A. Ourjoumtey, R. Tualle-Broui, J. Laurat, P. Grangier, *Science* **312**, 83 (2006).
9. J. S. Neergaard-Nielsen, B. M. Nielsen, C. Hettich, K. Mølmer, E. S. Polzik, *Phys. Rev. Lett.* **97**, 083604 (2006).
10. K. Wakui, H. Takahashi, A. Furusawa, M. Sasaki, *Opt. Exp.* **15**, 3568 (2007).
11. A. Ourjoumtey, H. Jeong, R. Tualle-Broui, P. Grangier, *Nature* **448**, 784 (2007).
12. See supporting material on Science Online.
13. H. Jeong, A. P. Lund, T. C. Ralph, *Phys. Rev. A* **72**, 013801 (2005).
14. M. Hillery, R. F. O'Connell, M. O. Scully, E. P. Wigner, *Phys. Rep.* **106**, 121 (1984).
15. D. T. Smith, M. Beck, M. G. Raymer, A. Faridani, *Phys. Rev. A* **70**, 1244 (1993).
16. A. I. Lvovsky, *J. Opt. B* **54**, S556 (2004).
17. S. L. Braunstein, H. J. Kimble, *Phys. Rev. Lett.* **80**, 869 (1998).
18. B. Schumacher, *Phys. Rev. A* **54**, 2614 (1996).
19. M. Ban, *Phys. Rev. A* **69**, 054304 (2004).
20. F. Grosshans, P. Grangier, *Phys. Rev. A* **64**, 010301(R) (2001).
21. L. Mišta Jr., R. Filip, A. Furusawa, *Phys. Rev. A* **82**, 012322 (2010).
22. H. Takahashi *et al.*, *Phys. Rev. Lett.* **101**, 233605 (2008).
23. J. S. Neergaard-Nielsen *et al.*, *Phys. Rev. Lett.* **105**, 053602 (2010).
24. D. Gottesman, A. Kitaev, J. Preskill, *Phys. Rev. A* **64**, 012310 (2001).
25. Supported by the Strategic Information and Communications R&D Promotion (SCOPE) program

of the Ministry of Internal Affairs and Communications of Japan, Special Coordination Funds for Promoting Science and Technology, Grants-in-Aid for Scientific Research, Global Center of Excellence, Advanced Photon Science Alliance, and Funding Program for World-Leading Innovative R&D on Science and Technology (FIRST) commissioned by the Ministry of Education, Culture, Sports, Science and Technology of Japan, Academy of Sciences of the Czech Republic, Japanese Society for the Promotion of Science, and the Australian Research Council, Center of Excellence (grant CE11E0096).

Supporting Online Material

www.sciencemag.org/cgi/content/full/332/6027/330/DC1
Materials and Methods

30 November 2010; accepted 14 February 2011
10.1126/science.1201034

Enhanced Enantioselectivity in Excitation of Chiral Molecules by Superchiral Light

Yiqiao Tang¹ and Adam E. Cohen^{1,2*}

A molecule or larger body is chiral if it cannot be superimposed on its mirror image (enantiomer). Electromagnetic fields may be chiral, too, with circularly polarized light (CPL) as the paradigmatic example. A recently introduced measure of the local degree of chiral dissymmetry in electromagnetic fields suggested the existence of optical modes more selective than circularly polarized plane waves in preferentially exciting single enantiomers in certain regions of space. By probing induced fluorescence intensity, we demonstrated experimentally an 11-fold enhancement over CPL in discrimination of the enantiomers of a biperylene derivative by precisely sculpted electromagnetic fields. This result, which agrees to within 15% with theoretical predictions, establishes that optical chirality is a fundamental and tunable property of light, with possible applications ranging from plasmonic sensors to absolute asymmetric synthesis.

Circular dichroism (CD) describes the differential absorption of left- and right-circularly polarized light by a chiral molecule (1). CD spectroscopy provides important structural information and is widely used for characterizing organic and biological molecules. Yet CD measurements are challenging because the signals are typically weak. For most small molecules, the absorption cross sections for left- and right-circularly polarized light differ by less than one part per thousand (2).

The weakness of CD is a consequence of the small size of most molecules relative to the wavelength of light: The circularly polarized field undergoes a barely perceptible twist over a distance of molecular dimensions (3). This twist provides only a weak perturbation to the overall rate of excitation. Finding ways to enhance CD could lead to improved sensors and may open the door to efficient absolute asymmetric synthesis in which light provides the chiral bias.

¹Department of Physics, Harvard University, 12 Oxford Street, Cambridge, MA 02138, USA. ²Department of Chemistry and Chemical Biology, Harvard University, 12 Oxford Street, Cambridge, MA 02138, USA.

*To whom correspondence should be addressed. E-mail: cohen@chemistry.harvard.edu

Substantial effort has been devoted to calculating CD spectra for a variety of molecules at multiple levels of theory (4, 5) and to designing molecules that show large optical dissymmetry at particular wavelengths (2). These treatments focused on the molecular aspects of CD, relying on circularly polarized plane waves as the source of excitation.

With the advent of near-field optics, plasmonics, photonic crystals, and metamaterials, scientists now construct electromagnetic fields that are far more contorted than is circularly polarized light (CPL) (6, 7). Several groups have sought to use metallic nanostructures to enhance chiroptical phenomena (8–10). Recently, Hendry *et al.* reported enhanced CD in samples of proteins adsorbed onto chiral metal nanostructures (11). These experiments may lead to important practical applications, but the complexity of the geometries has thus far prevented a quantitative comparison with theory. Other groups have applied techniques of coherent control to enantioselective excitation of chiral molecules, but these strategies are specific to a single compound or narrow class of compounds (12).

We wondered whether it would be possible to design non-plane-wave monochromatic solutions to Maxwell's equations that showed en-

hanced dissymmetry in their excitation of all chiral molecules, regardless of molecular structure. Our intuitive picture was that enhanced dissymmetry should occur if the field lines reoriented over a distance much shorter than the free-space wavelength, ideally over molecular dimensions. Then the spatial scales of chirality in the molecule and the light would match (13).

To guide the design of superchiral light, we sought a measure of optical chirality, a way to determine whether one field couples more strongly to molecular chirality than does another (14). Such a measure must have certain symmetries. Chirality is time even (a movie of a right-handed screw shows a right-handed screw whether the movie is played forward or backward), parity odd (a mirror image of a right-handed screw is a left-handed screw), and scalar (a right-handed screw remains right-handed no matter its orientation). A classification of the well-known conserved electrodynamic quantities by their symmetries (Fig. 1A) reveals a vacancy where there should be a time-even, parity-odd scalar. Any measure of optical chirality must lie in this empty fourth quadrant (15).

On the basis of these symmetry considerations, we proposed the existence of a physical quantity, optical chirality, defined in Fig. 1A. The mathematical structure of optical chirality captures the degree to which the electric and magnetic field vectors **E** and **B** wrap around a helical axis at each point in space. In the 1960s, Lipkin studied this same quantity, but he and others dismissed it as lacking physical significance (16, 17).

Is optical chirality observable? In the standard theory of CD, the dissymmetry factor, $g(\lambda)$, measures the fractional difference in rates of excitation between left- and right-circularly polarized light at wavelength λ (18). We generalized the theory of CD to include pairs of arbitrary mirror-image fields and found that the dissymmetry factor becomes (14)

$$g = g_{\text{CPL}} \left(\frac{cC}{2U_{\text{e}}\omega} \right) \quad (1)$$

where g_{CPL} is the dissymmetry factor under circularly polarized light, c is the speed of light,

C is the optical chirality, U_e is the local electric energy density, and ω is the angular frequency. The quantity g_{CPL} is purely molecular, a function of molecular transition moments and energy levels. The quantity $(cC/2\omega U_e)$ is purely electrodynamic. The fact that these two quantities combine in a simple product implies that, if one can enhance the ratio $(cC/2\omega U_e)$ relative to its value for CPL, then one can enhance the dissymmetry in light-matter interactions for all chiral molecules.

Equation 1 was derived for a model in which CD arises through an interference between electric dipole and magnetic dipole transitions. This model is valid in an isotropic sample, that is, one with a large number of molecules, all randomly oriented. The formula is equally valid for molecules that are freely tumbling, as in a liquid, or randomly immobilized, as in a polymer matrix. The possible contribution of electric dipole–electric quadrupole transitions in anisotropic samples is discussed below. Equation 1 does not apply to chiral structures of size comparable to the free-space wavelength, in which case higher multipole transitions contribute to CD.

In CPL, the field vectors rotate at a constant rate along the propagation direction, undergoing a complete revolution once per wavelength (Fig. 1B). In this case, the quantity $cC/2\omega U_e = 1$. Do Maxwell's equations permit solutions in which this quantity exceeds 1? We deduced the existence of superchiral light as follows. First, we drew a configuration of electric fields that appears highly chiral (Fig. 1C, bottom). The field vectors rotate through nearly 180° in a distance much shorter than half the free-space wavelength. Then we sought solutions to Maxwell's equations that generated these fields in at least one point in space. An optical standing wave was a promising candidate because near the nodes U_e is small, yet the field appears to have a strong twist. To achieve a chiral configuration, the standing wave is made from counterpropagating beams of CPL of opposite handedness and slightly different amplitude. The resulting superchiral field configuration is shown in Fig. 1C. Near the nodes of this standing wave, $g/g_{\text{CPL}} > 1$ (14).

Superchiral light is easily generated by reflecting CPL off a mirror with reflectivity $R < 1$: At normal incidence, the reflected wave has opposite handedness, slightly lower intensity, and a fixed phase relative to the incident wave—precisely the conditions needed to generate superchirality upon interference with the incident wave. If a chiral molecule is placed at a node in a superchiral wave, the dissymmetry is predicted to be enhanced by a factor of

$$g/g_{\text{CPL}} = (1 + \sqrt{R})/(1 - \sqrt{R}) \quad (2)$$

which becomes large as R approaches 1.

We performed a conceptually simple experiment to probe the interaction of superchiral light with chiral matter. Several factors combined to

dictate the choice of chiral molecule. The regions of enhanced chiral selectivity were too thin to detect by direct differential absorption, so we sought a fluorescent compound with which we could detect differential induced fluorescence (19). Many chiral molecules are fluorescent in the ultraviolet, but we sought a compound with visible excitation and emission because of the availability of better optics and more stable light

sources in the visible. The molecule also needed to have a large value of g_{CPL} at a wavelength close to an available laser line. The chiral biperylene derivative shown in Fig. 2A met these requirements (20).

The key challenge was to position a 10-nm-thick film of the chiral compound relative to a mirror with a separation that drifted by less than $\lambda/10^4 \approx 0.5 \text{ \AA}$ over the course of the experiment.

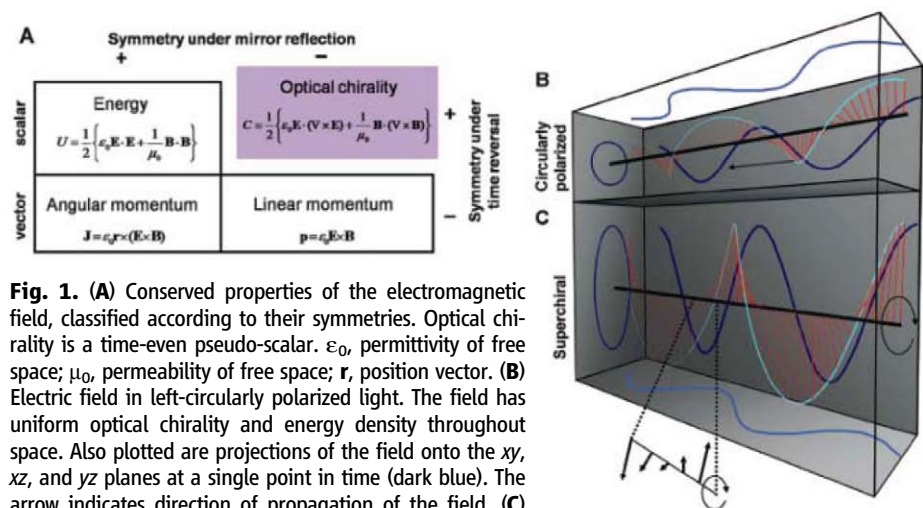


Fig. 1. (A) Conserved properties of the electromagnetic field, classified according to their symmetries. Optical chirality is a time-even pseudo-scalar. ϵ_0 , permittivity of free space; μ_0 , permeability of free space; \mathbf{r} , position vector. (B) Electric field in left-circularly polarized light. The field has uniform optical chirality and energy density throughout space. Also plotted are projections of the field onto the xy , xz , and yz planes at a single point in time (dark blue). The arrow indicates direction of propagation of the field. (C) Electric field in superchiral light, calculated from the analytical expression at a single point in time. The superchiral field rotates about its axis but does not propagate. At any instant, the projection of the field along the propagation axis is an ellipse, but over time the field at each point traces out a circle. Near the superchiral nodes, the ratio of optical chirality to electric energy density is larger than in CPL. In this plot, the ratio of the left- and right-field amplitudes is 2:1. In the experiment, the ratio was 1.17:1. (Bottom) Field configuration near a superchiral node.

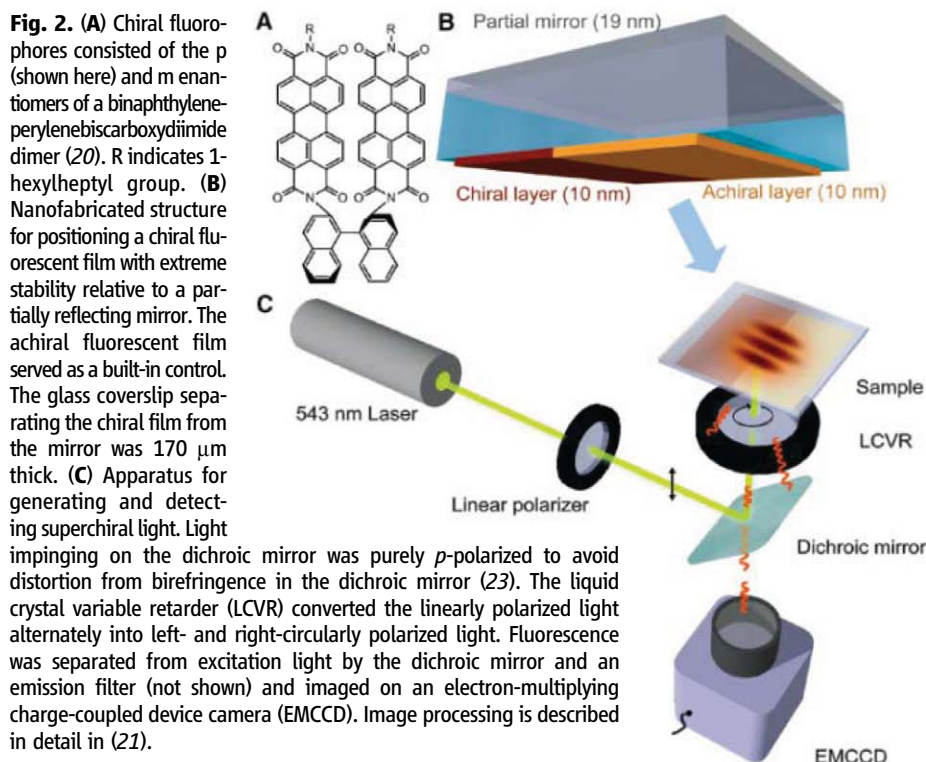


Fig. 2. (A) Chiral fluorophores consisted of the p (shown here) and m enantiomers of a binaphthylene-perylenebiscarboxydiimide dimer (20). R indicates 1-hexylheptyl group. (B) Nanofabricated structure for positioning a chiral fluorescent film with extreme stability relative to a partially reflecting mirror. The achiral fluorescent film served as a built-in control. The glass coverslip separating the chiral film from the mirror was $170 \mu\text{m}$ thick. (C) Apparatus for generating and detecting superchiral light. Light

impinging on the dichroic mirror was purely p -polarized to avoid distortion from birefringence in the dichroic mirror (23). The liquid crystal variable retarder (LCVR) converted the linearly polarized light alternately into left- and right-circularly polarized light. Fluorescence was separated from excitation light by the dichroic mirror and an emission filter (not shown) and imaged on an electron-multiplying charge-coupled device camera (EMCCD). Image processing is described in detail in (21).

To achieve this stability, we fabricated the sandwich geometry shown in Fig. 2B (21). A 19-nm-thick Al mirror was deposited on one side of a glass coverslip, yielding a reflectivity $R = 0.72$. The other side of the coverslip was coated with a 10-nm-thick film of the chiral fluorophores in an amorphous polymer host. Half of the chiral film was then removed by plasma etching and replaced with an equivalent film of an achiral perylene derivative to serve as a control. We made two samples containing opposite enantiomers in the chiral region.

The samples were placed in an optical system designed to generate superchiral light (Fig. 2C). CPL ($\lambda = 543$ nm) was directed through the chiral film onto the mirror at normal incidence, with the expectation that the partially reflected wave would interfere with the incident wave to generate a standing wave with superchiral nodes. A slight wedge angle between the faces of the coverslip caused different regions of the chiral film to reside in different parts of the standing wave, with an in-plane fringe spacing of 2 mm. We took measures to compensate for pointing instability and power fluctuations in the laser, as well as all systematic artifacts, allowing fluorescence intensity measurements to a fractional precision of 4×10^{-5} (21). We imaged the fluorescence from the film alternately under left- and right-superchiral light and calculated a dissymmetry factor at each point in the image, based on the fractional difference in fluorescence under mirror-image field configurations.

Figure 3, top, shows plots of the average fluorescence intensity as a function of position in

the superchiral standing wave, and Fig. 3, bottom, shows plots of the dissymmetry factor along a line cutting through a superchiral node. The superchiral nodes were located by their correspondence with a minimum in the average fluorescence intensity. The maximum dissymmetry factors were $g = 1.50 \times 10^{-2} \pm 0.08 \times 10^{-2}$ (SEM) and $g = -1.65 \times 10^{-2} \pm 0.08 \times 10^{-2}$ for the p and m enantiomers, respectively. The achiral control samples had $g \approx 0$ throughout the standing wave.

To determine the degree of superchiral enhancement, we repeated the experiments by using conventional CPL. Samples were prepared identically to above, except that the partially reflecting mirror was omitted so that no standing wave was generated. The dissymmetry factors under conventional CPL were $g_{\text{CPL}} = 1.41 \times 10^{-3} \pm 0.03 \times 10^{-3}$ (for p) and $g_{\text{CPL}} = -1.42 \times 10^{-3} \pm 0.04 \times 10^{-3}$ (for m) and were independent of position (fig. S4). Thus, the superchiral enhancements were 10.6 ± 0.6 (for the p enantiomer) and 11.6 ± 0.6 (for the m enantiomer).

A quantitative comparison of these results to theory requires consideration of the roles of several types of electronic transitions. Conventional CD in isotropic media (solid or liquid) arises through an electric dipole–magnetic dipole interference. This is the transition studied in (14) and described by Eq. 1. The present experiment involves molecules immobilized in an amorphous polymer host. Although we deem it unlikely, it is conceivable that the ensemble of fluorophores developed a net orientation through short-range interactions with the glass substrate during the deposition of the polymer film. In

oriented chiral molecules, electric dipole–electric quadrupole transitions may contribute to CD as well.

We recently calculated the contribution of electric dipole–electric quadrupole transitions to optical dissymmetry in arbitrary electromagnetic fields (22). The relevant local field property is a third-rank tensor, $\Theta_{ijk} = E_i \frac{\partial}{\partial x_j} E_k$, where i, j , and k each vary over the three Cartesian coordinates. Remarkably, for the superchiral fields studied here, the enhancement in optical dissymmetry due to electric dipole–electric quadrupole transitions is identical to the enhancement due to electric dipole–magnetic dipole transitions (22). Thus, the fields are truly superchiral in that they do not distinguish between the two sources of molecular optical dissymmetry.

On the basis of these considerations, we find that the enhancement in optical dissymmetry is expected to be a function only of the reflectivity of the Al mirror, given by Eq. 2, regardless of possible orientational order in the film. For a film with reflectivity $R = 0.72$, Eq. 2 predicts a 12.2-fold enhancement at the superchiral nodes, within 15% of the experimental value.

The physical origin of this enhancement is somewhat subtle. A simple calculation shows that the optical chirality is the sum of the optical chiralities of the incident and reflected waves. This quantity is independent of position—it shows no special features at the nodes. Where, then, does the enhanced dissymmetry come from? The enhanced dissymmetry comes from the suppression of the electric energy density at the nodes. Pure electric dipole transitions form an achiral background and are excited at a rate proportional to the electric energy density. At the nodes, the achiral background becomes small, and so the fractional difference in excitation between mirror-image fields becomes large. This fact is illustrated in Fig. 3, bottom, where the black lines are proportional to the inverse of the average fluorescence intensity. The enhanced dissymmetry factor comes at the expense of a decreased overall rate of excitation.

It is perhaps surprising that superchiral light can be created with far-field optics alone. One might expect near-field or plasmonic effects to be necessary to generate highly twisted fields. This observation led us to ask whether there are any local configurations of electric and magnetic fields and field gradients that can be made with near-field but not far-field optics. One could imagine that the constraints imposed on propagating plane waves might rule out certain local field configurations that were otherwise allowed by Maxwell's equations. In (22), we showed that any local field configuration allowed by Maxwell's equations can be created at a single point in space through judicious interference of multiple far-field plane waves. These exotic local fields can enhance a wide variety of molecular multipole transitions, of which the chiral ones discussed here are but one example. Many of these

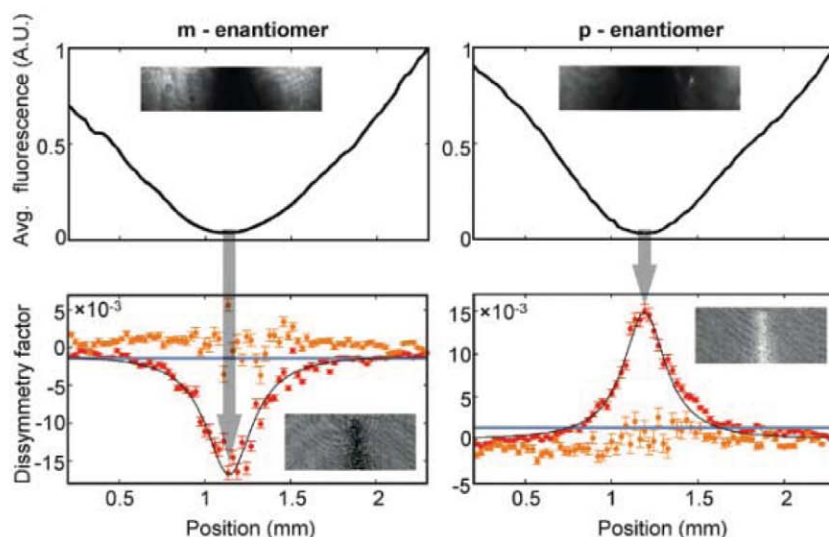


Fig. 3. Observation of enhanced optical dissymmetry in superchiral light. **(Top)** Average fluorescence intensity distribution in a superchiral standing wave. Superchiral nodes were identified by their correspondence with minima in the average fluorescence intensity. A.U., arbitrary units. (Insets) Images of the average fluorescence. **(Bottom)** Dissymmetry factor along a line cutting through a superchiral node in chiral (red) and achiral (orange) regions. Blue line marks the value of the position-independent dissymmetry factor measured in chiral films without superchiral enhancement. Black line is the theoretical prediction for the dissymmetry factor, calculated in (21). Error bars are SEM of 400 measurements. (Insets) Spatial maps of the dissymmetry factor near the superchiral nodes.

multipole spectroscopies have not previously been demonstrated.

The chiral enhancement reported here is not a fundamental limit. Larger enhancement may be obtained at the expense of lower overall excitation rate simply by choosing a mirror with a higher reflectivity. Enantioselective excitation with superchiral light can be performed on any chiral small molecule and requires only an inexpensive continuous-wave laser. The existence of superchiral light raises exciting possibilities to sculpt the three-dimensional shape of the electromagnetic field, to bring other dark transitions to light.

References and Notes

1. L. D. Barron, *Molecular Light Scattering and Optical Activity* (Cambridge Univ. Press, Cambridge, 2004).
2. N. Berova, K. Nakanishi, R. Woody, *Circular Dichroism: Principles and Applications* (Wiley, New York, 2000).
3. S. F. Mason, *Molecular Optical Activity and the Chiral Discriminations* (Cambridge Univ. Press, New York, 1982).
4. J. Autschbach, T. Ziegler, S. J. A. van Gisbergen, E. J. Baerends, *J. Chem. Phys.* **116**, 6930 (2002).
5. P. J. Stephens, *J. Phys. Chem.* **89**, 748 (1985).
6. E. Ozbay, *Science* **311**, 189 (2006).
7. M. Aeschlimann *et al.*, *Nature* **446**, 301 (2007).
8. I. Lieberman, G. Shemer, T. Fried, E. M. Kosower, G. Markovich, *Angew. Chem. Int. Ed.* **47**, 4855 (2008).
9. V. P. Drachev *et al.*, *J. Opt. Soc. Am. B* **18**, 1896 (2001).
10. V. A. Fedotov, A. S. Schwanecke, N. I. Zheludev, V. V. Khardikov, S. L. Prosvirnin, *Nano Lett.* **7**, 1996 (2007).
11. E. Hendry *et al.*, *Nat. Nanotechnol.* **5**, 783 (2010).
12. M. Shapiro, P. Brumer, *Rep. Prog. Phys.* **66**, 859 (2003).
13. N. Yang, Y. Tang, A. E. Cohen, *Nano Today* **4**, 269 (2009).
14. Y. Tang, A. E. Cohen, *Phys. Rev. Lett.* **104**, 163901 (2010).
15. L. D. Barron, *Nature* **238**, 17 (1972).
16. D. M. Lipkin, *J. Math. Phys.* **5**, 696 (1964).
17. T. W. B. Kibble, *J. Math. Phys.* **6**, 1022 (1965).
18. L. Rosenfeld, *Z. Phys. A Hadrons Nuclei* **52**, 161 (1929).
19. D. H. Turner, I. Tinoco Jr., M. Maestre, *J. Am. Chem. Soc.* **96**, 4340 (1974).
20. H. Langhals, J. Gold, *Liebigs Ann.* **1997**, 1151 (1997).
21. Materials and methods are detailed in supporting material available on Science Online.
22. N. Yang, A. E. Cohen, *J. Phys. Chem. B*, published online 6 January 2011 (10.1021/jp1092898).
23. Y. Tang, T. A. Cook, A. E. Cohen, *J. Phys. Chem. A* **113**, 6213 (2009).

Acknowledgments: We thank H. Langhals for the chiral biperylene compound and L. Men for help with the figures. Financial support was provided by the Nano-Enabled Technology Initiative of MITRE Corporation, a Defense Advanced Research Projects Agency Young Faculty Award, the Office of Naval Research Young Investigator Program, and the Harvard Center for Nanoscale Systems.

Supporting Online Material

www.sciencemag.org/cgi/content/full/332/6027/333/DC1
Materials and Methods
Figs. S1 to S4

13 January 2011; accepted 17 February 2011
10.1126/science.1202817

Deterministic Preparation of a Tunable Few-Fermion System

F. Serwane,^{1,2,3,*†} G. Zürn,^{1,2†} T. Lompe,^{1,2,3} T. B. Ottenstein,^{1,2,3} A. N. Wenz,^{1,2} S. Jochim^{1,2,3}

Systems consisting of few interacting fermions are the building blocks of matter, with atoms and nuclei being the most prominent examples. We have created a few-body quantum system with complete control over its quantum state using ultracold fermionic atoms in an optical dipole trap. Ground-state systems consisting of 1 to 10 particles are prepared with fidelities of ~90%. We can tune the interparticle interactions to arbitrary values using a Feshbach resonance and have observed the interaction-induced energy shift for a pair of repulsively interacting atoms. This work is expected to enable quantum simulation of strongly correlated few-body systems.

The exploration of naturally occurring few-body quantum systems such as atoms and nuclei has been extremely successful, largely because they could be prepared in well-defined quantum states. Because these systems have limited tunability, researchers created quantum dots—"artificial atoms"—in which properties such as particle number, interaction strength, and confining potential can be tuned (1, 2). However, quantum dots are generally strongly coupled to their environment, which hindered the deterministic preparation of well-defined quantum states.

In contrast, ultracold gases provide tunable systems in a highly isolated environment (3, 4). They have been proposed as a tool for quantum simulation (5, 6), which has been realized experimentally for various many-body systems (7–10). Achieving quantum simulation of few-body systems is more challenging because it requires complete control over all degrees of freedom: the particle number,

the internal and motional states of the particles, and the strength of the interparticle interactions. One possible approach to this goal is using a Mott insulator state of atoms in an optical lattice as a starting point. In this way, systems with up to four bosons per lattice site have been prepared in their ground state (11, 12). Recently, single lattice sites have been addressed individually (13).

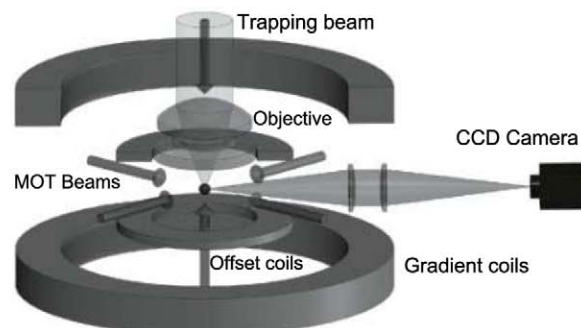
In single isolated trapping geometries, researchers could suppress atom number fluctuations by loading bosonic atoms into small-volume optical dipole traps (14–18). However, these experiments were not able to gain control over the system's quantum state.

We prepare few-body systems consisting of 1 to 10 fermionic atoms in a well-defined quan-

tum state, making use of Pauli's principle, which states that each single-particle state cannot be occupied by more than one identical fermion. Therefore, the occupation probability of the lowest-energy states approaches unity for a degenerate Fermi gas, and we can control the number of particles by controlling the number of available single-particle states. We realize this by deforming the confining potential such that quantum states above a well-defined energy become unbound. This approach requires a highly degenerate Fermi gas in a trap whose depth can be controlled with a precision much higher than the separation of its energy levels.

To fulfill these requirements, we use a small-volume optical dipole trap with large level spacing. This microtrap is created by the focus of a single laser beam (Fig. 1) with a waist of $w_0 \lesssim 1.8 \mu\text{m}$ and measured radial and axial trapping frequencies $(\omega_r, \omega_a) = 2\pi \times (14.0 \pm 0.1, 1.487 \pm 0.010) \text{ kHz}$ (19). We load the microtrap from a reservoir of cold atoms. The reservoir consists of a two-component mixture of ^6Li atoms in the two lowest-energy Zeeman substates $|F = 1/2, m_F = +1/2\rangle$ and $|F = 1/2, m_F = -1/2\rangle$ (labeled state |1⟩ and |2⟩) in a large-volume optical dipole trap. The reservoir has a degeneracy of $T/T_F \approx 0.5$ (19), where T_F is the Fermi temperature. We superimpose the microtrap with the reservoir and transfer about 600 atoms into the microtrap. After removal of the reservoir, the degeneracy of the system is determined by $T_F \approx 3 \mu\text{K}$ in the microtrap and the temperature $T \lesssim 250 \text{ nK}$

Fig. 1. Experimental setup. Systems with up to 10 fermions are prepared with ^6Li atoms in a micrometer-sized optical dipole trap created by the focus of a single laser beam. The number of atoms in the samples is detected with single-atom resolution by transferring them into a compressed magneto-optical-trap (MOT) and collecting their fluorescence on a CCD camera. A Feshbach resonance allows one to tune the interaction between the particles with a magnetic offset field.



¹Physikalisches Institut, Ruprecht-Karls-Universität Heidelberg, 69120 Heidelberg, Germany. ²Max-Planck-Institut für Kernphysik, Saupfercheckweg 1, 69117 Heidelberg, Germany. ³ExtreMe Matter Institute EMMI, GSI Helmholtzzentrum für Schwerionenforschung, 64291 Darmstadt, Germany.

*To whom correspondence should be addressed. E-mail: friedhelm.serwane@mpi-hd.mpg.de

†These authors contributed equally to this work.

‡Present address: DIOPTIC GmbH, Bergstraße 92A, 69469 Weinheim, Germany.

of the reservoir (20). Assuming thermal equilibrium between the microtrap and the reservoir, this corresponds to $T/T_F \lesssim 0.08$. According to Fermi-Dirac statistics, this yields an occupation probability for the lowest state exceeding 0.9999, which is large enough not to constrain our preparation scheme.

To spill the excess atoms from the microtrap, we add a linear potential in the axial direction by applying a magnetic field gradient. To obtain the same potential for both components, we apply the gradient at a large magnetic offset field where the difference in the magnetic moments of states $|1\rangle$ and $|2\rangle$ is negligible. A particular magnetic field is then chosen so that the interaction strength between atoms in the different states vanishes because of a nearby Feshbach resonance (fig. S2). By varying the depth of the microtrap and the strength of the magnetic field gradient, we can control the number of bound states in the potential (Fig. 2A). If fewer than 10 bound states remain, the system is essentially one-dimensional because of the approximate 1:10 aspect ratio of the trap; consequently, each energy level is occupied by one atom per spin state. During the spilling process, we adiabatically tilt the potential, wait to let atoms in unbound states escape, and then ramp the potential back up (19).

To probe the prepared systems, it is necessary to measure the number of atoms in the microtrap

with single-atom resolution and near-unity fidelity. We achieve this by releasing the atoms from the microtrap, recapturing them in a compressed magneto-optical trap, and then recording their fluorescence with a charge-coupled device (CCD) camera (Fig. 1). With this technique, we can count the total number of atoms in the magneto-optical trap with a fidelity exceeding 99% for 1 to 10 atoms (fig. S1).

Figure 2 shows the mean atom number and its variance as a function of the minimum microtrap depth during the spilling process. The atom number shows a step-like dependence on the trap depth with plateaus for even atom numbers. These plateaus appear at trap depths where the potential barrier for atoms in the uppermost level becomes so low that these atoms leave the trap on a time scale that is shorter than the duration of the spilling process. A simple estimation (21) shows that the lifetime of this state can be up to three orders of magnitude shorter than the lifetime of the lower states. When an appropriate trap depth is chosen, the fluctuations in the atom number are as low as $\text{var}/\langle N \rangle = \sigma^2/\langle N \rangle = 0.017$ for eight atoms, corresponding to a suppression of 18 dB compared to a system obeying Poissonian statistics. We can then calculate an upper bound for the degree of degeneracy in the microtrap of $T/T_F < 0.19$ by assuming that all fluctuations result from holes in the Fermi distribution; this provides a complemen-

tary method to probe the degeneracy of the lowest-energy states of an ultracold Fermi gas, which is conceptually related to recent studies of antibunching in degenerate Fermi gases (22, 23).

To estimate the probability of finding the system in its ground state after the spilling process, we bin the measured fluorescence signal into a histogram (Fig. 3B). For the preparation of systems consisting of two fermions, we obtain a fidelity of 96(1)%. The error is the statistical error calculated by assuming that the occurrence of samples with undesired atom number follows a Poissonian distribution. From combinatorial considerations (19), we deduce that only a negligible fraction of the prepared two-particle systems are not in the ground state before we ramp the potential back up at the end of the preparation process. To check whether we create excitations in the system by ramping up the potential, we perform the spilling process a second time. After the second spilling process, we measure a fidelity of 92(2)% for preparing two atoms. This yields an upper bound of 6(2)% for the excitation probability during the potential ramps (19). If we assume the same excitation probability for ramping up and down, we get an estimated fidelity of 93(2)% to prepare the system in its ground state after ramping the potential back up after the first spilling process. For eight atoms, we find a ground-state preparation probability of 84(2)%. By varying the time between the two spilling processes, we found the $1/e$ -lifetime of the prepared two-particle system in its ground state to be ~ 60 s, which shows the high degree of isolation from the environment.

To realize configurations with an arbitrary imbalance in the number of atoms in state $|1\rangle$ and $|2\rangle$, we prepare balanced systems and perform a second spilling process that only removes atoms in state $|1\rangle$. We do this by changing the value of the magnetic offset field to 40 G where atoms in state $|2\rangle$ have negligible magnetic moment and are therefore unaffected by the magnetic field gradient (fig. S2). Using this technique, we have created imbalanced systems with fidelities similar to those in the balanced case (19).

Precise control over the trapping potential is not only essential to prepare few-body samples, it is also an effective tool to probe strongly interacting systems. We use it to explore one of the simplest nontrivial few-body systems: two non-identical fermions with repulsive interactions in the ground state of a one-dimensional harmonic trap. We first prepare a noninteracting pair of atoms in states $|1\rangle$ and $|2\rangle$ in the ground state of the trap. Then we lower the potential barrier such that the two atoms slowly escape the trap on a time scale of $\tau = 630 \pm 120$ ms, which we measure by recording the decrease in the mean atom number as a function of hold time (Fig. 4B).

To repeat the measurement for two atoms with repulsive interaction, we tune the scattering length a to a large positive value, $a = 4100 a_0$, where a_0 is the Bohr radius, using a Feshbach resonance. In this case, we observe a much higher initial loss rate followed by a slow decay. This fast initial loss can

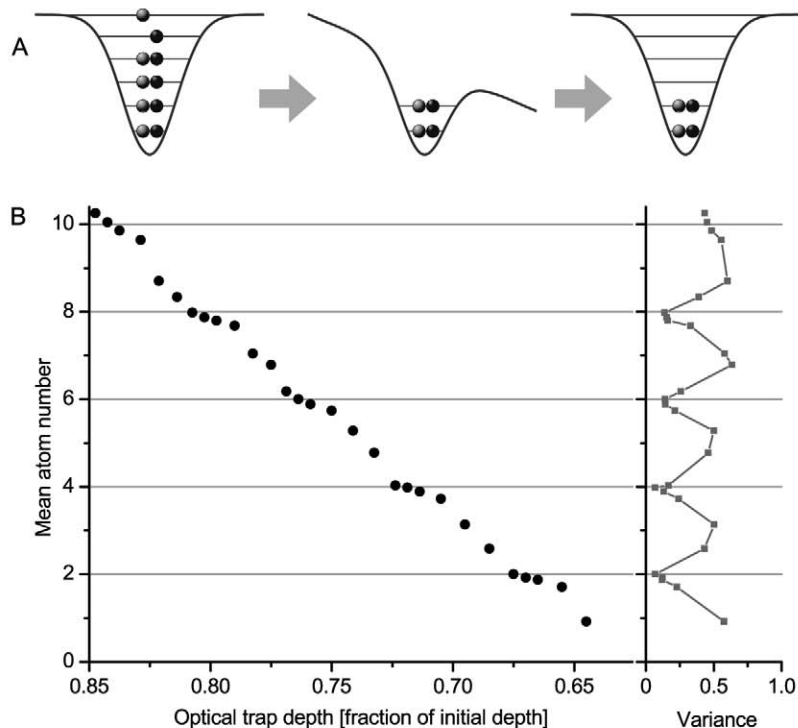


Fig. 2. (A) The spilling process. Starting from a degenerate two-component Fermi gas of about 600 atoms in the microtrap, we create few-particle samples by adiabatically deforming the potential to spill atoms in higher levels. After the potential has been restored, the system is in a well-defined few-particle quantum state. (B) Controlling the number of quantum states. When the trap depth is reduced, the mean atom number decreases in steps of two because each energy level in the trap is occupied by one atom per spin state. Each data point is the average of ~ 190 measurements with σ as the standard deviation and $\text{var} = \sigma^2$ as the variance (shown on the right) (C). For even atom numbers, the number fluctuations are strongly suppressed. For eight atoms, we achieve a suppression of 18 dB of $\text{var}/\langle N \rangle$ compared to a system obeying the Poissonian statistics.

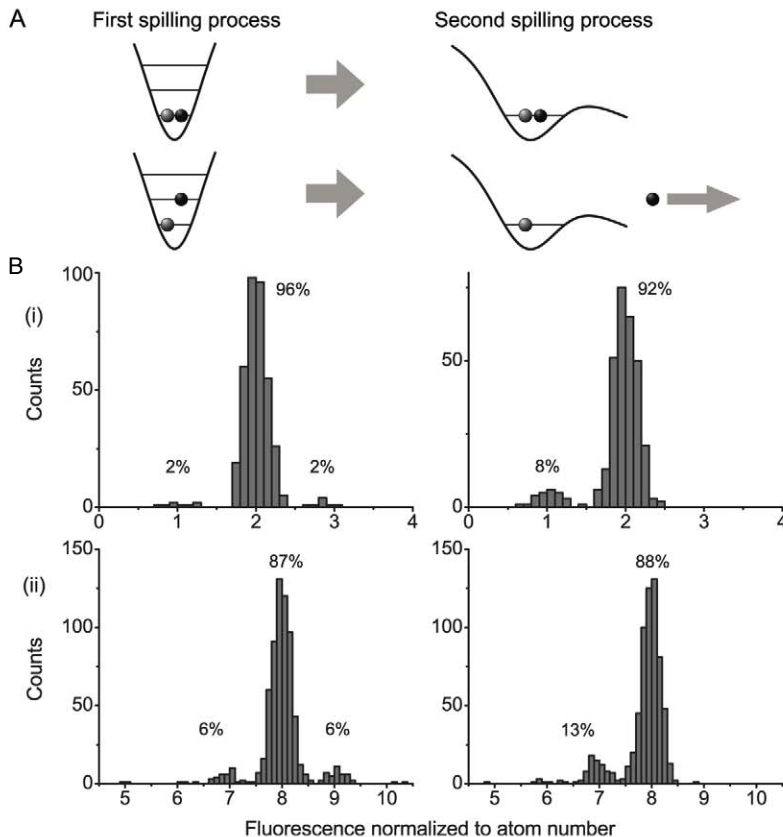
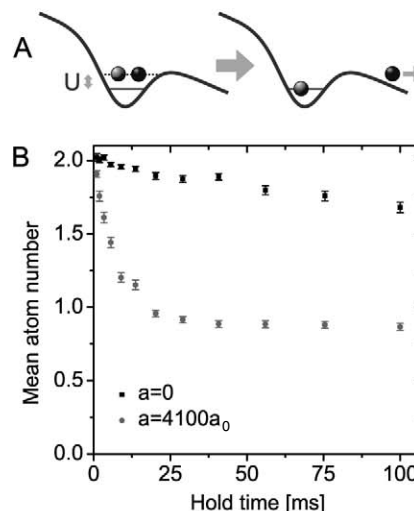


Fig. 3. (A) Fidelity of preparing systems in the ground state. To determine how many of the prepared few-particle systems are in their ground state, we repeat the spilling process. This removes atoms in higher levels but leaves the ground state unchanged. (B) Histograms after the first and second spilling process for the preparation of (i) two atoms and (ii) eight atoms. The numbers above the peaks give the relative occurrences of the counts within the corresponding peaks. The fidelity after the second spilling process (right) remains almost unchanged, indicating that the ground state is prepared with high fidelity.

Fig. 4. (A) By tuning the barrier height, we can prepare systems where the atoms leave the trap with a well-defined rate. Interactions cause an energy shift U and thereby change the effective height of the potential barrier. (B) The barrier is chosen such that two noninteracting atoms ($a = 0$) escape from the trap on a time scale of $\tau = 630 \pm 120$ ms (black squares). With repulsive interactions ($a = 4100a_0$), we observe a much faster escape of one atom. After this atom has left the trap, the loss of the second atom becomes suppressed (circles). Each data point is the average of ~ 190 measurements. The error bars show the SEM.



be explained by the energy shift U of the ground state due to repulsive interactions, which effectively decreases the height of the potential barrier (Fig. 4A). Because the system is quasi-one-dimensional for the lowest 10 axial states, one has to consider the radial confinement (24) for the calculation of U (25). Given the trap parameters, one expects a shift U on the order of half the axial level spacing per particle. After one of the atoms

has left the trap, the interaction energy drops to zero, leaving the remaining atom in the unperturbed ground state of the potential. Within our measurement accuracy, we measure an equal probability for the remaining atom to be in state $|1\rangle$ and $|2\rangle$. By developing theoretical models for these interaction-induced dynamics, one can use this method to quantitatively study strongly interacting systems.

The system we created is well suited for quantum simulation with fully controlled few-body systems. For attractive interactions, it can be used to study Bardeen-Cooper-Schrieffer (BCS)-like pairing in finite systems, which is a model used for the description of nuclei (26). Splitting a trap containing a repulsively interacting pair of atoms into a double well creates entangled pairs of neutral atoms, which can be used for quantum information processing (27, 28). By transferring the prepared ground-state samples into a periodic potential (29), our system can be used to overcome one of the current major challenges of studying quantum many-body physics with ultracold atoms: preparing systems with sufficiently low entropy to explore phenomena such as quantum magnetism.

References and Notes

- W. A. de Heer, *Rev. Mod. Phys.* **65**, 611 (1993).
- S. M. Reimann, M. Manninen, *Rev. Mod. Phys.* **74**, 1283 (2002).
- I. Bloch, J. Dalibard, W. Zwerger, *Rev. Mod. Phys.* **80**, 885 (2008).
- W. Ketterle, M. W. Zwiernik, in *Proceedings of the International School of Physics "Enrico Fermi," Course CLXIV, Varenna, Italy, 20 to 30 June 2006*, M. Inguscio, W. Ketterle, C. Salomon, Eds. (IOS Press, Amsterdam, 2008).
- S. Lloyd, *Science* **273**, 1073 (1996).
- D. Jaksch, C. Bruder, J. I. Cirac, C. W. Gardiner, P. Zoller, *Phys. Rev. Lett.* **81**, 3108 (1998).
- M. Greiner, O. Mandel, T. Esslinger, T. W. Hänsch, I. Bloch, *Nature* **415**, 39 (2002).
- R. Jördens, N. Strohmaier, K. Günter, H. Moritz, T. Esslinger, *Nature* **455**, 204 (2008).
- U. Schneider *et al.*, *Science* **322**, 1520 (2008).
- S. Nascimbène, N. Navon, K. J. Jiang, F. Chevy, C. Salomon, *Nature* **463**, 1057 (2010).
- J. F. Sherson *et al.*, *Nature* **467**, 68 (2010).
- W. S. Bakr *et al.*, *Science* **329**, 547 (2010).
- C. Weitenberg *et al.*, *Nature* **471**, 319 (2011).
- D. Frese *et al.*, *Phys. Rev. Lett.* **85**, 3777 (2000).
- N. Schlosser *et al.*, *Nature* **411**, 1024 (2001).
- C.-S. Chuu *et al.*, *Phys. Rev. Lett.* **95**, 260403 (2005).
- M. Weber *et al.*, *Phys. Rev. A* **73**, 043406 (2006).
- T. Grünzweig *et al.*, *Nat. Phys.* **6**, 951 (2010).
- Materials and methods are available as supporting material on Science Online.
- L. Viverit *et al.*, *Phys. Rev. A* **63**, 033603 (2001).
- T. B. Ottenstein, Few-body physics in ultracold fermi gases, thesis, University of Heidelberg (2010).
- C. Sanner *et al.*, *Phys. Rev. Lett.* **105**, 040402 (2010).
- T. Müller *et al.*, *Phys. Rev. Lett.* **105**, 040401 (2010).
- M. Olshanii, *Phys. Rev. Lett.* **81**, 938 (1998).
- T. Busch, B.-G. Englert, K. Rzażewski, M. Wilkens, *Found. Phys.* **28**, 549 (1998).
- A. Migdal, *Nucl. Phys.* **13**, 655 (1959).
- D. Hayes *et al.*, *Phys. Rev. Lett.* **98**, 070501 (2007).
- M. G. Raizen *et al.*, *Phys. Rev. A* **80**, 030302 (2009).
- B. Zimmermann *et al.*, <http://arxiv.org/abs/1011.1004> (2010).

Acknowledgments. We thank M. G. Raizen for inspiring discussions and M. Weidemüller for the loan of a fiber laser. This work was supported by the Helmholtz Alliance HA216/EMMI and the Heidelberg Center for Quantum Dynamics. We thank J. Ullrich and his group for their support. G.Z. and A.N.W. acknowledge support by the IMPRS-QD.

Supporting Online Material

www.sciencemag.org/cgi/content/full/332/6027/336/DC1
Materials and Methods
Figs. S1 and S2
References

7 December 2010; accepted 14 March 2011
10.1126/science.1201351

A Bicycle Can Be Self-Stable Without Gyroscopic or Caster Effects

J. D. G. Kooijman,¹ J. P. Meijaard,² Jim M. Papadopoulos,³ Andy Ruina,^{4*} A. L. Schwab¹

A riderless bicycle can automatically steer itself so as to recover from falls. The common view is that this self-steering is caused by gyroscopic precession of the front wheel, or by the wheel contact trailing like a caster behind the steer axis. We show that neither effect is necessary for self-stability. Using linearized stability calculations as a guide, we built a bicycle with extra counter-rotating wheels (canceling the wheel spin angular momentum) and with its front-wheel ground-contact forward of the steer axis (making the trailing distance negative). When laterally disturbed from rolling straight, this bicycle automatically recovers to upright travel. Our results show that various design variables, like the front mass location and the steer axis tilt, contribute to stability in complex interacting ways.

A bicycle and rider in forward motion balance by steering toward a fall, which brings the wheels back under the rider [supporting online material (SOM) text S1 and S2] (1). Normally, riders turn the handlebars with their hands to steer for balance. With hands off the handlebars, body-leaning relative to the bicycle frame can also cause appropriate steering. Amazingly, many moving bicycles with no rider can steer themselves so as to balance—likewise with a rigid rider whose hands are off the handlebars. For example, in 1876, Spencer (2, 3) noted that one could ride a bicycle while lying on the seat with hands off, and the film *Jour de Fête* by Jacques Tati, 1949, features a riderless bicycle self-balancing for long distances. Suspecting that bicycle rideability, with rider control, is correlated with self-stability of the passive bicycle, much theoretical research has focused on this bicycle self-stability.

The first analytic predictions of bicycle self-stability were presented independently by French mathematician Emmanuel Carvallo (1897) (4) and Cambridge undergraduate Francis Whipple (1899) (3, 5). In their models and in this paper, a bicycle is defined as a three-dimensional mechanism (Fig. 1A) made up of four rigid objects (the rear frame with rider body B, the handlebar assembly H, and two rolling wheels R and F) connected by three hinges. The more complete Whipple version has 25 geometry and mass parameters. Assuming small lean and steer angles, linear and angular momentum balance—as constrained by the hinges and rolling contact—lead to a pair of coupled second-order linear differential equations for leaning and steering (SOM text S3) (6). Solutions of these equations show that after small perturbations, the motions of a bicycle may exponentially decay in time to upright right straight-ahead motion (asymptotic stability).

This stability typically can occur at forward speeds v near to \sqrt{gL} , where g is gravity and L is a characteristic length (about 1 m for a modern bicycle). Limitations in the model include assumed linearity and the neglect of motions associated with tire and frame deformation, tire slip, and play and friction in the hinges. Nonetheless, modern experiments have demonstrated the accuracy of the Whipple model for a real bicycle without a rider (7).

The simple bicycle model above is energy-conserving. Thus, the asymptotic stability of a bicycle, that the lean and steer angles exponentially decay to zero after a perturbation, is jarring to those familiar with Hamiltonian dynamics. But because of the rolling (non-holonomic) contact of the bicycle wheels, the bicycle—although energy-conserving—is not Hamiltonian, and it is possible for a subset of variables to have exponential stability in time (6, 8). There is no contradiction between exponential decay and energy conservation because for a bicycle, the energy lost from decaying steering and leaning motions goes to increase the forward speed. Unresolved, how-

ever, is the cause of bicycle self-stability. In some sense, perhaps, a self-stable bicycle is something like a system with control, albeit self-imposed.

Rider-controlled stability of bicycles is indeed related to their self-stability. Experiments like those of Jones (9) and R. E. Klein (10) show that special experimental bicycles that are difficult for a person to ride, either with hands on or off, tend not to be self-stable. Both no-hands control (using body bending) and bicycle self-stability depend on “cross terms,” in which leaning causes steering or vice versa. The central question about what causes self-stability is thus reduced to, what causes the appropriate coupling between leaning and steering? The most often discussed of the coupling effects are those due to front-wheel gyroscopic torque and to caster effects from the wheel trailing behind the steer axis. Trail (or “caster trail”) is the distance c that the ground contact point trails behind the intersection of the steering axis with the ground (Fig. 1A).

There is near universal acceptance that either spin angular momentum (gyroscopic effect) or trail, or both, are necessary for bicycle self-stability (3). Active steering of a bicycle front wheel causes a gyroscopic torque on an upright frame and rider. Because the front wheel is relatively light as compared with the more massive bicycle and rider, the effect of this gyroscopic torque on the lean is generally small (SOM text S1) (11). However, coupling the other way—the effect of active bicycle-leaning on hands-free steering—is nonnegligible. For example, when the bicycle has a lean rate to the right the front axle also has a lean rate to the right, and the spinning wheel exerts a clockwise (looking down) reactive torque carried at least in part by the handlebar assembly. This reaction torque tends to turn the handlebars rightward. Thus, the common explanation of no-hands rider control: To steer to the right, the rider bends her upper body to the left, tilting the bicycle and wheels rightward (5). The bicycle

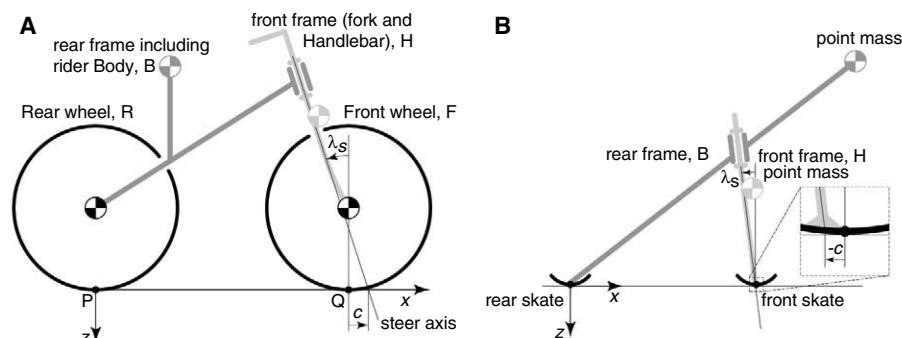


Fig. 1. (A) The bicycle model consists of two interconnected frames, B and H, connected to two wheels, R and F. The model has a total of 25 geometry and mass-distribution parameters. Central here are the rotary inertia I_{yy} of the front wheel, the steer axis angle (“rake”) λ_S , and the trail distance c (positive if contact is behind the steer axis). Depending on the parameter values, as well as gravity g and forward speed v , this bicycle can be self-stable or not. **(B)** A theoretical TMS bicycle is a special case. It is described with only nine free parameters (eight plus trail). The wheels have no net rotary inertia and thus function effectively as ice skates. The two frames each have a single point mass and no mass moments of inertia. A heavy point mass on the rear skate at the ground contact point can prevent the bicycle from tipping over forward; because it has no effect on the linearized dynamics, it is not shown. Even with negative trail ($c < 0$; inset), this non-gyroscopic bicycle can be self-stable.

¹Department of Mechanical Engineering, Delft University of Technology, Delft 2628 CD, Netherlands. ²Department of Engineering Technology, University of Twente, Enschede 7500 AE, Netherlands. ³Department of Engineering and Technology, University of Wisconsin–Stout, Menomonie, WI 54751, USA. ⁴Department of Mechanical Engineering, Cornell University, Ithaca, NY 14853, USA.

*To whom correspondence should be addressed. E-mail: ruina@cornell.edu.

handlebars, considered as freely rotating on the steer axis and forced by the gyroscopic front wheel, thus initially turn rightward. Such leaning-induced steering can be used for rider control of balance. Likewise, this gyroscopic coupling also contributes to a forward-moving passive bicycle self-steering toward a fall (12).

The most thorough discussion of the necessity of gyroscopic coupling of leaning to steering for bicycle self-stability is in the bicycle chapter of the fourth volume of the gyroscope treatise by Klein and Sommerfeld (11, 13). They took the example bicycle parameters from Whipple and eliminated just the spin angular momentum of the wheels. Using their own linearized dynamic stability analysis of the Whipple model, Klein and Sommerfeld concluded that, "... in the absence of gyroscopic actions, the speed range of complete stability would vanish" [(11) p. 866] and make what appears to be a strong general claim about bicycles: "The gyroscopic action, in spite of its smallness, is necessary for self-stability" [(11) p. 866].

They emphasized that the gyroscopic torque does not apply corrective lean torques to a bicycle directly, as others seem to have thought (14). Rather, through the gyroscopic torque, leaning causes steering, which in turn causes the righting accelerations: "The proper stabilizing force, which overwhelms the force of gravity, is the centrifugal force, and the gyroscopic action plays the role of a trigger" [(11) p. 881].

In Jones's famous search for an unrideable bicycle (URB) (9), he added a counter-rotating disk to the handlebar assembly, canceling the gyroscopic self-steering torque of the front wheel. He could still (barely) ride such a nongyro bicycle using no hands. Jones rightly deduced that the gyroscopic effect discussed in (11) was not the only coupling between leaning and steering. Jones emphasized the importance of the front-wheel ground contact being behind the steering axis (positive trail, $c > 0$) (Fig. 1A). Even though the front forks of

modern bicycles are typically bent forward slightly, with the wheel-center forward of the steering axis, all modern bicycles still have positive trail (typically from 2 to 10 cm on modern bicycles) because of the steering axis tilt $\lambda_s > 0$. When Jones modified his bicycle by placing the front-wheel ground contact in front of the steer axis (negative trail, $c < 0$), he could not ride using no hands.

In Jones's view, a bicycle wheel is in part like a caster wheel on a shopping cart, with the wheel trailing behind a vertical pivot axis. If a modern bicycle was rolled forward by guiding the rear frame in a straight line while it was held rigidly upright, the front wheel would quickly self-center like a shopping-cart caster. Jones noted, "The bicycle has only geometrical caster [sic] [trail] stability to provide its self-centering" [(9) p. 40]. Jones's main focus was a second trail effect: The vertical ground contact force on the front-wheel-ground contact point exerts a steering torque on a leaned bicycle even when the bicycle is steered straight. Jones calculated the steer torque caused by lean as a derivative of a static potential energy, neglecting the weight of the front assembly. If a typical modern bicycle is firmly held by the rear frame, leaned to the right, and pressed down hard, then the vertical ground contact force on the front wheel causes a rightward steering torque on the handlebars. The Jones torque can be felt on a normal bicycle by riding in a straight line and bending your upper body to the left, leaning the bicycle to the right: To maintain a straight path, the hands must fight the Jones torque and apply a leftward torque to the handlebars. According to Jones, this torque causes steering toward a fall only when the trail is positive. When the trail is zero, Jones's theory predicts no self-correcting steer torque. Jones seems to conclude that no-hands control authority (the ability to cause steering by body bending) and self-stability both depend on positive trail. A mixture of the two mechanisms Jones discusses certainly suggests that trail is a key part of bicycle stability.

Following Klein and Sommerfeld and Jones, it has become common belief that steering is stable because the front-wheel-ground contact drags behind the steering axis, and leaning is stable because some mixture of gyroscopic torques and trail causes an uncontrolled bicycle to steer in the direction of a fall (3).

Are gyroscopic terms or positive trail, together or separately, really either necessary or sufficient for bicycle self-stability? Following Carvallo, Whipple, Klein and Sommerfeld, and others since [see history in (6)], we began with the linearized equations of motion. Using the numerical values from the benchmark example in (6) and setting the gyroscopic terms to zero, we found that self-stability is lost (SOM text S6.1, which is similar to the result of Klein and Sommerfeld for the Whipple parameters). However, we also found bicycle designs that are self-stable even without gyroscopic terms.

The conflict with Klein and Sommerfeld is partly resolved by noting sign errors in their key stability term (3). Despite their calculation errors, the Whipple bicycle with Whipple's example parameters does indeed lose self-stability when the gyro terms are set to zero. But with their incorrect expressions, Klein and Sommerfeld could make slightly more general claims that are not valid when the sign errors are corrected (3). Whatever generality Klein and Sommerfeld intended (their wording is ambiguous), their result does not apply to bicycles in general.

Similarly, Jones's simplified static-energy calculation seems incomplete in the context of a dynamical system, such as the Whipple and Carvallo models. Jones's static energy calculation only calculates (incompletely) one term, $K_{0\delta_0}$, of the full dynamics equations (3, 6). In a full dynamic analysis, $K_{0\delta_0}$ does not predict the steering of a falling bicycle (3). For example, that term can be nonzero for a bicycle that falls with no self-corrective steering at all. And just as for the gy-

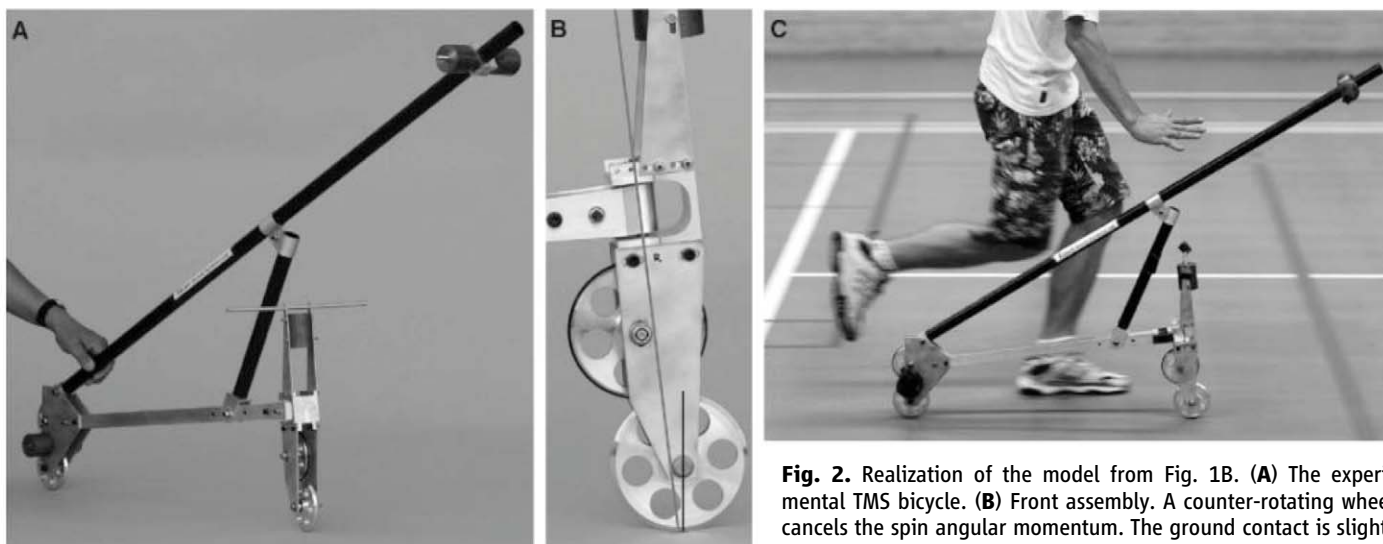


Fig. 2. Realization of the model from Fig. 1B. (A) The experimental TMS bicycle. (B) Front assembly. A counter-rotating wheel cancels the spin angular momentum. The ground contact is slightly ahead of the intersection of the long steer axis line with the

ground, showing the small negative trail (movie S3). (C) Self-stable experimental TMS bicycle rolling and balancing [photo for (C) by S. Rentmeester/FMAX].

roscopic term, we can find designs with zero or negative trail that we predict are self-stable (SOM text S6.2).

In contrast to the conventional claims above for the necessity of gyroscopic terms and trail, we have found no rigorous reasoning that demands either. To understand better what is needed for self-stability, we eliminated as many bicycle parameters as possible (15). Most centrally, we eliminated the gyroscopic terms and set the trail to zero ($c = 0$). We also reduced the mass distribution to just two point masses: one for the rear frame B and one for the steering assembly H (Fig. 1B). With these theoretical parameters, the wheels—having no net spin angular momentum—are mechanically equivalent to skates. These simplifications reduce the number of parameters from Whipple's 25 to a more manageable eight.

Stability analysis of this theoretical two-mass-skate (TMS) bicycle model (SOM text S7), confirmed by means of numerical solution of the governing differential equations, shows that neither gyroscopic terms nor positive trail are needed for self-stability [Routh-Hurwitz analysis shows that all eigenvalues of the theoretical TMS bicycle can have negative real parts at some forward speeds (16)].

We used the stable theoretical TMS bicycle parameters as a basis for building an experimental TMS bicycle (Fig. 2A and SOM text S8 and S9). We used small wheels to minimize the spin angular momentum. To further reduce the gyroscopic terms, following Jones we added counter-spinning disks that rotate backward relative to the lower wheels (Fig. 2B and movie S2). The experimental TMS bicycle was built to have a slightly negative trail ($c = -4 \text{ mm} < 0$) (movie S3). Although the experimental TMS bicycle

looks like a folding scooter, it is still a bicycle (two wheels, two frames, and three hinges).

Because all physical objects have distributed mass, the measured parameters of the experimental TMS bicycle were necessarily slightly different from those of the theoretical design, which was based on point masses. Using measured parameters, we calculated the stability plot of Fig. 3A (SOM text S7 and S8). For rolling speeds greater than 2.3 m/s, all eigenvalues have negative real parts (implying self-stability).

After an initial forward push, the coasting experimental TMS bicycle (Fig. 2C) would remain upright before it slowed down to about 2 m/s (SOM text S10 and S11 and movie S1). As it slowed below 2 m/s, the bicycle would begin to fall. In a perturbation experiment, the stable coasting bicycle ($v > 2.3 \text{ m/s}$) was hit sideways on the frame, causing a jump in the lean rate, followed by a recovery to straight-ahead upright rolling.

The lean and yaw rates were measured (telemetered). A data set was compared with theory in Fig. 3B (movie S4). One difference between experiment and theory is lateral wheel slip at the initial perturbation, which caused an initial jump in the measured yaw rate (Fig. 3B, triangles in the first 0.25 s). The theoretical model assumed no slip. High-speed video (movie S4) also shows a 20-Hz shimmy, which is due at least in part to unmodeled steering axis play (SOM text S11). Nonetheless, after the slipping period—even with the shimmy—the data reasonably track the low-dimensional linear model's predictions.

Both the theoretical analysis and physical experiment show that neither gyroscopic torques nor trail are necessary for bicycle self-stability. Nor are they sufficient. Many bicycle designs with gyroscopic front wheels and positive trail are unstable

at every forward speed (SOM text S6.3). Also, all known bicycle and motorcycle designs lose self-stability at high speeds because of gyroscopic terms [for example, (6)]. In contrast, the TMS bicycle does not have gyroscopic terms and is predicted to maintain stability at high speeds.

With no gyroscopic torque and no trail, why does our experimental TMS bicycle turn in the direction of a fall? A general bicycle is complicated, with various terms that can cause the needed coupling of leaning to steering. Only some of these terms depend on positive trail or on positive spin angular momentum in the front wheel. In the theoretical and experimental TMS designs, the front assembly mass is forward of the steering axis and lower than the rear-frame mass. When the TMS bicycle falls, the lower steering-mass would, on its own, fall faster than the higher frame-mass for the same reason that a short pencil balanced on end (an inverted pendulum) falls faster than a tall broomstick (a slower inverted pendulum). Because the frames are hinged together, the tendency for the front steering-assembly mass to fall faster causes steering in the fall direction. The importance of front assembly mass for Jones-like static torques has been noted before (8, 17, 18).

Why does this bicycle steer the proper amounts at the proper times to assure self-stability? We have found no simple physical explanation equivalent to the mathematical statement that all eigenvalues must have negative real parts (SOM text S4). For example, turning toward a fall is not sufficient to guarantee self-stability. For various candidate simple sufficient conditions X for stability, we have found designs that have X but that are not self-stable. For example, we have found bicycles with gyroscopic wheels and positive trail that are not stable at any speed (SOM text S6.3). We also have found no simple necessary conditions for self-stability. Besides the TMS design with no gyroscope and negative trail, we have found other counterexamples to common lore. We have found a bicycle that is self-stable with rear-wheel steering (SOM text S6.7). We also found an alternative theoretical TMS design that has, in addition to no-gyro and negative trail, also a negative head angle ($\lambda_s < 0$) (SOM text S6.6).

Are there any simply described design features that are universally needed for bicycle self-stability? Within the domain of our linearized equations, we have found one simple necessary condition (SOM text S5): To hold a self-stable bicycle in a right steady turn requires a left torque on the handlebars. Equivalently, if the hands are suddenly released from holding a self-stable bicycle in a steady turn to the right, the immediate first motion of the handlebars will be a turn further to the right. This is a rigorous version of the more general, as-yet-unproved claim that a stable bicycle must turn toward a fall.

Another simple necessary condition for self-stability is that at least one factor coupling lean to steer must be present [at least one of $M_{\delta\phi}$, $C_{\delta\phi}$, or $K_{\delta\phi}$ must be nonzero (SOM text S3)]. These coupling terms arise from combinations of trail,

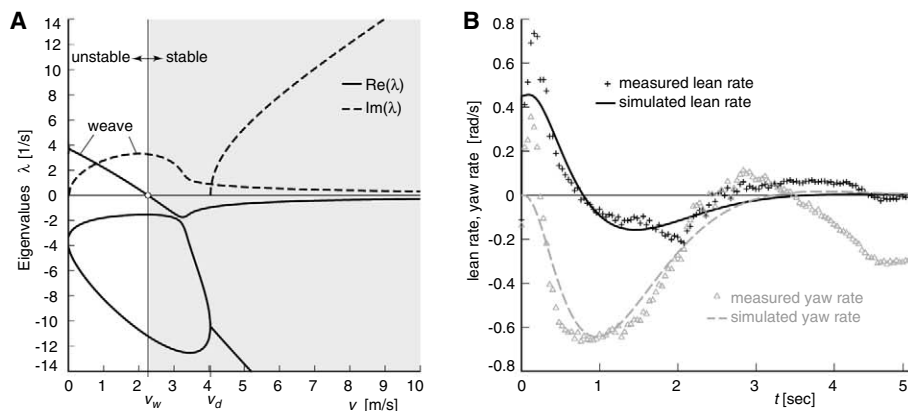


Fig. 3. (A) Stability plot for the experimental TMS stable bicycle. Solutions of the differential equations are exponential functions of time. Stability corresponds to all such solutions having exponential decay (rather than exponential growth). Such decay only occurs if all four of the eigenvalues λ_i (which are generally complex numbers) have negative real parts. The plot shows calculated eigenvalues as a function of forward speed v . For $v > 2.3 \text{ m/s}$ (the shaded region), the real parts (solid lines) of all eigenvalues are negative (below the horizontal axis), and the bicycle is self-stable. **(B)** Transient motion after a disturbance for the experimental TMS bicycle. Measured and predicted lean and yaw (heading) rates of the rear frame are shown. The predicted motions show the theoretical (oscillatory) exponential decay. Not visible in these plots, but visible in high-speed video (movie S4), is a 20-Hz shimmy that is not predicted by the low-dimensional linearized model (SOM text S10 and S11).

spin momentum, steer axis tilt, and center of mass locations and products of inertia of the front and rear assemblies.

Although we showed that neither front-wheel spin angular momentum nor trail are necessary for self-stability, we do not deny that both are often important contributors. But other parameters are also important, especially the front-assembly mass distribution, and all of the parameters interact in complex ways. As a rule, we have found that almost any self-stable bicycle can be made unstable by misadjusting only the trail, or only the front-wheel gyro, or only the front-assembly center-of-mass position. Conversely, many unstable bicycles can be made stable by appropriately adjusting any one of these three design variables, sometimes in an unusual way. These results hint that the evolutionary, and generally incremental, process that has led to common present bicycle designs might not yet have explored potentially useful regions in design space.

References and Notes

- W. J. M. Rankine, *The Engineer* **28**, 79 (in five parts) (1869).
- C. Spencer, *The Modern Bicycle* (Frederick Warne and Co., London, 1876), pp. 23–24.
- J. P. Meijaard, J. M. Papadopoulos, A. Ruina, A. L. Schwab, <http://ecommons.library.cornell.edu/handle/1813/22497> (2011).
- E. Carvallo, *Théorie du Mouvement du Monocycle et de la Bicyclette* (Gauthier-Villars, Paris, France, 1899).
- F. J. W. Whipple, *Quarterly Journal of Pure and Applied Mathematics* **30**, 312 (1899).
- J. P. Meijaard, J. M. Papadopoulos, A. Ruina, A. L. Schwab, *Proc. R. Soc. Lond. A* **463**, 1955 (2007).
- J. D. G. Kooijman, A. L. Schwab, J. P. Meijaard, *Multibody Syst. Dyn.* **19**, 115 (2008).
- J. I. Neimark, N. A. Fufaev, *Dynamics of Nonholonomic Systems* (Nauka, Moscow, 1967) [J. R. Barbour, transl. (American Mathematical Society, Providence, RI, 1972)].
- D. E. H. Jones, *Phys. Today* **23**, 34 (1970) [reprinted by *Phys. Today* **59**, 9 (2006), pp. 51–56].
- K. J. Åström, R. E. Klein, A. Lennartsson, *IEEE Contr. Syst. Mag.* **25**, 26 (2005).
- F. Klein, A. Sommerfeld, *Über die Theorie des Kreisels* (Teubner, Leipzig, 1910).
- J. A. Griffiths, *Proc. Inst. Mech. Eng.* **37**, 128 (1886).
- In the preface to (11), the authors credit Fritz Noether for the ideas in the bicycle chapter.
- W. Thomson, *Popular Lectures and Addresses* (Macmillan, London, 1889), **1**, pp. 142–146.
- J. M. Papadopoulos, Bicycle steering dynamics and self-stability: A summary report on work in progress (1987), Internal report from the Cornell Bicycle Research Project; available at http://ruina.tam.cornell.edu/research/topics/bicycle_mechanics/bicycle_steering.pdf.
- E. J. Routh, *Proc. Lond. Math. Soc.* **1**, 97 (1873).
- R. N. Collins, thesis, University of Wisconsin, Madison, WI (1963).
- C. Chateau, *La Nature* **20**, 353 (1892).
- R. S. Hand helped with the theory and experiments; A. Dressel helped with the eigenvalue analysis; J. van Frankenhuyzen helped with designing the experimental machine; and J. Moore helped with conducting the experiments. The manuscript was improved by comments from M. Broide, M. Cook, A. Dressel, J. Guckenheimer, R. Klein, D. Limebeer, C. Miller, J. Moore, R. Pohl, L. Schaffer, and D. van Nieuhuys. The research was initially supported by a NSF Presidential Young Investigators award to A.R. The original theory was mostly by J.M.P. with later refinement by A.L.S. J.P.M. found the error in (11). Experiments were performed mostly by J.D.G.K. and A.L.S. Writing was done mostly by A.R. and A.L.S.

Supporting Online Material

www.sciencemag.org/cgi/content/full/332/6027/339/DC1
Materials and Methods
SOM Text S1 to S11
Figs. S1 to S19
Tables S1 to S4
References
Movies S1 to S4

20 December 2010; accepted 10 March 2011
10.1126/science.1201959

DNA Origami with Complex Curvatures in Three-Dimensional Space

Dongran Han,^{1,2*} Suchetan Pal,^{1,2} Jeanette Nangreave,^{1,2} Zhengtao Deng,^{1,2} Yan Liu,^{1,2*} Hao Yan^{1,2*}

We present a strategy to design and construct self-assembling DNA nanostructures that define intricate curved surfaces in three-dimensional (3D) space using the DNA origami folding technique. Double-helical DNA is bent to follow the rounded contours of the target object, and potential strand crossovers are subsequently identified. Concentric rings of DNA are used to generate in-plane curvature, constrained to 2D by rationally designed geometries and crossover networks. Out-of-plane curvature is introduced by adjusting the particular position and pattern of crossovers between adjacent DNA double helices, whose conformation often deviates from the natural, B-form twist density. A series of DNA nanostructures with high curvature—such as 2D arrangements of concentric rings and 3D spherical shells, ellipsoidal shells, and a nanoflask—were assembled.

DNA nanotechnology can now be used to assemble nanoscale structures with a variety of geometric shapes (1–12) [for a recent review, see (13)]. Conventionally, a series of B-form double helices are brought together and arranged with their helical axes parallel to one another. The structure is held together by crossovers between neighboring helices, and the allowed crossover points are based on the pre-existing structural characteristics of B-form DNA. Many DNA nanostructures are variations of polygonal shapes and, although this level of complexity has been sufficient for many purposes, it remains a challenge to mimic the elaborate geom-

etries in nature because most biological molecules have globular shapes that contain intricate three-dimensional (3D) curves. Here, we reveal a DNA origami design strategy to engineer complex, arbitrarily shaped 3D DNA nanostructures that have substantial intrinsic curvatures. Our approach does not require strict adherence to conventional design “rules” but instead involves careful consideration of the ideal placement of crossovers and nick points into a conceptually prearranged scaffold to provide a combination of structural flexibility and stability.

The scaffolded DNA origami folding technique, in which numerous short single strands of DNA (staples) are used to direct the folding of a long single strand of DNA (scaffold), is thus far one of the most successful construction methods based on parallel, B-form DNA (14). The most commonly used scaffold (M13) is ~7000 nucleotides (nts) long and is routinely used to construct

objects with tens to hundreds of nanometer dimensions. Several basic, geometric 3D shapes such as hollow polygons and densely packed cuboids have been demonstrated, as well as a few examples of more complex structures, including a railed bridge and slotted or stacked crosses (15–17). The biggest limitation with conventional, block-based DNA origami designs is the level of detail that can be achieved. Analogous to digitally encoded images, DNA origami structures are usually organized in a finite, raster grid, with each square/rectangular unit cell within the grid (pixel) corresponding to a certain length of double-helical DNA. The target shape is achieved by populating the grid with a discrete number of DNA pixels (for most origami structures, each DNA pixel has a parallel orientation with respect to the other pixels) in a pattern that generates the details and curves of the shape. However, as with all finite pixel-based techniques, rounded elements are approximated and intricate details are often lost.

Recently, Shih and co-workers reported an elegant strategy to design and construct relatively complex 3D DNA origami nanostructures that contain various degrees of twist and curvatures (18). This strategy uses targeted insertion and deletion of base pairs (bps) in selected segments within a 3D building block (a tightly cross-linked bundle of helices) to induce the desired curvature. Nevertheless, it remains a daunting task to engineer subtle curvatures on a 3D surface. Our goal is to develop design principles that will allow researchers to model arbitrary 3D shapes with control over the degree of surface curvature. In an escape from a rigid lattice model, our versatile strategy begins by defining the desired surface features of a target object with the scaffold.

¹The Biodesign Institute, Arizona State University, Tempe, AZ 85287, USA. ²Department of Chemistry and Biochemistry, Arizona State University, Tempe, AZ 85287, USA.

*To whom correspondence should be addressed. E-mail: hao.yan@asu.edu (H.Y.); dongran.han@asu.edu (D.H.); yan_liu@asu.edu (Y.L.)

fold, followed by manipulation of DNA conformation and shaping of crossover networks to achieve the design.

First, we designed a series of curved 2D DNA origami structures to establish the basic design principles of our method (19). The first step is to create an outline of the desired shape. For illustration purposes, Fig. 1, C and D, show an example shape: a 7-nm-wide concentric ring structure. For this rounded structure, the shape is filled by following the contours of the outline and conceptually “winding” double-helical DNA into concentric rings. The structure is composed of three concentric rings of helices, with an interhelical distance (Δr) of 2.5 nm (from the axial center of one helix to the center of an adjacent helix). This value is based on the observed packing of parallel helices in conventional DNA

origami structures and is merely a first approximation for design purposes (20). The circumferences (c) of rings are designed to maintain the interhelical distance; therefore, Δc should equal 15.7 nm ($\Delta c = 2\pi \times 2.5$ nm). For B-form DNA, this is equivalent to 48.5 bps, a value that can be adjusted to 48 or 50 bps for ease and symmetry of design. In Fig. 1C, the inner, middle, and outer rings contain 100, 150, and 200 bps, respectively.

The second step is to incorporate a periodic array of crossovers between helices (19). Crossovers represent positions at which a strand of DNA following along one ring switches to an adjacent ring, bridging the interhelical gap. Without these crossovers between helices, the rigidity of double-helical DNA (with a persistence length of ~ 50 nm) (21) would cause the DNA in each ring to extend fully. The number and pattern of

crossovers are flexible and will depend on the overall design and on the size of each ring. Theoretically, any divisor of Δc (48 or 50) could be considered; however, a balance between flexibility and structural stability must be maintained. For rings with a Δc of 48 bps, this generally corresponds to 3, 4, 6, or 8 crossovers between helices. For those with a Δc of 50 bps, the number of crossovers should be adjusted to either 5 or 10. These values ensure that the pattern of crossovers is symmetric, with an integer number of bps between sequential crossovers. For helices that are connected to two neighboring rings (this condition applies to all but the inner and outermost rings), the pattern of crossovers must contain nucleotide positions that are facing both of the adjacent helices (tangent). In Fig. 1, the inner/middle and middle/outer rings are connected at five distinct crossover points. Thus, the inner, middle, and outer rings contain 20, 30, and 40 bps between crossovers, which is approximately equal to 2, 3, and 4 full turns (for B-form DNA), respectively. For the middle ring, the alternating crossover points between the inner and outer ring are spaced by 1.5 turns, which ensures that the three rings are approximately in the same plane.

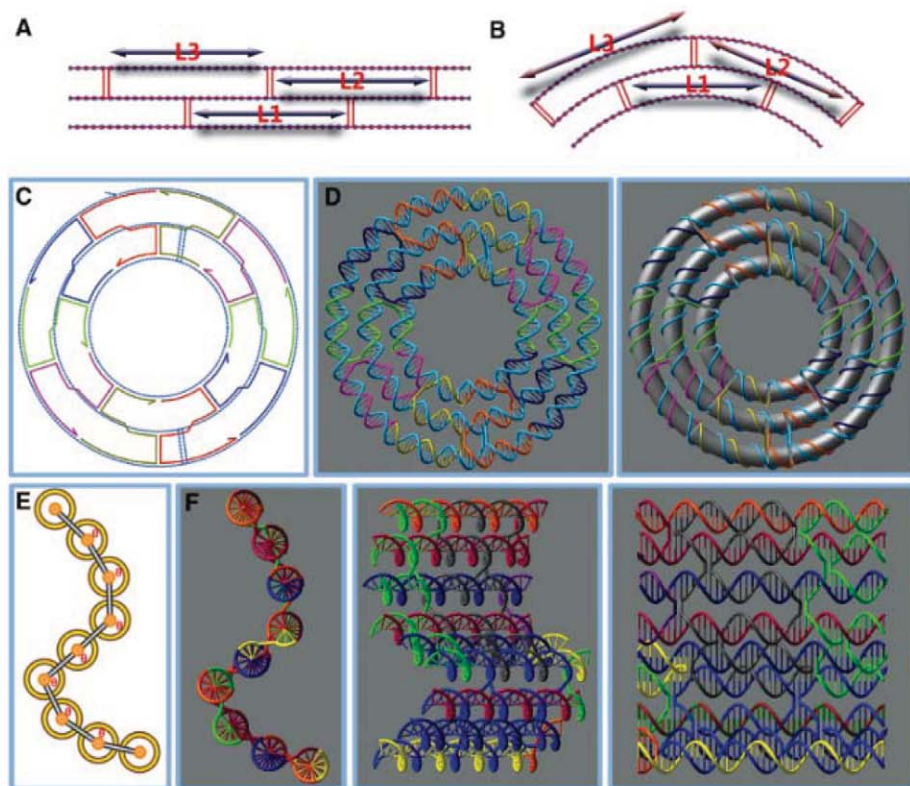


Fig. 1. Design principles for DNA origami with complex curvatures in 3D space. **(A)** A parallel arrangement of DNA double helices to make multihelical DNA nanostructures. The distance between consecutive crossovers connecting adjacent helices (L1, L2, and L3) is constant and generally corresponds to 21 or 32 bps (about two or three full turns of B-form DNA). **(B)** Bending of DNA helices into concentric rings to generate in-plane curvature. The distance between crossovers in the outer rings are greater than in the inner rings ($L3 > L2 > L1$). This distance is not required to be regular, or exactly equal to a whole number of full turns of B-form DNA for every helix. **(C)** Schematic diagram of a three-ring concentric structure. The long single-stranded DNA scaffold is shown in cyan, and short oligonucleotide staple strands are shown in various colors. Two scaffold crossovers are required between adjacent rings to achieve the three-ring arrangement. They are located far apart, on opposite sides of the rings. Five periodic, staple-strand crossovers connect the outer and middle rings and the middle and inner rings, respectively, constraining the three bent double-helical DNA rings to the same 2D plane. **(D)** Helical and cylindrical view of the three-ring concentric structure. **(E)** A general method to introduce out-of-plane curvature in a multihelical DNA structure. All DNA helices exhibit a natural B-form conformation. There are 10 possible values of θ ranging from $\sim 34^\circ$ to $\sim 343^\circ$. Due to steric hindrance, not all values are allowed. Only a few of these values are demonstrated here. **(F)** Various views of the structure shown in (E), viewed along the helical axes, tilted by 135° , and perpendicular to the helical axes.

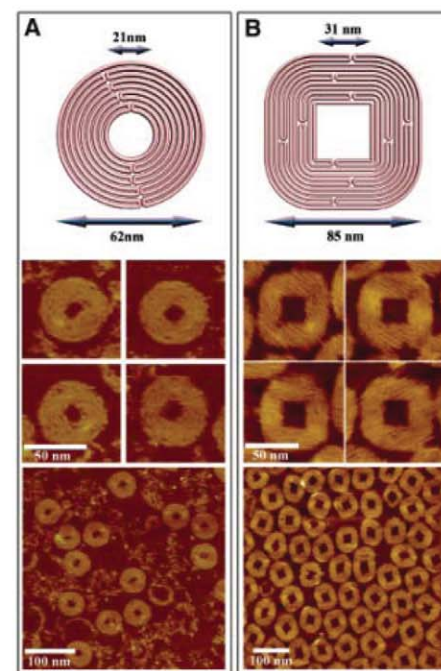


Fig. 2. Curved 2D DNA nanostructures with various structural features. **(Upper panels)** Schematic designs. **(Middle panels)** Zoom-in AFM images with 50-nm scale bars. **(Lower panels)** Zoom-out AFM images with 100-nm scale bars. **(A)** Nine-layer concentric ring structure. Only 3600 of 7249 nucleotides of the scaffold strand are used in this structure, and the remaining single-stranded loop is left unpaired, attached to the outer ring (often visible due to formation of secondary structures). **(B)** Eleven-layer modified concentric square frame structure with rounded outer corners and sharp inner corners.

In the final steps, a long single-stranded scaffold (7249 nts for the typical M13 scaffold, the cyan strands in Fig. 1, C and D) is wound so that it comprises one of the two strands in every helix; each time the scaffold moves from one ring to the next, a “scaffold crossover” is created. Watson-Crick complements to the scaffold (staples, the colored strands in Fig. 1, C and D) are subsequently designed to serve as the second strand in each helix and create the additional crossovers that maintain structural integrity (19). Each staple is generally 16 to 60 nts long and reverses direction after participating in a crossover, resulting in stable antiparallel crossover configurations (5). Once the folding path, crossover pattern, and staple position are determined, a list of staple sequences is generated (19). Several additional factors, including the ideal conformation of DNA double helices, must be considered to complete the design process.

The conformation of each double-helical ring (10 bps/turn) shown in Fig. 1, C and D, closely resembles B-form DNA (10.5 bps/turn), and while the concentric ring structure demonstrates in-plane bending of nonparallel helices, maintaining ~ 10 bps/turn sacrifices a certain level of design control. For example, sustaining ~ 10 bps/turn restricts the number of concentric rings that can be added to a structure. As the radius of a ring increases, additional crossover points are required to constrain the double helix to a 2D ring (i.e., 70 bps between crossovers is not expected to maintain the required level of rigidity). Consider adding a fourth, fifth, and sixth ring to the concentric ring structure in Fig. 1, C and D: The fourth ring would have 250 bps with five crossovers (50 bps between crossovers), the fifth ring would have 300 bps with five crossovers (60 bps between crossovers), and, following the same pattern, the sixth ring would have 350 bps with five crossovers (70 bps between crossovers). To stabilize the outer ring would most likely require at least one additional crossover, and the resulting double helix would no longer conform to 10 bps/turn.

DNA has been shown to be flexible enough to tolerate non-natural conformations in certain

DNA nanostructure arrangements (18). To determine the range of DNA conformations amenable to our current design, we constructed a series of three-ring structures (fig. S11) with different numbers of bps between adjacent crossovers and evaluated their stability (19). We found that a wide range of DNA conformations are compatible with DNA origami formation, as confirmed by the atomic force microscopy (AFM) images in fig. S13. As expected, structures in which the DNA most closely resembles its natural conformation (10 and 11 bps/turn) formed with the highest yield ($>96\%$), and those with the largest deviation from 10.5 bps/turn (8 and 13 bps/turn) formed with the lowest yield (fig. S14). The results suggest that it is not necessary to strictly conform to 10.5 bps/turn when designing DNA origami structures, and the flexibility in this design constraint supports more complex design schemes.

With each of these parameters in mind, we designed objects with more complex structural features. Figure 2A illustrates a more intricate concentric ring design, with nine layers of double-helical rings (fig. S26). The design is based on a Δc of 50 bps, and the number of bps/ring ranges from 200 in the innermost to 600 in the outermost ring (with an increment of 50 bps/ring). As the ring size increases, the outer layers need additional crossovers between helices to stabilize the overall structure and preserve the circular shape. The number of crossovers between adjacent helices is five for the two innermost rings, and 10 for the remaining outer rings. Table 1 lists the specific details of each concentric ring layer. The conformation of double-helical DNA in the nine-layer concentric ring structure ranges from 9 to 11.7 bps/turn, with several different distances between successive crossovers. The AFM images in Fig. 2A and fig. S16 reveal that the nine-layer ring structure forms with relatively high yield

($\sim 90\%$), despite the various degrees of bending in each of the helices and inclusion of non-B-form DNA (19).

A modified square frame (Fig. 2B) was designed to determine whether sharp and rounded elements could be combined in a single structure (figs. S31 to S33). Each side of the modified square frame is based on a conventional helix-parallel design scheme, whereas each corner corresponds to one-fourth of the concentric ring design. The AFM images (Fig. 2B and fig. S18) confirm that several design strategies can in fact be used to generate intricate details within a single structure (19). Several additional 2D designs with various structural features were also constructed (fig. S15). An “opened” version of the nine-layer ring structure was assembled (fig. S27), as well as an unmodified square frame with four well-defined sharp corners (figs. S28 to S30), and a three-point star motif (fig. S34).

To produce a complex 3D object, it is necessary to create curvatures both in and out of the plane. Out-of-plane curvature can be achieved by shifting the relative position of crossover points between DNA double helices (Fig. 1, E and F). Typically, two adjacent B-form helices (n and $n + 1$) are linked by crossovers that are spaced 21 bps apart (exactly two full turns), with the two axes of the helices defining a plane. The crossover pattern of the two-helix bundle and those of a third helix can be offset by any discrete number of individual nucleotides (not equal to any whole number of half turns, which would result in all three helices lying in the same plane), and in this way, the third helix can deviate from the plane of the previous two. However, with B-form DNA, the dihedral angle (θ)—the angle between the planes defined by n and $n + 1$, and $n + 1$ and $n + 2$ —can not be finely tuned, and $\sim 34.3^\circ/\text{bp}$ is the smallest increment of curvature that can be achieved.

Table 1. Design parameters for the nine-layer concentric-ring structure. The number of bps in each ring, number of crossovers between adjacent helices, conformation of the double helical DNA in bps/turn, and radius are listed, respectively.

Ring no.	bps	No. of crossovers	bps/turn	Radius (nm)
1	200	5	10	10.3
2	250	5	10	12.9
3	300	10	10	15.5
4	350	10	11.7	18
5	400	10	10	20.6
6	450	10	9	23.2
7	500	10	10	25.8
8	550	10	11	28.4
9	600	—	10	30.9

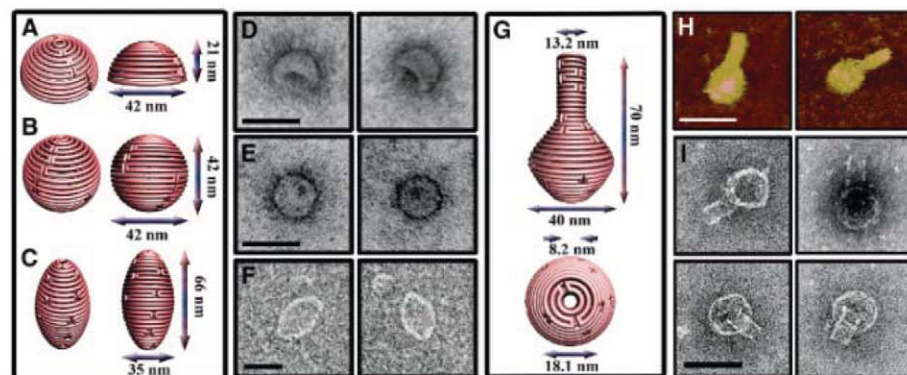


Fig. 3. DNA nanostructures with complex 3D curvatures. (A) Schematic representation of the hemisphere. (B) Schematic representation of the sphere. (C) Schematic representation of the ellipsoid. (D) TEM images of the hemisphere, randomly deposited on TEM grids. The concave surface is visible as a dark area. (E) TEM images of the sphere, randomly deposited on TEM grids. Due to the spherical symmetry, the orientation can not be determined. (F) TEM images of the ellipsoid. The outline of the ellipsoid is visible. Scale bar for the TEM images in (D), (E) and (F) is 50 nm. (G) Schematic representation of the nanoflask. (H) AFM images of the nanoflask. Scale bar is 75 nm. (I) TEM images of the nanoflask, randomly deposited on TEM grids. The cylindrical neck and rounded bottom of the flask are clearly visible in the images. Scale bar is 50 nm.

The use of non-B-form double-helical parameters presents an opportunity to fine-tune θ . Rationally designed crossover connections between double helices with unique conformations (generally ranging from 9 to 12 bps/turn) provides access to a wide selection of other bending angles between 0 and 360 degrees (tables S5 to S10). Although the extent to which we can manipulate the DNA double helices does not allow us to achieve every angle between 0° and 360° , DNA is flexible enough to approximate the curves found in even the most complex structures.

The design process for a 3D curved object decomposes the object into a wireframe representation (19). For example, a sphere would be decomposed just as Earth's surface is divided into latitude circles, which are smaller farther away from the equator (fig. S4). Using a sphere as an example, double-helical DNA is spooled around each latitudinal ring to form a spherical scaffold, starting at the north pole and continuously proceeding from one ring to the next, passing through the equator until finally reaching the south pole. The exact number of latitudinal units (concentric rings) can be varied and will depend on the total length of the available single-stranded DNA scaffold and desired size and diameter of the target object.

The next step is to generate in-plane curvature (latitudinal): i.e., to determine the ideal circumference (in number of bps) of each double-helical ring. When the wireframe is viewed from the top (along the axis defined by connecting the north and south poles), a 2D pattern of concentric circles is observed (fig. S5). Although the center-to-center distance between rings of helices is constant in 3D space, careful inspection of the 2D projection reveals a nontrivial relation between curvature along the latitude and longitude. In the 2D projection, as one moves from the ring corresponding to the north pole out to the equatorial ring, the Δr becomes smaller and smaller. The circumference (in bps) of any initial ring can be randomly defined (based on scaffold length and the desired sphere diameter), and the circumference of each remaining ring is determined by its relation to the initial ring.

After designing latitudinal curvature, out-of-plane (longitudinal) curvature must be introduced. It is helpful to visualize a longitudinal cross section that passes through the north and south poles revealing the helical axis of each latitudinal ring. Now consider only one-half of the cross section (either east or west); starting with ring n (the north pole) and $n + 1$, conceptualize a single plane that passes through the center of both helices. Continue this process and create a plane between $n + 1$ and $n + 2$ and each successive pair of rings until reaching the south pole. It is the total number of latitudinal rings that will determine the dihedral angles between adjacent planes (θ). For example, if a spherical wireframe were constructed from 10 double-helical rings, the angle between adjacent planes would be 162° ($180^\circ - 180^\circ/\text{number of rings}$). The crossover pat-

tern between adjacent helical rings (and position of the nucleotides that participate in each crossover) should be designed to approximate 162° angles.

Finally, a periodic array of crossovers (and staples) is introduced in the same manner and with the same considerations as in the 2D case. The size of each ring dictates the number of crossovers used to maintain overall structural stability and ring shape; the resulting number of bps between crossovers will determine the conformation of the DNA in each ring and, ultimately, the angles available for inducing the longitudinal curvature (tables S5 to S10). The in- and out-of-plane curvatures are actually coupled: Modifying the spherical radius and ring circumference will change the number of rings used to generate the sphere (because of the fixed diameter of a DNA double helix); thus, this will change θ . Conversely, adjustments in θ will alter the corresponding radius and circumference. At this point, each curved 3D origami structure must be manually designed, with careful consideration of how to best induce the in- and out-of-plane curvature, the ideal pattern of crossovers, and the appropriate placement and length of staples. Not every value of r and θ is compatible with one another and some cases may require sacrificing control over one parameter or the other to produce the desired structural details. A careful examination of the design schematics for all the reported 2D and 3D objects will provide a better understanding of the design process and the complex relation between r , θ , DNA conformation, crossover pattern, and staple placement. Based on these design principles, we have generated in- and out-of-plane curvature and created several examples of complex 3D DNA architectures, including a hemisphere, a sphere, an ellipsoidal shell, and a "rounded-bottom nanoflask" (Fig. 3).

The hemisphere shown in Fig. 3A contains 12 concentric latitudinal rings with diameters ranging from 5.6 nm at the north pole to 42.0 nm at the equator (fig. S35). θ is a constant 172.5° along the entire surface. The most obvious feature of the hemisphere that can be identified in the transmission electron microscopy (TEM) images in Fig. 3D and fig. S21 is the boundary of the equatorial rings, with the observed diameter of the equator in agreement with the expected value of 42.0 nm (19). Notably, the hollow cavity of the hemisphere can sometimes be seen in the TEM images (when it has been randomly deposited on the grid with a tilt) shown in Fig. 3D, providing evidence of its 3D structure.

The full sphere illustrated in Fig. 3B is composed of 24 rings and is an extension of the hemisphere design (fig. S35). Similar to the hemisphere, the diameter of the rings range from 5.6 nm at the north and south poles to 42.0 nm at the equator, and θ (172.5°) is constant along the entire surface. Spherical objects can be seen in the TEM images shown in Fig. 3E and fig. S20, each with the expected diameter of ~ 40 nm (19). The uniformity in the appearance of each ring in the TEM images suggests that the expected 3D

sphere successfully formed. If the structure had not assembled as designed, we would likely see variations of partially formed rings, or even rings of several different diameters. A full description of the design details for the sphere and hemisphere (rings 1 to 12) is shown in table S4.

Although the sphere and hemisphere structures demonstrate the ability of our method to produce 3D structures with varying latitudinal curvature (radii) and constant longitudinal curvature (θ), the ellipsoid shown in Fig. 3C tests our ability to create structures with simultaneously shifting radii and θ (fig. S36). This is important because the ability to gradually change the in- and out-of-plane curvature within a single structure is necessary to construct DNA nanostructures with more complicated designs. The ellipsoid contains 29 rings with diameters ranging from 9.8 nm at the poles to 34.6 nm at the equator (table S4). θ is smaller near the poles (severe curvature) and larger at the equator (gradual curvature). The TEM images in Fig. 3F and fig. S22 confirm the successful formation of the ellipsoid structure and provide further evidence of the utility of our method (19).

As a final demonstration, we sought to construct an asymmetric object with simultaneously shifting radii and θ . The "nanoflask" shown in Fig. 3G reflects the level of complexity that is found in most natural (e.g., phage virus particles) and non-natural objects (fig. S37). The flask consists of 35 concentric double-helical DNA rings (table S4). The rings that make up the neck of the flask have a constant diameter of 13.2 nm, whereas the round bottom is composed of several different ring sizes, with a diameter of 40 nm at the widest point. θ is a constant 180° in the neck and varies from 160° at the widest point in the round bottom to a maximum of 230° at the junction between the neck and the bottom. The AFM images in Fig. 3H, and TEM images in Fig. 3I and fig. S23, provide evidence of the successful formation of the nanoflasks (19). A clear outline of the flask is visible in the TEM images, emphasizing the 3D structural contours; the rounded bottom and the cylindrical neck can be clearly distinguished with the expected dimensions.

The method presented here is fairly easy to execute with comparable yield to the conventional scaffolded DNA origami method. However, for the technique to realize its full potential, several challenges need to be addressed. First, as with conventional DNA origami, the availability of diverse single-stranded scaffolds is limited. Ideally, if longer scaffold alternatives could be identified, larger objects with more complicated features could be constructed. Another important ongoing aim is to develop automated software to aid in the design process. At this point, manual consideration of the complex relations among the design parameters is the most time-consuming step and requires a substantial understanding of fundamental engineering principles and the behavior of interconnected DNA. Despite these future challenges, the current strategy improves our

ability to control the intricate structure of DNA nano-architectures and create more diverse building blocks for molecular engineering.

References and Notes

1. N. C. Seeman, *J. Theor. Biol.* **99**, 237 (1982).
2. N. C. Seeman, *Nature* **421**, 427 (2003).
3. T. J. Fu, N. C. Seeman, *Biochemistry* **32**, 3211 (1993).
4. J. H. Chen, N. C. Seeman, *Nature* **350**, 631 (1991).
5. E. Winfree, F. Liu, L. A. Wenzler, N. C. Seeman, *Nature* **394**, 539 (1998).
6. H. Yan, S. H. Park, G. Finkelstein, J. H. Reif, T. H. LaBean, *Science* **301**, 1882 (2003).
7. W. M. Shih, J. D. Quispe, G. F. Joyce, *Nature* **427**, 618 (2004).
8. F. Mathieu *et al.*, *Nano Lett.* **5**, 661 (2005).
9. R. P. Goodman *et al.*, *Science* **310**, 1661 (2005).
10. F. A. Aldaye, H. F. Sleiman, *J. Am. Chem. Soc.* **129**, 13376 (2007).
11. Y. He *et al.*, *Nature* **452**, 198 (2008).
12. C. Zhang *et al.*, *Proc. Natl. Acad. Sci. U.S.A.* **105**, 10665 (2008).
13. C. Lin, Y. Liu, H. Yan, *Biochemistry* **48**, 1663 (2009).
14. P. W. K. Rothmund, *Nature* **440**, 297 (2006).
15. E. S. Andersen *et al.*, *Nature* **459**, 73 (2009).
16. S. M. Douglas *et al.*, *Nature* **459**, 414 (2009).
17. Y. Ke *et al.*, *J. Am. Chem. Soc.* **131**, 15903 (2009).
18. H. Dietz, S. M. Douglas, W. M. Shih, *Science* **325**, 725 (2009).
19. Materials and methods are available as supporting material on Science Online.
20. P. W. K. Rothmund *et al.*, *J. Am. Chem. Soc.* **126**, 16344 (2004).
21. P. J. Hagerman, *Annu. Rev. Biophys. Chem.* **17**, 265 (1988).

Acknowledgments: We thank the AFM applications group at Bruker Nanosurfaces for assistance in acquiring some of the high-resolution AFM images, using Peak Force Tapping with ScanAsyst on the MultiMode 8. This research was partly supported by grants from the Office of Naval

Research, Army Research Office, National Science Foundation, Department of Energy, and National Institutes of Health to H.Y. and Y.L. and from the Sloan Research Foundation to H.Y. Y.L. and H.Y. were supported by the Technology and Research Initiative Fund from Arizona State University and as part of the Center for Bio-Inspired Solar Fuel Production, an Energy Frontier Research Center funded by the U.S. Department of Energy, Office of Science, Office of Basic Energy Sciences under award DE-SC0001016.

Supporting Online Material

www.sciencemag.org/cgi/content/full/332/6027/342/DC1
Materials and Methods
SOM Text
Figs. S1 to S39
Tables S1 to S19
Reference 22

18 January 2011; accepted 4 March 2011
10.1126/science.1202998

Phonemic Diversity Supports a Serial Founder Effect Model of Language Expansion from Africa

Quentin D. Atkinson^{1,2*}

Human genetic and phenotypic diversity declines with distance from Africa, as predicted by a serial founder effect in which successive population bottlenecks during range expansion progressively reduce diversity, underpinning support for an African origin of modern humans. Recent work suggests that a similar founder effect may operate on human culture and language. Here I show that the number of phonemes used in a global sample of 504 languages is also clinal and fits a serial founder–effect model of expansion from an inferred origin in Africa. This result, which is not explained by more recent demographic history, local language diversity, or statistical non-independence within language families, points to parallel mechanisms shaping genetic and linguistic diversity and supports an African origin of modern human languages.

The number of phonemes—perceptually distinct units of sound that differentiate words—in a language is positively correlated with the size of its speaker population (1) in such a way that small populations have fewer phonemes. Languages continually gain and lose phonemes because of stochastic processes (2, 3). If phoneme distinctions are more likely to be lost in small founder populations, then a succession of founder events during range expansion should progressively reduce phonemic diversity with increasing distance from the point of origin, paralleling the serial founder effect observed in population genetics (4–9). A founder effect has already been used to explain patterns of variation in other cultural replicators, including human material culture (10–13) and birdsong (14). A range of possible mechanisms (15) predicts similar dynamics govern-

ing the evolution of phonemes (11, 16) and language generally (17–20). This raises the possibility that the serial founder–effect model used to trace our genetic origins to a recent expansion from Africa (4–9) could also be applied to global phonemic diversity to investigate the origin and expansion of modern human languages. Here I examine geographic variation in phoneme inventory size using data on vowel, consonant, and tone inventories taken from 504 languages in the World Atlas of Language Structures (WALS) (21), together with information on language location, taxonomic affiliation, and speaker demography (Fig. 1 and table S1) (15).

Consistent with previous work (1), speaker population size is a significant predictor of phonemic diversity (Pearson's correlation $r = 0.385$, $df = 503$, $P < 0.001$), with smaller population size predicting smaller overall phoneme inventories (fig. S1A). The same relationship holds for vowel ($r = 0.378$, $df = 503$, $P < 0.001$) and tone ($r = 0.230$, $df = 503$, $P < 0.001$) inventories separately, with a weaker, though still significant, effect of population size on consonant diversity ($r =$

0.131 , $df = 503$, $P = 0.003$). To account for any non-independence within language families, the analysis was repeated, first using mean values at the language family level (table S2) and then using a hierarchical linear regression framework to model nested dependencies in variation at the family, subfamily, and genus levels (15). These analyses confirm that, consistent with a founder effect model, smaller population size predicts reduced phoneme inventory size both between families (family-level analysis $r = 0.468$, $df = 49$, $P < 0.001$; fig. S1B) and within families, controlling for taxonomic affiliation [hierarchical linear model: fixed-effect coefficient (β) = 0.0338 to 0.0985 [95% highest posterior density (HPD)], $P = 0.009$].

Figure 1B shows clear regional differences in phonemic diversity, with the largest phoneme inventories in Africa and the smallest in South America and Oceania. A series of linear regressions was used to predict phoneme inventory size from the log of speaker population size and distance from 2560 potential origin locations around the world (15). Incorporating modern speaker population size into the model controls for geographic patterning in population size and means that the analysis is conservative about the amount of variation attributed to ancient demography. Model fit was evaluated with the Bayesian information criterion (BIC) (22). Following previous work (5, 6), the set of origin locations within four BIC units of the best-fit location was taken to be the most likely area of origin under a serial founder–effect model.

The origin locations producing the strongest decline in phonemic diversity and best-fit model lie across central and southern Africa (Fig. 2A). This region could represent either a single origin for modern languages or the main origin under a polygenesis scenario. The best-fit model incorporating population size and distance from the origin explains 31% of the variance in phoneme inventory size [correlation coefficient (R) = 0.558, $F_{2,501} = 113.463$, $P < 0.001$] (Fig. 3). Both population size ($r_{\text{population}} = 0.146$, $P = 0.002$)

¹Department of Psychology, University of Auckland, Private Bag 92019, Auckland, New Zealand. ²Institute of Cognitive and Evolutionary Anthropology, University of Oxford, 64 Banbury Road, Oxford OX2 6PN, UK.

*E-mail: q.atkinson@auckland.ac.nz

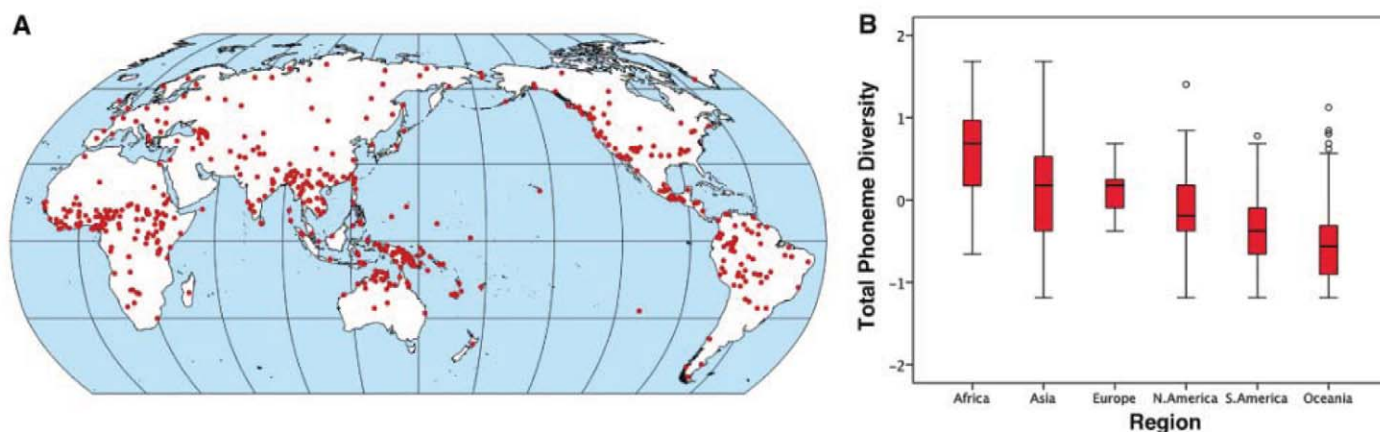


Fig. 1. Language locations and regional variation in phonemic diversity. **(A)** Map showing the location of the 504 sampled languages for which phoneme data was compiled from the WALS database. **(B)** Box plots of overall phonemic diversity by

region reveal substantial regional variation ($\chi^2 = 188.7$, $df = 5$, $P < 0.001$), with the highest diversity in Africa and the lowest diversity in Oceania and South America. The same regional pattern also applies at the language family level (fig. S2).

and distance from origin ($r_{\text{distance}} = -0.438$, $P < 0.001$) are significant predictors in the model. Controlling for population size, distance from origin accounts for 19% of the variance in phonemic diversity. A model using only distance as a predictor gives a broadly equivalent origin area (fig. S3) and explains 30% of the variation in phonemic diversity ($r = 0.545$, $P < 0.001$). The relationship also holds for vowel ($r = -0.394$, $P < 0.001$), consonant ($r = -0.260$, $P < 0.001$), and tone diversity ($r = -0.391$, $P < 0.001$) separately.

To account for relatedness within families, I repeated the above regressions using mean values across language families (table S2) and under a hierarchical linear model comprising the three taxonomic levels recorded in WALS (15). The hierarchical model results closely matched those of the individual language analysis (fig. S4). Adding an interaction effect did not significantly improve model fit, indicating that the patterns reported here reflect a consistent trend that holds across the globe. The family-level analysis was consistent with the individual language analyses, although the credible region of origin is expanded to include all of Africa (Fig. 2B). Distance from the best fit origin ($r_{\text{distance}} = -0.401$, $P = 0.004$) and population size ($r_{\text{population}} = 0.300$, $P = 0.036$) are both significant predictors and account for 39% of the variance in phonemic diversity between families ($R = 0.627$, $F_{2,47} = 15.190$, $P < 0.001$; fig. S5). As a further test of the robustness of these findings, individual regressions were repeated using partial Mantel tests, which allow for non-independence between data points and avoid assumptions about the statistical distributions underlying the variables of interest (15). The results of this analysis matched the findings reported above (table S3).

To examine the possibility of language polygenesis, distance from a second origin location was added as a predictor to a model incorporating population size and distance from the best-fit origin in Africa. The best-fit models in this anal-

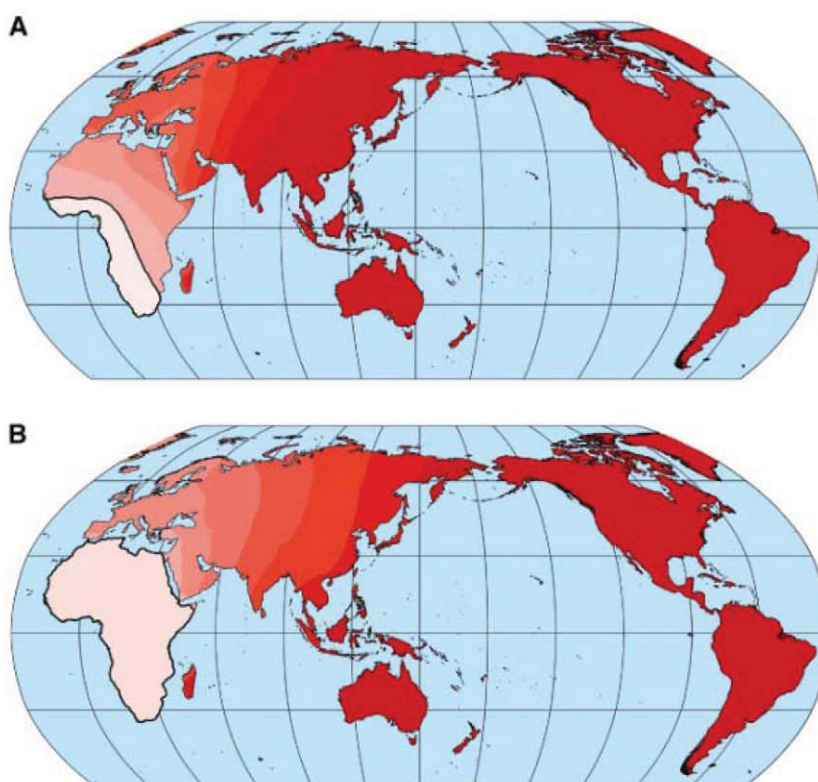
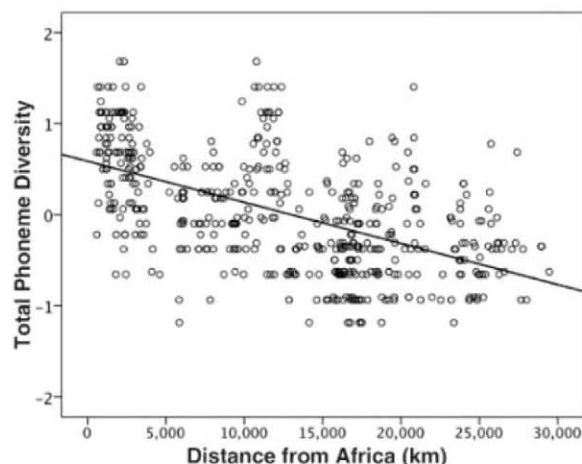


Fig. 2. Likely area of language origin. Maps show the likely location of a single language origin under a founder effect model of phonemic diversity (controlling for population size) inferred from **(A)** individual languages and **(B)** mean diversity across language families. Lighter shading implies a stronger inverse relationship between phonemic diversity and distance from the origin and better fit of the model, as measured by the BIC. The most likely region of origin, comprising those locations within four BIC units of the best-fit origin location, is the area of lightest shading outlined in bold.

ysis did not show a significant negative correlation between distance from a second origin and phonemic diversity. Restricting the analysis to second origin locations that do show an inverse relationship, a region of best fit can be identified in South America (fig. S6). However, this pattern

does not appear under the hierarchical linear model or language family-level analysis; adding a second origin does not improve the fit of either model as measured by the BIC, and all putative second origin locations are within four BIC units. The area identified in the individual-level analysis may

Fig. 3. Phonemic diversity versus distance from the best-fit origin in Africa. A plot of distance from the best-fit origin location in Africa against overall phoneme inventory size is shown. Distance from the origin alone explains 30% of the variation in phonemic diversity (fitted line; $r = -0.545$, $n = 504$ languages, $P < 0.001$) and 19.2% of the variation after controlling for modern speaker population size ($r_{\text{distance}} = -0.438$, $P < 0.001$; $r_{\text{population}} = 0.146$, $P < 0.001$; $R = 0.558$, $F_{2,501} = 113.463$, $P < 0.001$).



be an artefact of slightly higher diversity levels in the Americas than in Oceania, despite the two being comparable distances from Africa, possibly because of a stronger founder effect across the remote Pacific (18–20, 23). When the languages of Oceania are removed from the individual analysis, the effect of distance from an African origin remains ($r_{\text{distance1}} = -0.447$, $P < 0.001$) but there is no significant effect of distance from the secondary origin ($r_{\text{distance2}} = -0.065$, $P = 0.192$). As expected if language spread south with the initial colonization of the Americas, distance from the Bering Strait is inversely correlated with phoneme inventory size within the Americas after controlling for population size ($r_{\text{distance}} = -0.173$, $P = 0.043$).

An ostensibly global cline in phonemic diversity supporting an expansion from Africa could also arise as an artefact of a series of more recent expansions after the Last Glacial Maximum (LGM) into northern Eurasia, the Americas, and the remote Pacific. Languages in these regions show lower average phonemic diversity than in the rest of the world ($t = -6.597$, $df = 503$, $P < 0.001$), which is consistent with a more recent colonization. However, expansion after the LGM does not account for the global cline in phonemic diversity. Distance from Africa remains a significant predictor of phonemic diversity after controlling for colonization since the LGM ($r_{\text{distance}} = -0.401$, $P < 0.001$; $r_{\text{population}} = 0.152$, $P = 0.001$; $r_{\text{LGM}} = 0.032$, $P = 0.419$), as well as when these more recently colonized areas are excluded from the analysis altogether ($r_{\text{distance}} = -0.511$, $P < 0.001$; $r_{\text{population}} = 0.253$, $P < 0.001$) (19).

Demographic factors other than population size may also influence phonemic diversity, particularly those affecting levels of contact and borrowing between groups of speakers. Because neighboring populations at similar points in an expansion are more likely to have similar phonemes and levels of diversity, moderate horizontal transfer between populations can maintain a cline, as has been the case for human genetic diversity (24). However, geographic variation in language diversity (the number of languages per

unit of area), population density (the number of speakers per unit of area), or language area (the total area over which a language is spoken) could affect regional phonemic diversity by increasing contact within and between groups and creating more opportunities to borrow new phonemes. To test whether any such effect could explain the observed global cline in phonemic diversity, these additional measures were included, together with population size and distance from the best-fit origin in Africa, in a regression model predicting phoneme inventory size (15). Controlling for other demographic variables in this way, sub-Saharan Africa remains the most likely area of origin (fig. S7). Distance from the best-fit origin location is a significant predictor at the individual language level ($r_{\text{distance}} = -0.413$, $P < 0.001$), family level ($r_{\text{distance}} = -0.384$, $P < 0.008$), and in the hierarchical linear model [$\beta = -3.419 \times 10^{-5}$ to -2.223×10^{-5} (95% HPD), $P < 0.001$]. The demographic variables are highly correlated and did not show significant independent effects on phonemic diversity. Stepwise regressions indicated that a model incorporating distance from Africa, population size, and (at the individual language level only) language area best explained phoneme inventory size (15).

The single major cline in phonemic diversity is consistent with a linguistic founder effect operating under conditions of rapid expansion from a most likely origin in Africa. This supports a picture of language spread that is congruent with similar analyses of human genetic (4, 5, 7, 8) and phenotypic (6, 9) diversity. Phonemic diversity appears to be highly stable within major language families (15), indicating that, despite the many sociolinguistic processes at work (2, 3), robust statistical patterns in global variation can persist for many millennia and could plausibly reflect a time scale on the order of the African exodus. Outside Africa, the highest levels of phonemic diversity are found in language families thought to be autochthonous to Southeast Asia. This also fits with genetic evidence (25, 26), indicating that Southeast Asia experienced particularly pronounced popula-

tion growth immediately after the African exodus, meaning that languages in this region should have been least affected by population bottlenecks and would have had the most time to recover diversity.

Although distance from Africa explains much less of the variation in phonemic diversity (19%) than in neutral genetic markers (80 to 85%) (5, 7), the effect is comparable to that obtained from analysis of human mitochondrial DNA (18%) (8) or phenotypic data (14 to 28%) (6). To the extent that language can be taken as an example of cultural evolution more generally, these findings support the proposal that a cultural founder effect operated during our colonization of the globe, potentially limiting the size and cultural complexity of societies at the vanguard of the human expansion (10, 11). An origin of modern languages predating the African exodus 50,000 to 70,000 years ago puts complex language alongside the earliest archaeological evidence of symbolic culture in Africa 80,000 to 160,000 years ago (27, 28). Truly modern language, akin to languages spoken today, may thus have been the key cultural innovation that allowed the emergence of these and other hallmarks of behavioral modernity and ultimately led to our colonization of the globe (29).

References and Notes

1. J. Hay, L. Bauer, *Language* **83**, 388 (2007).
2. C. D. Yang, *Knowledge and Learning in Natural Language* (Oxford Univ. Press, Oxford, 2003).
3. W. Labov, *Principles of Linguistic Change: Social Factors* (Blackwell, Oxford, UK, 2001).
4. S. Ramachandran et al., *Proc. Natl. Acad. Sci. U.S.A.* **102**, 15942 (2005).
5. F. Prugnolle, A. Manica, F. Balloux, *Curr. Biol.* **15**, R159 (2005).
6. A. Manica, W. Amos, F. Balloux, T. Hanihara, *Nature* **448**, 346 (2007).
7. J. Z. Li et al., *Science* **319**, 1100 (2008).
8. F. Balloux, L. J. L. Handley, T. Jombart, H. Liu, A. Manica, *Proc. Biol. Sci.* **276**, 3447 (2009).
9. L. Betti, F. Balloux, W. Amos, T. Hanihara, A. Manica, *Proc. Biol. Sci.* **276**, 809 (2009).
10. J. Diamond, *Nature* **273**, 185 (1978).
11. J. Henrich, *Am. Antiq.* **69**, 197 (2004).
12. S. J. Lycett, N. von Cramon-Taubadel, *J. Archaeol. Sci.* **35**, 553 (2008).
13. D. S. Rogers, M. W. Feldman, P. R. Ehrlich, *Proc. Biol. Sci.* **276**, 3835 (2009).
14. A. J. Baker, P. F. Jenkins, *Anim. Behav.* **35**, 1793 (1987).
15. Materials and methods are available as supporting material on Science Online.
16. B. de Boer, *J. Phonetics* **28**, 441 (2000).
17. L. Cavalli-Sforza, M. W. Feldman, *Cultural Transmission and Evolution: A Quantitative Approach* (Princeton Univ. Press, Princeton, NJ, 1981).
18. Q. D. Atkinson, R. D. Gray, *Syst. Biol.* **54**, 513 (2005).
19. Q. D. Atkinson, A. Meade, C. Venditti, S. J. Greenhill, M. Pagel, *Science* **319**, 588 (2008).
20. P. Trudgill, *Linguist. Typol.* **8**, 305 (2004).
21. M. Haspelmath, M. S. Dryer, D. Gil, B. Comrie, Eds., *The World Atlas of Language Structures Online* (Max Planck Digital Library, Munich, 2008).
22. K. P. Burnham, D. R. Anderson, *Model Selection and Inferences* (Springer, New York, 1998).
23. P. V. Kirch, R. C. Green, *Curr. Anthropol.* **28**, 431 (1987).
24. L. J. L. Handley, A. Manica, J. Goudet, F. Balloux, *Trends Genet.* **23**, 432 (2007).

25. M. G. Palanichamy *et al.*, *Am. J. Hum. Genet.* **75**, 966 (2004).
26. Q. D. Atkinson, R. D. Gray, A. J. Drummond, *Mol. Biol. Evol.* **25**, 468 (2008).
27. C. Henshilwood, F. d'Errico, M. Vanhaeren, K. van Niekerk, Z. Jacobs, *Science* **304**, 404 (2004).
28. C. W. Marean *et al.*, *Nature* **449**, 905 (2007).
29. I. Tattersall, *Proc. Natl. Acad. Sci. U.S.A.* **106**, 16018.
30. Thanks to M. Pagel, O. Curry, R. Dunbar, M. Dunn, R. Gray, S. Greenhill, M. Grove, S. Roberts, R. Ross, and S. Schultz for useful advice and/or comments on the manuscript. I declare no competing financial interest.

Supporting Online Material

www.sciencemag.org/cgi/content/full/332/6027/346/DC1
Materials and Methods

SOM Text
Figs. S1 to S8
Tables S1 to S4
References

19 October 2010; accepted 4 March 2011
10.1126/science.1199295

Interplay Between Changing Climate and Species' Ecology Drives Macroevolutionary Dynamics

Thomas H. G. Ezard,^{1,2*} Tracy Aze,³ Paul N. Pearson,³ Andy Purvis¹

Ecological change provokes speciation and extinction, but our knowledge of the interplay among the biotic and abiotic drivers of macroevolution remains limited. Using the unparalleled fossil record of Cenozoic macroperforate planktonic foraminifera, we demonstrate that macroevolutionary dynamics depend on the interaction between species' ecology and the changing climate. This interplay drives diversification but differs between speciation probability and extinction risk: Speciation was more strongly shaped by diversity dependence than by climate change, whereas the reverse was true for extinction. Crucially, no single ecology was optimal in all environments, and species with distinct ecologies had significantly different probabilities of speciation and extinction. The ensuing macroevolutionary dynamics depend fundamentally on the ecological structure of species' assemblages.

The wide-ranging mechanisms that generate and maintain biodiversity have been grouped in many different ways, but a fundamental distinction exists between biotic and abiotic drivers (1–5). If interactions among species are the dominant drivers of evolution, as in the “Red Queen” model (1, 4), then diversification rates among groups of interacting species are expected to show diversity-dependent dynamics with ongoing turnover at equilibrium. A consequence of this mechanism is that diversification rates are expected to decrease as a function of diversity. Conversely, if evolution is driven chiefly by changes in the physical environment—as in the “Court Jester” model (3), named to contrast with the Red Queen—macroevolutionary dynamics should be dominated by cladewide effects of abrupt abiotic perturbations. Although the interplay between these alternative drivers has long been recognized as fundamental for regulating diversity (6, 7), progress toward understanding their interaction has been slow (2). The incompleteness of the fossil record often necessitates temporally and taxonomically coarse paleontological analyses (7–10), whereas molecular phylogenies are restricted to extant species

and therefore offer little insight into extinction (11, 12). To distinguish how interwoven biotic and abiotic processes regulate diversity, high-

resolution data on multiple forcing mechanisms should be allied to paleontological, species-level phylogenies constructed on sufficiently complete fossil records over substantial periods of evolutionary history. This resolution is rare (2, 6), but Cenozoic macroperforate planktonic foraminifera provide a suitable record for testing these hypotheses (13).

Planktonic foraminifera are sexually reproducing protists distributed throughout the world's oceans. The calcium carbonate “shells” (known as “tests”) of dead individuals rain down on the ocean floor and can, under favorable conditions, generate continuous microfossil sequences that span millions of years. The group's usefulness for stratigraphic correlation (14) and paleoclimatic reconstruction (15) has led to extensive documentation of its morphology (14) and depth habitats (13). The phylogenetic relationships within the macroperforate clade of the Cenozoic have recently been revised comprehensively (13), via the application of Simpson's evolutionary species concept (16). Under this concept, each species is intended to represent a single line of descent (16) that begins with a speciation (clado-

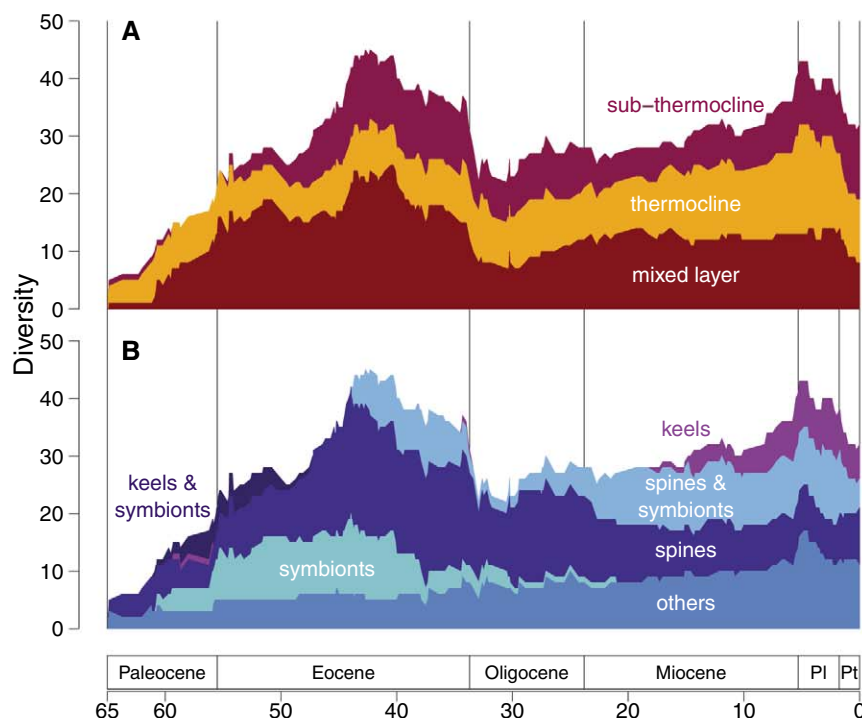


Fig. 1. The relative frequencies of depth habitats (A) and morphologies (B) of macroperforate planktonic foraminifer species across the Cenozoic (13) has fluctuated substantially. Time (million years before the present) is based on the marine geological time scale (14). Pl, Pliocene; Pt, Pleistocene.

¹Division of Biology, Silwood Park Campus, Imperial College London, Ascot, Berkshire, SL5 7PY, UK. ²Department of Mathematics, Faculty of Engineering and Physical Sciences, University of Surrey, Guildford, Surrey, GU2 7XH, UK. ³School of Earth and Ocean Sciences, Cardiff University, Cardiff, CF10 3YE, UK.

*To whom correspondence should be addressed. E-mail: t.ezard@surrey.ac.uk

genetic) event and ends in extinction. The completeness of this group's fossil record is such that species have at least an 81% chance of being detected per million-year interval (fig. S2). Therefore, this species-level fossil record is at least as good as the best-preserved genus-level records of macro-invertebrates (17).

The macroporiferate clade has diversified from two species that survived the end-Cretaceous mass extinction into 32 morphologically distinct species today, though the rise in diversity has been far from smooth (Fig. 1). The sharpest fall in diversity occurred during the Eocene-Oligocene transition, when rapid global cooling led to the development of the Antarctic ice cap (15). This suggests that climate change has been important in macroevolution, so we used the mean and variability of oxygen isotopic composition of deep-sea carbonates to approximate the complex, multifaceted climate system (15, 18). Clade growth $\left[\ln\left(\frac{N_{t+1}}{N_t}\right)\right]$, detrended, where N_t is the number of species in each 1-million-year bin t was poorly predicted by climate (Fig. 2A and table S1) (18). Models based on diversity-dependence used diversity only at the start of each bin and assume a constant limit to niche availability (a taxonomic

analog to a demographic “carrying capacity”), but predictions were similarly poor (Fig. 2B and table S1). Thus, the clade's macroevolutionary dynamics are not well predicted by either a strictly abiotic (Fig. 2A) or a strictly biotic model (Fig. 2B).

Any clade will be composed of species with distinct ecologies. If these ecologies have conferred a macroevolutionary advantage on certain species over others, models that incorporate ecology will provide a better description of observed changes in macroevolutionary dynamics than if all species are assumed equal. To test this hypothesis, we grouped species by their depth habitat and morphology, which, taken together, we used as a proxy for species' ecology (18). Although it is impossible to obtain an experimental link between traits and fitness in fossils, certain traits are thought to indicate functional differences that reflect different ways of life. For example, the acquisition of spines occurred in the earliest Cenozoic and is hypothesized to indicate the transition to a carnivorous diet (19) and to have initiated the hosting of photosynthetic algal symbionts (20), whereas the evolution of a keel is thought in some instances to be associated with the invasion of new depth habitats (21). The as-

semblage in the warm Eocene oceans was dominated by species inhabiting the mixed layer, whereas most species in the stratified oceans of the Pliocene lived and reproduced near the thermocline, where the temperature gradient is much steeper than elsewhere in the water column. The ecological composition of the clade has fluctuated (Fig. 1), with the relative dominance of each group apparently waxing and waning with the changing climate.

Ecology is more strongly predictive of clade growth than either climate or diversity, but model fit is moderate at best (Fig. 2C and table S1). Models containing interactions among pairs of these variables are significantly better, but model support was strong only when species with distinct ecologies were permitted to respond differently to changes in diversity and climate (evidence weight > 0.99) (Fig. 2F and table S1). The importance of interactions among climate, diversity, and ecology suggests that ecological variation enabled the clade's standing diversity to respond rapidly to climatic fluctuations. This interpretation strengthens arguments that the Red Queen and the Court Jester are not mutually exclusive hypotheses of evolutionary diversification (2).

Discrete-time analysis (as is described above) may introduce bias when diversification occurs in continuous time, because there is no ideal bin length to maximize the accuracy of clade-growth estimates (22). Here, we use the Euler-Lotka equation (22, 23) to provide an estimate of per-capita growth for an ecologically structured clade with ongoing speciation and extinction. We used parametric survival analysis with censoring (24) to obtain parsimonious extinction and spe-

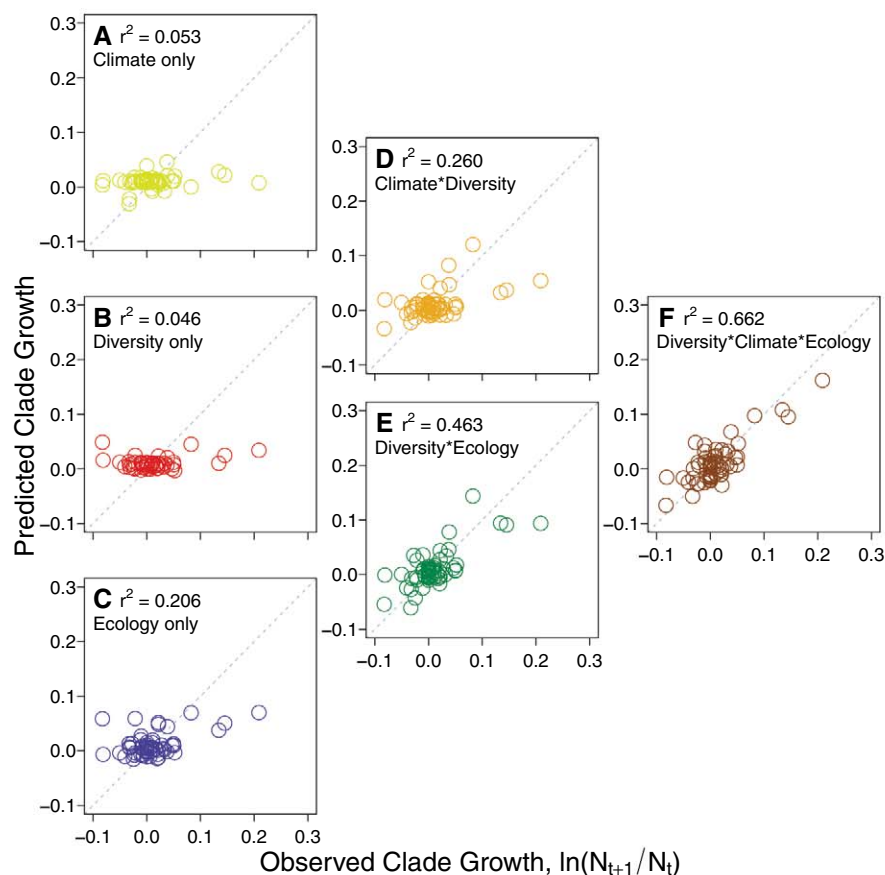


Fig. 2. (A to F) Discrete time models incorporating interactions among diversity, climate, and species' ecology outperformed all others. The dashed gray line is $y = x$; a model that predicts observed clade growth perfectly would have points only on this line. For all summary statistics and models, see table S1. r^2 , fraction of total variance explained by the model.

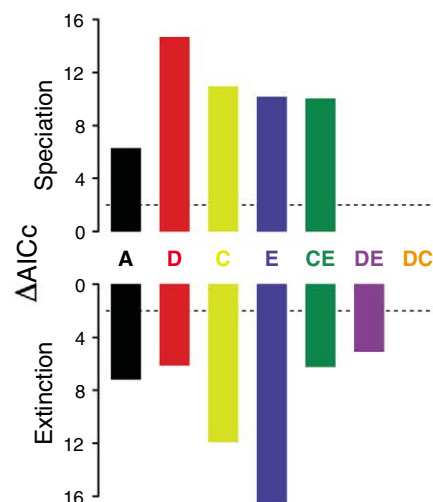


Fig. 3. Speciation probability and extinction risk varied significantly with species' age (A), diversity (D), climate (C), species' ecology (E), and their interactions (letter combinations). The dashed lines denote a difference in corrected Akaike information criterion ($\Delta AICc$) of 2; interactions that did not reach this threshold for “substantial” support and inclusion in the model (25) are not shown (18).

ciation functions (18, 25). This approach does not resort to discretizing a continuous process and allows direct testing of two cornerstone assumptions of macroevolutionary theory (26): The age of a species does not influence its chances of going extinct [i.e., Van Valen's law (1)] or of speciating.

Extinction risk increased with age when diversity dependence, climate change, and species' ecology were incorporated. This suggests rejection of Van Valen's law [for similar patterns in morphospecies, see (27)], though we note that the lower extinction risk of young species may reflect a veil line in the detection probability of short-lived species over the 65-million-year-long Cenozoic era. We also found that the species most likely to speciate were young (fig. S3). This result is consistent with the frequently observed "early burst" pattern of diversification, in which rapid clade growth occurs over short periods of geological time early in a clade's history and slows thereafter due to diversity dependence (28). Speciation probability was affected more by biotic variables than by abiotic ones, whereas the opposite was true for extinction risk (Fig. 3). Species' ecology meant that the impacts of diversity and climatic fluctuations were not felt uniformly across the phylogeny: The extinction and speciation functions differed among species with photosymbionts, keels, and spines, and between greenhouse and icehouse oceans (fig. S3). Identifying a fixed carrying capacity is nontrivial, because the response of any assemblage to climate change depends on the species within it (fig. S4) and differs between speciation probability and extinction risk (Fig. 3). Not all species are one and

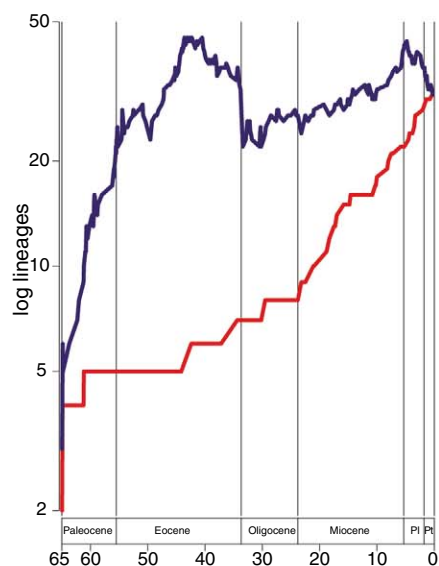


Fig. 4. The impact of extinction on macroevolutionary dynamics of macroforaminate planktonic foraminifera is clear when fossil species are used (blue), but not when analysis is based solely on extant lineages (red). Time (million years before the present) is based on the marine geological time scale (14).

the same: Ignoring their ecological differences limits understanding of the clade's macroevolutionary dynamics.

The continuous-time model gives a deterministic measure of clade growth. We incorporated the impact of changing diversity and climate by parameterizing these variables at speciation and thus assume that conditions early in a species' existence have long-lasting evolutionary consequences. Taking an approach that spans the Cenozoic maximizes the number of bursts of diversification under investigation but restricts our ability to disentangle complex components of climate change and how they affect biodiversity. Despite these limiting assumptions, the continuous-time model captured key features of the macroevolutionary dynamics, such as highest clade growth in greenhouse and highly stratified oceans (fig. S4). The binned analysis is complementary to the continuous-time analysis because it incorporates climate variability during a species' existence (though still assumes a single proxy for climate). The consistency of conclusions from the two approaches supports our interpretation that diversity dependence, climate change, and species' ecology interact to drive macroevolutionary dynamics. Approaches based only on extant diversity can identify some components of diversification (table S4), but they neglect competition among now-extinct species and therefore cannot reveal how biotic interactions among them affected diversity patterns in past environments (Fig. 4).

What biotic and abiotic factors should models of diversification consider? An often-invoked null hypothesis is constancy of birth and death rates; for instance, the constant-rates Markov model (26). The ubiquitous importance of species-level diversity dependence in the models presented here violates this fundamental assumption. The less restrictive, equal-rates Markov model permits speciation and extinction probabilities to change through time, provided that they do not vary among contemporaneous species (26). This assumption is opposed by our result that young species with similar ecologies are more likely to speciate under particular climatic conditions than older species with other ecologies (Fig. 3 and fig. S4). Finally, speciation probability was more strongly shaped by diversity dependence than by climate change, whereas the reverse was true for extinction risk (Fig. 3). Decomposing macroevolutionary dynamics into its constituent parts is a useful step toward a more complete understanding of how biodiversity is generated and destroyed (8).

We conclude that neither the Red Queen nor the Court Jester hypothesis is the dominant macroevolutionary force; instead, it is the interplay of biotic and abiotic variables that regulates diversity and drives speciation and extinction (Figs. 2 and 3). Contrary to recent analyses of global marine diversity patterns (9), our results suggest that species' ecology plays a key role in determining overall diversity and

gives clearer insights into macroevolutionary dynamics than is possible by treating clades as homogeneous wholes.

References and Notes

1. L. Van Valen, *Evol. Theory* **1**, 1 (1973).
2. M. J. Benton, *Science* **323**, 728 (2009).
3. A. D. Barnosky, *J. Vertebr. Paleontol.* **21**, 172 (2001).
4. N. C. Stenseth, J. M. Smith, *Evolution* **38**, 870 (1984).
5. C. Venditti, A. Meade, M. Pagel, *Nature* **463**, 349 (2010).
6. J. W. Valentine, *Paleobiology* **6**, 444 (1980).
7. D. Jablonski, *Annu. Rev. Ecol. Evol. Syst.* **39**, 501 (2008).
8. J. Alroy, *Proc. Natl. Acad. Sci. U.S.A.* **105** (suppl. 1), 11536 (2008).
9. J. Alroy, *Science* **329**, 1191 (2010).
10. M. Foote, *Paleobiology* **26**, 578 (2000).
11. A. Purvis, *Annu. Rev. Ecol. Evol. Syst.* **39**, 301 (2008).
12. T. B. Quental, C. R. Marshall, *Trends Ecol. Evol.* **25**, 434 (2010).
13. T. Aze *et al.*, *Biol. Rev. Camb. Philos. Soc.* (2011); 10.1111/j.1469-185X.2011.00178.x.
14. W. A. Berggren, D. V. Kent, C. C. Swisher III, M.-P. Aubry, *A Revised Cenozoic Geochronology and Chronostratigraphy* (Society for Sedimentary Geology, Tulsa, OK, 1995).
15. J. Zachos, M. Pagani, L. Sloan, E. Thomas, K. Billups, *Science* **292**, 686 (2001).
16. G. G. Simpson, *Principles of Animal Taxonomy* (Columbia Univ. Press, New York, 1961).
17. M. Foote, J. J. Sepkoski Jr., *Nature* **398**, 415 (1999).
18. Materials and methods are available as supporting material on Science Online.
19. C. Hemleben, D. Mühlen, R. K. Olsson, W. A. Berggren, *Geol. Jahrbuch A* **128**, 117 (1991).
20. R. D. Norris, *Paleobiology* **22**, 461 (1996).
21. R. D. Norris, *Palaeogeogr. Palaeoclimatol. Palaeoecol.* **95**, 1 (1992).
22. A. M. De Roos, *Ecol. Lett.* **11**, 1 (2008).
23. F. R. Sharpe, A. J. Lotka, *Philos. Mag. Ser. B* **21**, 435 (1911).
24. J. Kalbfleisch, R. L. Prentice, *The Statistical Analysis of Failure Time Data* (John Wiley, New York, 1980).
25. K. P. Burnham, D. R. Anderson, *Model Selection and Multimodel Inference: A Practical Information-Theoretical Approach* (Springer, New York, 2002).
26. S. Nee, *Annu. Rev. Ecol. Evol. Syst.* **37**, 1 (2006).
27. N. A. Doran, A. J. Arnold, W. C. Parker, F. W. Huffer, *Palaio* **21**, 571 (2006).
28. A. B. Phillimore, T. D. Price, *PLoS Biol.* **6**, e71 (2008).

Acknowledgments: We thank the Natural Environment Research Council (UK) for funding (grant NE/E015956/1 to A.P. and P.N.P.) and G. Mace, T. Barraclough, N. Bunnefeld, L.-M. Chevin, T. Coulson, L. McInnes, I. Owens, A. Phillimore, G. Thomas, and two anonymous reviewers for insightful comments that improved our work. The data we analyzed are deposited as online appendices to (13).

Supporting Online Material

www.sciencemag.org/cgi/content/full/332/6027/349/DC1
Materials and Methods
Figs. S1 to S4
Tables S1 to S4
References and Notes

19 January 2011; accepted 15 March 2011
10.1126/science.1203060

pH-Dependent Gating in a FocA Formate Channel

Wei Lü, Juan Du, Tobias Wacker, Elke Gerbig-Smentek, Susana L. A. Andrade, Oliver Einsle*

The formate transporter FocA was described to switch its mode of operation from a passive export channel at high external pH to a secondary active formate/H⁺ importer at low pH. The crystal structure of *Salmonella typhimurium* FocA at pH 4.0 shows that this switch involves a major rearrangement of the amino termini of individual protomers in the pentameric channel. The amino-terminal helices open or block transport in a concerted, cooperative action that indicates how FocA is gated in a pH-dependent way. Electrophysiological studies show that the protein acts as a specific formate channel at pH 7.0 and that it closes upon a shift of pH to 5.1.

Many enterobacterial species grow by anaerobic mixed-acid fermentation, whereby pyruvate, the end product of glycolysis, is converted to acetyl-coenzyme A and formate by a pyruvate:formate lyase (PFL) rather than being oxidized to yield CO₂ as is the case in mitochondria (1). This process releases one-third of the carbon atom content of carbohydrates as formate, which, if left to accumulate in the cytoplasm, would potentially lead to critical acidification due to its low pK_a (acid dissociation constant) of 3.77. Formate is therefore rapidly oxidized to CO₂ by one of three formate dehydrogenase (FDH) enzymes, termed FDH-N, FDH-O, and FDH-H (1). In the presence of a terminal electron acceptor such as nitrate, nitrite (2, 3), or fumarate (4), formate is efficiently excreted from the cytoplasm to serve as a low-potential ($E^{\circ} = -420$ mV) electron donor for the periplasmic enzymes FDH-N or FDH-O (5). These membrane protein complexes directly reduce the quinone pool and generate proton motive force as part of a Q-loop system with a corresponding quinol dehydrogenase (6, 7). The proton released upon formate oxidation in the periplasm contributes further to energizing the membrane. Export of anionic formate across the cytoplasmic membrane is mediated by the formate transporter FocA ("formate channel"), encoded in the *pfl* operon (8). The integral membrane protein FocA consists of six to eight trans-membrane helices and has homologs in bacteria, archaea, and yeast but not in higher eukaryotes. Together with the nitrite transporter NirC, as characterized in *Escherichia coli* (9), and the formate-uptake permease of *Methanobacterium thermoformicum*, FdhC (10), FocA belongs to a transporter family for short-chain acids, designated as the formate/nitrite transporter (FNT) family (transport protein classification 2.A.44) (11).

If the generation of proton motive force through respiratory oxidation of formate is no longer desirable, or if the pH of the growth medium drops below 6.8, the bacteria switch to rapid reuptake of formate (12) for disproportionation

into CO₂ and H₂ by the cytoplasmic formate: hydrogen lyase complex (FHL) (13). FHL is composed of formate dehydrogenase FDH-H and of various hydrogenases, and its reaction circumvents the problem of cytoplasmic acidification, yielding H₂ that by itself is an excellent electron donor. The uptake of formate is also mediated by FocA, so that the protein must undergo a pH-dependent, functional switch (8). Although the export of formate at high pH seems to be a passive process, the import at low pH was proposed to be an active formate/H⁺ symport on the basis of in vivo studies (14). Recent high-resolution crystal structures of FocA from *Esche-*

richia coli (EcFocA) (15) and *Vibrio cholerae* (VcFocA) (16) showed a pentamer that is homologous in structure—but not in sequence—to aquaporins (17) and glyceroporins (18). Both structures were obtained at pH 7.5 and thus represent the high-pH form, in which FocA was suggested to function as a facilitator for the formate anion. Substrate channels in each protomer were open and a selectivity filter was identified (fig. S2).

We purified and crystallized FocA from *Salmonella typhimurium* (StFocA) at pH 4.0 and solved its structure at a resolution of 2.8 Å (19). The crystals belonged to space group *P*2₁ and the asymmetric unit contained two pentamers that packed together with their cytoplasmic faces juxtaposed in an asymmetric arrangement, rotated by 20° and tilted by 10° with respect to their central five-fold axes. All further packing interactions between stacks of two FocA₅ units were mediated by the periplasmic parts of the protein (fig. S1). The overall structure of StFocA is similar to those of EcFocA and VcFocA, forming the same pentameric arrangement with both termini of the peptide chain on the cytoplasmic side of the membrane. In accordance with von Heijne's positive inside rule (20), the cytoplasmic face of StFocA shows a positive electrostatic surface potential, whereas the periplasmic face is negatively

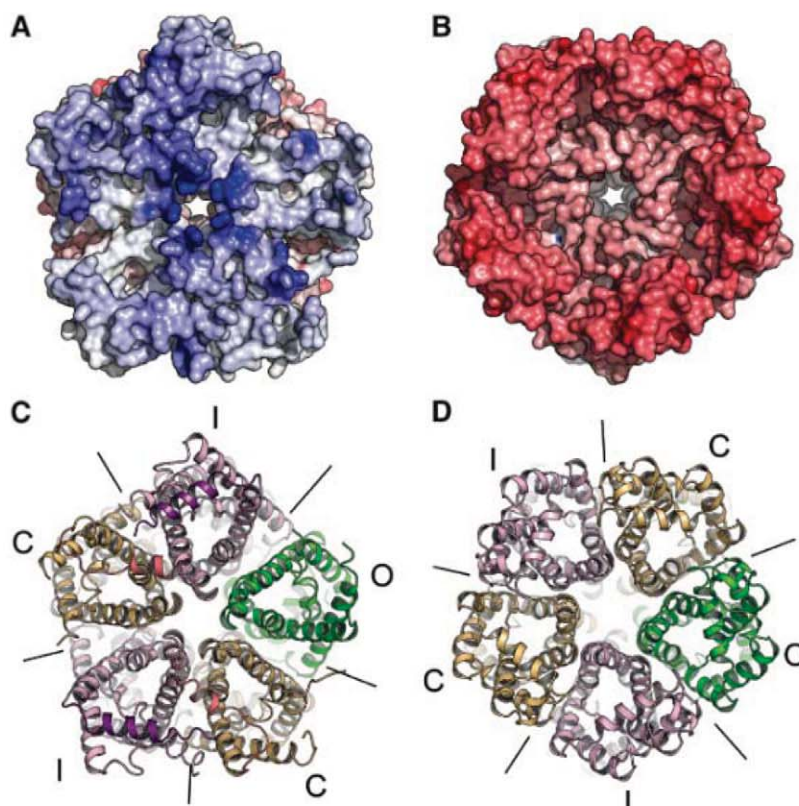


Fig. 1. Structure of *S. typhimurium* FocA at pH 4. An electrostatic surface potential rendering of the cytoplasmic (A) and the periplasmic (B) face of the pentamer shows the typical positive-inside charge distribution of membrane proteins, but also a cytoplasmic asymmetry that is not reflected on the other side. Cartoon representations of the cytoplasmic side (C) and the periplasmic side (D) show three different conformations: open (O, green), intermediate (I, purple) and closed (C, light orange).

Lehrstuhl für Biochemie, Institut für organische Chemie und Biochemie, Albert-Ludwigs-Universität Freiburg, Albertstrasse 21, 79104 Freiburg, Germany.

*To whom correspondence should be addressed. E-mail: einsle@biochemie.uni-freiburg.de

charged (Fig. 1). However, notable differences were observed at the N termini of the peptide chains. In *EcFocA*, 21 N-terminal residues were truncated to improve crystal packing and diffrac-

tion quality (15). Unfortunately, this intervention makes a comparison with the *StFocA* structure difficult. We will consequently focus on the differences between *VcFocA*, crystallized as a full-

length protein at pH 7.5 with all N termini of the protomers in a disordered state (16), and the full-length pH 4.0 structure of *StFocA*. The amino acid sequences of the two proteins display 55% identity. In *VcFocA* two different conformations of a loop region in the structure were described, in a segment between Phe⁸⁹ and Thr¹³⁴ that the authors termed the Ω loop. It was suggested that the Ω loop, and in particular a structural flexibility of residue Thr⁹⁰, would play a key role in the gating of *VcFocA*. However, this small shift influenced the cytoplasmic entrance only slightly and the channel remained open (16), as seen in the open form of *StFocA* (fig. S2).

The structure of *StFocA* instead suggests a different mechanism of FocA gating. At pH 4.0 the N termini of the monomers are largely well ordered, although they show an asymmetry and flexibility that both explains the difficulties in obtaining well-diffracting crystals and suggests a gating mechanism. The N-terminal amino acid residues of the 10 monomers in the asymmetric unit of the *StFocA* crystal are structurally distinct and show three different conformations (Fig. 2). In one single monomer per pentamer, the N terminus is disordered, similar to the structure observed for *VcFocA*, and the substrate channel is freely accessible (open state, Fig. 2A). In the second form, the N terminus forms a helix that passes the cytoplasmic entrance funnel and narrows it, but an open pathway remains (intermediate state, Fig. 2B). In the third conformation, the N-terminal helix crosses the cytoplasmic entrance of the substrate channel, closing it off for formate molecules (closed state, Fig. 2C). Within the two pentamers in the asymmetric unit, the order of these subunit conformations is identical, with the N termini of the intermediate and closed forms in direct contact in a way that seems to be mutually stabilizing (Fig. 1C). Two channels in each pentamer are thus closed, while the other three likely remain open. The conformation of the loop region termed the Ω loop in *VcFocA* is strongly influenced by the corresponding conformation of the N-terminal helix. The Ω loop is fully ordered only in the intermediate state of the transporter, where it interacts with the N-terminal helix (Fig. 2B). In both the open and closed states, the loop is disordered to different degrees. Upon transition from the intermediate to the closed state, the N-terminal helix rotates by 80° across the cytoplasmic face of the protein and releases the interaction with the Ω loop, which consequently relocates by up to 4 Å (Fig. 2C).

The transition between the states represented by *VcFocA* and *StFocA* should be dependent on pH, but to date functional data are exclusively available from whole-cell studies (8). However, passive permeation of formate anions through FocA is an electrogenic process, making it amenable for electrophysiological studies. We have therefore reconstituted *StFocA* in planar lipid bilayer membranes consisting of *E. coli* polar lipid extracts (19). In a series of voltage-clamp experiments, macroscopic currents were recorded

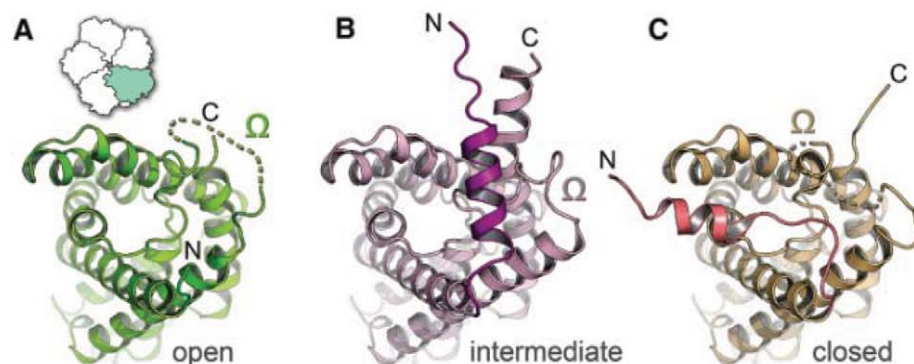


Fig. 2. Conformational changes in FocA. The three states observed in the protomers of the pentameric channel in the open (A), intermediate (B), and closed (C) forms in identical orientations. The inset in (A) shows the relative position within the pentamer. Structural changes are restricted to the N-terminal helical region, the C terminus of the protein, and a loop region termed the Ω loop. In the open state, all three segments show substantial disorder, whereas the transition to the intermediate state leads to interactions of the N and the C terminus concomitant with an ordering of the Ω loop. In the closed state, the N terminus rotates by 80° to cover the substrate channel, and both the Ω loop and the C terminus lose their ordered conformations.

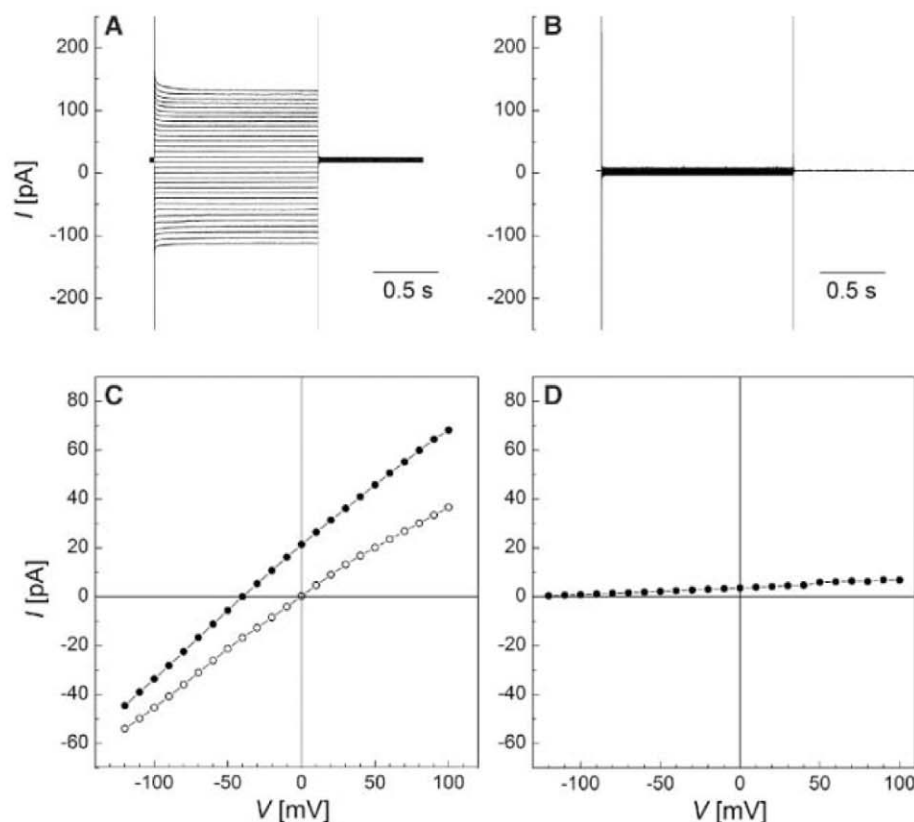


Fig. 3. pH-dependent gating of FocA reconstituted in a planar lipid bilayer. (A) Macroscopic currents observed with a formate gradient of 200 mM (cis) to 19.6 mM (trans) at pH 7.0. (B) Upon a shift of pH to 5.1 (trans), the observed currents are reduced almost to baseline. The formate gradient used was the same as in (A). (C) Current-voltage diagram of the experiment shown in (A) (●) and a control with reconstituted protein, but no formate gradient (○). The observed reversal potential corresponds to the Nernst potential associated with the formate gradient. (D) Current-voltage diagram for the experiment shown in (B).

that showed a reversal potential corresponding to the Nernst potential of the applied gradient of formate, and the resulting reversal potential with identical amounts of formate on both sides of the bilayer was zero (Fig. 3, A and C). Formate gradients were chosen so that the cis side of the lipid bilayer had a higher (200 mM) concentration than the trans side (19.6 mM), in order to emulate the cytoplasmic release of formate in high amounts by PFL. In subsequent experiments, the pH on the trans side (the “periplasmic side”) was acidified by a stepwise addition of HCl. A strong effect occurred at pH 5.1, when the formate current abruptly ceased. This effect was reversible (fig. S3) and constitutes a direct observation of pH-dependent gating in FocA. Although the transition point is still far above the pH of 4.0 in the crystallization condition for *SfFocA*, it falls clearly below the pH of 6.8 determined as the switch point for the growth medium (12). The difference might be explained by the influence of the charged membrane surface on the ion concentration and thus the pH value in its immediate surroundings, as commonly described with Gouy-Chapman theory (21, 22).

This study confirms that FocA acts as a specific channel for anionic formate at higher pH and is gated in a pH-dependent manner. Gating is mediated through the N termini of the peptide chains that order and reorient in a concerted fashion, and one might speculate that protonation of a histidine might be the basis for pH sensing. Earlier functional studies in vivo proposed

that FocA operates as a H^+ /formate symporter at low pH (8). Although our electrophysiological studies cannot address this electroneutral process directly, we note that the observed gating leaves the transmembrane formate channel within FocA unobstructed. Formate in the periplasm can still cross the membrane to reach a vestibule that is sealed off from the cytoplasm only by the N-terminal helix (fig. S2). A possible mechanism for active uptake could thus involve a cycling of the individual protomers through the three conformational states, whereby a transient opening of the cytoplasmic vestibule would release a formate anion trapped there while export would be hindered by the transport-rate-limiting selectivity filter (fig. S2). Active transport would result if the conformational changes were triggered by proton translocation.

References and Notes

1. J. Knappe, G. Sawers, *FEMS Microbiol. Rev.* **75**, 383 (1990).
2. J. Cole, *FEMS Microbiol. Lett.* **136**, 1 (1996).
3. J. W. Wimpenny, J. A. Cole, *Biochim. Biophys. Acta* **148**, 233 (1967).
4. J. Macy, H. Kulla, G. Gottschalk, *J. Bacteriol.* **125**, 423 (1976).
5. S. Leonhartsberger, I. Korsa, A. Böck, *J. Mol. Microbiol. Biotechnol.* **4**, 269 (2002).
6. B. L. Berg, J. Li, J. Heider, V. Stewart, *J. Biol. Chem.* **266**, 22380 (1991).
7. R. G. Sawers, *Antonie Leeuwenhoek* **66**, 57 (1994).
8. B. Suppmann, G. Sawers, *Mol. Microbiol.* **11**, 965 (1994).
9. S. Clegg, F. Yu, L. Griffiths, J. A. Cole, *Mol. Microbiol.* **44**, 143 (2002).

10. W. B. White, J. G. Ferry, *J. Bacteriol.* **174**, 4997 (1992).
11. M. H. Saier Jr. et al., *Biochim. Biophys. Acta* **1422**, 1 (1999).
12. R. G. Sawers, *Biochem. Soc. Trans.* **33**, 42 (2005).
13. M. Hakobyan, H. Sargsyan, K. A. Bagramyan, *Biophys. Chem.* **118**, 135 (2005).
14. R. Rossmann, G. Sawers, A. Böck, *Mol. Microbiol.* **5**, 2807 (1991).
15. Y. Wang et al., *Nature* **462**, 467 (2009).
16. A. B. Waight, J. Love, D. N. Wang, *Nat. Struct. Mol. Biol.* **17**, 31 (2010).
17. P. Agre et al., *J. Physiol.* **542**, 3 (2002).
18. R. M. Stroud, P. Nollert, L. Miercke, *Adv. Protein Chem.* **63**, 291 (2003).
19. Materials and Methods are available as supporting material on Science Online.
20. G. von Heijne, Y. Gavel, *Eur. J. Biochem.* **174**, 671 (1988).
21. S. Stankowski, *Biophys. J.* **60**, 341 (1991).
22. R. Aveyard, D. A. Haydon, *An Introduction to the Principles of Surface Chemistry* (Cambridge Univ. Press, Cambridge, 1973).

Acknowledgments. We thank the staff at beamline X06SA at the Swiss Light Source, in particular T. Tomizaki, for assistance with data collection and W. Hardt (ETH Zürich) for genomic DNA of *S. typhimurium*. R. Dutzler (University of Zürich) is acknowledged for helpful discussions. This work was supported by Deutsche Forschungsgemeinschaft (Ei-520/3 to O.E., An-676/1 to S.L.A.A., and IRTG 1478). The structural model and structure factors have been deposited with the Protein Data Bank (accession code 3Q7K).

Supporting Online Material

www.sciencemag.org/cgi/content/full/332/6027/352/DC1
Materials and Methods

Figs. S1 to S3

Table S1

References

14 October 2010; accepted 17 March 2011
10.1126/science.1199098

Specificity of *Drosophila* Cytonemes for Distinct Signaling Pathways

Sougata Roy, Frank Hsiung,* Thomas B. Kornberg†

Cytonemes are types of filopodia in the *Drosophila* wing imaginal disc that are proposed to serve as conduits in which morphogen signaling proteins move between producing and target cells. We investigated the specificity of cytonemes that are made by target cells. Cells in wing discs made cytonemes that responded specifically to Decapentaplegic (Dpp) and cells in eye discs made cytonemes that responded specifically to Spitz (the *Drosophila* epidermal growth factor protein). Tracheal cells had at least two types: one made in response to Branchless (a *Drosophila* fibroblast growth factor protein, Bnl), to which they segregate the Bnl receptor, and another to which they segregate the Dpp receptor. We conclude that cells can make several types of cytonemes, each of which responds specifically to a signaling pathway by means of the selective presence of a particular signaling protein receptor that has been localized to that cytoneme.

Cells in developing tissues are influenced by multiple signals that they process and integrate to control cell fate, proliferation, and patterning. An example is in the *Drosophila* wing imaginal disc, where cells depend on several signaling systems that are intrinsic to the disc. Decapentaplegic (Dpp), Wingless (Wg), Hedgehog (Hh), and epidermal growth factor (EGF) are produced and released by different sets of disc

cells, and receipt of these signaling proteins programs their neighbors to develop and grow. The mechanisms by which morphogen signaling proteins influence target cells must ensure both specificity and accuracy, and one possibility is that these proteins transfer at points of direct contact (1). Imaginal discs are flattened sacs that have a monolayer of columnar cells on one side and squamous peripodial cells on the other (Fig. 1, A and B).

Many cells in wing discs make filopodial extensions that lie along the surfaces of the monolayers, oriented toward morphogen-producing cells (2). These extensions have been termed cytonemes to denote their appearance as cytoplasmic threads and to distinguish them as specialized structures that polarize toward morphogen-producing regions.

In wing discs dissected from third instar larvae, cytonemes can be seen as filaments extending from randomly generated somatic clones (3) (fig. S1) engineered to express a fluorescent protein such as soluble, cytoplasmic green fluorescent protein (GFP) (2, 4) or a membrane-bound form such as mCD8:GFP (the extracellular and transmembrane domains of the mouse lymphocyte protein CD8 fused to GFP) (5). To image disc cytonemes, we placed unfixed discs peripodial side down on a coverslip, covered them with a 1-mm-square glass, and mounted them over a depression slide with the disc hanging from the

Cardiovascular Research Institute and Department of Biochemistry and Biophysics, University of California, San Francisco, CA 94158, USA.

*Present address: BioRad Laboratories, Hercules, CA 94547, USA.

†To whom correspondence should be addressed. E-mail: tkornberg@ucsf.edu

coverslip [details in (5)]. Because fluorescence levels in cytonemes were low relative to background, recorded images were processed to increase intensity and were subjected to deconvolution (3). Expression of CD8:GFP in wing disc clones revealed cytonemes emanating from both the apical and basal surfaces of columnar cells, as well as from peripodial cells (whose apical and basal surfaces could not be distinguished) (Fig. 1, A and B; fig. S1, A to C; and table S1). Most cytonemes were perpendicular to the anterior/posterior (A/P) axis of the disc and oriented toward the cells that produce Dpp at the A/P compartment border; others were oriented toward the cells that produce Wingless at the dorsal/ventral (D/V) compartment border (5). Disc-associated myoblasts also had filopodia (fig. S1D).

In the eye disc, cells in the columnar layer organize into ommatidial clusters as a wave of differentiation [the morphogenetic furrow (MF)] passes from posterior to anterior (Fig. 1C) [reviewed in (6)]. A second axis, centered at the equator, is orthogonal to the MF and defines a line of mirror-image symmetry where dorsal and ventral ommatidia are juxtaposed [reviewed in (7)]. The columnar cells divide during the third instar period but stop or divide only once after the MF passes. We induced CD8:GFP expression in somatic clones and examined the columnar cells. Whereas clones of six to eight cells were present on both sides of the MF, only cells anterior to the MF had visible cytonemes. Cytonemes emanating from these clones oriented either toward the axis defined by the MF or toward the axis defined by the equator (Fig. 1, D and E). Single clones with cytonemes oriented both toward the MF and toward the equator were not observed, and there was no apparent correlation between clone position and cytoneme orientation or cytoneme length (Fig. 1C). Cells in the peripodial layer of the eye disc also had cytonemes (fig. S1E).

The EGF pathway is a key signaling system for eye development [(8); reviewed in (9)], and cells in the MF express the EGF protein Spitz [Spi (10)]. Because one of the two types of anterior cell cytonemes extended toward the MF (Fig. 1D) and to explore the distribution of membrane-bound receptor proteins, we induced clones that expressed an epidermal growth factor receptor:GFP [EGFR:GFP (11)] fusion protein. Anterior cells expressing EGFR:GFP had cytonemes that oriented toward the MF, and most of these cytonemes had fluorescent puncta (Fig. 1F); no cytonemes that were marked by EGFR:GFP oriented toward the equator ($n = 125$ clones). Other than their “furrow-only” orientation, the cytonemes marked by EGFR:GFP were similar to those marked by CD8:GFP. In contrast, co-expression of CD8:GFP with (nonfluorescent) EGFR marked both furrow-directed and equator-directed cytonemes (fig. S1, G and H). Thus, expression of EGFR:GFP does not eliminate the specific localization of EGFR:GFP to furrow-

directed cytonemes is not a consequence of ectopic (over)expression of this fusion protein.

Evidence that the furrow-directed cytonemes depend on Spi/EGF signaling was obtained by expressing a dominant negative form of EGFR (12). Although EGFR is required for cell proliferation in the disc, small clones expressing EGFR^{DN} (12) were recovered that co-expressed EGFR^{DN} and CD8:GFP; in these clones, only cytonemes that appeared to be randomly oriented were present (Fig. 1G), indicating that the long, furrow-directed cytonemes (Fig. 1, D and F) may require EGFR signal transduction in the cytoneme-producing cells.

Wing disc-associated tracheal cells also make cytonemes (13, 14). The transverse connective (TC) is a tracheal tube that nestles against the basal surface of the wing disc columnar epithelium and that sprouts a new branch [the air sac primordium (ASP)] during the third instar period

in response to Branchless (Bnl) expressed by the wing disc (Fig. 1, A and B, and fig. S1, I to K) (14). Tracheal tubes are composed of a monolayer of polarized cells whose apical surfaces line a lumen. Expression of CD8:GFP throughout the trachea (*btl-Gal4 UAS-CD8:GFP*) made it possible for us to detect GFP fluorescence in several types of cytonemes emanating from the basal surfaces of the TC and ASP. Cytonemes at the tip of the ASP (Fig. 1A and fig. S1K) (length range, 12 to 50 μm ; average length of 23 μm) contained the Breathless (Btl); the *Drosophila* fibroblast growth factor receptor (FGFR) and appeared to contact disc cells that express Bnl (14). Short cytonemes (length range, 2 to 15 μm ; average length of 8.5 μm) extended from the TC cells in the vicinity of the ASP (fig. S1J and table S1).

We tested whether Dpp, Spi, Bnl, and Hh affected wing disc, eye disc, and tracheal cytonemes differentially. Ubiquitous expression of Spi, Bnl,

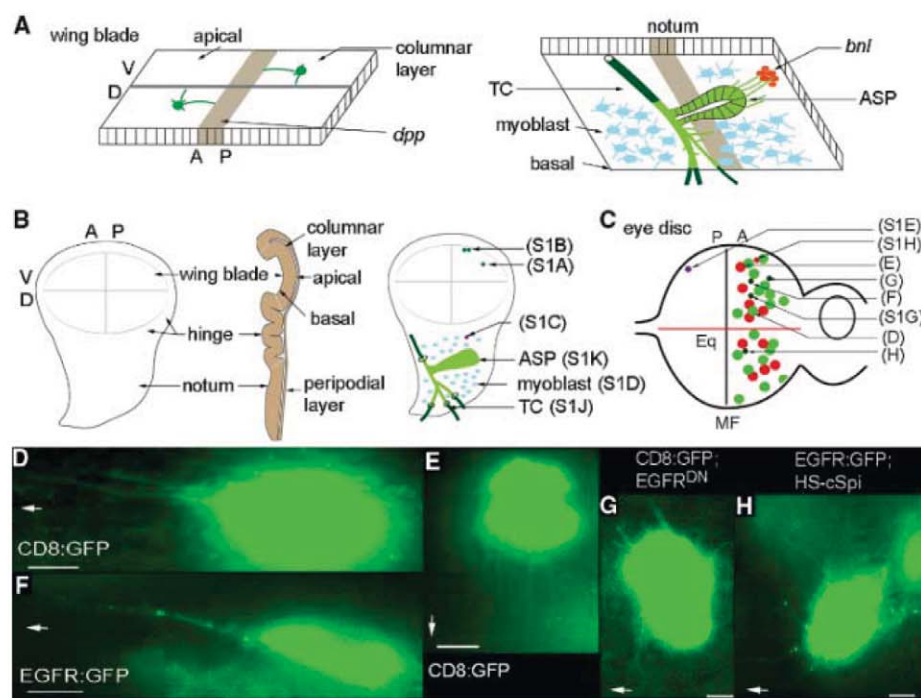


Fig. 1. Oriented cytonemes in the wing and eye discs. (A) Representation of cytonemes on the apical surface of the columnar layer of the wing disc (left) and of cytonemes at the basal surface of the wing disc emanating from the ASP (right). *bnl*- and *dpp*-expressing regions are in red and brown, respectively; the disc-associated Tr2 TC is partly external to the disc basal lamina (dark green) and partly within the disc basal lamina [light green (12)]; ASP is shown in light green; myoblasts, blue. (B) Drawings of third instar wing discs viewed from the columnar epithelial side (left), viewed through to the basal side (right), and viewed in cross section (middle). Positions of CD8:GFP-expressing clones cross-referenced (in parentheses) to supporting online material (SOM) figure panels. (C) Drawing of third instar eye-antennal disc with eye primordium to left, antenna primordium to right; equator, Eq; area posterior to MF, P; area anterior to MF, A. Approximate locations of CD8:GFP-expressing clones are shown [cross-referenced in parentheses to (D) to (H) and SOM figure panels] in the columnar layer with cytonemes directed toward the morphogenetic furrow (green), toward the equator (red), or in the peripodial layer (purple). Clones in overexpression genetic backgrounds are shown with small circles. (D and E) Cytonemes oriented toward the MF (D) or toward the equator (E) extended from anterior clones in the columnar layer. (F) An EGFR:GFP-expressing clone in the columnar layer illuminated puncta in cytonemes oriented to the MF. (G) A clone expressing CD8:GFP and EGFR^{DN} extended short cytonemes. (H) EGFR:GFP-containing cytonemes radiate in many directions after ubiquitous expression of cSpi. In (D), and (F) to (H), MF is to left as indicated by arrows, and equator is down, as indicated by arrow in (E). Scale bars, 5 μm .

or Hh [induced by heat shock (Fig. 2, A and C to E) (3)] did not alter the A/P-oriented apical cytonemes in the wing disc, and, in the eye disc, the long cytonemes of the columnar layer were unaltered after ubiquitous expression of Dpp, Bnl, or Hh (Fig. 2, F, G, I, and J, and table S2). In contrast, long oriented cytonemes were absent in wing discs after ubiquitous expression of Dpp, and only short cytonemes that appeared to be randomly oriented were observed (Fig. 2B). Similarly, 0.5 to 3 hours after cSpi, a constitutively active form of EGF (15), was expressed ectopically by heat shock induction, clones expressing CD8:GFP in the eye disc had many short cytonemes that lacked apparent directional bias (Fig. 2H); in contrast to controls (Fig. 2F), no long cytonemes oriented toward the MF were observed. Cytonemes with normal orientation and length (including MF-directed cytonemes) were present in eye discs that were examined later, 8 hours after a pulse of cSpi expression (fig. S1F). To monitor EGFR-containing cytonemes for sensitivity and responsiveness to Spi, we expressed cSpi by heat shock induction and examined cells in clones expressing EGFR:GFP. After a pulse of cSpi expression, the extensions oriented outward without apparent directional bias, and the EGFR:GFP puncta were present in all cytonemes (Fig. 1, F and H).

To examine responses of the ASP tip cytonemes, we overexpressed Hh, Spi, Dpp, and Bnl by heat shock and examined GFP-marked cytonemes at the ASP tip (Fig. 2, K to P; tables S2 and S3; and fig. S2). No differences in number of cytonemes were detected until about 3 hours after heat shock. Four to 5 hours after heat shock, expression of Bnl increased the number of tip cytonemes by ~2.6 times, and although most of the cytonemes were <30 μm , the cytonemes >30 μm also increased (~3.2 times). Most of the long cytonemes in these preparations were oriented in directions other than toward the cells that normally express Bnl. The number of long cytonemes >30 μm did not change after overexpression of Hh, Spi, and Dpp (0.6 to 0.8 times); the number of short cytonemes increased after Dpp overexpression (~1.7 times) but not after overexpression of Hh or Spi.

Thus, the responses of apical wing disc cytonemes to overexpressed Dpp (Fig. 2, A and B), of eye disc cytonemes to ubiquitous Spi (Fig. 2, F and H), and of ASP tip cytonemes to exogenous Bnl (*Drosophila* FGF) (Fig. 2, K and N) (14) are similar. These results suggest that the cytonemes we detected in the wing discs and eye discs may have orientations and lengths that are dependent specifically on the respective sources of Dpp and Spi, whereas the ASP may extend cytonemes in response to more than one signaling protein. These results are, however, complicated by the heat shock mode of induction because both the cells that expressed GFP (and extended marked cytonemes) as well as the surrounding cells expressed the signaling proteins. To overcome this problem, we developed a meth-

od to induce two types of somatic clones in the same tissue, one that expressed GFP and another that expressed Dpp.

We used the GAL4 system to label cytonemes with CD8:GFP. Clones of GAL4-expressing cells were generated with heat shock–induced flippase (FLP recombinase). The second type of clone expressed a Dpp:Cherry fusion and was generated with a variant Cre-progesterone receptor recombinase that could be activated with a regime of heat shock and RU486 (3). By adjusting the timing and strength of induction, we produced wing discs with small, independent, and relatively infrequent clones. In discs with clones that expressed ectopic Dpp as well as clones that expressed CD8:GFP, apical cytonemes tagged with GFP were detected that oriented toward nearby Dpp:Cherry-expressing cells and not toward either the A/P or D/V signaling centers (Fig. 2, Q and R) ($n = 5$). Such “abnormally directed” cytonemes were never observed in control discs ($n > 200$). The abnormally oriented cytonemes suggest that apical cytonemes in the wing blade respond directly to sources of Dpp and that their orientation reflects extant sources of signaling protein.

To characterize the relationship between tracheal ASP tip cytonemes and FGF signaling from the wing disc, we examined the distribution of Btl (FGFR) in ASP cells and in ASP cytonemes. In preparations from larvae with tracheal expression of both CD8:GFP and Btl:Cherry (*btl-GAL4 UAS-CD8:GFP; UAS-Btl:Cherry*), cytonemes were marked by CD8:GFP, some of which had fluorescent Btl:Cherry puncta (Fig. 3A). Each ASP had only a few long (>30 μm) cytonemes, most of which contained Btl:Cherry puncta. Few of the more numerous short cytonemes (<30 μm) contained Btl:Cherry puncta. To characterize Btl:Cherry after overexpression of Bnl, we focused on preparations obtained 1 to 2 hours post-induction (genotype *btl-GAL4 UAS-CD8:GFP/Hs-Bnl; UAS-Btl:Cherry/Gal80^{ts}*), because during this time interval the ASP morphology was close to normal but cytonemes had changed (Fig. 3, D to J, and table S4). We did not focus on ASPs after longer postinduction intervals because of major malformations to ASP morphology after 3 to 4 hours [fig. S3 and SOM; in contrast, changes to ASP cytonemes were not observed until 3 to 5 hours after overexpression of Bnl and CD8:GFP, and ASP morphology was normal at this time

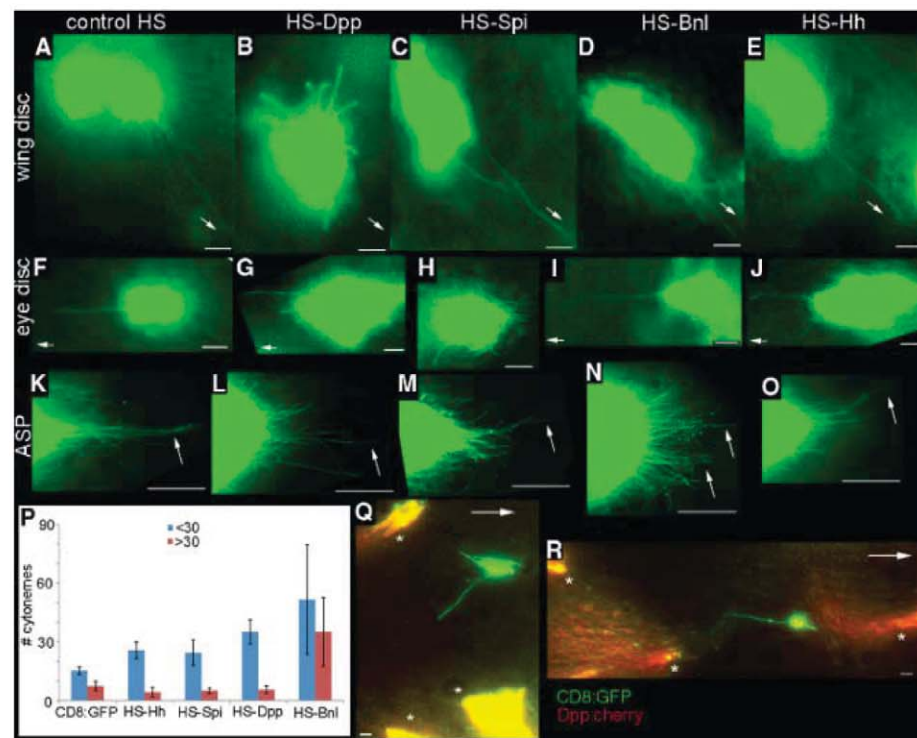


Fig. 2. Ligand-specificity of cytonemes. Dpp, Spi, Bnl, and Hh were expressed ubiquitously by heat shock 1/2 to 2 hours before imaging CD8:GFP in columnar cell clones in the wing disc (B to E), in columnar cell clones in the eye disc (G to J), or 3 to 5 hours before imaging CD8:GFP in ASPs in which expression was driven by *btl-Gal4* (K to O). CD8:GFP larvae heat-shocked although lacking the respective heat shock (HS) expression transgenes served as controls [(A), (F), and (K)]. (P) Chart tabulating number of long (>30 μm , red) and short (<30 μm , blue) cytonemes at the ASP tip (100- μm circumferential arc at the tip, average of five specimens, error bars represent SD). (Q and R) Images from wing discs with independent clones that express Dpp:Cherry (*) or CD8:GFP (green). Arrows point toward A/P signaling center [(A) to (E), (Q), and (R)], toward the MF [(F) to (J)], or to long cytonemes at the ASP tip [(K) to (O)]. Scale bars for (A) to (J), (Q), and (R), 5 μm ; for (K) to (O), 30 μm .

interval for this genotype (Fig. 2)]. Long cytonemes with Btl:Cherry puncta were present 1 hour after a pulse of Bnl expression (Fig. 3E); but 2 hours after the pulse, most ASPs had no long cytonemes (Fig. 3F), and the number of short puncta-containing cytonemes increased at the tip (Fig. 3F) and along the shaft of the ASPs (Fig. 3G). After control heat shock or heat shock–induced expression of Dpp, the distribution of Btl:Cherry puncta in the ASP tip cytonemes was similar to normal controls: Long cytonemes had Btl:Cherry puncta, but most short cytonemes did not (Fig. 3, A to C, and table S4).

We also documented the distribution of Btl:Cherry in response to ectopic Bnl by imaging the entire ASP at lower magnification (Fig. 3, H to J). These views show Btl-containing puncta in the ASP cells and reveal an increase in number of puncta after induction of Bnl expression (per 20 ASP cells, the approximate number of Btl:Cherry puncta at the tip were 80 at time $t = 0$, 435 at $t =$

1 hour, and 710 at $t = 2$ hours; in the middle region of the ASP numbers were 61 at $t = 0$, 415 at $t = 1$ hour, and 750 at $t = 2$ hours). Two hours after Bnl expression was induced, the number of cytonemes increased all around the ASP periphery, and these cytonemes were densely populated with Btl:Cherry puncta (Fig. 3, H to J).

Because we found that the number of small cytonemes at the ASP tip may have increased after ectopic Dpp expression (fig. S2 and table S3), we investigated whether the *thickveins* (*tkv*) gene (*16*), which encodes a subunit of the Dpp receptor, is expressed in the ASP. We detected expression of the *tkv* reporter, *tkv-lacZ* (*P{lacW}tkv¹⁶⁷¹³*), in the ASP (fig. S4A). When we expressed Tkv:GFP and Btl:Cherry together, Tkv:GFP and Btl:Cherry segregated to separate tip cytonemes at the ASP tip (Fig. 3, K to M, and fig. S4, B to K). Whereas Tkv-containing cytonemes were short (<30 μ m), most of the Btl-containing cytonemes were longer (three of four of the Btl:Cherry-containing

cytonemes were longer than 30 μ m), and they lay in focal planes closer to the disc (Fig. 3K, fig. S4H, and table S5). These properties were consistent in all preparations we examined in which both green Tkv and red Btl cytonemes were intact ($n = 29$). Imaging these marked ASPs revealed that overexpressed Tkv:GFP and Btl:Cherry were present not only in the plasma membranes (as expected) but also in separate puncta in the cell bodies (Fig. 3N and fig. S4, L to N). This shows that Tkv and Btl receptors also segregated to separate locations in the ASP cell bodies.

Our findings suggest that the ASP has long cytonemes that are specific to Bnl and specifically harbor Btl-containing puncta and that the ASP also has cytonemes that are specific to Dpp and specifically harbor Tkv. Similarly in the eye disc, the presence of EGFR:GFP in furrow-oriented cytonemes and not in equator-oriented cytonemes suggests that cytonemes in the eye disc also selectively localize receptors (Fig. 1F). And as we previously showed, apical cytonemes in the wing disc selectively localize Tkv (5). The apparent ligand specificities and contrasting make-up of these cytonemes suggest a diversity of functionally distinct subtypes: Cells appear to make cytonemes that respond specifically to the Dpp, EGF, or Bnl signaling proteins. [The basal filopodia implicated in Delta-Notch signaling in the wing disc (17) may represent yet another type.]

The mechanism that endows cytonemes with specificity for a particular signaling protein cannot be based solely on tissue-specific expression of a receptor. Spi, Dpp, and Hh are active in eye discs, but only changes in Spi signaling affected the furrow-directed cytonemes. And in the wing disc, both the Hh and EGF signal transduction pathways are active in cells at the A/P compartment border, but the apical cytonemes only responded to overexpressed Dpp. Our findings that tracheal cells in the ASP respond to both Dpp and Bnl and that the Tkv and Btl receptors are present in different cytonemes that the ASP cells extend suggest that specificity may be a consequence of the constitution of the cytoneme, not on which receptors the cells make. The mechanism that localizes receptors to different cytonemes is not known, but because the marked receptors we expressed also segregated to different intracellular puncta, the processes that concentrate these receptors in separate locations may not be exclusive to cytonemes. There is a precedent for segregation of proteins to different cellular extensions, neurons segregate proteins to dendrites or axons, so extending projections with specific and distinct attributes may be a general property of cells.

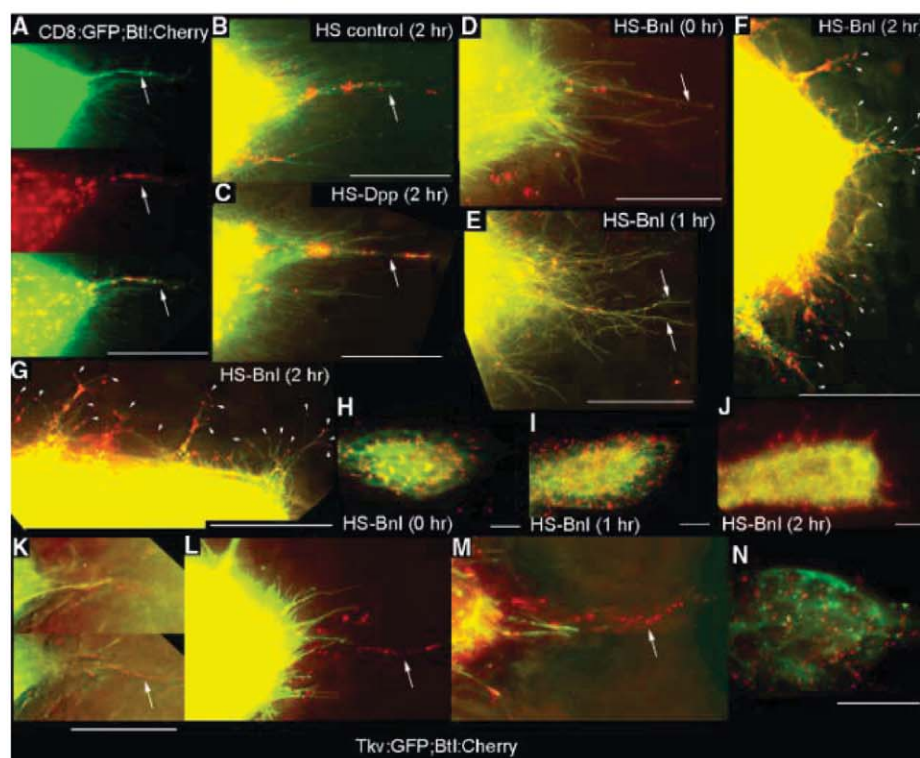


Fig. 3. Dpp and FGF receptors segregate to separate locations in the ASP. (A to J) Expression of Btl:Cherry and CD8:GFP driven by *btl-Gal4* mark ASP cytonemes (green) with Btl-containing puncta (red). [(A) and (B)] ASP tips from larvae lacking a HS transgene with (B) or without (A) heat shock. (C) Btl:Cherry puncta in ASP tip cytonemes after ectopic expression of Dpp. [(D) to (F) and (H) to (J)] Expression of Btl:Cherry and CD8:GFP released from Gal80^{ts} repression by temperature elevation (3) and subjected to heat shock for the indicated times. (E) Image of ASP tip 1 hour after heat shock. (F) Image of ASP tip 2 hours after heat shock [also see table S4 and (3)]. (G) Image of one side of the ASP tube between the TC and tip of (F). Arrowheads in (F) and (G) indicate short cytonemes containing Btl:Cherry puncta. [(H) to (J)] Low-resolution (40 \times) images showing distribution of Btl:Cherry after overexpression of Bnl. (F), (G), and (J) are images of the same preparation. (K to N) Tip of ASPs expressing Tkv:GFP and Btl:Cherry driven by *btl-Gal4*. (K) Two focal planes from z-sections in which Tkv:GFP-containing cytonemes were in a focal plane (top) less proximal to the disc than those with Btl:Cherry (bottom). [(L) and (M)] Projection images show distinct Tkv:GFP and Btl:Cherry-containing cytonemes at ASP tip. (N) Image of mid-distal ASP. Arrows in (A) to (D) and (K) to (M) indicate long cytonemes containing Btl:Cherry puncta. All images oriented ASP tip to right. Scale bars, 30 μ m.

References and Notes

1. T. B. Kornberg, A. Guha, *Curr. Opin. Genet. Dev.* **17**, 264 (2007).
2. F. A. Ramirez-Weber, T. B. Kornberg, *Cell* **97**, 599 (1999).
3. Materials and methods are available as supporting material on Science Online.
4. T. T. Yang, L. Cheng, S. R. Kain, *Nucleic Acids Res.* **24**, 4592 (1996).
5. F. Hsiung, F. A. Ramirez-Weber, D. D. Iwaki, T. B. Kornberg, *Nature* **437**, 560 (2005).

6. J. Y. Roignant, J. E. Treisman, *Int. J. Dev. Biol.* **53**, 795 (2009).
 7. R. Reifegerste, K. Moses, *Bioessays* **21**, 275 (1999).
 8. J. P. Kumar, K. Moses, *Cell* **104**, 687 (2001).
 9. C. Jones, K. Moses, *Semin. Cell Dev. Biol.* **15**, 75 (2004).
 10. A. Schlesinger, A. Kiger, N. Perrimon, B. Z. Shilo, *Dev. Cell* **7**, 535 (2004).
 11. D. Alvarado, A. H. Rice, J. B. Duffy, *Genetics* **167**, 187 (2004).
 12. M. Freeman, *Cell* **87**, 651 (1996).
 13. A. Guha, L. Lin, T. B. Kornberg, *Dev. Biol.* **335**, 317 (2009).
 14. M. Sato, T. B. Kornberg, *Dev. Cell* **3**, 195 (2002).
 15. R. Schweitzer, M. Shaharabany, R. Seger, B. Z. Shilo, *Genes Dev.* **9**, 1518 (1995).
 16. E. Ruberte, T. Marty, D. Nellen, M. Affolter, K. Basler, *Cell* **80**, 889 (1995).
 17. M. Cohen, M. Georgiou, N. L. Stevenson, M. Miodownik, B. Baum, *Dev. Cell* **19**, 78 (2010).
- Acknowledgments:** We thank H. Li and K. Kechris for help with data analysis; S. Liu for technical help; the Bloomington *Drosophila* Stock Center, I. Guerrero, E. Bier, M. Krasnow, J. Duffy, M. Sato, and K. Wharton for fly stocks; and T. Wunderlich for hCre⁺PR⁺. This work was supported in part by a Herbert Boyer Postdoctoral

Fellowship (to S.R.) and by grants from the National Institute of General Medical Studies and the National Heart, Lung, and Blood Institute to T.B.K.

Supporting Online Material

www.sciencemag.org/cgi/content/full/332/6027/354/DC1
Materials and Methods
Figs. S1 to S4
Tables S1 to S5
References

12 October 2010; accepted 1 March 2011
10.1126/science.1198949

Noncanonical TGFβ Signaling Contributes to Aortic Aneurysm Progression in Marfan Syndrome Mice

Tammy M. Holm,^{1,*} Jennifer P. Habashi,^{1,2,*} Jefferson J. Doyle,^{1,*} Djahida Bedja,³
YiChun Chen,¹ Christel van Erp,¹ Mark E. Lindsay,^{1,2} David Kim,¹ Florian Schoenhoff,¹
Ronald D. Cohn,^{1,2} Bart L. Loeys,⁴ Craig J. Thomas,⁵ Samarjit Patnaik,⁵ Juan J. Marugan,⁵
Daniel P. Judge,⁶ Harry C. Dietz^{1,2,6,†}

Transforming growth factor-β (TGFβ) signaling drives aneurysm progression in multiple disorders, including Marfan syndrome (MFS), and therapies that inhibit this signaling cascade are in clinical trials. TGFβ can stimulate multiple intracellular signaling pathways, but it is unclear which of these pathways drives aortic disease and, when inhibited, which result in disease amelioration. Here we show that extracellular signal-regulated kinase (ERK) 1 and 2 and Smad2 are activated in a mouse model of MFS, and both are inhibited by therapies directed against TGFβ. Whereas selective inhibition of ERK1/2 activation ameliorated aortic growth, Smad4 deficiency exacerbated aortic disease and caused premature death in MFS mice. Smad4-deficient MFS mice uniquely showed activation of Jun N-terminal kinase-1 (JNK1), and a JNK antagonist ameliorated aortic growth in MFS mice that lacked or retained full Smad4 expression. Thus, noncanonical (Smad-independent) TGFβ signaling is a prominent driver of aortic disease in MFS mice, and inhibition of the ERK1/2 or JNK1 pathways is a potential therapeutic strategy for the disease.

The transforming growth factor-β (TGFβ) ligands belong to a family of cytokines that regulates diverse cellular functions, including proliferation, differentiation, and synthetic repertoire. TGFβ is secreted from cells as part of a large latent complex that binds to extracellular matrix (ECM) proteins including fibrillin-1 (1), the deficient gene product in Marfan syndrome (MFS). Current models posit that ECM sequestration of TGFβ inhibits its activation, thereby limiting its ability to stimulate cell surface receptors, TβRI and TβRII (2, 3). In canonical

signaling, the TβRI/II complex phosphorylates receptor-activated Smad2 and/or Smad3 (to pSmad2 and pSmad3, respectively), which leads to recruitment of Smad4, translocation to the nucleus, and the transcription of Smad-dependent genes (4). Recent work has shown that TGFβ also induces other (noncanonical) pathways, including the RhoA and mitogen-activated protein kinase (MAPK) cascades, the latter of which includes extracellular signal-regulated kinase (ERK), Jun N-terminal kinase (JNK), and p38 (5–7). TGFβ activates these by phosphorylation to pERK, pJNK, and pp38, respectively. In light of these findings, the exclusive focus on Smad signaling in TGFβ-related pathogenetic models needs to be reconsidered.

Increased Smad2/3 activation and increased expression of Smad-responsive genes (e.g., connective tissue growth factor and plasminogen-activator inhibitor-1, PAI-1) have been observed in the lung, skeletal muscle, mitral valve, and aortic wall in humans and a mouse model of MFS (8–11). Treatment of MFS mice with TGFβ-neutralizing antibody (TGFβNAb) ameliorates the phenotype in all of these tissues, in association with attenuated pSmad2/3 signaling (8–11). A

similar rescue is achieved by using the angiotensin II type 1 receptor-blocker losartan (8–11), which is known to reduce the expression of TGFβ ligands, receptors, and activators (12–14). It has also been shown that mutations in TβRI or II, which lead to a paradoxical increase in pSmad2 signaling in the aortic wall, cause Loeys-Dietz syndrome, a condition that has considerable phenotypic overlap with MFS, including aortic aneurysm (15, 16). Together, these earlier observations suggested that canonical TGFβ signaling drives disease pathogenesis in MFS. We have now explored the relative contributions of canonical and noncanonical TGFβ signaling cascades in MFS mice, by either genetically or pharmacologically inhibiting each cascade and analyzing the resultant phenotypic consequences.

We performed Western blot analysis on the proximal ascending aorta of 12-month-old mice heterozygous for a missense mutation in *Fbn1* (*Fbn1*^{C1039G/+}), a validated animal model of MFS (17). Compared with wild-type (WT) littermates, *Fbn1*^{C1039G/+} mice showed a significant increase in activation of Smad2, ERK1/2, and MAPK kinase 1 (MEK1), the upstream activator of ERK1/2 ($P < 0.05$, $P < 0.001$, and $P < 0.05$, respectively) (Fig. 1A). In contrast, there was no difference in the activation of Smad3; JNK1; p38; ERK5; Rho-associated coiled-coil containing protein kinase-1 (ROCK1); or LIMK1, a downstream target of ROCK1 (Fig. 1A and fig. S1) (18). Furthermore, an in vivo trial of fasudil, a well-established inhibitor of the RhoA/ROCK pathway [details discussed in (18)] failed to attenuate aortic root growth in *Fbn1*^{C1039G/+} mice (fig. S2).

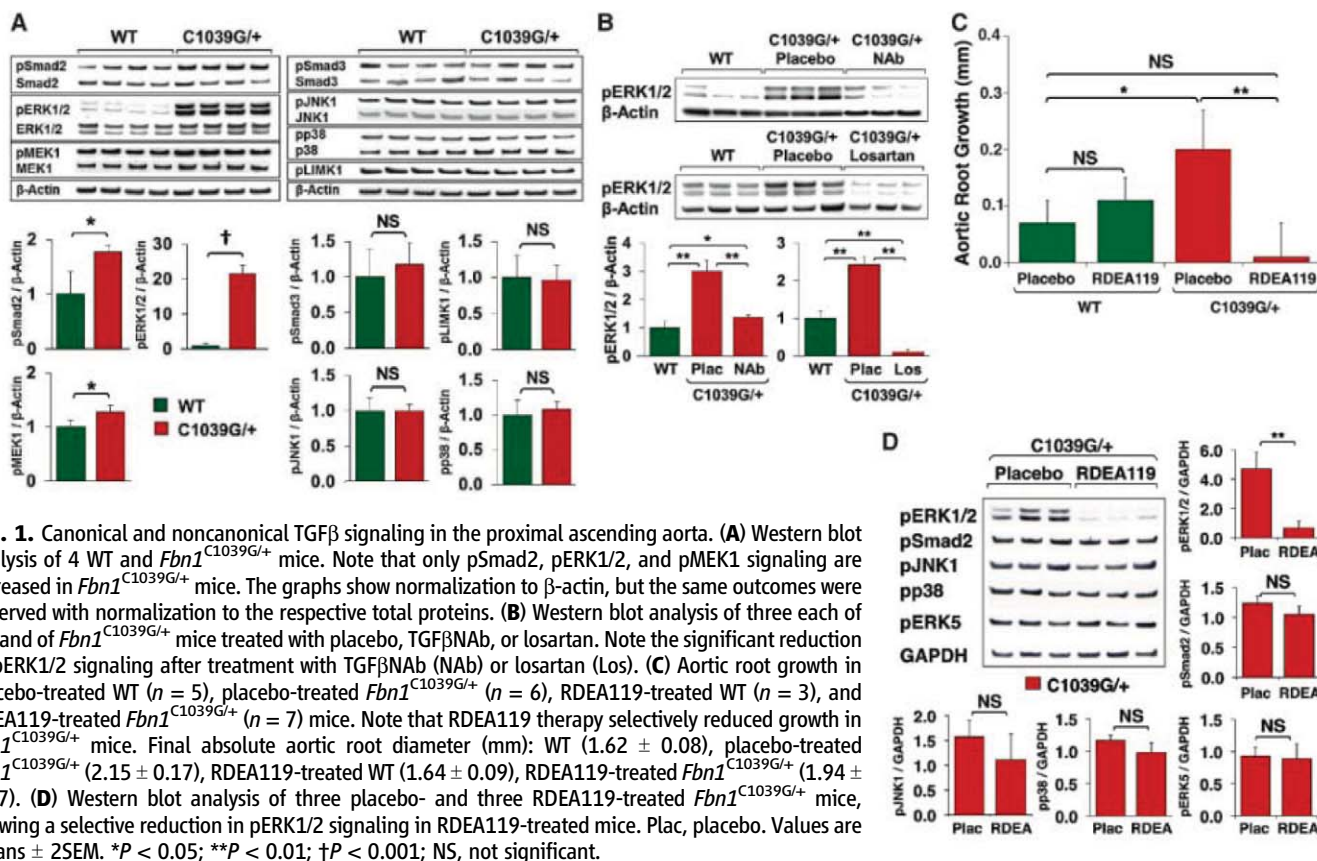
Because TGFβNAb and losartan attenuate aortic root growth in *Fbn1*^{C1039G/+} mice (fig. S3) (10), if Smad2 or ERK1/2 are important mediators of aortic disease in MFS, one would expect their activation to be reduced by these agents. Prior work demonstrated that Smad2 activation is decreased by both therapies (10). We now find that compared with placebo-treated littermates, *Fbn1*^{C1039G/+} mice treated with either TGFβNAb or losartan also show a significant reduction in ERK1/2 activation ($P < 0.01$ for both) (Fig. 1B).

To confirm that ERK1/2 is a driver, rather than simply a marker, of aortic aneurysm progression, 2-month-old *Fbn1*^{C1039G/+} mice were treated for 2 months with the selective MEK1/2 inhibitor RDEA119 (19). Aortic root size was measured by echocardiography at 2 months (baseline before treatment) and 4 months of age (Fig.

¹Howard Hughes Medical Institute and Institute of Genetic Medicine, Johns Hopkins University School of Medicine, Baltimore, MD 21205, USA. ²Division of Pediatric Cardiology, Department of Pediatrics, Johns Hopkins University School of Medicine, Baltimore, MD 21205, USA. ³Department of Molecular and Comparative Pathobiology, Johns Hopkins University School of Medicine, Baltimore, MD 21205, USA. ⁴Centre for Medical Genetics, Ghent University, 9000 Ghent, Belgium. ⁵National Institutes of Health Chemical Genomics Center, Rockville, MD 20850, USA. ⁶Department of Medicine, Johns Hopkins University School of Medicine, Baltimore, MD 21205, USA.

*These authors contributed equally to this work.

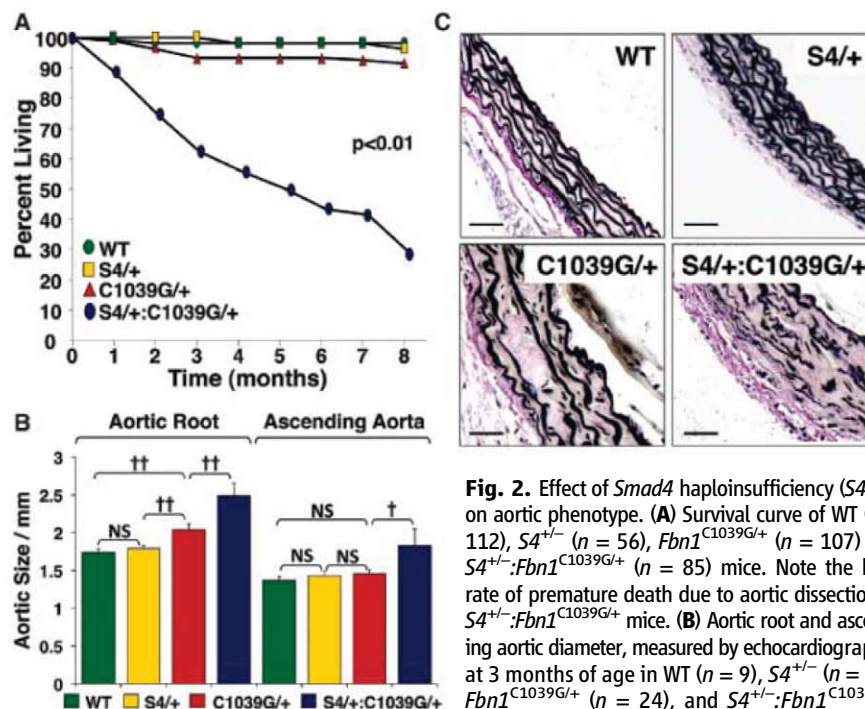
†To whom correspondence should be addressed. E-mail: hdietz@jhmi.edu.



IC). Aortic root growth was significantly greater in placebo-treated *Fbn1*^{C1039G/+} mice, compared with WT littermates ($P < 0.05$). Aortic root growth in RDEA119-treated *Fbn1*^{C1039G/+} mice was significantly less than that of placebo-treated *Fbn1*^{C1039G/+} littermates ($P < 0.01$) and indistinguishable from that observed in WT mice ($P = 0.15$). RDEA119 therapy had no significant effect in WT mice ($P = 0.24$), which illustrated that inhibition of ERK1/2 activation specifically targets MFS-associated pathological aortic root growth, while still allowing for normal physiological growth.

The specificity of RDEA119 was confirmed by Western blot analysis of the proximal ascending aorta. Compared with placebo-treated *Fbn1*^{C1039G/+} littermates, RDEA119-treated *Fbn1*^{C1039G/+} mice showed a significant reduction in ERK1/2 activation ($P < 0.01$), whereas Smad2, JNK1, p38 and ERK5 activation was unchanged (Fig. 1D). This result also shows that Smad2 activation in *Fbn1*^{C1039G/+} mice is not ERK-dependent. Together, these data suggest that TGF β -driven ERK1/2 activation contributes to aortic aneurysm progression in MFS mice and that antagonism of this pathway may be therapeutically useful.

To determine whether canonical signaling contributes to aortic disease progression in MFS, we introduced haploinsufficiency for Smad4, a critical mediator of canonical TGF β signaling, into our MFS mouse model. We bred *Fbn1*^{C1039G/+} mice to mice harboring a deletion of exon 8 of



a selective increase in aortic root diameter compared with WT littermates, *S4*^{+/-}:*Fbn1*^{C1039G/+} mice demonstrated an increase in both aortic root and ascending aortic diameter, compared with all other genotypes. **(C)** VVG staining of representative sections of the proximal ascending aorta. Compared with WT littermates, *Fbn1*^{C1039G/+} mice demonstrated medial thickening and elastic fiber fragmentation, both of which are exacerbated in *S4*^{+/-}:*Fbn1*^{C1039G/+} mice. Values are means \pm 2 SEM. † $P < 0.001$; †† $P < 0.0001$; NS, not significant.

the *Smad4* gene. Homozygosity for this *Smad4* allele ($S4^{-/-}$) results in the death of embryos (20). In contrast, haploinsufficient mice ($S4^{+/-}$) are fertile, have normal life spans, and show clinically relevant attenuation of Smad-dependent signaling in several tissues, including the stomach, breast, and intestine (20).

The *Fbn1*^{C1039G/+} MFS mouse model shows progressive aortic root dilatation, but does not typically progress to aortic dissection or pre-

mature death. Whereas almost all WT, $S4^{+/-}$ and *Fbn1*^{C1039G/+} mice survived to 8 months of age, $S4^{+/-};Fbn1^{C1039G/+}$ mice died prematurely. This was first evident by 1 month of age; by 3 months 40% had died, and by 8 months 70% had died (Fig. 2A). Necropsy of these animals revealed hemothorax and homopericardium in all cases, indicative of proximal aortic rupture; there was no evidence of aortic rupture in any WT, $S4^{+/-}$, or *Fbn1*^{C1039G/+} mice.

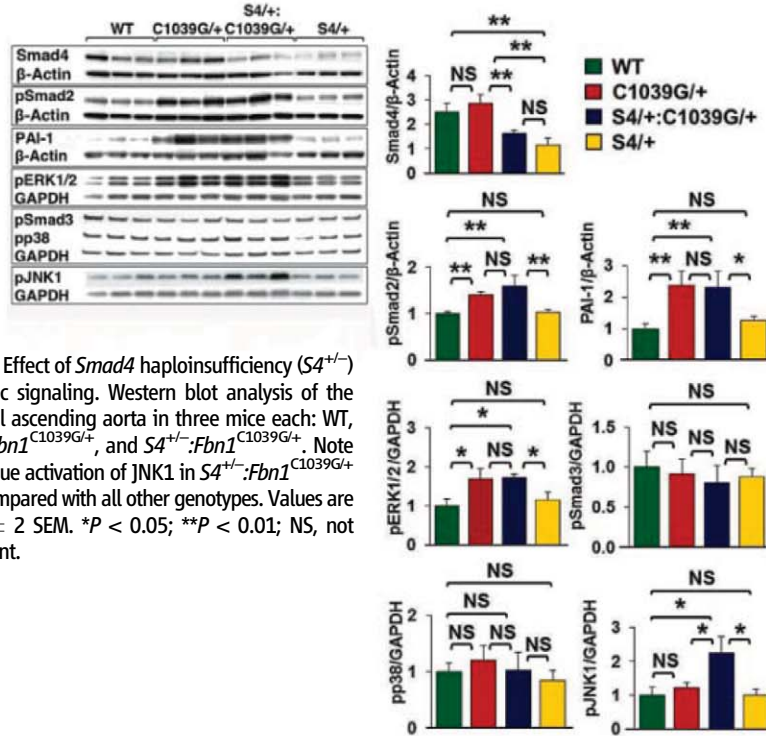


Fig. 3. Effect of *Smad4* haploinsufficiency ($S4^{+/-}$) on aortic signaling. Western blot analysis of the proximal ascending aorta in three mice each: WT, $S4^{+/-}$, *Fbn1*^{C1039G/+}, and $S4^{+/-};Fbn1^{C1039G/+}$. Note the unique activation of JNK1 in $S4^{+/-};Fbn1^{C1039G/+}$ mice compared with all other genotypes. Values are means \pm 2 SEM. *P < 0.05; **P < 0.01; NS, not significant.

Echocardiography at 3 months of age revealed significant enlargement of both the aortic root and the ascending aorta in $S4^{+/-};Fbn1^{C1039G/+}$ mice, compared with *Fbn1*^{C1039G/+} littermates ($P < 0.0001$ and $P < 0.001$, respectively) (Fig. 2B). These data provide a conservative estimate of the effect of *Smad4* haploinsufficiency, because premature deaths in the $S4^{+/-};Fbn1^{C1039G/+}$ cohort effectively eliminated more severe cases from the analysis. No difference in aortic root or ascending aortic size was observed between WT and $S4^{+/-}$ mice ($P = 0.20$ and $P = 0.20$, respectively) (Fig. 2B), which indicated that the deleterious effect of *Smad4* haploinsufficiency was limited to MFS mice.

After death of the mice, we performed Verhoeff–Van Gieson (VVG) staining of the proximal ascending aorta to assess whether there were any abnormalities in aortic architecture (Fig. 2C). Compared with WT littermates, *Fbn1*^{C1039G/+} mice showed increased aortic medial thickening, elastic fiber fragmentation, and elastic fiber disarray, collectively quantified as an aortic architecture score ($P < 0.0001$) (fig. S4). $S4^{+/-};Fbn1^{C1039G/+}$ mice showed an exaggeration of these pathologic changes ($P < 0.05$). By contrast, there was no significant difference between WT and $S4^{+/-}$ mice ($P = 0.94$). The histological changes in the aorta therefore paralleled the echocardiography findings and support the conclusion that *Smad4* haploinsufficiency exacerbates aortic disease in MFS mice.

Using Western blot analysis, we evaluated the effect of *Smad4* haploinsufficiency on canonical and noncanonical TGFβ signaling in the proximal ascending aorta (Fig. 3). As anticipated, $S4^{+/-}$ and $S4^{+/-};Fbn1^{C1039G/+}$ mice showed a roughly 50% reduction in expression of Smad4 protein, compared with WT and *Fbn1*^{C1039G/+} mice. Compared with WT animals, *Fbn1*^{C1039G/+} mice showed significantly greater activation of Smad2 and ERK1/2 ($P < 0.01$ and $P < 0.05$, respectively) and a significant increase in expression of the Smad2-responsive gene product PAI-1 ($P < 0.01$). However, there was no further increase in Smad2 activation, ERK1/2 activation, or PAI-1 expression in $S4^{+/-};Fbn1^{C1039G/+}$ mice ($P = 0.35$, $P = 0.90$, and $P = 0.85$, respectively). This indicates that *Smad4* haploinsufficiency did not attenuate Smad-dependent signaling and that increased Smad2 or ERK1/2 activation could not be invoked as the cause of the aortic disease exacerbation seen in $S4^{+/-};Fbn1^{C1039G/+}$ mice.

We next assessed whether other TGFβ-dependent canonical or noncanonical pathways could account for these changes (Fig. 3). There was no significant difference in Smad3 or p38 activation in WT, *Fbn1*^{C1039G/+}, or $S4^{+/-};Fbn1^{C1039G/+}$ mice. Although there was no significant difference in JNK1 activation between *Fbn1*^{C1039G/+} and WT mice, $S4^{+/-};Fbn1^{C1039G/+}$ mice demonstrated unique activation of JNK1 ($P < 0.05$). We therefore treated a cohort of $S4^{+/-};Fbn1^{C1039G/+}$ mice with SP600125, a selective JNK inhibitor (21). SP600125 treatment led to a significant re-

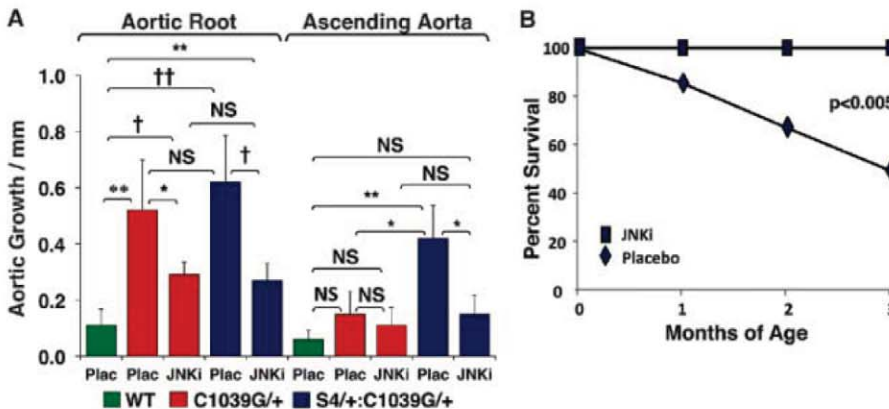


Fig. 4. Effect of JNK antagonism in the presence of SP600125. (A) Aortic root and ascending aortic growth, as measured by echocardiography, in WT mice ($n = 6$) and *Fbn1*^{C1039G/+} placebo- ($n = 5$) or SP600125-treated ($n = 5$) mice, as well as placebo- ($n = 8$) or SP600125-treated ($n = 11$) $S4^{+/-};Fbn1^{C1039G/+}$ littermates. Note that JNK inhibition decreased aortic root growth in $S4^{+/-};Fbn1^{C1039G/+}$ and *Fbn1*^{C1039G/+} mice and reduced ascending aortic growth in $S4^{+/-};Fbn1^{C1039G/+}$ mice. Final absolute aortic root and ascending aortic diameter (mm): WT (1.66 ± 0.06 ; 1.33 ± 0.06), placebo- (2.31 ± 0.02 ; 1.43 ± 0.10) or SP600125-treated (1.97 ± 0.16 ; 1.38 ± 0.06) *Fbn1*^{C1039G/+} mice, placebo- (2.33 ± 0.38 ; 1.85 ± 0.37) or SP600125-treated (2.09 ± 0.16 ; 1.47 ± 0.14) $S4^{+/-};Fbn1^{C1039G/+}$ mice. (B) Survival curve for $S4^{+/-};Fbn1^{C1039G/+}$ mice treated with either placebo ($n = 8$) or SP600125 ($n = 11$), showing prevention of premature death in SP600125-treated animals. JNKi, JNK inhibitor SP600125; Plac, placebo. Values are means \pm 2 SEM. *P < 0.05; **P < 0.01; †P < 0.001; ††P < 0.0001; NS, not significant.

duction in both aortic root and ascending aortic growth in $S4^{+/-};Fbn1^{C1039G/+}$ mice, compared with placebo-treated littermates ($P < 0.001$ and $P < 0.05$, respectively) (Fig. 4A). Furthermore, SP600125 treatment prevented the premature death due to aortic dissection seen in these animals. At 3 months of age, 50% of placebo-treated $S4^{+/-};Fbn1^{C1039G/+}$ mice had died from aortic dissection, whereas all of the SP600125-treated $S4^{+/-};Fbn1^{C1039G/+}$ mice were still alive (Fig. 4B).

Although JNK1 activation is not increased in the aortas of $Fbn1^{C1039G/+}$ mice, SP600125 treatment ameliorated their aortic root growth, compared with placebo-treated $Fbn1^{C1039G/+}$ littermates ($P < 0.05$) (Fig. 4A). This correlated with a reduction of JNK1 activation to levels below baseline, whereas ERK1/2 activation remained unaffected, in SP600125-treated $Fbn1^{C1039G/+}$ animals (fig. S5). This observation is consistent with prior work showing that SP600125 can ameliorate abdominal aortic aneurysm induced by the periaortic application of calcium chloride, in association with reduced JNK1 activation (22). These data suggest that both ERK1/2 and JNK1 can contribute to aortic disease in fibrillin-1-deficient mice; whether or not this relies upon downstream cross-talk between these signaling cascades remains to be determined. Taken together, these data further support the conclusion that noncanonical TGF β signaling is a prominent determinant of aortic aneurysm progression in MFS mice.

ERK activation was recently shown to occur in the aorta of a fibrillin-4-deficient mouse model of cutis laxa with aneurysm, although a mechanistic link remains to be elucidated (23). ERK

activation also appears to be central to the pathogenesis of cardiovascular disease in Noonan syndrome (24, 25). Although aortic aneurysm has been described in this condition (26, 27), it is not highly penetrant, which suggests as yet undefined context specificity. It is also notable that the combination of aortic root and ascending aortic aneurysm seen in $S4^{+/-};Fbn1^{C1039G/+}$ mice is similar to that observed in individuals with either Loeys-Dietz syndrome or bicuspid aortic valve and aneurysm. Both conditions are associated with increased TGF β signaling in the aortic wall (15, 28), but the contribution of non-canonical TGF β signaling cascades has not been revealed.

In summary, this work defines a critical role for noncanonical TGF β -dependent signaling in aneurysm pathogenesis in MFS mice. It also defines inhibition of ERK1/2 or JNK1 activation as possible therapeutic strategies for MFS and suggests that such therapies may find broader application. Finally, it focuses attention on non-canonical TGF β signaling cascades in MFS-related conditions, where etiology or pathogenesis remains poorly understood.

References and Notes

1. Z. Isogai et al., *J. Biol. Chem.* **278**, 2750 (2003).
2. H. C. Dietz, *J. Clin. Invest.* **120**, 403 (2010).
3. R. O. Hynes, *Science* **326**, 1216 (2009).
4. J. S. Kang, C. Liu, R. Derynck, *Trends Cell Biol.* **19**, 385 (2009).
5. R. Derynck, Y. E. Zhang, *Nature* **425**, 577 (2003).
6. M. K. Lee et al., *EMBO J.* **26**, 3957 (2007).
7. M. Yamashita et al., *Mol. Cell* **31**, 918 (2008).
8. E. R. Neptune et al., *Nat. Genet.* **33**, 407 (2003).
9. C. M. Ng et al., *J. Clin. Invest.* **114**, 1586 (2004).
10. J. P. Habashi et al., *Science* **312**, 117 (2006).
11. R. D. Cohn et al., *Nat. Med.* **13**, 204 (2007).

12. G. Wolf, F. N. Ziyadeh, R. A. Stahl, *J. Mol. Med.* **77**, 556 (1999).
13. N. Fukuda et al., *Am. J. Hypertens.* **13**, 191 (2000).
14. T. Naito et al., *Am. J. Physiol. Renal Physiol.* **286**, F278 (2004).
15. B. L. Loeys et al., *Nat. Genet.* **37**, 275 (2005).
16. B. L. Loeys et al., *N. Engl. J. Med.* **355**, 788 (2006).
17. D. P. Judge et al., *J. Clin. Invest.* **114**, 172 (2004).
18. Materials and methods are available as supporting material on Science Online.
19. C. Iverson et al., *Cancer Res.* **69**, 6839 (2009).
20. X. Xu et al., *Oncogene* **19**, 1868 (2000).
21. B. L. Bennett et al., *Proc. Natl. Acad. Sci. U.S.A.* **98**, 13681 (2001).
22. K. Yoshimura et al., *Nat. Med.* **11**, 1330 (2005).
23. J. Huang et al., *Circ. Res.* **106**, 583 (2010).
24. T. Araki et al., *Nat. Med.* **10**, 849 (2004).
25. T. Nakamura et al., *J. Clin. Invest.* **117**, 2123 (2007).
26. J. M. Morgan, M. O. Coupe, M. Honey, G. A. Miller, *Eur. Heart J.* **10**, 190 (1989).
27. R. Purnell, I. Williams, U. Von Oppell, A. Wood, *Eur. J. Cardiothorac. Surg.* **28**, 346 (2005).
28. D. Gomez et al., *J. Pathol.* **218**, 131 (2009).
29. Supported by the National Institutes of Health (H.C.D. and D.P.J.), Howard Hughes Medical Institute (H.C.D.), National Marfan Foundation (H.C.D., J.P.H., and J.J.D.), Cellular and Molecular Medicine Training Program (J.J.D.), National Human Genome Research Institute Intramural Research Program and the NIH Therapeutics for Rare and Neglected Diseases Program (C.J.T., S.P., and J.J.M.), and the Smilow Center for Marfan Syndrome Research (H.C.D.). We thank Dr. C. Deng for the *Smad4*-targeted mice. Johns Hopkins University and the authors (H.C.D., J.P.H., D.P.J., and R.C.) have filed a patent relating to the use of TGF β antagonists, including angiotensin II type 1 receptor blockers, for the treatment of Marfan syndrome.

Supporting Online Material

www.sciencemag.org/cgi/content/full/332/6027/358/DC1
Materials and Methods
Figs. S1 to S7
References

11 May 2010; accepted 4 March 2011
10.1126/science.1192149

Angiotensin II Type 2 Receptor Signaling Attenuates Aortic Aneurysm in Mice Through ERK Antagonism

Jennifer P. Habashi,^{1,2*} Jefferson J. Doyle,^{1*} Tammy M. Holm,¹ Hamza Aziz,¹ Florian Schoenhoff,¹ Djahida Bedja,³ YiChun Chen,¹ Alexandra N. Modiri,¹ Daniel P. Judge,⁴ Harry C. Dietz^{1,2,4†}

Angiotensin II (AngII) mediates progression of aortic aneurysm, but the relative contribution of its type 1 (AT1) and type 2 (AT2) receptors remains unknown. We show that loss of AT2 expression accelerates the aberrant growth and rupture of the aorta in a mouse model of Marfan syndrome (MFS). The selective AT1 receptor blocker (ARB) losartan abrogated aneurysm progression in the mice; full protection required intact AT2 signaling. The angiotensin-converting enzyme inhibitor (ACEi) enalapril, which limits signaling through both receptors, was less effective. Both drugs attenuated canonical transforming growth factor- β (TGF β) signaling in the aorta, but losartan uniquely inhibited TGF β -mediated activation of extracellular signal-regulated kinase (ERK), by allowing continued signaling through AT2. These data highlight the protective nature of AT2 signaling and potentially inform the choice of therapies in MFS and related disorders.

Marfan syndrome (MFS) is an autosomal dominant connective tissue disorder that includes a predisposition for aortic root aneurysm and aortic rupture. MFS is caused

by a deficiency of the microfibrillar constituent protein fibrillin-1 that is imposed by heterozygous mutations in *FBN1*. In prior work, we demonstrated that transforming growth factor- β

(TGF β) signaling was elevated in affected tissues of mice heterozygous for a cysteine substitution in an epidermal growth factor-like domain of fibrillin-1 ($Fbn1^{C1039G/+}$), the most common class of mutation in people with MFS (1–4). Many disease manifestations—including aortic aneurysm (1), developmental emphysema (2), myxomatous degeneration of the atrioventricular valves (3), and skeletal muscle myopathy (4)—are attenuated by systemic administration of a pan-specific polyclonal TGF β -neutralizing antibody (TGF β NAb) in fibrillin-1-deficient mice. Similar protection was achieved by treating $Fbn1^{C1039G/+}$ mice with the angiotensin II (AngII) type 1 (AT1) receptor blocker (ARB) losartan (1, 4). ARBs can attenuate

¹Howard Hughes Medical Institute and Institute of Genetic Medicine, Johns Hopkins University School of Medicine, Baltimore, MD 21205, USA. ²Division of Pediatric Cardiology, Department of Pediatrics, Johns Hopkins University School of Medicine, Baltimore, MD 21205, USA. ³Department of Molecular and Comparative Pathobiology, Johns Hopkins University School of Medicine, Baltimore, MD 21205, USA. ⁴Department of Medicine, Johns Hopkins University School of Medicine, Baltimore, MD 21205, USA.

*These authors contributed equally to this work.

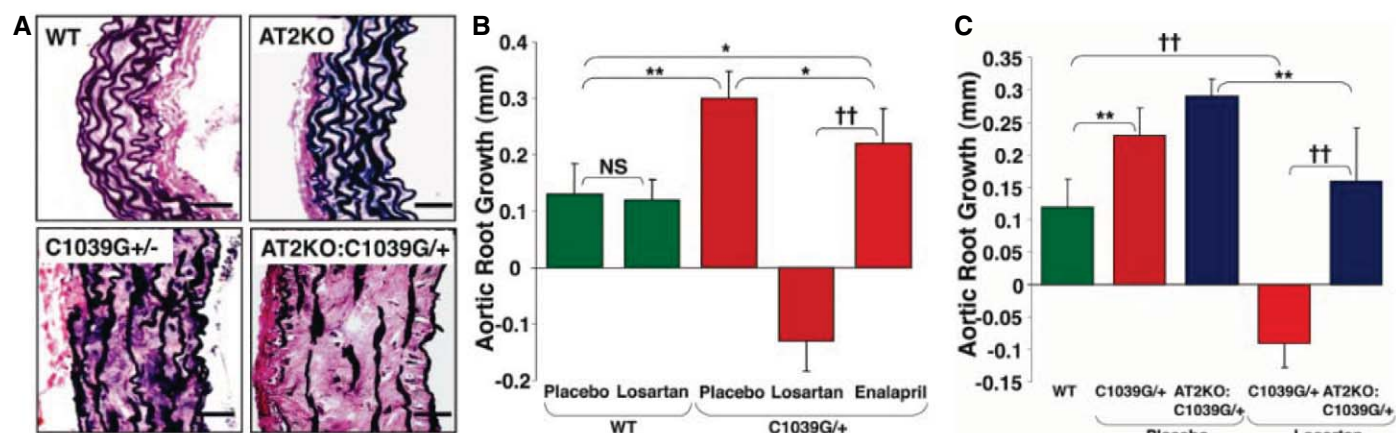
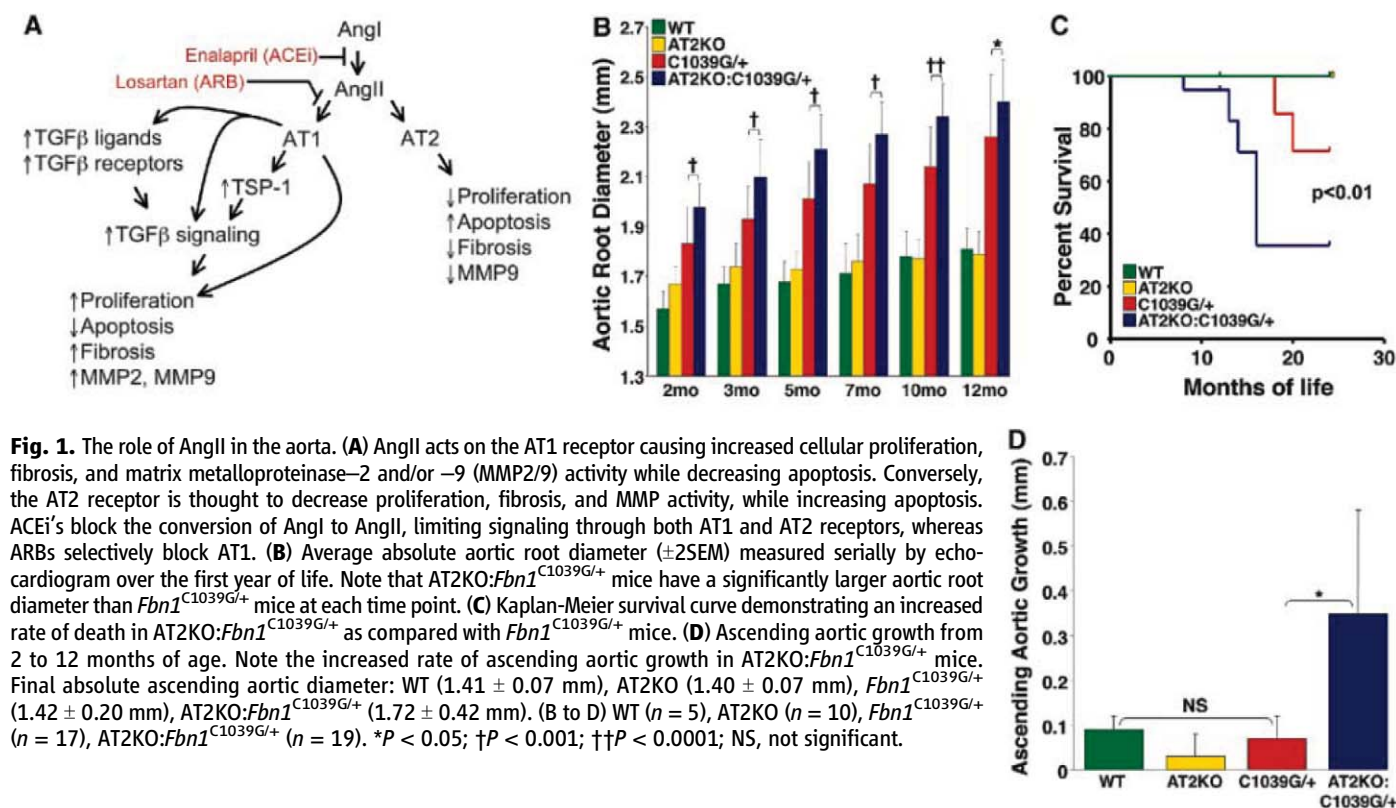
†To whom correspondence should be addressed. E-mail: hdietz@jhmi.edu

TGF β signaling in some tissues by lowering the expression of TGF β ligands, receptors, and activators (5–7). In this mouse model of MFS, losartan's protection correlated with decreased phosphorylation and nuclear translocation of Smad2 (pSmad2), a direct effector of canonical TGF β signaling,

and decreased expression of prototypical Smad-dependent TGF β -responsive gene products, such as connective tissue growth factor and collagens.

The contribution of AT2 to aortic aneurysm progression remains controversial. AT2 signaling can oppose AT1-mediated enhancement of TGF β

signaling in some cell types and tissues (Fig. 1A) (8, 9). It can also induce vascular smooth muscle cell (VSMC) apoptosis, theoretically contributing to aortic wall damage. Apoptosis was observed in cultured cells derived from end-stage aneurysms in people with MFS (10), but has not been found



Fbn1^{C1039G/+} (2.19 \pm 0.19 mm), losartan-treated *Fbn1*^{C1039G/+} (1.96 \pm 0.09 mm), and enalapril-treated *Fbn1*^{C1039G/+} (2.18 \pm 0.18 mm). **(C)** Average aortic root growth (\pm 2SEM) over 7 months of treatment in WT (*n* = 8), placebo- (*n* = 22), and losartan- (*n* = 11) treated *Fbn1*^{C1039G/+} mice and placebo- (*n* = 19) and losartan- (*n* = 6) treated AT2KO:*Fbn1*^{C1039G/+} mice. Note the diminished effectiveness of losartan treatment in AT2KO:*Fbn1*^{C1039G/+} mice, as compared with losartan treatment in *Fbn1*^{C1039G/+} mice. Final absolute aortic root diameter: WT (1.77 \pm 0.10 mm), *Fbn1*^{C1039G/+} (2.13 \pm 0.16 mm), AT2KO:*Fbn1*^{C1039G/+} (2.34 \pm 0.13 mm), losartan-treated *Fbn1*^{C1039G/+} (1.96 \pm 0.09 mm), and losartan-treated AT2KO:*Fbn1*^{C1039G/+} (2.06 \pm 0.07 mm). **P* < 0.05; ***P* < 0.01; †*P* < 0.001; ††*P* < 0.0001; NS, not significant.

in early- or intermediate-stage aortic wall lesions in MFS mice (1). Vascular expression of AT2 is largely limited to prenatal life, but it may continue to be relevant postnatally in the context of certain disease states, as evidenced by the acceleration of inflammatory aneurysms in AngII-infused mice treated with an AT2 antagonist (11). In contrast, β -aminopropionitrile monofumarate (BAPN)-induced aortic aneurysm and dissection in rats, which was associated with increased expression of AT2 and VSMC apoptosis, was ameliorated by limiting AngII production with angiotensin-converting enzyme inhibitor (ACEi) but not by selective AT1 receptor blockade (12). AT2 signaling has the capacity to attenuate both canonical (Smad-dependent) and noncanonical (mitogen-activated protein kinase or MAPK) TGF β signaling cascades, most notably the extracellular signal-regulated kinase (ERK), in some tissues (13, 14). Thus, AT2 signaling can both augment and inhibit the pathogenesis of aneurysm in pre-clinical models, and the mechanistic explanation for the discordance is unclear. This has direct clinical relevance, as it leaves open to question the relative therapeutic merits of selective AT1 blockade with ARBs versus limiting signaling through both AT1 and AT2 with ACEi, despite small trials suggesting that either approach has potential in MFS (15–17).

To assess the role of the AT2 receptor in MFS, we bred mice with a disrupted *Agtr2* allele (encoding AT2; AT2KO) (18, 19) with *Fbn1*^{C1039G/+} mice, our established model of MFS (20). *Agtr2* is encoded on the X chromosome in humans and mice, and the AT2KO allele associates with loss of mRNA and protein expression, as assessed by radioligand binding, in either homozygous females or hemizygous males. The AT2KO mice develop normally, with no evidence of cardiovascular pathology or early mortality (21).

We followed the progression of aortic root aneurysm by echocardiogram until the mice were killed at 12 months (Fig. 1B). There was a small difference in aortic root size between wild-type (WT) and AT2KO mice ($P < 0.05$) at 2 months, but this difference was absent at all future time points ($P = 0.70$). The aortic root diameter of AT2KO:*Fbn1*^{C1039G/+} mice was significantly larger than that seen in *Fbn1*^{C1039G/+} mice at 2 months of age ($P < 0.001$), and this difference was maintained through to 12 months of life ($P < 0.05$). The postnatal aortic root growth over 10 months was not different between *Fbn1*^{C1039G/+} mice with or without AT2 expression ($P = 0.80$). This could reflect postnatal waning of AT2 receptor expression, attainment of an absolute threshold of aortic root growth rate in AT2KO:*Fbn1*^{C1039G/+} mice,

and/or the accelerated death observed in AT2KO:*Fbn1*^{C1039G/+} mice that effectively removed the most severely affected animals from later analyses. We found that 32% of AT2KO:*Fbn1*^{C1039G/+} mice died before the scheduled killing, compared with 12% of *Fbn1*^{C1039G/+} mice ($P < 0.01$) and 0% of AT2KO or WT mice (Fig. 1C). Growth of the more distal ascending aorta over 10 months was significantly greater in AT2KO:*Fbn1*^{C1039G/+} mice compared with *Fbn1*^{C1039G/+} littermates ($P < 0.05$), whereas there was no significant difference between WT, AT2KO, and *Fbn1*^{C1039G/+} mice (Fig. 1D).

Histological and morphometric analyses of the aortic media were performed at 12 months. AT2KO:*Fbn1*^{C1039G/+} mice showed medial thickening, reduced elastin content, and increased elastic fiber fragmentation (Fig. 2A and figs. S1 to S3) compared with *Fbn1*^{C1039G/+} or AT2KO mice ($P < 0.01$ for all comparisons). These parameters were not significantly different in AT2KO and WT mice ($P = 0.07$, $P = 0.68$, and $P = 1.0$, respectively). Therefore, the histological changes in the aorta paralleled the echocardiography findings, which supported the conclusion that AT2 receptor elimination exacerbates aortic disease in MFS mice.

The potential for exacerbation of the MFS phenotype outside of the cardiovascular system

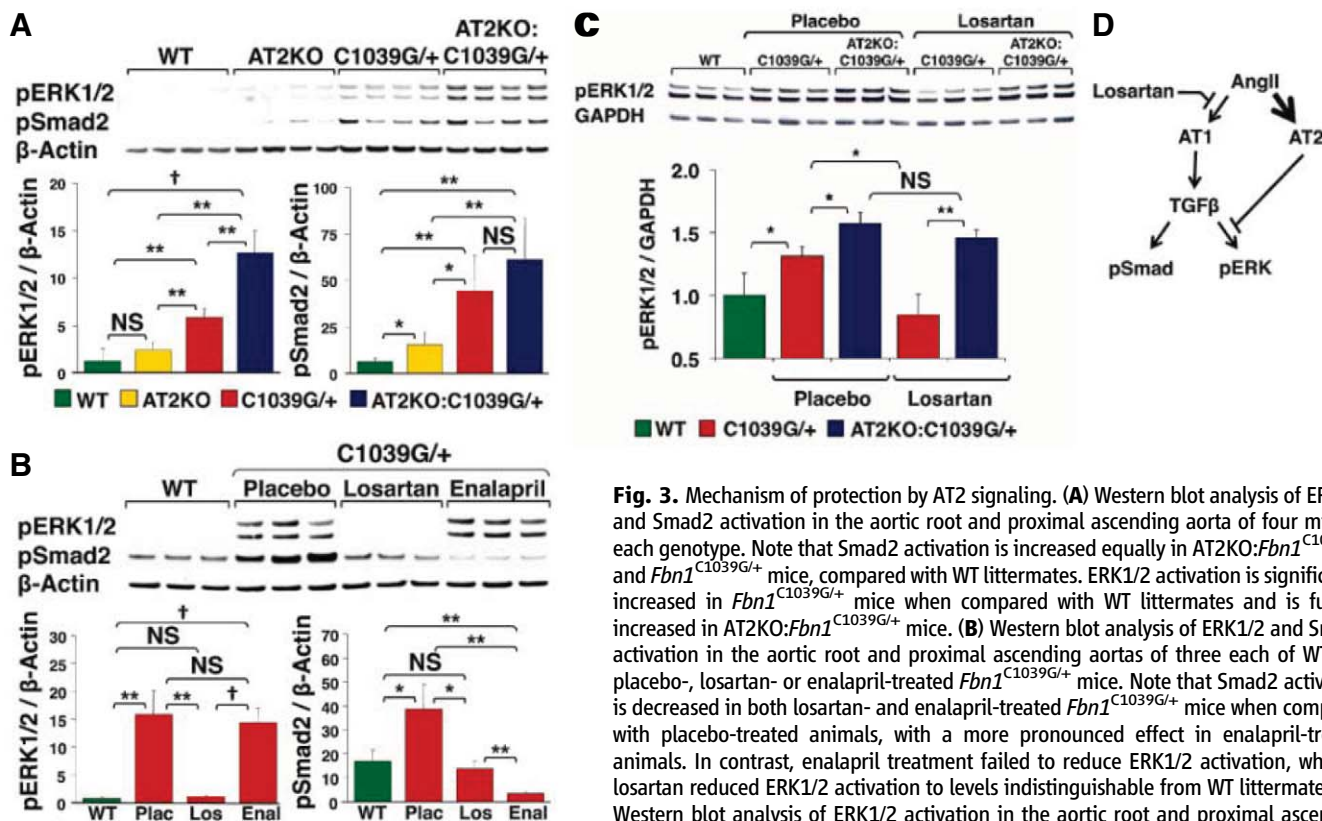


Fig. 3. Mechanism of protection by AT2 signaling. (A) Western blot analysis of ERK1/2 and Smad2 activation in the aortic root and proximal ascending aorta of four mice of each genotype. Note that Smad2 activation is increased equally in AT2KO:*Fbn1*^{C1039G/+} and *Fbn1*^{C1039G/+} mice, compared with WT littermates. ERK1/2 activation is significantly increased in *Fbn1*^{C1039G/+} mice when compared with WT littermates and is further increased in AT2KO:*Fbn1*^{C1039G/+} mice. (B) Western blot analysis of ERK1/2 and Smad2 activation in the aortic root and proximal ascending aortas of three each of WT and placebo-, losartan- or enalapril-treated *Fbn1*^{C1039G/+} mice. Note that Smad2 activation is decreased in both losartan- and enalapril-treated *Fbn1*^{C1039G/+} mice when compared with placebo-treated animals, with a more pronounced effect in enalapril-treated animals. In contrast, enalapril treatment failed to reduce ERK1/2 activation, whereas losartan reduced ERK1/2 activation to levels indistinguishable from WT littermates. (C) Western blot analysis of ERK1/2 activation in the aortic root and proximal ascending aorta of three WT, AT2KO, and placebo- or losartan-treated AT2KO:*Fbn1*^{C1039G/+} mice.

Note that losartan loses its ability to decrease ERK1/2 activation in AT2KO:*Fbn1*^{C1039G/+} mice, demonstrating that the inhibition of ERK1/2 activation is mediated by the AT2 receptor. (D) Summary of the effects of AngII receptors on both canonical and noncanonical TGF β signaling. AT1 receptor stimulation drives ERK1/2 activation, whereas AT2 receptor stimulation inhibits it. Losartan attenuates ERK1/2 activation by blocking the AT1 cascade while simultaneously shunting signaling through the AT2 receptor. $*P < 0.05$; $**P < 0.01$; $\dagger P < 0.001$; NS, not significant.

was also assessed. At 12 months, excised lungs were inflated with agar, sectioned, and stained for histological and morphometric analyses (figs. S4 and S5). Increased distal airspace caliber, a marker of impaired distal alveolar septation and emphysematous lung disease, can be quantified by calculating a mean linear intercept (MLI). There was no significant difference in MLI between WT and AT2KO mice ($P = 1.0$). Compared with WT and AT2KO littermates, *Fbn1*^{C1039G/+} mice had a significant increase in MLI ($P < 0.05$), whereas AT2KO:*Fbn1*^{C1039G/+} mice had a yet further increase in MLI ($P < 0.05$). This confirms that AT2 receptor elimination can exacerbate the MFS phenotype outside of the cardiovascular system.

We next performed a head-to-head comparison of ACEi versus ARBs. *Fbn1*^{C1039G/+} mice and WT littermates were treated with hemodynamically equivalent doses (fig. S6) of either the ACEi enalapril (10 to 15 mg/kg of body weight per day) or the ARB losartan (40 to 60 mg/kg per day) (22), beginning at 8 weeks of age, and were assessed with serial echocardiograms. Aortic root growth over the 7 months of treatment was significantly greater in placebo-treated *Fbn1*^{C1039G/+} mice compared with WT littermates ($P < 0.01$), whereas losartan led to a significant regression in growth in *Fbn1*^{C1039G/+} mice ($P < 0.0001$), to rates that were significantly less than that seen in WT littermates ($P < 0.0001$) (I). It is noteworthy that losartan reduced aortic root growth in *Fbn1*^{C1039G/+} mice, but had no effect in WT littermates ($P = 0.27$). Enalapril treatment had significantly less effect than losartan in *Fbn1*^{C1039G/+} mice ($P < 0.0001$); in fact, it was only marginally better than placebo treatment ($P = 0.05$) (Fig. 2B). Enalapril was also no more beneficial than placebo in improving aortic architecture score in *Fbn1*^{C1039G/+} mice ($P = 0.19$), whereas losartan was significantly more beneficial than both placebo and enalapril treatment ($P < 0.05$ for both) (fig. S7).

We next assessed whether AT2 signaling is needed to achieve losartan's full therapeutic benefit. AT2KO:*Fbn1*^{C1039G/+} mice were treated with losartan from 8 weeks of age and followed by serial echocardiography until they were killed at 9 months of age (Fig. 2C). Although there was a trend for increased aortic root growth in AT2KO:*Fbn1*^{C1039G/+} mice compared with *Fbn1*^{C1039G/+} littermates ($P = 0.06$), the decrease in aortic root growth seen in AT2KO:*Fbn1*^{C1039G/+} mice treated with losartan was only 40% of that seen in *Fbn1*^{C1039G/+} animals that expressed AT2 ($P < 0.001$), despite there being no difference in blood pressure between the groups (Fig. 2C and fig. S6). The modest reduction in aortic root growth seen in losartan-treated AT2KO:*Fbn1*^{C1039G/+} mice was comparable to that previously observed with propranolol, and it may be similarly attributable to a decline in blood pressure rather than a modulation of cytokine signaling (I).

Together, these experiments suggest that AT2 signaling protectively modifies MFS and that the therapeutic effect of ACEi likely relates to AT1

receptor blockade or antihypertensive effects. In addition, we have shown that selective AT1 antagonism with the ARB losartan is beneficial in *Fbn1*^{C1039G/+} mice and that AT2 signaling is needed to achieve the full potential of ARBs. Both the canonical (Smad-dependent) and non-canonical (MAPK, predominantly ERK1/2 but also JNK in some experimental contexts) TGF β signaling cascades are activated in *Fbn1*^{C1039G/+} mice in a TGF β - and AT1 receptor-dependent manner (23). To investigate the mechanism of protection by AT2 receptor signaling, we monitored the status of both canonical and noncanonical TGF β signaling in *Fbn1*^{C1039G/+} mice lacking the AT2 receptor or in response to losartan or enalapril treatment. Western blot analysis showed that Smad2 activation was significantly greater in the aortic root and proximal ascending aorta of *Fbn1*^{C1039G/+} mice compared with WT controls ($P < 0.01$) but that there was no significant difference between AT2KO:*Fbn1*^{C1039G/+} and *Fbn1*^{C1039G/+} mice ($P = 0.30$). In contrast, ERK1/2 activation was significantly greater in *Fbn1*^{C1039G/+} mice compared with WT littermates ($P < 0.01$) and was further increased in AT2KO:*Fbn1*^{C1039G/+} mice compared with *Fbn1*^{C1039G/+} ($P < 0.01$), AT2KO ($P < 0.01$), and WT littermates ($P < 0.001$) (Fig. 3A). The difference in ERK1/2 activation was specific to the aortic root and proximal ascending aorta, the areas most predisposed to aneurysm formation in MFS, as there was no significant difference in the descending thoracic aortas of the same animals (fig. S8). No significant differences in JNK1 or p38 activation were observed (fig. S9).

In our comparison of ARBs versus ACEi, Smad2 activation was significantly greater in *Fbn1*^{C1039G/+} mice compared with WT controls ($P < 0.05$), and losartan treatment significantly decreased Smad2 activation in *Fbn1*^{C1039G/+} mice ($P < 0.05$) to levels indistinguishable from WT ($P = 0.31$) (Fig. 3B). Enalapril reduced Smad2 activation in *Fbn1*^{C1039G/+} mice significantly more than losartan ($P < 0.01$), a finding that did not parallel the therapeutic effects of these agents (Fig. 2B). ERK1/2 activation was significantly greater in *Fbn1*^{C1039G/+} mice compared with WT controls ($P < 0.01$), and treatment with losartan reduced it to WT levels ($P = 0.80$). In contrast, enalapril treatment had significantly less effect on ERK1/2 activation than losartan ($P < 0.001$); in fact, it was no more effective than placebo ($P = 0.50$). JNK1 and p38 activation was similar in *Fbn1*^{C1039G/+} and WT mice; both losartan and enalapril caused a modest reduction in JNK1 activation ($P < 0.01$), but neither had any effect on p38 activation (fig. S10). Thus, the biochemical status of the noncanonical ERK1/2, but not the canonical Smad, TGF β signaling cascade correlated with the therapeutic effects of these agents. In keeping with this finding, losartan had a reduced ability to lower ERK1/2 activation in *Fbn1*^{C1039G/+} mice lacking the AT2 receptor ($P < 0.01$) (Fig. 3C). By contrast, there was no significant difference in Smad2, JNK1, or p38

activation in losartan-treated *Fbn1*^{C1039G/+} mice that did or did not express AT2 (fig. S11).

To assess for a contribution of other components of the renin-angiotensin-aldosterone system, we treated *Fbn1*^{C1039G/+} mice with the aldosterone receptor antagonist spironolactone (24). We found no significant inhibition of aortic root growth over 7 months time ($P = 0.23$) (fig. S12).

In conclusion, dual blockade of AT1 receptor-mediated ERK1/2 activation and AT2 receptor-mediated ERK1/2 inhibition, as occurs either with the use of ACEi in *Fbn1*^{C1039G/+} mice or the use of losartan in AT2KO:*Fbn1*^{C1039G/+} mice, results in no net change in ERK1/2 activation status and adds a very modest therapeutic benefit. By contrast, losartan reduces ERK1/2 phosphorylation through a combination of both inhibiting AT1 receptor-mediated ERK activation and by shunting AngII signaling through the AT2 receptor. This indicates that, in the presence of AT1 receptor blockade, ongoing AT2 receptor signaling is required for the attenuation of ERK phosphorylation and that enalapril's lack of effect on ERK is attributable to the loss of AT2 receptor signaling potential with this agent (Fig. 3D). Given that the small reduction in aortic root growth in *Fbn1*^{C1039G/+} mice achieved by enalapril in this study was comparable to that achieved previously by propranolol (I), this suggests that its small beneficial effect may well have been mediated by blood pressure reduction. Although the concordant effects of prior manipulations and therapies on canonical and noncanonical TGF β signaling made it impossible to dissect their relative contributions, the differential effects of enalapril treatment suggest that TGF β -mediated ERK1/2 activation is the predominant driver of aneurysm progression in MFS. In light of this, analysis of ERK1/2 activation status may permit the optimization of dosing regimens for losartan or other ARBs in ongoing or future clinical trials in people with MFS. Furthermore, focused attention on the ERK1/2 signaling cascade may unveil new therapeutic targets in the treatment of aortic aneurysm disease.

References and Notes

1. J. P. Habashi et al., *Science* **312**, 117 (2006).
2. E. R. Neptune et al., *Nat. Genet.* **33**, 407 (2003).
3. C. M. Ng et al., *J. Clin. Invest.* **114**, 1586 (2004).
4. R. D. Cohn et al., *Nat. Med.* **13**, 204 (2007).
5. G. Wolf, F. N. Ziyadeh, R. A. Stahl, *J. Mol. Med.* **77**, 556 (1999).
6. N. Fukuda et al., *Am. J. Hypertens.* **13**, 191 (2000).
7. T. Naito et al., *Am. J. Physiol. Renal Physiol.* **286**, F278 (2004).
8. E. S. Jones, M. J. Black, R. E. Widdop, *J. Mol. Cell. Cardiol.* **37**, 1023 (2004).
9. J. Rodríguez-Vita et al., *Circulation* **111**, 2509 (2005).
10. H. Nagashima et al., *Circulation* **104** (suppl. 1), I282 (2001).
11. A. Daugherty, M. W. Manning, L. A. Cassis, *Br. J. Pharmacol.* **134**, 865 (2001).
12. H. Nagashima et al., *J. Vasc. Surg.* **36**, 818 (2002).

13. B. Ulmasov, Z. Xu, L. H. Tetri, T. Inagami, B. A. Neuschwander-Tetri, *Am. J. Physiol. Gastrointest. Liver Physiol.* **296**, G284 (2009).
14. M. Akishita *et al.*, *J. Clin. Invest.* **103**, 63 (1999).
15. B. S. Brooke *et al.*, *N. Engl. J. Med.* **358**, 2787 (2008).
16. A. T. Yetman, R. A. Bornemeier, B. W. McCrindle, *Am. J. Cardiol.* **95**, 1125 (2005).
17. A. A. Ahimastos *et al.*, *JAMA* **298**, 1539 (2007).
18. Materials and methods are available as supporting material on Science Online.
19. T. Ichiki *et al.*, *Nature* **377**, 748 (1995).
20. D. P. Judge *et al.*, *J. Clin. Invest.* **114**, 172 (2004).
21. H. M. Siragy, T. Inagami, T. Ichiki, R. M. Carey, *Proc. Natl. Acad. Sci. U.S.A.* **96**, 6506 (1999).
22. R. D. Patten *et al.*, *Clin. Sci.* **104**, 109 (2003).
23. T. Holm *et al.*, *Science* **332**, 358 (2011).
24. S. Sakurabayashi-Kitade *et al.*, *Atherosclerosis* **206**, 54 (2009).
25. Supported by the NIH (H.C.D., D.P.J.); Howard Hughes Medical Institute (H.C.D.); the National Marfan Foundation (H.C.D., J.P.H., J.J.D.); the Cellular and Molecular Medicine Training Program, Johns Hopkins School of Medicine (J.J.D.); and the Smilow Center for Marfan Syndrome Research (H.C.D.). We thank T. Inagami for the AT2KO mice. Johns Hopkins

University and the authors (H.C.D., J.P.H., D.P.J.) have filed a patent relating to the use of TGF β antagonists, including AT1 receptor blockers, for the treatment of Marfan syndrome.

Supporting Online Material

www.sciencemag.org/cgi/content/full/332/6027/361/DC1

Materials and Methods

Figs. S1 to S12

References

11 May 2010; accepted 4 March 2011

10.1126/science.1192152

Sequential Synaptic Excitation and Inhibition Shape Readiness Discharge for Voluntary Behavior

Katsushi Kagaya* and Masakazu Takahata

How do animals initiate voluntary behavior? A key phenomenon in neuroscience is the readiness or preparatory neural activity in specific regions of the animal brain. The neurons and synaptic mechanisms mediating this activity are unknown. We found that the readiness discharge is shaped by sequential synaptic excitation and inhibition in the brain of crayfish (*Procambarus clarkii*). The readiness discharge neurons extended axon collaterals that appeared to activate recurring local interneurons. Therefore, we propose that the readiness discharge is formed by sequential synaptic events within the brain without feedback signals from downstream ganglia. The circuit involved is suited for signal processing for self-generated voluntary initiation of behavior.

Before the initiation of voluntary behavior, neuronal activity shows a remarkable and characteristic change in specific brain regions (1–8). The spike activity called readiness discharge that transiently precedes the voluntary initiation of behavior has been reported extensively in primates (2–4) and rodents (5–7). However, the membrane potential dynamics underlying the readiness discharge are yet to be seen on the dendritic processes of relevant neurons in the brain. The readiness discharge in the brain of crayfish *Procambarus clarkii* (8) might offer a clue to understanding the cellular mechanisms subserving the readiness discharge in relation to voluntary initiation of behavior. In crayfish, the readiness discharge can be recorded in the circumesophageal commissure (8), which contains axons of brain neurons descending to thoracic ganglia where the central pattern generator for walking resides (9). They increase their spike discharge rate a few seconds before the behavioral onset and decrease it once the walking behavior is initiated (8). The transient spike activity before the voluntary behavioral initiation is a common key feature of the readiness discharge. However, it is unknown what the synaptic mechanisms of the readiness discharge are and what

types of neurons are involved in shaping the spike activity.

To investigate the neurophysiological mechanisms underlying the voluntary initiation of walking behavior, we performed intracellular recordings from single cells in the brains of behaving crayfish on a spherical treadmill (8). No external stimulus was applied so that they initiated, continued, and terminated walking behavior at their own disposal. We obtained physiological data from 69 neurons, which were successfully stained with the fluorescent dye Lucifer yellow. Identified neurons were categorized into three groups functionally and into two groups morphologically. Functional categorization was based on the timing of their spike activity in relation to the onset and offset of behavior that were statistically estimated on the basis of electromyographic (EMG) recording from the mero-carpopodite flexor muscle of the second walking leg on either side (10). Because the muscles of all eight walking legs were activated almost simultaneously within the time range of 65.89 ± 6.40 msec before the onset of leg movement (10), we categorized the synaptic and spike activities as “preceding” when the change occurred more than 500 msec before the behavioral onset. Morphologically, we categorized the neurons into descending neurons with their axons in the commissure and local interneurons whose neuritic projection was confined to within the brain. Because the initiation and motor control of locomotion have been re-

lated to the central complex in insects (11, 12), we scrutinized the homologous neuropils (13) in the crayfish brain and characterized the distribution of dendritic processes of behaviorally relevant interneurons to identify the main region of synaptic activation involved in the voluntary behavior.

We successfully penetrated the dendrite of one readiness discharge neuron and recorded the membrane potential change associated with voluntary initiation of walking 18 times (Fig. 1A). The animal showed a variety of walking including forward and backward walking (Fig. 1A). Irrespective of walking direction, the membrane potential showed a transient depolarization before the behavioral onset (Fig. 1A). It then showed a long-lasting hyperpolarization once the animal started walking (Fig. 1A). This sequential change of membrane potential controlled the transient discharge of action potentials before the behavioral onset. Eighteen superimposed traces of membrane potential and smoothed electromyographic recordings indicate the consistency of the sequential change (Fig. 1B). The peri-onset time spike histogram (Fig. 1B) shows that the spike discharge transiently increased before the onset and then decreased sustainedly (Fig. 1B). This change in the spike discharge rate is similar to the readiness spike activity recorded in the circumesophageal commissure (8).

Membrane potential change that would cause transient spike discharges preceding the onset of walking can be based on synaptic input from other upstream cells or endogenous conductance change as in pacemaker cells. When a slight positive (+0.1, +0.2, +0.3 nA) current was injected into the neuron, the number of action potentials increased before the behavioral onset, whereas after the onset the hyperpolarization was remarkably enhanced with no spike discharge superimposed (Fig. 1C). Injection of a stronger depolarizing current caused spike discharges of the cell (25 to 65 spikes/sec), but no noticeable motor effect was observed in the EMG activity. When a negative current (–1 nA) was injected into the neuron, the number of spikes decreased and a slight depolarization was observed before the behavioral onset (Fig. 1C). When a stronger negative current (–2 nA) was injected, the transient spike discharge before the behavioral onset completely disappeared and the membrane potential showed a noticeable depolarization after

Department of Biological Sciences, Faculty of Science, Hokkaido University, Sapporo 060-0810, Japan.

*To whom correspondence should be addressed. E-mail: kagaya@sci.hokudai.ac.jp

the onset (Fig. 1C). These findings suggest that the transient spike discharge before the behavioral onset of walking is caused by excitatory synaptic input followed by inhibitory synaptic input. To investigate the membrane conductance change during these synaptic inputs, we injected constant current pulses into the neuron (-1 nA, 2 Hz) with the bridge balance circuit kept optimized (Fig. 1C). The voltage response was transiently decreased before the onset corresponding to the period of readiness discharge, subsequently recovered the magnitude observed at rest, and then began to decrease gradually about 5 s after the behavioral onset (Fig. 1, C and D). The first transient decrease in the membrane resistance suggests that the readiness discharge before the behavioral onset of walking could be caused by an excitatory synaptic input, whereas the late sustained decrease in the membrane resistance suggests that the later phase of postonset hyperpolarization is caused by an inhibitory synaptic input. The early phase of hyperpolarization that immediately follows the behavioral onset is thought to be

caused by another inhibitory synaptic input that is located on the dendrite electrotonically more distant than the late inhibitory input because no membrane conductance change was detected for the early hyperpolarization. Before the behavioral onset (from -5 s to 0 s) compared with at rest (from -25 s to -20 s), we observed a significant rise (paired t test, $P < 0.01$) in the variance of membrane potential fluctuation from which action potentials were removed (Fig. 1E, gray filled circles). Furthermore, a notable rise in the variance of membrane potential fluctuation was observed when the cell was hyperpolarized (Fig. 1E, black filled circles), when most voltage-gated ion channels are considered to be closed. These observations suggest that the increased membrane conductance before the behavioral onset is due not to endogenous but to synaptic mechanisms.

The morphology of the readiness discharge neurons shown in Fig. 1 was investigated by iontophoretically injecting Lucifer yellow into the cells. The neurons extended their axons through the medial and ventral region of the esophageal

neuropil where they branched into many collaterals, down to the circumesophageal commissure in its ventromedial quarter (fig. S1) corresponding to the Wiersma's area 70 (14). This area contained the fibers that evoked walking behavior upon electrical stimulation (8, 15, 16). The somata were located in the ventral paired anterior cluster (VPAC) of the protocerebrum. The neurons projected their dendrites contralaterally in the anterior and posterior medial protocerebral neuropil (AMPN and PMPN), as well as in the medial antennal neuropil (MAN) of the deutocerebrum (Fig. 2, A to D). These characteristics were mostly shared with candidate readiness discharge units obtained by backfill staining from the cut end of a small bundle including the unit (8) (Fig. 2C). It should be noted here that the branches in the esophageal neuropil (OEN) and the antennal neuropil (AnN) showed varicose ramifications (Fig. 2, A, B, and E), suggesting that these were presynaptic arborizations. Thus, they were not dendritic branches but axonal collaterals for sending the corollary signal of readiness discharge within the brain.

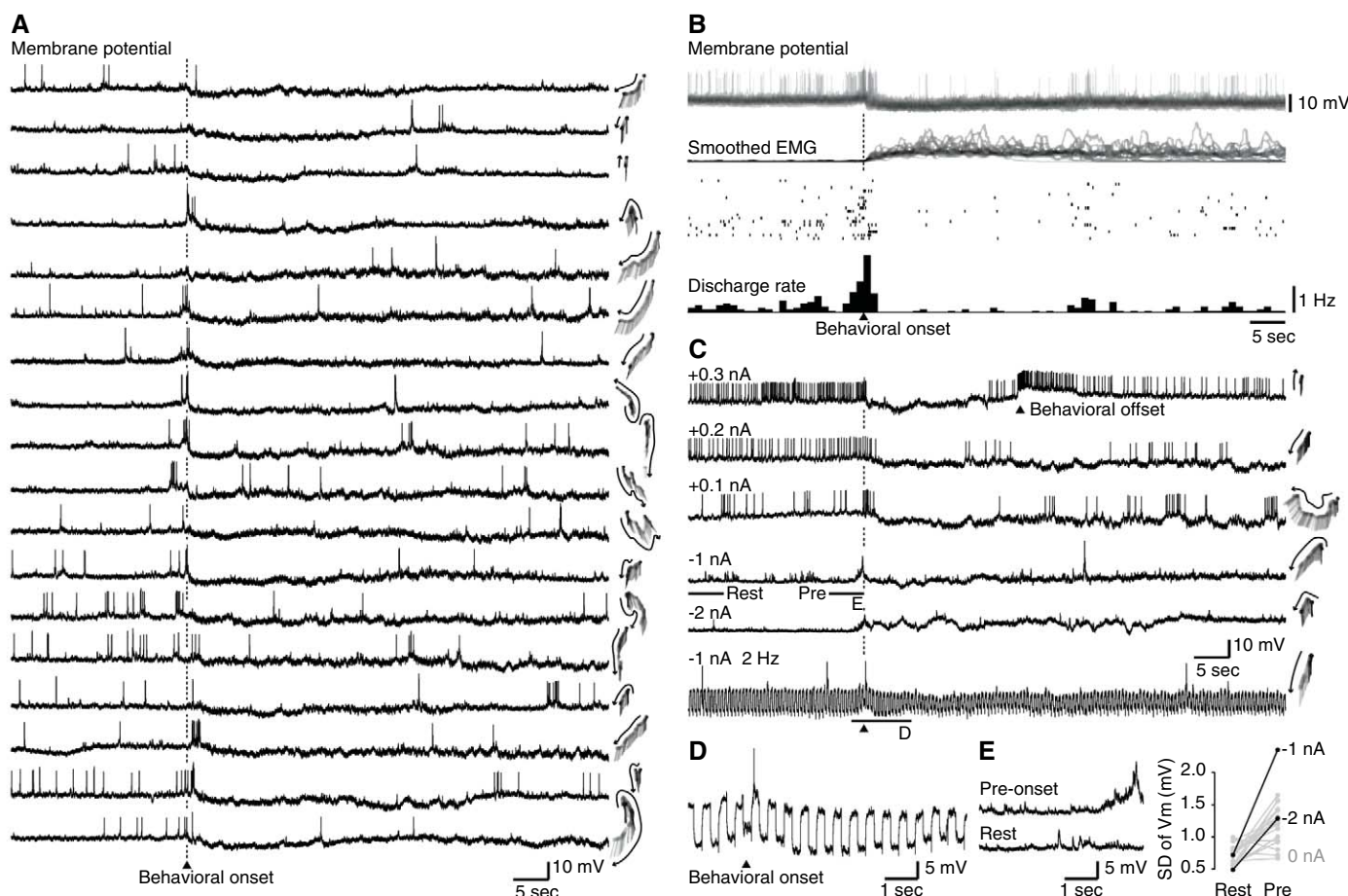


Fig. 1. Membrane potential dynamics of a readiness discharge neuron. (A) Membrane potential (V_m) changes of a readiness discharge neuron aligned to the behavioral onset with walking trajectories shown on the right. (B) (Top) An overlay of the membrane potential traces and of the smoothed muscle activity traces. (Bottom) Raster display and peri-onset time histogram illustrating the

spike activity. (C) (Top) Effects of current injection into the cell on the responses to synaptic input. (Bottom) Voltage responses of the cell to constant-current pulse injection. (D and E) Expanded voltage changes shown with the bars in (C). (E) (Right) Comparison of standard deviation (SD) of V_m between at-rest and pre-onset.

In a previous study based on extracellular recordings, we proposed a descending parallel scheme for voluntary initiation, continuation, and termination of walking behavior (8). In this study, we also identified descending interneurons that represent the continuation and termination pathways, respectively (Fig. 3). The continuation neurons increased their spike discharge rate before the behavioral onset and a high rate was maintained during walking (Fig. 3A). The termination neurons were activated before the voluntary behavioral offset and became silent after the offset (Fig. 3B). Thus, the continuation and termination neurons were sequentially activated to complete voluntary walking.

In either type of descending neuron, intracellular recordings revealed that synaptic activity changed preceding the initiation of walking. However, in the termination neuron, the subthreshold change did not produce consistent action potentials before onset (Fig. 3B). The continuation neurons mainly projected their dendrites to the neuropils [AMPN, PMPN, and central body (CB)] and additionally to the MAN and OEN

(Fig. 3C). The termination neurons mainly projected to the PMPN and AMPN (Fig. 3D).

We identified 45 additional descending neurons, including those that showed changes in synaptic activity without spike activity changes preceding, following, and delayed to the behavioral onset. The preceding and following types of neurons tended to project their dendrites to the medial protocerebral neuropil rather than the neuropils in the deutocerebrum or the tritocerebrum, whereas delayed-type neurons tended to project to the deutocerebrum and tritocerebrum (fig. S6A). Therefore, the confined arborization in the medial protocerebral neuropils and those synaptic activities suggest that the main synaptic activation for voluntarily initiated walking of crayfish takes place in the medial protocerebrum.

We demonstrated that the readiness discharge was regulated by synaptic excitation, followed by subsequent synaptic inhibition. A possibility to be considered here in relation to the inhibition is that it is caused by continuation neurons. The varicose arborization of the readiness discharge neurons

(Fig. 2) and continuation neurons within the brain (Fig. 3C and fig. S2) could send signals on their own activity to other neurons within the brain. Because the dendritic regions of the readiness discharge neurons did not overlap with the output regions of the continuation neurons, their synaptic and spike activities are not directly but polysynaptically transmitted to the readiness discharge neuron. For voluntary locomotion, the parallel and sequential recruitment of descending neurons thus has to be organized locally within the brain. In this study, we encountered local neurons that showed activity changes associated with spontaneous initiation of walking (figs. S3 to S5). Although it remains unknown whether the descending neurons are organized by direct synaptic contacts of the local neurons, those spiking and nonspiking activities showed remarkable changes in association with the self-generated voluntary walking (figs. S3 and S4). Further experiments are necessary to define their connections and causal relationships. However, our data clarified the physiological and morphological characteristics of the brain neurons

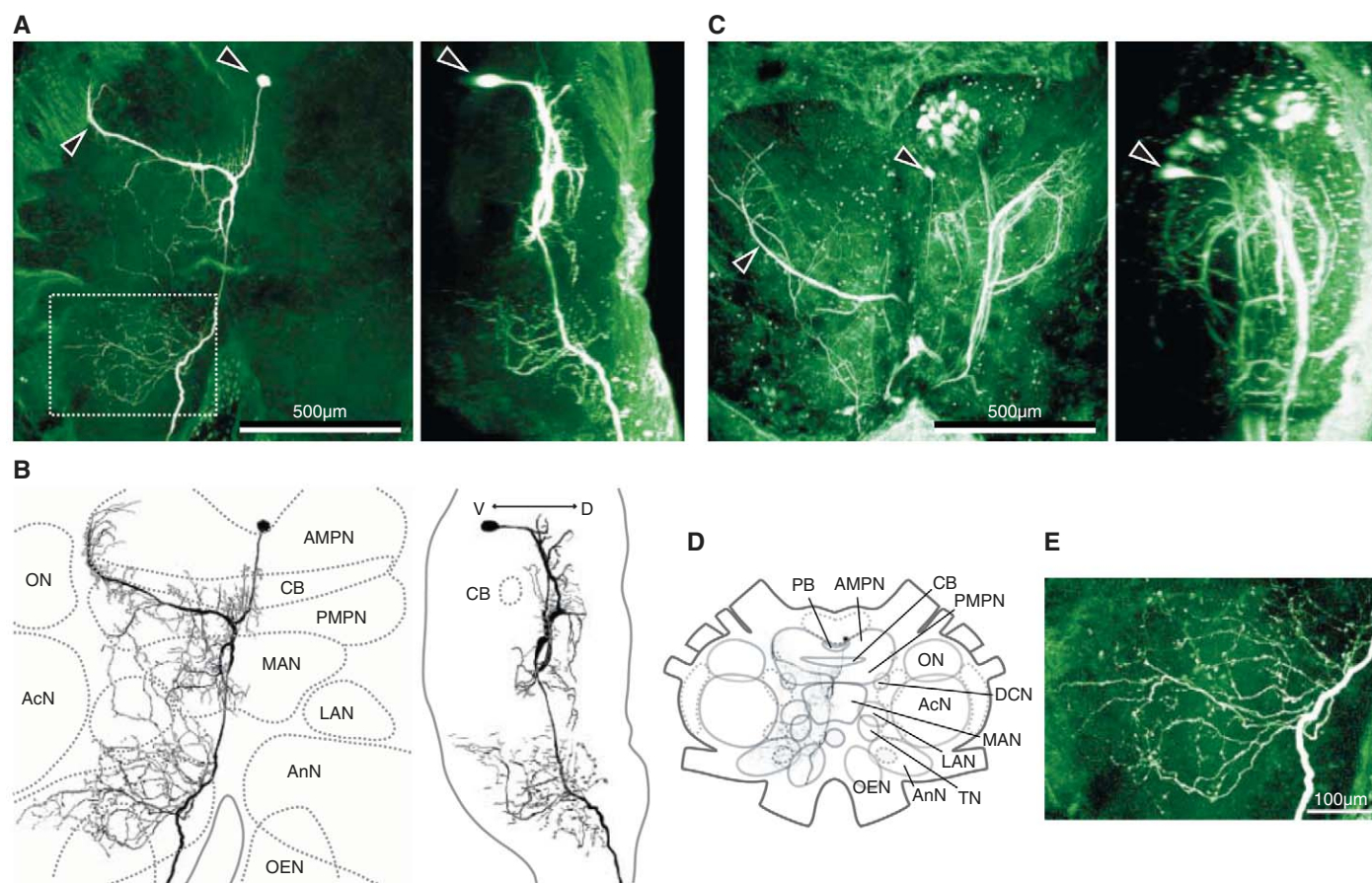


Fig. 2. Morphology of readiness discharge neurons. (A) Horizontal (left) and sagittal (right) projection images of the neuron stained after recording (Fig. 1). (B) Dendritic structure of the neuron on the horizontal (left) and sagittal (right) planes. (C) Horizontal (left) and sagittal (right) projection images of the neurons obtained by backfill staining. The left figure was adapted for the present comparison from our previous publication (8). (D) A schematic drawing of the crayfish brain. PB, protocerebral bridge;

AMPN, anterior medial protocerebral neuropil; CB, central body; PMPN, posterior medial protocerebral neuropil; ON, olfactory neuropil; DCN, deutocerebral commissure neuropil; AcN, accessory lobe; LAN, lateral antenna I neuropil; MAN, medial antenna I neuropil; TN, tegumentary neuropil; AnN, antenna II neuropil; OEN, esophageal neuropil. (E) Varicose arborization of the neuron. The region shown by a dashed rectangle in (A) was enlarged.

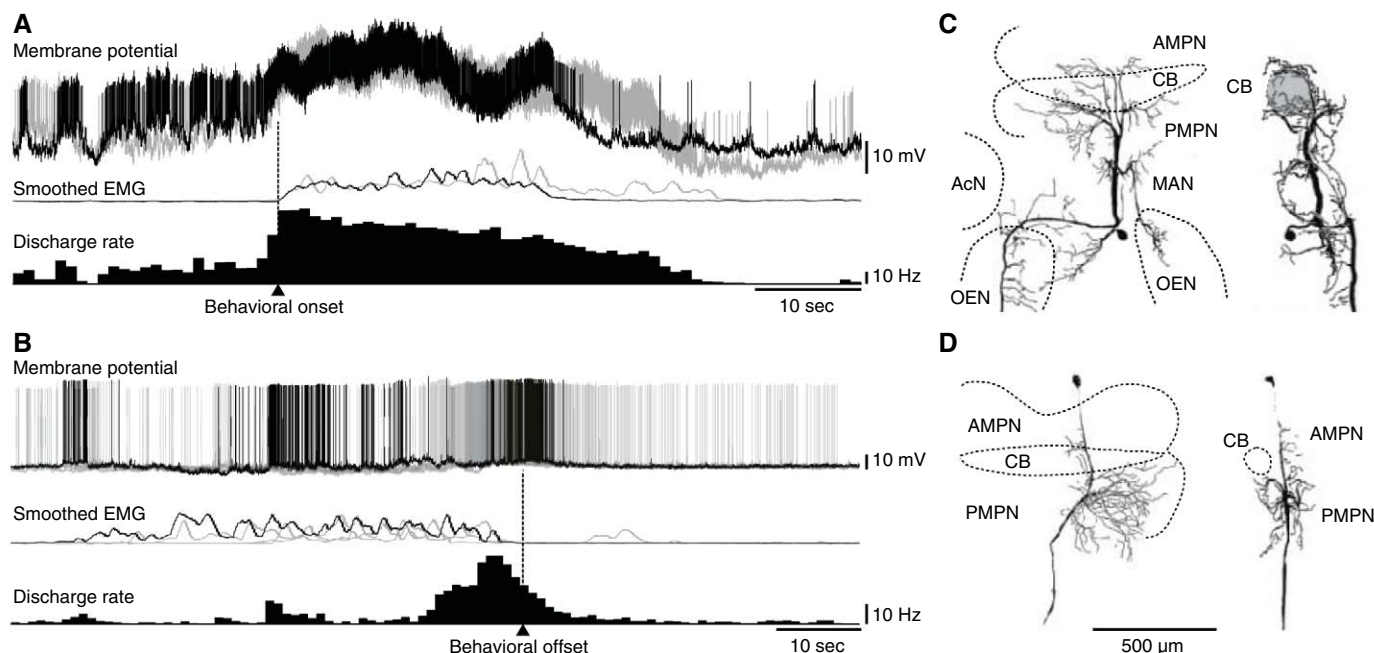


Fig. 3. Physiology and morphology of continuation and termination neurons. **(A)** (Top) An overlay of two membrane potential traces of a continuation neuron. (Middle) An overlay of smoothed traces of muscle activity. (Bottom) A peri-onset time histogram illustrating the spike activity during walking. **(B)** (Top) An overlay of four membrane potential traces of a termination neuron.

(Middle) An overlay of smoothed traces of muscle activity. (Bottom) Peri-offset time histogram illustrating spike activity at the time of behavioral offset. **(C)** Dendritic projection of a continuation neuron on the horizontal (left) and the sagittal (right) planes. **(D)** Dendritic projection of a termination neuron on the horizontal (left) and sagittal (right) planes.

relevant for self-initiated voluntary walking in crayfish and showed that they are organized and activated by presynaptic brain neurons, not by endogenous mechanisms.

References and Notes

1. A. L. Roskies, *Annu. Rev. Neurosci.* **33**, 109 (2010).
2. K. Okano, J. Tanji, *Exp. Brain Res.* **66**, 155 (1987).
3. W. Schultz, R. Romo, *Exp. Brain Res.* **91**, 363 (1992).
4. G. Maimon, J. A. Assad, *J. Neurosci.* **26**, 2487 (2006).
5. B. Hyland, *Behav. Brain Res.* **94**, 255 (1998).
6. J. K. Chapin, K. A. Moxon, R. S. Markowitz, M. A. Nicolelis, *Nat. Neurosci.* **2**, 664 (1999).
7. Y. Isomura, R. Harukuni, T. Takekawa, H. Aizawa, T. Fukai, *Nat. Neurosci.* **12**, 1586 (2009).
8. K. Kagaya, M. Takahata, *J. Neurosci.* **30**, 1348 (2010).
9. A. Chlachri, F. Clarac, *J. Neurosci.* **10**, 707 (1990).
10. K. Chikamoto, K. Kagaya, M. Takahata, *Zoolog. Sci.* **25**, 783 (2008).
11. J. R. Martin, T. Raabe, M. Heisenberg, *J. Comp. Physiol. A Neuroethol. Sens. Neural Behav. Physiol.* **185**, 277 (1999).
12. J. A. Bender, A. J. Pollack, R. E. Ritzmann, *Curr. Biol.* **20**, 921 (2010).
13. D. Sandeman, R. Sandeman, C. Derby, M. Schmidt, *Biol. Bull.* **183**, 304 (1992).
14. C. A. G. Wiersma, *J. Comp. Neurol.* **110**, 421 (1958).
15. H. L. Atwood, C. A. G. Wiersma, *J. Exp. Biol.* **46**, 249 (1967).
16. R. F. Bowerman, J. L. Larimer, *J. Exp. Biol.* **60**, 119 (1974).

Acknowledgments: This work was supported by Grants-in-Aid for Scientific Research from the Ministry of Education, Culture, Sports, Science and Technology, Japan (18657025 and 20370028).

Supporting Online Material

www.sciencemag.org/cgi/content/full/332/6027/365/DC1
Materials and Methods
Figs. S1 to S6
References

27 December 2010; accepted 10 March 2011
10.1126/science.1202244

CENTRIFUGE SYSTEM

The Sorvall RC BIOS centrifuge system is designed for high-speed, high-volume batch bioprocessing applications. The system integrates a six-liter Thermo Scientific Fiberlite carbon fiber rotor and true fit one-liter Thermo Scientific Nalgene bottles to achieve superior yields with faster processing time, making it ideal for bacterial and mammalian cell pelleting, large microbial cultures, and harvesting cell and tissue cultures. The Sorvall RC BIOS centrifuge system can spin up to 15,860 x g, significantly reducing cycle times. Its small footprint and quiet performance make it ideal for convenient in-lab placement. The high-capacity centrifuge system has a power-saving design that reduces overall processing and development costs, and a robust refrigeration system ensures sample quality that, in turn, reduces lot-to-lot variability.

Thermo Fisher Scientific

For info: 866-984-3766 | www.thermoscientific.com/centrifuge



EPIGENETICS DETECTION ASSAYS

A new panel of epigenetics-based detection reagents enable high throughput screening (HTS) for new drug candidates. The new assay kits can screen for epigenetic factors to assist researching diseases such as neurodegeneration and cancer. Drug targets related to epigenetics, the study of heritable changes in genome function not related to DNA sequence changes, are of growing interest in drug discovery due to their relevance in human diseases. The new panel of reagents, which employ LANCE Ultra and AlphaLISA detection technologies, accelerate cancer and neurobiology research by facilitating screening for modulators of DNA activity. The assays are designed to help researchers measure the activity of several epigenetic targets, such as histone methyltransferases (HMTs) and histone acetyltransferases (HATs) that methylate and acetylate histone peptides and proteins. The epigenetics reagents are the only no-wash, nonradiometric antibody-based screening solutions available for medium and high throughput screening laboratories.

PerkinElmer

For info: 800-762-4000 | www.perkinelmer.com

INFUSION SYRINGE PUMP

The Legato 100 Syringe Pump is a new single-syringe infusion-only pump with a touch screen interface that offers a wide flow rate range of 1.28 pl/min to 88.28 ml/min, accuracy of $\pm 0.5\%$, and reproducibility of $\pm 0.05\%$, making it the perfect syringe pump for flow cytometry, electrospraying, mass spectrometry calibrant delivery, microfluidics, neuroscience applications, and more. Stainless steel, plastic, or glass syringes can be used in the unit. The syringes are held in place by a robust new clamping mechanism. Syringes from 0.5 μ l to 60 ml can be used. The large color display on the Legato 100 allows the user to see the pump's operating parameters to ensure proper operation during the experiments. Syringe size and flow rates are displayed as well as the volume delivered and the elapsed time.

Dorton Analytical

For info: +44-(0)-7872-520670 | www.dortonanalytical.co.uk

mRNA AMPLIFICATION KITS

ExpressArt mRNA Amplification Kits offer an elegant technological solution for real-time reverse-transcription polymerase chain reac-

tion and gene expression array studies that overcomes the limitations of sample quality and quantity. ExpressArt technology allows reproducible and precise analysis of challenging samples including formalin-fixed paraffin-embedded tissue, laser captured microdissections, needle biopsies, and circulating tumor cells. Based on a unique non-Eberwine method using patented TRinucleotide primers and reagents, ExpressArt minimizes loss of sequence associated with two-round amplification procedures and eliminates 3' bias in amplified products. The resultant RNA produces accurate data on differential expression of low copy number genes that fail to give sufficient signal intensities using alternative methods, allowing direct comparison of data from a wide range of input sample sizes. In addition, using this exclusive primer technology, ExpressArt is able to amplify severely degraded RNA sequences thereby enabling an accurate analysis of RNA with extremely poor RIN values.

AMS Biotechnology

For info: +44-(0)-1235-828200 | www.amsbio.com

TUNABLE NEAR-INFRARED BANDPASS FILTER

The VersaChrome TBP01-800/12 is a widely tunable thin-film optical filter that is pushing tunable imaging into near-infrared territory with a wavelength tuning range of over 100 nm. Unique in the marketplace, VersaChrome filters offer wavelength tunability over a very wide range of wavelengths by adjusting the angle of incidence with essentially no change in spectral performance. VersaChrome tunable filters combine all the performance advantages of thin-film optical filters—including high-average transmission, steep edges, and wide out-of-band blocking—with the center wavelength tuning flexibility of a diffraction grating. The complete set of bandpass filters covers wavelengths from 390 nm to 800 nm. Rectangular filters are immediately available from stock in 25 mm x 36 mm x 2.0 mm size, and custom-sized filters are available in less than a week. These tunable filters are ideal for fluorescence microscopy and measurement applications as well as hyperspectral imaging, high throughput spectroscopy, and any other optical system that can benefit from the spectral and two-dimensional imaging performance of thin-film filters.

Semrock

For info: 866-736-7625 | www.semrock.com

Electronically submit your new product description or product literature information! Go to www.sciencemag.org/products/newproducts.dtl for more information.

Newly offered instrumentation, apparatus, and laboratory materials of interest to researchers in all disciplines in academic, industrial, and governmental organizations are featured in this space. Emphasis is given to purpose, chief characteristics, and availability of products and materials. Endorsement by *Science* or AAAS of any products or materials mentioned is not implied. Additional information may be obtained from the manufacturer or supplier.

Science Careers

From the journal *Science*



Science Careers Advertising

For full advertising details, go to ScienceCareers.org and click For Employers, or call one of our representatives.

Tracy Holmes

Worldwide Associate Director
Science Careers
Phone: +44 (0) 1223 326525

UNITED STATES & CANADA

E-mail: advertise@sciencecareers.org
Fax: 202-289-6742

Tina Burks

Midwest/West Coast/
South Central/Canada
Phone: 202-326-6577

Elizabeth Early

East Coast & Industry
Phone: 202-326-6578

Marci Gallun

Sales Administrator
Phone: 202-326-6582

Online Job Posting Questions
Phone: 202-326-6577

EUROPE & REST OF WORLD

E-mail: ads@science-int.co.uk
Fax: +44 (0) 1223 326532

Alex Palmer

Phone: +44 (0) 1223 326527

Susanne Kharraz

Phone: +44 (0) 1223 326529

Dan Pennington

Phone: +44 (0) 1223 326517

Lisa Patterson

Phone: +44 (0) 1223 326528

JAPAN

ASCA Corporation

Jie Chin
Phone: +81-3-6802-4616
Fax: +81-3-6802-4615
E-mail: careerads@sciencemag.jp

CHINA & TAIWAN

Ruolei Wu

Phone: +86-1367-1015-294
E-mail: rwu@aaaas.org

All ads submitted for publication must comply with applicable U.S. and non-U.S. laws. *Science* reserves the right to refuse any advertisement at its sole discretion for any reason, including without limitation for offensive language or inappropriate content, and all advertising is subject to publisher approval. *Science* encourages our readers to alert us to any ads that they feel may be discriminatory or offensive.



www.reading.ac.uk/jobs

Grantham Chair in Climate Science

Department of Meteorology, School of Mathematical and Physical Sciences

This appointment is full-time, permanent
Salary is negotiable

We are seeking an outstanding Scientist to take up the newly-established Grantham Chair in Climate Science.

You will play a leading role in the development of research into the earth's climate system, working in partnership with the Grantham Institute for Climate Change at Imperial College London and other organisations to develop and communicate climate science through involvement in international bodies.

You will have:

- outstanding expertise in climate science, with a focus on future climate change
- the ability to initiate and lead research programmes and to work effectively with experts
- first-class skills as an educator and communicator
- a record of leading participation in international research or review activities

Informal enquiries: contact the Head of Academic Staff and Teaching, Professor Giles Harrison on +44(0)118 378 5588 or email g.harrison@reading.ac.uk. Alternatively, contact the Director of the Walker Institute for Climate System Research, Professor Nigel Arnell on +44(0)118 378 7392 or email n.arnell@reading.ac.uk

Closing date: 17 May 2011

To apply please visit www.reading.ac.uk/jobs or contact Human Resources, University of Reading, Whiteknights, PO Box 217, Reading RG6 6AH.
Telephone +44(0)118 378 6771 (voicemail)

Please quote reference number CH11008

We value a diverse workforce and welcome applications from all sections of the community



Director, Center for Cardiovascular Research

The Division of Cardiology at Washington University School of Medicine seeks applications and nominations for Director, Center for Cardiovascular Research (CCR).

Investigators in the CCR focus on identifying the fundamental biological processes that are responsible for cardiovascular disease, with the intent of developing novel therapies for disease. The CCR is comprised of faculty members within the Cardiovascular Division at Washington University, as well as scientists with primary appointments in other departments throughout Washington University.

The successful candidate will have a distinguished record of current and sustained funding in cardiovascular research, a track record of mentoring trainees, and fostering an environment to stimulate research. Qualified candidates will possess an M.D., Ph.D or M.D./Ph.D. degree and an academic rank as Associate or Professor. The position is supported by an endowed chair, as well as a separate research endowment.

Applicants should email a curriculum vitae and letter stating their interest and career goals to the **Douglas L. Mann** at dmann@dom.wustl.edu. All inquiries will be held in strict confidence.

Washington University is an Affirmative Action, Equal Opportunity, and Equal Access Employer.

Download your free copy.

ScienceCareers.org/booklets



Science Careers
From the journal *Science* AAAS

Tenure-Eligible/Tenure-Track Position in Viral Disease Ecology Laboratory of Virology

The National Institute of Allergy and Infectious Diseases (NIAID), Division of Intramural Research (DIR), Laboratory of Virology (LV) at Rocky Mountain Laboratories (RML) in Hamilton, MT, seeks applicants for a tenure-eligible/tenure-track position (assistant/associate professor equivalent) to conduct independent research on viral agents requiring high or maximum containment.

LV conducts high-impact, innovative scientific research on viral agents requiring high or maximum containment, including arenaviruses, bunyaviruses, filoviruses, flaviviruses, paramyxoviruses, and orthomyxoviruses, with the goal of developing diagnostics, vaccines, and therapeutics. The research conducted in LV includes studies of vector/reservoir transmission and the pathogenesis, pathophysiology, and host immune response of high containment viral pathogens. Candidates must be able to develop an independent research program in infectious disease ecology, supervise staff and fellows, and collaborate with RML/DIR researchers working on other infectious diseases. An interest in and commitment to research in the field and a high-containment biosafety level 3 and 4 (BSL-3 and BSL-4) environment is essential. Other requirements are listed below.

The selected candidate is expected to implement and direct a vigorous, independent research program in viral disease ecology, including field and laboratory studies targeted toward understanding virus persistence in natural reservoirs, transmission from natural reservoirs and/or intermediate hosts to end hosts, and reservoir ecology. This program is expected to include studies in animals, and preference will be given to candidates with experience in infectious disease animal models.

Facilities at existing NIAID field sites in Africa and Asia are available to the incumbent. In addition, LV currently operates established field sites in Mali and the Republic of the Congo. An interest and ability to develop programs at established field sites is highly desirable.

Candidates must hold a Ph.D., D.V.M., M.D., or equivalent degree and have relevant post-doctoral experience. Independent resources including space, support personnel, and an annual budget for services, supplies, and salaries are committed to the position. These are appointments under Title 42. Salary is dependent on experience and qualifications.

RML's state-of-the-art facilities include an operational BSL-3 facility; a BSL-4 laboratory and animal facility that can accommodate work with both small animal and nonhuman primate models; and outstanding support facilities for genomics, electron microscopy, flow cytometry, and other advanced techniques dedicated to scientific collaboration.

Other RML research programs focus on prions, retroviruses, pathogenic prokaryotic organisms, and pathogen transmission by arthropod vectors. RML is located in the scenic Bitterroot Valley of western Montana within easy access to some of the finest outdoor recreational opportunities in North America.

To apply, e-mail curriculum vitae, bibliography, and a two- to three-page description of your proposed research program to Ms. Bao-Hanh Ngo at lvsearch@mail.nih.gov. In addition, three letters of recommendation must be sent directly from the referees to Dr. Tom Schwan, Chair, NIAID Search Committee, c/o Ms. Bao-Hanh Ngo at lvsearch@mail.nih.gov or 10 Center Drive, MSC 1356, Building 10, Room 4A30, Bethesda, MD 20892-1356. E-mail is preferred.

The selected candidate may be asked for additional references.

Key Requirements:

- Applicants must be U.S. citizens, resident aliens, or nonresident aliens with or eligible to obtain a valid employment-authorizing visa.
- Applicants must be able to fulfill, acquire, and maintain a favorable Access National Agency Check and Inquiries (ANACI) background investigation, select agent clearance, and other NIH biosecurity requirements.

Applications will be reviewed starting **May 31, 2011**, and will be accepted until the position is filled. Additional information on this position can be obtained by contacting Dr. Heinz Feldmann at feldmannh@niaid.nih.gov.

Further information about LV is available at www.niaid.nih.gov/labs/aboutlabs/lv, information about DIR laboratories is available at www.niaid.nih.gov/about/organization/dir, and information about working at NIAID is available at www.niaid.nih.gov/careers/ve.

NIAID

National Institute of Allergy and Infectious Diseases



US DEPARTMENT OF HEALTH AND HUMAN SERVICES
 National Institutes of Health



National Institute of Allergy and Infectious Diseases
 Proud to be Equal Opportunity Employers



Eidgenössische Technische Hochschule Zürich
Swiss Federal Institute of Technology Zurich

Associate or Full Professor of Microbial Interactions

ETH Zurich and the Department of Biology (www.biol.ethz.ch) invite applications for above mentioned professorship from candidates with an outstanding research profile and proven teaching abilities.

The position is at the associate or full Professor level and is expected to cover the area of Microbial Interactions. ETH Zurich, the Department of Biology and the Institute of Microbiology offer outstanding scientific opportunities to participate in interdisciplinary research projects, including close interactions with SystemsX.ch, the Swiss initiative for systems biology, Life Science Zurich, a well-established platform for teaching and research, the Functional Genomics Center Zurich, as well as a network of more than 40 research laboratories in microbiology, immunology and related disciplines.

Candidates are expected to entertain a world-class research program in the area of microbial interactions with strong links to biochemistry, systems biology, and ecology or health science. Research areas include, but are not limited to, microbial biology within complex environments of ecosystems or eukaryotic hosts, methods development for enabling technologies in imaging, single cell biology, and microbe-microbe interactions. The successful candidate will be a member of the Institute of Microbiology, and will demonstrate competitive acquisition of third party funding.

The appointed professor will be expected to teach undergraduate level courses (German or English) and graduate level courses (English). This refers to the biology teaching program which includes a Master's curriculum of Microbiology and Immunology.

Please apply online at www.facultyaffairs.ethz.ch. Your application should include your curriculum vitae, a list of publications, and a statement of your research and teaching interests. The letter of application should be addressed to the President of ETH Zurich, Prof. Dr. Ralph Eichler. The closing date for applications is May 31, 2011. With a view towards increasing the number of women in leading academic positions, ETH Zurich specifically encourages women to apply.

Functional Genomics and Epigenomics of Cancer

The Wistar Institute, an independent, non-profit research institute with a primary focus on cancer research, seeks an outstanding candidate with a doctoral degree or equivalent for a leadership position within the recently formed Center for Systems and Computational Biology. An endowed chair faculty appointment at the rank of Associate Professor/Professor is anticipated. The candidate's research focus should include state-of-the-art approaches in functional genomics using high-throughput sequencing approaches combined with sophisticated data analysis to tackle cancer-related problems. The successful candidate is expected to demonstrate evidence of a vigorous, independent extramurally-funded research program, as well as high-impact publications in the area of cancer research.

The Wistar Institute, an NCI-designated Cancer Center, offers highly competitive start-up support, salary and fringe benefits, in addition to a superb and interactive research environment, including state-of-the-art core facilities with multiple laboratories that are increasingly emphasizing systems biology approaches to basic biological processes, cancer and other human diseases. The Institute's location on the University of Pennsylvania campus and adjacent to Drexel University provides potential academic and clinical collaborators, as well as opportunities for training graduate students. Direct questions to Search Committee Chair Ramin Shiekhataar at shiekhataar@wistar.org.

Applications will be reviewed as received and will be accepted until the position is filled. To ensure timely consideration, applicants should submit applications before July 1. The application should include curriculum vitae, brief summary of past and future research interests, history of research funding support (if applicable) and the names of five potential references. Applications should be sent by e-mail to: **Ramin Shiekhataar, Search Committee Chair, c/o Maria Colelli (Colelli@wistar.org), The Wistar Institute, 3601 Spruce Street, Philadelphia, PA 19104. EOE/AA/M/F/D/V.**



THE WISTAR INSTITUTE

An NCI-designated Cancer Center

For more information about us, visit our Web site at
www.wistar.org

Associate or Full Medical Professor (2 positions) Tenured or Tenure-Track CUNY Med School at CCNY

The Sophie Davis School of Biomedical Education (CUNY Med School) offers an innovative seven-year integrated curriculum leading to the B.S./M.D. degrees. Located on the campus of the City College of New York (CCNY), the flagship science institution of CUNY with a long history of excellence and leadership in the basic sciences, the Sophie Davis School seeks candidates with outstanding scholarly records for two (2) Associate or Full Medical Professor positions.

Medical Biochemistry Position in the Department of Cell Biology and Anatomy: Candidates should have active research in an area of cell or molecular biology, biochemistry, mammalian developmental genetics, medical genetics or reproductive biology. Responsibilities will include teaching medical biochemistry, cell biology or genetics to medical students.

Physiology Position in the Department of Physiology, Pharmacology and Neuroscience: Candidates should have an active research program that employs systems, molecular or biochemical approaches in any area of physiology. Responsibilities will include teaching medical physiology/pharmacology to medical students.

Candidates should possess a M.D. and/or Ph.D. and an outstanding academic/scholarly record. Preference will be given to candidates with vigorous externally funded research programs in area(s) of expertise as noted above. Salary is commensurate with appointment rank, qualifications and experience. Submit CV, a statement of accomplishments including current and long-term research plans, and names and addresses of three references electronically to dlawrence@med.cuny.edu or mail to:

**Office of the Dean
The Sophie Davis School of Biomedical Education
Harris Hall Suite 107
160 Convent Avenue, New York, NY 10031**

The City College of New York and The Sophie Davis School of Biomedical Education have strong institutional commitment to the principle of diversity. In that spirit, we are particularly interested in receiving applications from a broad spectrum of individuals, including women and members of under-represented ethnic groups.



Faculty Position

BACKGROUND

We are seeking an innovative investigator with a strong research background to lead an independent research program within the Victor Chang Cardiac Research Institute (VCCRI)—an independent research organization committed to excellence in basic and translational biomedical research that is affiliated with the University of New South Wales (UNSW), and is a member of the St. Vincent's Research Precinct that also includes the Garvan Institute for Medical Research and the St. Vincent's Centre for Applied Medical Research.

Preference will be given to Individuals whose research addresses gene regulation at the transcriptional or post-transcriptional levels; vascular biology, particularly in terms of neoangiogenesis or vasoregulatory mechanisms; stem cell biology and therapeutic approaches; structural biology; genomics; signal transduction; tissue/organ regeneration, or tissue bioengineering.

The successful candidate will be provided with an office and laboratory space in a state-of-the-art research facility, and significant financial support to rapidly establish their program, and will be eligible for an academic appointment at UNSW.

RESPONSIBILITIES

The successful candidate will be expected develop or continue a “cutting-edge” independent research program that is supported by extramural peer-reviewed grant funding, in the areas of cardiovascular science or in disciplines that are relevant to understanding cardiovascular biology or disease pathogenesis at the physiological, molecular, cellular and structural levels, and to participate in graduate and postdoctoral training.

REQUIREMENTS

PhD/DPhil/MD with relevant postdoctoral training; a track record of outstanding research achievements; excellent verbal and written communication skills; relevant teaching experience; a record of peer-reviewed publications, and a strong interest in innovative and interactive research.

Program Leader in Bioinformatics

BACKGROUND

We are seeking an innovative investigator with a strong research background in Bioinformatics/Computational Biology to lead an independent research program within the Victor Chang Cardiac Research Institute (VCCRI) — an independent research organization committed to excellence in basic and translational biomedical research that is affiliated with the University of New South Wales (UNSW), and is a member of the St. Vincent's Research Precinct that also involves the Garvan Institute for Medical Research and the St. Vincent's Centre for Applied Medical Research.

Preference will be given to individuals applying next generation sequencing or other high throughput technologies and bioinformatics and computational tools to identify alleles, genes and pathways contributing to common disease.

The successful candidate will be provided with office and support space, and significant financial support to rapidly establish their program, and will be eligible for an academic appointment at UNSW.

RESPONSIBILITIES

Your genomics research program might focus on one or more of the following areas, closely linked with experimental science within the VCCRI: transcriptional regulation, epigenetics, transcriptomics, noncoding RNAs, imprinting, disease susceptibility, structural variation, and evolution. The successful applicant will be expected to develop or continue a vigorous independent research program, maintain extramural research funding, and participate in graduate and postdoctoral training.

REQUIREMENTS

PhD/DPhil/MD in the fields of computational biology, genetics or genomics. Candidates will have expertise that includes high throughput data generation and analysis, excellent verbal and written communication skills, relevant research and teaching experience, a record of peer-reviewed publications, and a strong interest in innovative and interactive research.

HOW TO APPLY

Interested candidates should submit their curriculum vitae, statement of research interest and names of three references to m.voukenas@victorchang.edu.au

CLOSING DATE

Applications will be accepted until May 31, 2011.

POLICY

The VCCRI is an Equal Opportunity/Affirmative Action employer and boasts a record of gender parity at all levels of the organization.



Assistant/Associate Professor Position School of Medicine & Biomedical Sciences

Positions are available immediately in the disciplines of bioinformatics and computational biology at the rank of Assistant and/or Associate Professor (tenure track) in the School of Medicine and Biomedical Sciences at the State University of New York at Buffalo. The candidate will have an appointment in one of several Departments that could include Biochemistry, Biomedical Engineering, Microbiology, Pharmacology and Toxicology, Physiology and Biophysics, or Structural and Computational Biology. We are particularly seeking individuals with outstanding biological and quantitative expertise and a successful track record of collaborating with interdisciplinary scientific teams. Successful candidates will have expertise in multilevel analysis and integration of genomic, epigenomic, proteomic, or preclinical/clinical datasets, as well as strong data mining abilities aimed at generating testable hypotheses. Preference will be given to candidates with experience in high resolution/high-throughput data analysis, including the development and utilization of bioinformatic/computational tools to research areas such as complex genetic disease, metagenomics, infectious disease, oncology, model systems and translational biomedical research. State-of-the-Art Facilities: Space exists in the Center of Excellence in Bioinformatics and Life Sciences building situated adjacent to the Hauptman-Woodward Institute, and in close proximity to the new Clinical and Translational Research Center on the Buffalo Niagara Medical Campus. The Centers have a modern, state-of-the-art experimental infrastructure in biomedical sciences including core facilities for next generation sequencing, genomics, proteomics, and imaging and are also home to the Center for Computational Research (CCR). CCR maintains a high-performance computing environment, high-end visualization laboratories, and support staff of 13 with expertise in high-performance computing, software engineering, grid computing, database engineering, and advanced networking.

Candidate Requirements: The successful applicants will have a Ph.D., or MD/Ph.D. in bioinformatics, computational biology or related field with postdoctoral and professional experience appropriate to the rank of the appointment. Duties include development of an independent research program, and teaching undergraduate, graduate, and professional students. **Applications:** Applications for this position will only be accepted online. To apply, please visit: www.ubjobs.buffalo.edu/applicants/Central?quickFind=54111.

The University at Buffalo is an Equal Opportunity/Affirmative Action Employer/Recruiter

Boston University School of Medicine

Boston University School of Medicine Faculty Positions Whitaker Cardiovascular Institute

Applications are invited from scientists for faculty positions in the Whitaker Cardiovascular Institute at Boston University School of Medicine. Faculty rank from Assistant Professor to Full Professor is open, dependent on level of achievement.

The Institute conducts and coordinates research and training related to the prevention and treatment of cardiovascular disease. Over the past three decades, the Institute's research has focused in the areas of hypertension, atherogenesis, heart failure, angiogenesis, endothelial function, thrombosis, free radical biology and lipid chemistry. We are interested in candidates who have an active research program in one or more of these areas and a skill set that will complement the Institute's existing strengths. Candidates must have an M.D. or Ph.D., postdoctoral experience and a strong publication record. Individuals are expected to establish an independent, extramurally-funded research program.

Applicants should submit a cover letter and curriculum vitae listing publications, grant support and a list of references along with a description of your research interests and goals. Applications should be transmitted by e-mail to **Nancy E Clinton (nclinton@bu.edu)** with a cc to **Director, Kenneth Walsh, PhD, Professor of Medicine (kxwalsh@bu.edu)**.



Boston University is an Equal Opportunity/
Affirmative Action Employer

www.bumc.bu.edu



Research Fellow Positions at Suzhou Institute of Biomedical Engineering and Technology (SIBET), Chinese Academy of Sciences (CAS) Suzhou, Jiangsu, China

SIBET is situated in Suzhou, an ancient city near Shanghai in China. SIBET is focusing on the breakthrough of core technologies in detection based on spectroscopy, nuclear medical detectors, micro-nano sensors and medical semiconductor laser by integrating high technology in fields of biology, photoelectricity, nuclear medicine and computer. SIBET is dedicated to develop mature products in the medical instrumentation, medical materials and biomedical reagents to meet the demands of public health and domestic medical industry development. Currently, the R&D fields include medical laser, biomedical measurement, medical imaging, biomedical electronics, biomaterials and biomedical reagents.

We are seeking candidates for research fellow positions at Associate Professor/Professor levels to work in the fields of (1) medical laser, (2) medical imaging, (3) clinical diagnosis and analysis, (4) biomedical electronics, (5) biomedical reagents, (6) artificial organ and (7) biological and medical materials.

Generous start-up packages to develop successful labs and competitive salaries and benefits will be provided.

Candidates should have a Ph.D., an outstanding track record of scientific productivity, the ability to manage labs and research projects independently, and excellent communication skills in Chinese and English.

Send curriculum vitae, a statement of research interests and future plans, and a list of three references to:

Prof. Xuan Ming,
President, Suzhou Institute of Biomedical Engineering and Technology
(SIBET)
Human Resource Department of SIBET
88 Keling Road, SND, Suzhou 215163, China
Tel: 86-512-69588025; Fax: 86-512-69588088
Email: talent@sibet.ac.cn

Burnett School of Biomedical Sciences College of Medicine

Scientist/Administrator to serve as Associate Director

Burnett School of Biomedical Sciences, College of Medicine seeks an Associate Director to provide leadership to its research enterprise. The school is expanding its research programs in Cancer, Cardiovascular and Metabolic, Neurodegenerative and Infectious diseases into the new 198,000 sq.ft. Burnett Biomedical Science Building. The school will be recruiting more than a dozen new faculty within the next few years. The Burnett School has over 2400 majors and 16,000 students are enrolled in the courses taught by the school faculty. The school offers MS and PhD degrees and MS/MBA and PhD/MBA programs.

The Associate Director is expected to maintain a highly funded research program in any of the four focus areas of the school and provide leadership to the entire research enterprise and graduate programs of the school. The successful candidate must hold an earned doctorate in a discipline appropriate to the school and must have a distinguished record of scholarly accomplishment meriting appointment with tenure at the rank of professor in the school.

A leadership role in recruiting new faculty will be expected. State of the art research facilities including shared core instrumentation and a large transgenic animal facility are available in the Burnett School. UCF the nation's third largest university, ranked third in innovation and patents, is located in the great metropolitan area of Orlando. The Burnett Biomedical Science building is located in the new Health Science campus at Lake Nona that is home also for the new College of Medicine, Sanford-Burnham Medical Research Institute, Nemours Children's Hospital and VA hospital, the beginnings of an exciting major medical city in Central Florida. Further information is available at <http://www.biomed.ucf.edu>



Please submit nominations or a CV and a list of at least four references to pk@mail.ucf.edu

The University of Central Florida is an equal opportunity, equal access, and affirmative action employer. As a member of the Florida State University System, all application materials and selection procedures are available for public review.





Stiftung Alfred-Wegener-Institut
für Polar- und Meeresforschung
in der Helmholtz-Gemeinschaft



The Climate Dynamics section (Ocean Dynamics section until 31. May 2011) at the Alfred Wegener Institute for Polar and Marine Research (AWI) in Bremerhaven, Germany, is seeking to appoint a

Scientist position

with a background in climate research, oceanography, meteorology or physics.

Background and tasks: The section is concerned with the understanding, modeling and prediction of the coupled climate system. The emphasis is on the polar regions and their role in the global climate system. The successful applicant will (1) contribute to the development of coupled models, (2) setup, run and analyse numerical experiments with coupled models, (3) give scientific and technical support to other members of the group, (4) secure external funding and (5) be involved in teaching activities on a stand-in basis at the University of Bremen.

Requirements: PhD in climate, ocean, atmospheric, physical sciences or mathematics. Demonstrated skill/proficiency in Fortran or C, fluency in English, experience with complex models of the coupled climate system (or their subcomponents) and a proven record in publishing and securing external funding are all distinct advantages.

Length of contract: This is a tenure-track position. It will be reviewed after 1 ½ years with the possibility of permanency after 2 years.

Salary: Payment will be in accordance with the German Tarifvertrag für den öffentlichen Dienst (TVöD).

For further information: Prof. Dr. Th. Jung (E-Mail: Thomas.Jung@awi.de; Phone: +49(0)471-4831-1761).

AWI aims to increase the number of women in the scientific staff and therefore encourages women to apply.

Disabled applicants with identical technical and personal suitability will be preferentially selected, please see our notification on our homepage under job offers / jobs.

The AWI supports balanced work-life career development via a variety of alternatives. In Bremerhaven, the AWI operates its own nursery.

Applications including CV, degree certificates, a statement of research interests and names and addresses of two referees should be submitted under reference number **36/G/KL-tt** to: **Alfred-Wegener-Institut für Polar- und Meeresforschung, Personalabteilung (human resources), Postfach 12 01 61, 27515 Bremerhaven / Germany** (<http://www.awi.de>). Applications will be received until **May 15, 2011**.

Aker/Zvonkovic Photography



Our World-Class Research Institute Is Looking for Scientific Leaders

Since its inception, The Methodist Hospital Research Institute has challenged the notion of "by-the-book" medical research. Led by Mauro Ferrari, Ph.D., President and CEO, the Research Institute is a 440,000-square-foot research enterprise for The Methodist Hospital System in Houston, TX, and is affiliated with the Weill Cornell Medical College in New York City. Methodist is transforming medicine with emerging techniques, and a staff that is developing real treatments and cures every day. Our laboratories are equipped with advanced technology and facilities that include a cyclotron, pre-clinical and clinical imaging, flow cytometry and microscopy, small and large animal vivariums; and a GMP facility for nanoparticles, contrast agents, vaccines, and therapeutic molecules. Our facility is a vertically integrated state-of-the-art laboratory for translational and clinical research where translational researchers and physician scientists bring ideas to clinical applications.

We are now searching for research professionals to serve in a variety of capacities.

Program leaders in the fields of:

- *Neurodegenerative Diseases and Repair of the Nervous System* (Methodist Neurological Institute)
- *Cardiovascular Science* (Methodist DeBakey Heart & Vascular Center)
- *Cancer Biology* (Methodist Cancer Center)

Senior scientists in the fields of:

- *Diabetes and Metabolic Disorders* (Methodist Center for Diabetes, Obesity and Lipids)
- *Transplant Immunology* (Methodist Transplant Center)

Candidates should be nationally and internationally recognized leaders with an outstanding track record of scientific discovery, funded research, programmatic leadership and academic mentorship. We will provide you with a position in the epicenter of medical research. You'll discover an excellent research environment, state-of-the-art equipment, and the chance to follow your research from discovery to clinical application in a single facility.

Applicants should submit a Statement of Scientific Interest, a Curriculum Vitae, and the names of three references to: Tong Sun, Director of Central Research Administration, The Methodist Hospital Research Institute, 6670 Bertner St., M.S. R2-216, Houston, TX 77030, or email facultyapplications@tmhs.org (please specify applying field in the subject line of email). Our success as an organization is due to the diversity of our team. We are an equal opportunity employer.

www.tmhri.org

www.MethodistHealth.com



The Methodist Hospital
Research Institute®

Houston, TX

LEADING MEDICINE®

The Methodist Hospital System is the official health care provider of the Houston Texans, Houston Astros, Houston Dynamo, Rice Athletics, Houston Ballet, Houston Grand Opera and Houston Symphony.

Chief Scientific Officer

Keystone Symposia on Molecular and Cellular Biology is seeking a Chief Scientific Officer (CSO) to work full-time who will be a strong leader and can put into practice the scientific mission and vision of the organization.

Keystone Symposia on Molecular and Cellular Biology, a 501(c)(3) nonprofit educational organization, plans and conducts 55-60 scientific conferences annually. Since its inception in 1972, the organization has convened symposia on life science topics primarily in North America, but since 2005 Keystone Symposia has expanded globally. Conferences have been convened in Australia, Austria, China, England, Ireland, Japan, Singapore, South Africa, Tanzania, Thailand and Uganda, and plans are being made for meetings in India, Sweden and Brazil. Keystone Symposia's Board of Directors and Management are committed to a robust globalization strategy that promotes opportunity and participation of scientists worldwide in the highest-quality international conferences. Priorities for the organization are connecting scientists with diverse research interests; catalyzing scientific collaboration; developing scientific talent worldwide, especially the next generation of scientists; and accelerating life science discoveries that benefit the world.

The CSO will be responsible for maximizing the impact of Keystone Symposia's scientific priorities; proposing and developing new scientific policies, programs and activities; and through interactions with the experienced staff, contributing to the effective implementation of those policies, programs and activities. Among other specific responsibilities, the CSO will: 1) develop the annual program portfolio strategic goals in close collaboration with the CEO, Senior Director of Program Development & Implementation and other senior staff members; 2) work closely with the Keystone Symposia team to execute on these goals; 3) serve as the main point of contact between Keystone Symposia and its Scientific Advisory Board composed of leading international scientists; 4) collaborate with the Director of Diversity and Director of Development to achieve diversity and fundraising objectives; and 5) take the lead in ensuring the quality of Keystone Symposia programs. The position also requires outreach to local, national and international collaborators. The CSO will have direct supervisory responsibility for a Senior Grant Coordinator/Program Analyst and an Administrative Assistant. A more detailed job description can be viewed on our website at www.keystonesymposia.org/CSOJob.

Requirements for the position include a doctoral degree in biological (Ph.D.) and/or medical sciences (M.D., D.V.M.), a well-rounded knowledge of the life sciences, excellent communication skills, and the desire and ability to work in a team-oriented environment. Relevant experience includes conducting and/or managing research activities in the biological/medical sciences, a record of high-quality publication and/or scientific journal editing experience, and writing and/or participating in peer review of research grants. National and international travel will be required. Willingness to relocate to the Keystone Symposia offices in Summit County, Colorado – located approximately 60 miles west of Denver in a recreational paradise – is considered crucial to maintain the interactive teamwork culture of the organization. Interested individuals should email a CV/resume and cover letter to the CEO at aiken@keystonesymposia.org or contact Mary Jo Roal, HR Director, at 970 262 2674.

KEYSTONE SYMPOSIA
on Molecular and Cellular Biology

Accelerating Life Science Discovery

PO Box 1630 • 221 Summit Place #272
Silverthorne, CO 80498 • www.keystonesymposia.org



MEDICAL SCHOOL FACULTY Microbiology with Biochemistry

St. Kitts Medical Campus

The University of Medicine and Health Sciences is a premier, for-profit boutique off shore medical school located on the exotic Caribbean Island of St. Kitts. Our ocean front state of the art campus is comparable to the best medical schools in the United States. We maintain small classes and provide a personalized education catering to the individual needs of the students. To date we have invested over 50 million dollars into our campus facilities and infrastructure.

We are seeking a full time medical microbiologist preferably with a minimum of 4 years experience teaching in a U.S. or Canadian medical school. Candidates must have a minimum of an earned PhD in microbiology. Candidates additionally holding an M.D. degree will be given preference. Candidate should also be able to teach portions of biochemistry as well. Salaries and benefits are competitive and commensurate with experience. A significant portion of the salary is offered tax free.

Candidates should forward their CV's
and cover letter to: hr@umhs-sk.net

For further details about

The University of Medicine and Health Sciences
For further details about our university please visit www.umhs-sk.org

EDUCATING THE NEXT
GENERATION OF PHYSICIANS

UMHS

Max Planck Institute for the Physics of Complex Systems



Group leader in theoretical AMO physics

In the department Finite Systems of the Max Planck Institute for the Physics of Complex Systems, headed by Prof. Dr. Jan Michael Rost, a group leader position (salary scale TVÖD 15) is available (successor to Prof. Dr. Klaus Hornberger).

The successful candidate is expected to have a strong research record and can form his/her own research group in the department. Possible research areas include atomic and molecular physics, strong field physics including attosecond dynamics and intense x-ray science, as well as quantum optics including quantum information.

Research in Dresden is intense and diverse with ample opportunities for collaboration, at the institute itself, with the local university, and the partners of our international PhD school (IMPRS), through which also PhD students can be recruited. The position is not tenured and runs for five years with the possibility of an extension. The starting date is flexible.

Applications - containing CV, publication list, statement of research plans and interests, and at least three letters of recommendation - should be sent to Gabriele Makolies, quoting 'GLFS11' as reference, either by electronic (makolies@pks.mpg.de) or regular mail (Max-Planck-Institut für Physik komplexer Systeme, Nöthnitzer Str. 38, 01187 Dresden, Germany). Applications will be accepted until the position is filled; the deadline for primary consideration is **June 1st, 2011**.

The Max-Planck-Institute aims to increase the number of women in scientific positions. Female candidates are therefore particularly encouraged to apply. In case of equal qualifications, candidates with disabilities will take precedence.



ExxonMobil

Taking on the world's toughest energy challenges.™

Member of Technical Staff – Algae Biofuels

ExxonMobil Research and Engineering has an immediate opening for a Member of the Technical Staff in its Corporate Strategic Research laboratory located in Annandale, NJ.

Candidates are sought to fill a bioengineer position in the Algae Biofuels program, which is part of ExxonMobil's strategic alliance with Synthetic Genomics, Inc. This program is a new long-term investment focused on biofuel production from photosynthetic algae. If successful, these next generation biofuels could augment the world's transportation fuel supply and assist in reducing greenhouse gas emissions in the decades to come.

The successful candidate will be part of a team working on the design, operation and testing of reactor systems to grow and harvest algae. Responsibilities will include implementing, testing and modifying prototype photo bioreactors, algae harvesting equipment and oil recovery systems. This individual will also interact with design teams and contractors. A PhD in chemical or mechanical engineering or related field is required. Requirements include reactor engineering expertise, bioreactor design experience, as well as experience in experimental design. A background in photosynthesis is a plus.

ExxonMobil's Corporate Strategic Research (CSR) laboratory is a dynamic and exciting place to work. CSR is located in scenic western New Jersey, about an hour west of New York City and 45 minutes northwest of Princeton. Within CSR, active research programs exist in all areas of the company's business and include the traditional fields of chemical engineering, materials science, chemistry, physics, geoscience and mechanical engineering. Interdisciplinary research is the norm, and close ties are maintained with the academic and national laboratory communities through publication and presentation of results.

ExxonMobil offers an excellent working environment and a competitive compensation and benefits package. Please submit your cover letter and resume to our website at www.exxonmobil.com/ex and apply to Bioengineer.

**ExxonMobil is an
Equal Opportunity Employer**

ExxonMobil

Taking on the world's toughest energy challenges.™

Member of Technical Staff – Algae Biofuels

ExxonMobil Research and Engineering has an immediate opening for a Member of the Technical Staff in its Corporate Strategic Research laboratory located in Annandale, NJ.

Candidates are sought to fill a phycology position in the Algae Biofuels program, which is part of ExxonMobil's strategic alliance with Synthetic Genomics, Inc. This program is a new long-term investment focused on biofuel production from photosynthetic algae. If successful, these next generation biofuels could augment the world's transportation fuel supply and assist in reducing greenhouse gas emissions in the decades to come.

The successful candidate will be part of a team working on all areas related to algae strain selection, improvement and cultivation at lab, pilot and demonstration scale. Responsibilities will include defining and executing an experimental program aimed at maximizing the production of oils from microalgae to manufacture a full range of transportation fuels (gasoline, jet or diesel) which meet the same specifications as today's products. The successful candidate will have a strong background in phycology, algae aquaculture, algae ecology and biology. Additionally, a background in photosynthesis and photo-physics is a plus. Ideally, the successful candidate would also have practical experience in large scale algae production and an understanding of biology and engineering fundamentals for carrying out large-scale aquaculture. A PhD in phycology or biology or related field is required. The candidate must be capable of independently developing high-level and broad-based research programs, have excellent analytical skills, demonstrate strong leadership skills, and have outstanding communication skills.

ExxonMobil's Corporate Strategic Research (CSR) laboratory is a dynamic and exciting place to work. CSR is located in scenic western New Jersey, about an hour west of New York City and 45 minutes northwest of Princeton. Within CSR, active research programs exist in all areas of the company's business and include the traditional fields of chemical engineering, materials science, chemistry, physics, geoscience and mechanical engineering. Interdisciplinary research is the norm, and close ties are maintained with the academic and national laboratory communities through publication and presentation of results.

ExxonMobil offers an excellent working environment and a competitive compensation and benefits package. Please submit your cover letter and resume to our website at www.exxonmobil.com/ex and apply to Phycologist.

**ExxonMobil is an
Equal Opportunity Employer**

WOMEN IN SCIENCE

forging new pathways in green science

Read inspiring stories of women working in "Green Science" who are blending a unique combination of enthusiasm for science and concern for others to make the world a better place.

Download this free booklet
ScienceCareers.org/LOrealWiS



This booklet is brought to you by the
AAAS/Science Business Office in partnership
with the L'Oréal Foundation



Carol Grotnes Belk Endowed Professor of Bioinformatics and Genomics Department of Bioinformatics and Genomics College of Computing and Informatics

The University of North Carolina at Charlotte invites applications for the Carol Grotnes Belk Endowed Distinguished Professorship of Bioinformatics and Genomics. The Department (www.bioinformatics.uncc.edu) seeks candidates who have outstanding research programs directed toward critical issues in 21st century biology using computational techniques, alone or in combination with experimental approaches. The primary appointment for this tenured position will be in the recently established Department of Bioinformatics and Genomics. The successful candidate will have an earned doctorate, significant scholarship, and a history of funded research. The Department has the leadership role in bioinformatics for the North Carolina Research Campus, an emerging \$1 billion biotechnology and research hub in nearby Kannapolis, N.C. The position has a competitive salary, a generous startup package, and continuing funding from the endowment.

Applications and Nominations: Applications must be made electronically at jobs.uncc.edu (position #1070) and must include a cover letter, a CV, a list of four references with contact information, and statements on research, teaching, and leadership. Applicants are also encouraged to contact the Search Committee Chair, **Dr. Lawrence Mays** (lemays@uncc.edu) or **Rent Consulting Group**, which is assisting in the search (704-366-2388 or info@rentconsultinggroup.com). Nominations should be sent to the committee chair at the Department of Bioinformatics and Genomics. Review will begin on **16 May 2011** and continues until the position is filled. All inquiries and applications will be treated as confidential. The finalist will be subject to a background check.

The University of North Carolina at Charlotte is an EOE/AA Employer and an NSF ADVANCE Institution.



RENT CONSULTING GROUP, LLC
Executive Search / Organizational and Leadership Development / Strategic Planning and Marketing



TEXAS TECH UNIVERSITY
HEALTH SCIENCES CENTER
at Amarillo

Faculty Position in Cancer Research

The Department of Biomedical Sciences, School of Pharmacy at Texas Tech University Health Sciences Center (TTUHSC), Amarillo, TX seeks applicants for a tenure-track faculty position at the Associate Professor level. The successful candidate will join a vibrant and expanding group of extramurally funded biomedical and pharmaceutical researchers (<http://www.ttuhsc.edu/sop/biomedicalsciences>) who are part of TTUHSC Cancer Center. Applicants must have a doctoral degree with an established extramurally funded research program in cancer biology, genetics, chemoprevention, or therapeutics. Expertise in pharmacogenetic/genomics/proteomics, genetic models, medicinal and synthetic chemistry, cancer stem cells, microRNA and epigenetics, computational/systems biology is desirable. The successful candidate will be expected to teach Pharm.D. and Ph.D. students. Competitive salary, start-up package, and laboratory space are available. For finalist applying from outside of the State of Texas, the School will work with him/her to apply for one of the recruitment grant mechanisms from the Cancer Prevention Institute of Texas (CPRIT) (<http://www.cprit.state.tx.us>).

Applicants should submit documents online at <http://jobs.texastech.edu> (job requisition number: 83277). Please include curriculum vitae, a summary of research accomplishments/interests, future directions, teaching philosophy and experience and names and addresses of three references. TTUHSC in Amarillo includes the School of Pharmacy (Departments of Biomedical Sciences, Pharmaceutical Sciences, and Pharmacy Practice) and School of Medicine. The Biomedical Sciences Department has 18 full-time faculty with research interests in cancer biology, therapeutics and chemoprevention as well as immunology and vascular and renal physiology, and state-of-the-art core facilities. Please contact the search committee chair, **Dr. Sanjay K. Srivastava**. E-mail: sanjay.srivastava@ttuhsc.edu. Telephone: (806) 356-4750 ext 224.

*TTUHSC is an Equal Opportunity/Affirmative Action Institution.
Minorities and women are encouraged to apply.*



KYUSHU UNIVERSITY



International Institute for Carbon-Neutral Energy Research

The International Institute for Carbon-Neutral Energy Research (I²CNER) at Kyushu University in Japan is actively seeking candidates for open-rank faculty and post-doctoral research associates.

Outline: The International Institute for Carbon-Neutral Energy Research (I²CNER) is a member of the World Premier International Research Center Initiative established by the Japanese Ministry of Education, Culture, Science and Technology (MEXT). Faculty members and researchers associated with I²CNER are dedicated to the Institute's mission to contribute to the creation of a sustainable and environmentally friendly society by advancing fundamental science to reduce CO₂ emissions and the realization of a hydrogen economy. The ITO Campus of the Kyushu University houses extensive state-of-the-art experimental and computational facilities.

Qualifications: The successful candidate will have experimental or computational expertise in the physics, chemistry, mechanics, and materials science aspects of:

- Basic science issues underlying CO₂ separation/concentration and geologic/oceanic capture and sequestration
- Hydrogen embrittlement
- Solar/chemical hydrogen production

Faculty members are expected to initiate and sustain vigorous research programs that both advance and are relevant to the mission of I²CNER. Candidates for faculty positions must have achieved national and international recognition for their research accomplishments. Post-doctoral research associates will join research groups relevant to their field of expertise and education.

Application process: Applicants must provide (1) Application Form (the designated form is on the website); (2) curriculum vitae that details research experience and interests; (3) a list of publications; (4) the names and contact information of four references. All materials must be submitted in English.

Starting Date: As soon as possible after closing date

Salary: Commensurate with qualifications and experience

Application Deadline: 17:00 (Japan Time), June 8th (WED), 2011; Interviews may take place prior to the closing date; however, no final decisions will be made until after this time.

Applications should be submitted to: send the attachment files to the e-mail address below

E-mail: wpi-office@i2cner.kyushu-u.ac.jp

For more information: <http://i2cner.kyushu-u.ac.jp/en/recruit/recruit.php>

Contact: For questions on the application procedures please contact at wpi-office@i2cner.kyushu-u.ac.jp

International Institute for Carbon-Neutral Energy Research (I²CNER), Kyushu University, 744 Motooka, Nishi-ku, Fukuoka, Postal Code 819-0395, JAPAN

TEL: +81-(0)92-802-6932 FAX: +81-(0)92-802-6939

Kyushu University is an Equal Opportunity/Affirmative Action Employer. The administration, faculty and staff embrace diversity and are committed to attracting qualified candidates who also embrace and value diversity and inclusivity.

The Gatsby Charitable Foundation



UNIVERSITY OF
CAMBRIDGE

Research Group Leader, Sainsbury Laboratory, Cambridge University

The Gatsby Charitable Foundation invites applications for Research Group Leader positions to be held at the Sainsbury Laboratory at the University of Cambridge.

The positions are open to applicants of any nationality. The Gatsby Charitable Foundation intends that the positions will be awarded across a broad range of seniority, but applicants would typically have postdoctoral experience in a field related to the overall scientific focus of the Laboratory in plant development and in computational modelling of development. Applicants should be able to provide strong evidence of their potential to become independent scientific group leaders. Applicants who currently hold a permanent post in a University or other Research Organisation are welcome to apply.

Funding will initially be provided for five years, with a possible extension for a further five year term, with no overall limit on number of extensions. The laboratory has excellent core facilities, including growth room, glass-house and computing facilities. Group Leaders will be provided with an annual research grant exceeding £250,000 per annum in addition to their salary. Once in post, group leaders will be eligible to apply for research grant funding from other sources.

Applications should be submitted electronically as PDF files and include a full CV, a research proposal for the initial five year period as group leader, and the names of at least three referees. Further guidance and details about the laboratory can be obtained by e-mailing Sainsburylaboratory@admin.cam.ac.uk. Completed applications should be sent by e-mail to Sainsbury.applications@admin.cam.ac.uk.

Applications can be submitted at any time. Applications will be peer reviewed by the Gatsby Charitable Foundation at least three times annually.



ISTITUTO ITALIANO DI TECNOLOGIA
ISI GENOMICS CENTER OF GENOMIC SCIENCE

Screening Unit, Center of Genomic Science of IIT@SEM, Istituto Italiano di Tecnologia, Milan, Italy

Istituto Italiano di Tecnologia (IIT, <http://www.iit.it>) has created an IIT-Network comprising nine outstations at Italian research institutions. The IIT@SEM outstation is affiliated with the European School of Molecular Medicine (SEMM; <http://www.semm.it>) at the IFOM-IEO Campus in Milan (<http://www.ifom-ieo-campus.it>), a research center dedicated to basic and translational cancer biology, home to state-of-the-art technological services. IIT@SEM focuses on Genomic Science, and in particular Cancer Genomics (<http://genomics.iit.it>). The program includes a Screening Unit, which will perform high-throughput cell-based phenotypic screens. Both small molecule and genetic screens will be performed, with a variety of endpoints including homogenous assay formats (primarily fluorescence and luminescence) and high content imaging (microscopy-based readouts). The following positions are available within the unit:

Cell Biologist

We are seeking a cell biologist who will be responsible for the translation of benchtop assays to high throughput format. Experience with functional genomics (siRNA or cDNA screens) is required, and knowledge of image acquisition and analysis is preferred. Experience in the development and validation of cell-based assays will be at a distinct advantage. The successful applicant will also design or evaluate novel screening approaches. He/she is expected to thrive on the technical challenges that the role presents, and must have the ability to interact with colleagues with diverse skills.

Lab Automation Specialist

The Lab Automation Specialist will utilize modular and integrated robotics platforms in order to facilitate screening campaigns within the Unit. The successful candidate will be expected to provide hands-on training to collaborators on automated screening equipment. Experience with compound or siRNA library management, automated liquid handling, assay plate replication and re-formatting is required. Candidates with experience in programming and troubleshooting automated equipment will be at an advantage. A background in life sciences is preferred, but not essential.

Computational Biologist

The Computational Biologist will utilize existing software, and develop custom-made algorithms in order to analyze and prioritize data generated during screening campaigns. He/she will interact with a strong IT department on site, as well as external screening units in order to develop an internal laboratory management (LIMS) system and data sharing platforms for internal and external collaborators. Expertise with Java (in particular Spring/JSP) and Python programming languages is required. Experience with bio-analytical tools for pathway analysis and the R statistical programming language is a distinct plus.

The above positions will be subject to Post-doctoral contracts and require a PhD degree with or without post-doctoral experience. Candidates should submit a CV, names and e-mail addresses of 3 referees and personal statement (2 pages max) focusing on their skills and interests to Dr. Mark Wade, Coordinator of the Screening Unit (Mark.Wade@iit.it). **Application deadline: May 16, 2011**

In order to comply with the Italian law (art. 23 of Privacy Law of the Italian Legislative Decree n. 196/03), we kindly ask every candidate to provide his/her consent to allow IIT to process his/her personal data. The Italian Institute of Technology is an Equal Opportunity Employer that actively seeks diversity in the workforce.

POSITIONS OPEN

VISITING INSTRUCTOR
PHYSIOLOGIST

The Biology Department at the University of Richmond seeks to fill a one-year visiting instructor position beginning August 1, 2011. We are looking for a broadly trained biologist with expertise in cell, plant, and animal physiology. We seek individuals with a strong commitment to high quality undergraduate education, which includes working closely with a team of instructors in multi-section lecture and laboratory courses. Teaching expectations include participation in our Cell Biology and Integrative (plant and animal) Physiology courses. Candidates are encouraged to provide evidence of teaching excellence.

The application deadline is May 15, 2011, but applicants will be considered until the position is filled. Qualified applicants should hold a Ph.D. degree. Applicants should submit curriculum vitae, a statement of teaching philosophy, a description of research background, and names of references electronically to **Dr. Roni Kingsley** (e-mail: rkingsley@richmond.edu), Department of Biology, University of Richmond, Richmond VA 23173.

The University of Richmond is committed to developing a diverse workforce and student body and to being an inclusive community. We strongly encourage applications from candidates who will contribute to these goals. For more information on the department, resources, and teaching responsibilities, see [website: http://biology.richmond.edu/](http://biology.richmond.edu/).

POSTDOCTORAL POSITIONS
Center for Cardiovascular Sciences
Albany Medical College

A postdoctoral position is available at the Center for Cardiovascular Sciences, Albany Medical College, Albany, New York. Our research interest is on the proteins that control lipid droplet metabolism in macrophage/foam cells and their role in atherosclerosis. Recent Ph.D.s with skills in molecular and cellular biology and experience working with mice are encouraged to apply. Applicants should respond electronically with curriculum vitae, a statement of research interest, copies of at least two representative manuscripts, and a list of three individuals who can serve as reference to: **Antoni Paul, Ph.D., Assistant Professor**, Albany Medical College, Albany, NY 12208. E-mail: paula@mail.amc.edu.

AMC supports a diversified, smoke-free environment and is proud to be an Equal Opportunity/Affirmative Action Employer, encouraging women, and minorities to apply. In support of a safe, drug-free environment, criminal background checks and drug testing are part of our hiring process.

ASSISTANT RESEARCH SCIENTIST position is available in plant genomics and systems biology. A successful applicant (\$30K–\$45K) must have a Ph.D. in biology and extensive laboratory expertise, skills, and experience in the field, particularly in large-scale cloning of agronomic genes and QTLs, gene network construction, BIBAC transformation in cotton and rice, digitally integrative physical/genetic mapping, and gene copy number assay. To apply, send curriculum vitae and five references before May 6, 2011: **Dr. H.-B. Zhang** (e-mail: hbz7049@tamu.edu), Department of Soil & Crop Sciences, Texas A&M University, College Station, TX 77843-2474.

SENIOR POSTDOCTORAL ASSOCIATE
Boston University

Required expertise in transgenic rats, ultrasound molecular imaging, arterial stiffness analysis, and sonoporation, FACS, MoFlo, confocal microscopy. M.D. or Ph.D., \$40,000/year. Send curriculum vitae to **Nancy Clinton**, ncClinton@bu.edu. Equal Opportunity Employer/Affirmative Action.

POSITIONS OPEN

LECTURER in Quantitative Biology
Req #00782

The Biological Sciences Collegiate Division at the University of Chicago invites applications for a full-time Lecturer in quantitative biology to develop and teach courses on quantitative methods for students in the biological sciences. This position is part of a broader effort to create an integrated biological sciences curriculum that serves the needs of future biological and medical scientists, by giving them the mathematical and computational skills necessary to model the mechanisms of biological processes and to analyze complex biological data.

The ideal candidate will have a passion for student learning, evidenced by a record of excellence in teaching, and must either: (a) hold a Ph.D. in a quantitative field (including, but not limited to, computer science, statistics, or applied mathematics) and have a record of significant contribution to biological research; or (b) hold a Ph.D. in a field of biological sciences and have expertise in application of computational or mathematical methods to biological problems.

Contingent upon funding, this position will start on September 1, 2011, and the appointment will be for a term of three years, with the possibility of renewal. Applicants must apply online at the University of Chicago's Academic Career Opportunities [website: http://academiccareers.uchicago.edu](http://academiccareers.uchicago.edu) and select requisition #00782.

Applicants are required to upload the following materials: cover letter, curriculum vitae, statement of teaching interests, and names and contact information for three references. Your application and supporting materials must be uploaded by May 23, 2011.

The University of Chicago is an Affirmative Action/Equal Opportunity Employer.

POSTDOCTORAL POSITION in
Molecular Toxicology at
University of California, Los Angeles

You will perform research in one of the following areas: Environmental causation of Parkinson's disease in the laboratories of Jeff Bronstein, Marie-Françoise Chesselet, David Krantz, or Beate Ritz; Chemical carcinogenesis and mutagenesis with John Froines, Oliver Hankinson, Jeffrey Miller, or Robert Schiestl; Nanotoxicology with Andre Nel; or Cardiotoxicology with Jesus Araujo.

Please see [website: http://www.ph.ucla.edu/moltox/faculty.php](http://www.ph.ucla.edu/moltox/faculty.php) for further details. *Applicants must be citizen or non-citizen nationals of the United States, or permanent residents.* The stipend varies from \$37,740 to \$52,068, depending on years of experience. Health insurance will also be provided.

One (or perhaps two) positions will be available on July 1, 2011.

Contact **Dr. Oliver Hankinson** at e-mail: ohank@mednet.ucla.edu.

POSTDOCTORAL RESEARCHERS to study Salmonella pathogenesis. The first project is to study Salmonella interactions with the normal microbiota. The candidate will use TraSH or Tn-seq to identify Salmonella genes required for fitness in gnotobiotic mice. The second project is to characterize Salmonella metabolism during infection and to determine the SirA and CsrA regulons using ChIP/RNA-seq.

Candidates are required to have a Doctorate in Microbiology or related field. Qualified applicants should send curriculum vitae, three letters of reference, and relevant reprints by e-mail to **Brian Ahmer** (e-mail: ahmer.1@osu.edu).

To build a diverse workforce the Ohio State University encourages applications from minorities, veterans, women, and individuals with disabilities. Flexible work options available. Ohio State is an NSF ADVANCE Institution. Equal Employment Opportunity/Affirmative Action employer.

POSITIONS OPEN

POSTDOCTORAL POSITIONS in
Cardiovascular Research

NIH-funded positions are available in the Department of Molecular Cardiology at the Cleveland Clinic to study newly discovered transmembrane proteases involved in cardiovascular disease. Research projects include biochemical analysis of novel enzymes and phenotypic characterization of knockout mouse models ([website: http://www.lerner.ccf.org/moleccard/wu/](http://www.lerner.ccf.org/moleccard/wu/)). Recent graduates with a Ph.D. and/or M.D. and strong background in protein chemistry and mouse models are encouraged to apply. Previous experience in cardiovascular research will be advantageous. Send your curriculum vitae and a list of three references to **Qingyu Wu, M.D., Ph.D.** at e-mail: wuq@ccf.org.

Your career is our cause.

Get help
from the
experts.

[www.
sciencecareers.org](http://www.sciencecareers.org)

- Job Postings
- Job Alerts
- Resume/CV Database
- Career Advice
- Career Forum

Science Careers
From the journal Science 

Find your future here.



Science Careers
From the journal Science 

www.ScienceCareers.org

Who's helping you get more for your retirement?

Take the Fidelity Challenge: Put your savings and current retirement savings provider to the test. We're already helping thousands of higher education professionals like you take a fresh look at their investments.

THE FIDELITY CHALLENGE

- ☐ **Start with a plan.** One that gives you the flexibility to make adjustments as your needs change.
- ☐ **Find the right mix.** Determine how to divide up your portfolio to help you meet your goals.
- ☐ **Compare investments.** Evaluate what you own now and explore other choices to consider.



Take the Fidelity Challenge today

Schedule your one-on-one consultation with a Fidelity Planning and Guidance Consultant, and bring us your questions. You don't have to be a Fidelity client — and there's no cost or obligation. Let us help you feel more comfortable about your retirement.

Start now.

866.715.6111
Fidelity.com/challenge

Turn here®



Keep in mind investing involves risk. The value of your investment will fluctuate over time and you may gain or lose money.

Although consultations are one on one, guidance provided by Fidelity is educational in nature, is not individualized, and is not intended to serve as the primary or sole basis for your investment or tax-planning decisions.

Fidelity Brokerage Services LLC, Member NYSE, SIPC. © 2011 FMR LLC. All rights reserved. 578417.1.0

Cancer

Development

Endocrinology

Glycobiology

Immunology

Neuroscience

Proteases

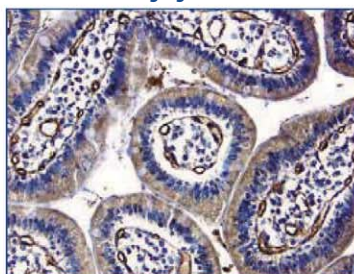
Signal Transduction

Stem Cells

R&D Systems Specialized Tools for Cancer Research

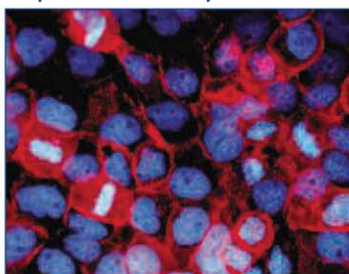
Cancer is a disease of cellular dysfunction involving a range of biological activities that promote unregulated proliferation. To help advance the understanding of this complex disease, R&D Systems offers an expansive selection of quality products, including **high performance antibodies, proteins, ELISAs, & arrays**, for investigating various cancer-related factors. Every product from R&D Systems undergoes rigorous quality control testing to ensure industry leading reliability.

Angiogenesis



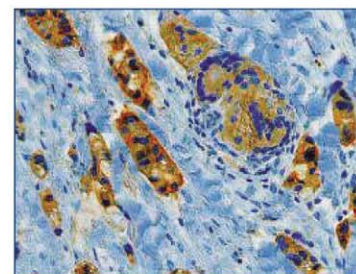
Angiopoietin-2 (Catalog # AF623)
Human Gastrointestinal Cancer Tissue

Epithelial to Mesenchymal Transition



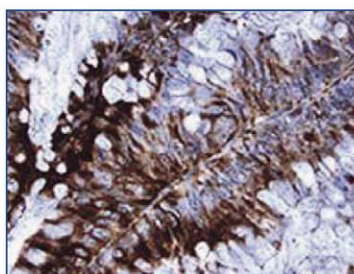
E-Cadherin (Catalog # AF648)
Human Epidermoid Carcinoma Cells

Cancer Biomarkers



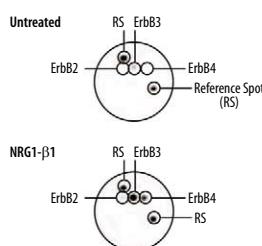
BRCA1 (Catalog # MAB22101)
Human Breast Cancer Tissue

Inflammation



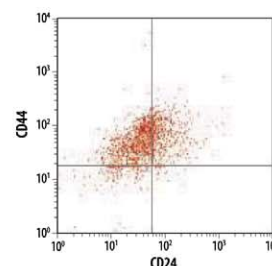
EMAP-II (Catalog # AF1910)
Human Colon Cancer Tissue

Growth Factor/Receptor Signaling



Proteome Profiler™ 96 Phospho-RTK Antibody
Array (Catalog # ARZ001)
MDA-MB-453 Cell Line

Cancer Stem Cells



MagCollect CD24- CD44+ Breast Cancer
Stem Cell Isolation Kit (Catalog # MAGH111)
MCF-7 Cell Line

For more information visit our website at www.RnDSystems.com/go/Cancer

For research use only. Not for use in diagnostic procedures.

R&D Systems, Inc. www.RnDSystems.com

R&D Systems Europe, Ltd. www.RnDSystems.co.uk

R&D Systems China Co., Ltd. www.RnDSystemsChina.com.cn

R&D
SYSTEMS®